

TKK Dissertations 42
Espoo 2006

**TRANSIENT BASED EARTH FAULT LOCATION IN
110 KV SUBTRANSMISSION NETWORKS**

Doctoral Dissertation

Peter Imriš



**Helsinki University of Technology
Department of Electrical and Communications Engineering
Power Systems and High Voltage Engineering**

TKK Dissertations 42
Espoo 2006

TRANSIENT BASED EARTH FAULT LOCATION IN 110 KV SUBTRANSMISSION NETWORKS

Doctoral Dissertation

Peter Imriš

Dissertation for the degree of Doctor of Science in Technology to be presented with due permission of the Department of Electrical and Communications Engineering for public examination and debate in Auditorium S5 at Helsinki University of Technology (Espoo, Finland) on the 5th of October, 2006, at 12 noon.

**Helsinki University of Technology
Department of Electrical and Communications Engineering
Power Systems and High Voltage Engineering**

**Teknillinen korkeakoulu
Sähkö- ja tietoliikennetekniikan osasto
Sähköverkot ja suurjännitetekniikka**

Distribution:

Helsinki University of Technology
Department of Electrical and Communications Engineering
Power Systems and High Voltage Engineering
P.O. Box 3000
FI - 02015 TKK
FINLAND
URL: <http://powersystems.tkk.fi/eng/>
Tel. +358-9-4511
Fax +358-9-451 5012
E-mail: peter.imris@tkk.fi

© 2006 Peter Imriš

ISBN 951-22-8370-0
ISBN 951-22-8371-9 (PDF)
ISSN 1795-2239
ISSN 1795-4584 (PDF)
URL: <http://lib.tkk.fi/Diss/2006/isbn9512283719/>

TKK-DISS-2173

Edita Prima Oy
Helsinki 2006



HELSINKI UNIVERSITY OF TECHNOLOGY P. O. BOX 1000, FI-02015 TKK http://www.tkk.fi		ABSTRACT OF DOCTORAL DISSERTATION	
Author Peter Imriš			
Name of the dissertation Transient based earth fault location in 110 kV subtransmission networks			
Date of manuscript August 2006		Date of the dissertation 5th October 2006	
<input checked="" type="checkbox"/> Monograph		<input type="checkbox"/> Article dissertation (summary + original articles)	
Department Department of Electrical and Communications Engineering			
Laboratory Power Systems and High Voltage Engineering			
Field of research Power systems			
Opponent(s) Professor, Linas Markevičius, Dr. Seppo Hänninen			
Supervisor Professor Matti Lehtonen			
Abstract <p>This thesis deals with ground fault location in subtransmission networks. The main subject of the thesis is transient based ground fault location using low frequency fault generated transients. However, the thesis also considers the conventional fault location methods and reviews the various other methods. Low frequency transient based methods, in general, are more precise and more reliable than the conventional methods based on fundamental frequency. They also avoid the need for further investment in existing systems that would be required, for example, for the implementation of travelling wave fault location, as existing transient recorders can be used.</p> <p>As a byproduct of the thorough investigation of conventional fault location and the presentation of its properties and limitations, a new error estimation technique is proposed.</p> <p>Fault generated transients are presented and tested, and their potential to aid fault location using the phase or neutral current is studied. The thesis also tries to solve some of the problems related to fault transient generation and propagation, as well as measurements and signal processing. The network configuration and transformer neutral grounding type receive special attention. The thesis shows the network conditions under which the method works reliably and accurately, and for critical conditions it proposes appropriate correction factors. The studies are performed for the 110 kV overhead lines under the jurisdiction of Fingrid (the Finnish electricity transmission system operator) for all kinds of neutral configurations. The EMTP/ATP software package is used as the network simulator. The results of the simulations as well as real ground fault recordings are analysed and processed in a fault locator developed by the author and implemented in Matlab.</p>			
Keywords Fault location, Single-phase to ground faults, Fault transients, Subtransmission network, Wavelets			
ISBN (printed) 951-22-8370-0		ISSN (printed) 1795-2239	
ISBN (pdf) 951-22-8371-9		ISSN (pdf) 1795-4584	
ISBN (others)		Number of pages 156 p.+ app. 45 p.	
Publisher Helsinki University of Technology, Power Systems and High Voltage Engineering			
Print distribution Helsinki University of Technology, Power Systems and High Voltage Engineering			
<input checked="" type="checkbox"/> The dissertation can be read at http://lib.tkk.fi/Diss/2006/isbn9512283719/			

Acknowledgements

This thesis was prepared at the Helsinki University of Technology (HUT) during the years 2003-2006. The research project was sponsored by the Finnish electricity transmission system operator (Fingrid Oyj).

In the first place I would like to express my thanks to Prof. Matti Lehtonen, the head of the Power Systems and High Voltage Engineering laboratory at HUT, for his guidance and help as supervisor of this work. Personally, I also thank the leading expert for technology and development, Jarmo Elovaara, MSc., and also Simo Välimaa, MSc., and Patrik Lindblad, MSc., the protection experts in Fingrid, for their valuable comments on this work. Thanks also for the pre-examination and comments on this thesis, namely, to Dr. Seppo Hänninen, Senior Research Scientist at VTT (Technical research centre of Finland), and to Ülo Treufeldt, associate professor, PhD., at the Department of Electrical Power Engineering of the Tallinn University of Technology. I am also thankful to John Millar, who helped me to correct the language errors in the original document, since English is not my mother tongue. Many thanks also to Prof. Tapani Jokinen, who helped me during my first stay in Finland in 2001.

I am very grateful to all the financial supporters of this research. In particular, I am very thankful for the financial support of Fingrid over three years and for the technical data. The support of the Power Systems and High Voltage Engineering laboratory over the final period of this work is very much appreciated. Many thanks also to the Fortum company for supporting the writing of this thesis by awarding me with the stipendium “Fortumin säätiö - B3”, in the year 2006. Thanks also to the Graduate School of Electrical and Communications Engineering for their scholarships.

My stay in the Power Systems and High Voltage Engineering laboratory would not be so pleasant without its staff. I would like to thank to all members of the Power system and High Voltage Engineering laboratory for their friendship and support over the past years.

At last but most significantly, thanks to my parents and grandparents for everything.

In Otaniemi, October 5th 2006, A.D.+
Peter Imriš

Author's contribution

Conventional methods

The conventional method for fault location in radially operated solidly earthed network is based on estimation of the fault loop impedance. This method has limitations, mainly imposed by the load current and fault resistance. The error is linearly dependent with fault resistance. This sensitivity to the fault resistance can be reduced by the improved conventional method. This approach takes into account only the reactance of the fault loop and this way the fault resistance effect is reduced (supposing the fault is purely resistive). The reduction in the influence of the fault resistance is significant, but it also means that the fault location will have more limited usage under certain conditions, namely if the relation between the load and fault current is unfavourable. This area is theoretically described and tested with simulated data, and an error estimation algorithm is developed. The new error estimation algorithm is based on the measured load/fault current ratio and the line parameters.

Signal processing

So far the wavelet algorithm has only been tested with the wavelet transform. However, fault transients can be filtered out of fault signals by either the wavelet transform or the wavelet filter. The wavelet transform is very good for visualisation of the signal in different frequency bands, but its application for fault location purposes may be rather risky in some cases. The wavelet transform might in practice fail in cases where the transient appears close to the scale border. In such cases the scale borders should be changed. Therefore, for practical applications, it is more convenient to use the wavelet filter instead. In this thesis, both techniques are used in the wavelet algorithm. The utilisation of the wavelet filter with the wavelet algorithm is a new approach in this area and makes fault distance calculation more accurate in subtransmission networks.

Modelling of the voltage transformer

A new model of 110 kV voltage transformers is developed for use with transients. The modelling is based on open and short circuit measurements at 50 Hz to calculate the lumped resistances and inductances. In order to make the model frequency response similar to a real transformer, capacitances are added. These capacitances are achieved from an impulse measurement on the real transformer and are recalculated by a new method for the model. The developed model of the instrument transformer can be used for correction of the measured signals in real fault recording.

Transient propagation through the network

A typical subtransmission network is modelled and shows that the fault transient returns via the ground wires rather than via the ground. This makes the transient less dependent on the unstable ground resistivity.

Correction factors

The transient based fault location method can be used in networks with solidly grounded neutrals. Use of the method in a network with some grounding impedance (Petersen coil, low-reactance, or isolated) depends on the existence of a return path to the substation. The zero-sequence current in the measurement point is increased by the connected lines or by compensation capacitors placed on the busbar (with grounded neutral). The longer the connected lines and shorter the line section behind the fault, the more precise the fault location will be. However, this phenomenon is mathematically described and the critical area can be corrected by the method proposed.

Table of contents

1	Introduction	1
2	Finnish transmission networks.....	4
2.1	Network description	4
2.2	Fingrid's fault policy	7
3	Fault locators.....	9
3.1	Division of fault locators	9
3.1.1	Fault locators using fault generated signals	9
3.1.2	Fault locators using external signal sources	11
3.2	Low frequency transient based fault location	12
3.2.1	Wavelet algorithm	13
3.2.2	Differential equation algorithm	13
3.3	Literature review.....	14
4	Conventional fault location.....	15
4.1	Conventional method.....	15
4.1.1	Method error	17
4.1.2	EMTP/ATP simulations	19
4.2	Improved conventional fault location	22
4.2.1	Method error	22
4.2.2	Example of zero-crossing calculation.....	25
4.2.3	EMTP/ATP Simulations.....	27
4.2.4	Principle of error estimation	29
4.3	Conventional methods vs. neutral grounding	30
4.4	Conventional methods vs. real ground faults	32
4.5	Utilising the zero-sequence current in conventional fault location	33
4.5.1	EMTP/ATP Simulations.....	33
4.5.2	Real faults from the Pyhäkoski – Rautaruukki line	35
4.6	Discussion.....	36
5	General study of fault transients.....	38
5.1	Charge transient.....	39
5.2	Discharge transient	42
5.3	Suppression coil current transient.....	44

6	Signal processing methods	47
6.1	Pre-processing of the signal.....	47
6.2	Spectrum analysis	49
6.3	Time-frequency representation of the signal	50
6.3.1	Windowed Fourier transform	51
6.3.2	Wavelet transform	53
6.4	Wavelet filter	55
7	Obtaining the fault distance from fault transients	56
7.1	Fault transients.....	56
7.2	Frequency identification of fault transients	57
7.3	Fault location algorithms	60
7.3.1	Wavelet algorithm with the wavelet transform	60
7.3.2	Wavelet algorithm with the wavelet filter	62
7.3.3	Differential equation algorithm	64
7.4	Automatic fault distance detection	65
7.5	Discussion.....	66
8	EMTP/ATP fault transient simulation	68
8.1	Description of the simulated network in EMTP/ATP	68
8.2	Fault transients versus fault location	68
8.2.1	Charge transient	70
8.2.2	Discharge transients.....	71
8.3	Fault transients versus fault conditions	72
8.3.1	Fault resistance	72
8.3.2	Fault voltage inception angle.....	75
8.4	Fault transients versus neutral grounding type	76
8.5	Double-ended method.....	78
8.6	Discussion.....	79
9	Modelling of the 110 kV instrument transformers for transients	81
9.1	Voltage transformer	82
9.1.1	The model's backbone.....	82
9.1.2	Calculation of the equivalent model capacitances.....	84
9.1.3	Model analysis with EMTP/ATP	88
9.1.4	Analysis of the impact of the model components on the frequency response	92
9.2	Burden of the voltage transformer	94
9.3	Current transformer	95
10	Line reactances at transient frequencies	98
10.1	Zero-sequence impedance of the line	100

Table of contents

10.2	Self and mutual inductance of a conductor.....	101
10.3	Reduction factor	102
10.4	Matrix method	105
10.4.1	The effect of counterpoises.....	112
10.5	Line parameter calculation by the Carson formula.....	115
10.6	Discussion.....	119
11	Correction factors.....	120
11.1	Ground fault studies using symmetrical components and line models.....	120
11.1.1	EMTP/ATP modelling of the network	120
11.1.2	Correction factor definition	123
11.1.3	Comparison of the Clark network model with the symmetrical component model	123
11.2	Evaluation of a correction factor for transient based fault location.....	125
11.2.1	Data acquisition	126
11.2.2	EMTP-ATP model.....	126
11.2.3	Error source	126
11.2.4	Comparison of designed correction factor with simulations	130
11.3	Impact of the neutral grounding on fault location accuracy	133
11.4	Error estimation for the transient based ground fault location	135
11.5	Discussion.....	136
12	Transients in real networks	137
12.1	Faults in the 110 kV Pyhäkoski – Rautaruukki line	138
12.2	Faults in the 400 kV Alapitkä – Huutokoski line	140
12.3	Faults in MV networks	141
12.4	Discussion.....	143
13	Fault location program	144
14	Conclusions	151
	References.....	153
	Appendices	157
A	Fault simulations.....	158
A.1	Parameters of the simulated network.....	158
A.2	Simulation results	159
A.2.1	Transient fault location	159
A.2.2	Conventional fault location.....	162
A.3	Pyhäkoski – Rautaruukki faults	165
A.3.1	Real faults	165

Table of contents

A.3.2 Simulated faults	166
A.4 Developing of the equation for improved conventional fault location	167
A.5 Correction factor	168
B Modelling of instrument transformers.....	170
B.1 Parameters of the measured transformers	170
B.2 Lists of performed measurements	178
B.3 Capacitance measurements of PT1	179
Capacitance P-S1	180
Capacitance P-S2.....	181
Capacitance S1-S2.....	182
Capacitance P-B	183
Capacitance S1-B	184
Capacitance S2-B	185
B.4 Detailed calculation of the PT's capacitances.....	186
B.5 Measurement of the cable capacitance.....	187
C Transient propagation in HV OH lines	189
C.1 Description of the overhead line	189
C.2 Detailed calculations of reduction factor	190
C.3 Detailed calculations for the matrix method	194
C.4 Carson's formula.....	195
C.4.1 Definition	195
C.4.2 Terms and definitions	196
C.5 Line impedance transformation.....	200

Terms and Abbreviations

AC	Alternating current
CFL	Conventional fault location
CT	Current transformer at 110 kV level (also CT1, CT2, CT3 and CT4)
DEA	Differential equation algorithm
DC	Direct current
DEM	Double-ended method
Den	Denominator of the fault location equation
DFT	Discrete Fourier transform
DWF	Discrete wavelet filter
DWT	Discrete wavelet transform
EMTP/ATP	Electromagnetic Transients Program-Alternative Transient Program
FEM	Finite element method
Fingrid	Finnish electricity transmission system operator
FIR	Finite impulse response
FL	Fault locator
Fortum	Energy company in the Nordic countries
FT	Fourier transform
GMD	Geometric mean distance
GMR	Geometric mean radius
HUT	Helsinki University of Technology, Finland
HV	High voltage
ICFL	Improved conventional fault location
MEM	Multi-ended method
MRA	Multi-resolution analysis
MV	Medium voltage
OH	Overhead (lines)
P	Primary of the transformer
PSS/E	Power system simulator for engineering
PT	Potential (voltage) transformer at 110 kV level (also PT1, PT2 and PT3)
S	Secondary of the transformer (also S1, S2)
SEM	Single-ended method
VTT	Technical research centre of Finland
WA	Wavelet algorithm
WDFT	Window discrete Fourier transform
WF	Wavelet filter

Terms and Abbreviations

WFT	Window Fourier transform
WT	Wavelet transform
a	Scale
b	Translation
b_i	Carson's coefficient
c	The speed of light
C	Capacitance
C_0'	Zero-sequence capacitance of the line per km
C_1'	Positive-sequence capacitance of the line per km
C_2'	Negative-sequence capacitance of the line per km
C_{12}	Measured capacitance between the primary (P) and secondary (S1) of the transformer
C_{13}	Measured capacitance between the primary (P) and secondary (S2) of the transformer
C_{14}	Measured capacitance between the primary (P) and body (b) of the transformer
C_{24}	Measured capacitance between the secondary (S1) and body (b) of the transformer
C_{34}	Measured capacitance between the secondary (S2) and body (b) of the transformer
C_{23}	Measured capacitance between the secondary (S1) and secondary (S2) of the transformer
C_B	Busbar capacitance
C_E	Phase to earth capacitance of the line
C_E'	Phase to earth capacitance of the connected line
C_{eq}	Equivalent capacitance of the line
C_{eq}'	Equivalent capacitance of the connected line
C_f	Correction factor
C_i	Carson's coefficient
C_{pb}	Capacitance between the primary winding (P) and body (b) of the transformer
C_{pp}	Phase to phase capacitance of the line
C_{pp}'	Phase to phase capacitance of the connected line
C_{ps1}	Capacitance between the primary winding (P) and secondary (S1) of the transformer

Terms and Abbreviations

C_{ps2}	Capacitance between the primary winding (P) and secondary (S2) of the transformer
C_{s1b}	Capacitance between the secondary (S1) and body (b) of the transformer
C_{s2b}	Capacitance between the secondary (S2) and body (b) of the transformer
C_{s1s2}	Capacitance between the secondary (S1) and secondary (S2) of the transformer
$C(\omega)$	Frequency dependent capacitance
D	Distance between the conductors
D_{123}	Equivalent distance between the phase conductors
D_{aa}	Self GMD of the composite line conductor
D_{ag}	GMD between line conductors and ground wires
D_e	Depth of equivalent ground conductor
DFT(v)	Spectrum of the voltage
DFT(i)	Spectrum of the current
D_{gg}	Self GMD of the composite ground wire
D_h	Height of the phase conductor over ground
d_i	Carson's coefficient
D_{ij}	Distance between conductor i and image of conductor j
d_{ij}	Distance between conductors i and j
D_{kk}	GMR of a conductor
$D_{k'k'}$	GMR of a fictional ground conductor
$D_{kk'}$	Depth of equivalent ground conductor
D_x	Height of overhead ground conductors above phase conductors
D_y	Horizontal spacing of the conductors
D_z	Horizontal spacing of the conductors
f	Frequency
F_0	Magnetic flux of the transformer
f_c	Frequency of charge transient
f_{c1}	Lower cutoff frequency of band-pass FIR filter
f_{c2}	Higher cutoff frequency of band-pass FIR filter
f_d	Frequency of discharge transient
$f[n]$	Original signal - discrete function of the samples
f_s	Sampling frequency
$g[n]$	New signal - discrete function of the samples
$h(k)$	Filter coefficients

Terms and Abbreviations

h_i	Average height above ground of conductor i
i	Current
\underline{I}	Current
\underline{I}_0	Zero-sequence current
\underline{I}_a	Phase current
\hat{i}_c	Initial amplitude of the charge transient in an undamped case
i_c	Current of charge transient
i_d	Current of discharge transient
\hat{i}_e	Uncompensated steady state fault current peak value with zero fault resistance
\underline{I}_f	Fault current
\underline{I}_{gr}	Ground current
\underline{I}_L	Load current
\underline{I}_n	Nominal current
\underline{I}_{ogw}	Overhead ground wire current
\underline{I}_{OM}	Current through magnetizing branch of the transformer
k	Integer variable parameter
k_e	Earth fault factor
k_m	Variable
k_u	Reduction factor
l	Length
l'	Calculated fault distance
L	Inductance
L_0'	Zero-sequence inductance of the line per km
L_1'	Positive-sequence inductance of the line per km
L_2'	Negative-sequence inductance of the line per km
L_a	Inductance per km of a phase conductor
L_{aa}	Inductance of phase conductor-ground loop
L_b	Inductance per km of a phase conductor
L_c	Inductance per km of a phase conductor
L_{eq}	Equivalent inductance
l_{cl}	Length of the connected line
l_f	Fault distance
L_f	Fault path inductance
L_{gg}	Inductance of overhead ground conductor-ground loop

Terms and Abbreviations

L_{int}	Internal inductance of the conductor
L_m	Magnetizing inductance of the transformer
L_{n1}	Inductance per km of an overhead ground conductor
L_{n2}	Inductance per km of an overhead ground conductor
L_p	Inductance of transformer primary
L_{ps1}	Short circuit inductance of the transformer, primary (P) to secondary (S1)
L_s	Inductance of transformer secondary winding
L'_{s1}	Inductance of the transformer secondary (S1) recalculated to the primary
L'_{s2}	Inductance of transformer secondary (S2) recalculated to the primary
L_{sc}	Sum of the inductances of the suppression coil, coupling transformer winding, faulty line length and fault
L_T	Substation transformer inductance
m	Integer variable parameter
M	Mutual inductance
M_{ag}	Mutual inductance between the “phase conductor-ground loop” and the “overhead ground conductor-ground loop”
n	Integer variable parameter
n_0	Number of overhead ground wires
N	Number of samples
N_{50}	Number of samples related to 20 ms (if system frequency is 50 Hz)
n_{grw}	Number of wires representing ground
R	Resistance
R_0'	Zero-sequence resistance of the line per km
R_1'	Positive-sequence resistance of the line per km
R_2'	Negative-sequence resistance of the line per km
r	Radius
r_a	Radius of phase conductor
r_a'	Equivalent radius of phase conductor
R_a	Resistance per km of the phase conductor
R_b	Resistance per km of the phase conductor
R_c	Resistance per km of the phase conductor
R_f	Fault resistance
R_F	Fault path resistance
R_g	Carson’s correction term for self resistance due to the earth
R_{gm}	Carson’s correction term for mutual resistance due to the earth
R_{gr}	Resistance of the ground return circuit

Terms and Abbreviations

r_i	Radius of conductor i
R_{int}	AC resistance of the conductor
R_{kk}	Resistance of the conductor
$R_{k'k'}$	Resistance of the ground return circuit
R_m	Resistance in magnetizing branch
R_{n1}	Resistance per km of the overhead ground conductor
R_{n2}	Resistance per km of the overhead ground conductor
r_{ogw}	Radius of overhead ground wire
r_{ogw}'	Equivalent radius of ground wire
R_{ogw}	Resistance per km of the overhead ground wire
R_p	Resistance of the transformer primary
R_{ps1}	Short circuit resistance of the transformer, primary (P) to secondary (S1)
R_s	Resistance of the transformer secondary
R'_{s1}	Resistance of the transformer secondary (S1) recalculated to the primary
R'_{s2}	Resistance of the transformer secondary (S2) recalculated to the primary
R_{sc}	Sum of the resistances of the suppression coil, coupling transformer winding, faulty line length and fault
t	Time
T	Period
t_f	Time when the fault happened
v	Voltage
\underline{V}_0	Zero-sequence voltage
$V1$	Primary voltage of the transformer
$V2$	Secondary voltage of the transformer
\underline{V}_{Aa}	Voltage drop
\underline{V}_{ae}	Voltage drop
$\underline{V}_{a'e'}$	Voltage drop
v_c	Voltage of charge transient
v_d	Voltage of discharge transient
v_e	Instantaneous phase to earth voltage at the fault moment
\underline{V}_f	Fault phase voltage
\underline{V}_{ge}	Voltage drop
$\underline{V}_{g'e'}$	Voltage drop
\underline{V}_{nN}	Voltage drop
\underline{V}_{rp}	Rated voltage in primary winding of the transformer

Terms and Abbreviations

\underline{V}_{rs}	Rated voltage in secondary winding of the transformer
w	Window function
X_0'	Zero-sequence reactance of the line per km
X_1'	Positive-sequence reactance of the line per km
X_2'	Negative-sequence reactance of the line per km
x	Length of line section
$x[n]$	Discrete function of the samples
$x(t)$	Continuous function of time
X_g	Carson's correction term for self reactance due to the earth
X_{gm}	Carson's correction term for mutual reactance due to the earth
y	Length of line section
Y	Admittance
z	Length of line section
Z	Impedance
\underline{Z}_0	Zero-sequence impedance of the line
\underline{Z}_0'	Zero-sequence impedance of the line per km
\underline{Z}_1'	Positive-sequence impedance of the line per km
\underline{Z}_2'	Negative-sequence impedance of the line per km
\underline{Z}_{aa}	Self-impedance of phase conductor-ground loop
\underline{Z}_{ag}	Mutual impedance between the "phase conductor-ground loop" and the "overhead ground conductor-ground loop"
Z_C	Characteristic impedance of the line
\underline{Z}_{ext}	External impedance of the wire
Z_f	Fault impedance
$\Delta\underline{Z}_g$	Carson's correction term for earth self impedance
\underline{Z}_{gg}	Self-impedance of overhead ground conductor-ground loop
$\Delta\underline{Z}_{gm}$	Carson's correction term for earth mutual impedance
\underline{Z}_{int}	Internal impedance of the wire
\underline{Z}_{ij}'	Mutual impedance of the two conductors i and j
\underline{Z}_L	Load impedance
Z_p	Open circuit impedance of the transformer from primary side
Z_{ps1}	Short circuit impedance of the transformer, primary (P) to secondary (S1)
Z_T	Terminal impedance of the line
α	Constant
δ	Standard deviation

Terms and Abbreviations

δ_f	Error of fault distance computation (also δ_1 , δ_2 and δ_3)
ϵ_0	Permittivity of free space
μ_0	Permeability of free space
μ_r	Relative permeability
v	Velocity of the traveling wave
θ	Angle
ρ	Ground resistivity
ρ_{Al}	Resistivity of aluminium
ρ_{Fe}	Resistivity of steel
ρ_i	Reflection coefficient for current
ρ_v	Reflection coefficient for voltage
τ	Translation
φ	Initial phase angle
φ_0	Zero-crossing angle
φ_∞	Border angle
φ_{cr}	Critical angle
φ_f	Inception angle of fault voltage (from zero crossing) in fault phase
φ_F	Fault current angle
φ_L	Load current angle
φ_{z1}	Angle of positive-sequence impedance of the line
ψ	Mother wavelet
ψ_1	flux linkage
ω	Angular frequency
ω_0	Normalised angular frequency of the wavelet
ω_c	Angular frequency of charge transient
ω_d	Angular frequency of discharge transient
ω_f	Fundamental angular frequency

1 Introduction

Fault location in power systems is not a new task. From the very beginning of power system transmission many techniques have already been applied. One of the first approaches, most probably because of its easy implementation, was based on 50 Hz measurements. This so-called conventional fault location method is still applied in many operating power systems because of its simplicity. Both the accuracy and reliability, however, very much depend on the conditions and behaviour of both the fault and the network. This is the main reason why new fault location methods have been, and still are being, developed in power systems. Nevertheless, not all approaches lead to practical implementation. Many methods based on post fault circuit analysis with outside signal sources, such as the bridge and travelling wave radar methods, are in many cases not applicable. This is most probably because they are slow, require human control and can not detect non-permanent faults. Therefore, the usage of fault generated signals in fault location is highly reasonable.

Due to high fault currents, the location of two- or three- phase short circuits is not a problem. However, the majority of all faults in the 110 kV overhead lines in Finland are of the single-phase to ground type. Their share of all fault types has been in the range of 73-81% during the past 20 years, [27], [10]. Therefore, only this kind of fault is investigated in this thesis. Fault behaviour and hence fault signals (power frequency component and transients) can vary with the neutral grounding type of the network. Therefore, the different kinds of neutral grounding impedances must be taken into account in any general study of fault location. In the network of Fingrid, the Finnish electricity transmission system operator, compensated, reactance grounded and ungrounded neutrals predominate. Most of the 400 and 220 kV transmission networks throughout Finland are effectively grounded. The 110 kV subtransmission networks are for the most part partially grounded via grounding coils. A small part of the 110 kV network is grounded via Petersen coils, mainly in northern Finland. Conventional fault location methods can therefore be effectively used on all 400 kV and 220 kV lines and some of the 110 kV lines, due to the low earthing impedance of the network neutral. However, in the case of a compensated network neutral with Petersen coils, they cannot be used due to the low fault currents. For this part of the network, transient based fault location can be the solution.

Nowadays the trend is to locate faults quickly, reliably and, if possible, without human intervention. This is made directly possible by utilising fault generated signals. A fault

1. Introduction

produces a wide spectrum of signals that contains information about the fault distance. These signals are the power frequency component and the transients. The transients can be used in fault location for both repair and protection purposes instead of the power frequency. This is possible because the fault transients develop much faster and are less dependent on network configuration than the power frequency component. Travelling wave fault locators have already been applied in power systems with success. The travelling waves are of short duration and a high sampling frequency is needed [3] along with a special transducer. Another group of fault locators is based on lower frequency transients, which result from the charging or discharging of the network capacitances. Previous studies of this matter in MV networks are in [1], [2], but their accuracy and reliability are still unknown in HV systems. However, there is the potential to use these transients for fault location, because they do not depend on parameters such as the load as much as conventional fault location based on 50 Hz, and do not need as high an additional investment to the existing system as is required for travelling wave fault location. These methods will be discussed in this thesis, especially the low frequency transient method. Low frequency transient in this work means the charge transient or the suppression coil current transient. The high frequency transients are the discharge transient and travelling waves and are mentioned as well.

Because the fault transients are of different frequencies (higher) than the fundamental frequency, the following aspects must be investigated: 1) The conditions under which the fault transients will be of sufficient amplitude and frequency for fault location. 2) The transients are affected by the network itself during their propagation in fault loop. The line parameters are not constant for different transient frequencies and ground impedances. Also, the way by which the transient returns to the substation might be influential. The return path of the fault current will depend on the overhead ground wires, the network configuration (mainly the connected lines) and also the neutral grounding type. 3) The measurements of the transients are usually performed by instrument transformers, which are designed for 50 Hz. Using these devices for fault transients might not be as accurate as for 50 Hz. The fault transients can be obtained from the measurement of voltages and current at the substation. In practice, the phase voltages and current sum are usually recorded and in some substations the phase voltages and phase currents are recorded. 4) Fault signals are of the special “non-stationary signal” type. In practice these signals also contain a lot of noise and transients other than the needed component. The transient might also be of small amplitude and length. Therefore, for good fault estimation, a suitable signal processing must be chosen.

The objective of the thesis is to develop earth fault distance computation methods for 110 kV subtransmission systems, especially for Petersen coil earthed systems.

1. Introduction

The above mentioned issues are considered in this thesis as follows: The Finnish transmission network and the fault policy in networks of different voltage levels is described in Chapter 2. Chapter 3 reviews “Fault locators”, which in general use the fault generated signals. Special attention is paid to those that use the transients. The conventional method of fault location based on 50 Hz is studied in Chapter 4. Chapter 5, “General study of fault transients”, introduces some theoretical background relevant to fault transient phenomena. “Signal processing methods”, needed for fault location signal processing, are described in Chapter 6. Chapter 7, “Obtaining the fault distance from fault transients”, attempts to explain the principle of fault location implementation in fault signals. “EMTP/ATP fault transient simulation” is presented in Chapter 8. The study of measurement transformer behaviour at transient frequencies is described in Chapter 9, “Modelling of the 110 kV instrument transformers for transients”. Chapter 10, “Line reactances at transient frequencies”, shows line parameter calculation according to the Carson theory and also deals with fault transient penetration into overhead ground wires or the ground, respectively. Chapter 11, “Correction factors”, shows the application area of transient fault location from the network configuration point of view, proposes the necessary corrections and estimates the total error in the transient based method. “Transients in real networks” are studied in Chapter 12. Chapter 13 describes the fault location program developed as a practical implementation of the algorithms studied in this work. The thesis also contains 3 appendices, A, B and C.

2 Finnish transmission networks

The Finnish transmission system consists of 3 voltage levels, 400 kV, 220 kV and 110 kV. The networks consist of overhead lines only. Most of the network is effectively grounded or grounded via low impedance reactors and some of the 110 kV network is compensated by Petersen coils. Some of the network operates radially and some in a loop. Accurate fault location systems for single-phase to ground faults cover most of the transmission network. The exception is the compensated part of the 110 kV network. Section 2.1 describes the Finnish network in detail. Section 2.2 describes Fingrid's fault policy.

2.1 Network description

The 400 kV transmission network throughout the whole of Finland is effectively grounded (earth fault factor $k_e \leq 1.4$). Each transformer's 400 kV neutral is earthed at every substation, usually via a low-reactance earthing coil of about 100 Ω size, in order to decrease the earth fault currents to a reasonable level. That is, only some transformer neutrals are directly earthed.

The 220 kV transmission network is also effectively grounded, but the need for limiting earthing coils is restricted to some substations, i.e. the transformer 220 kV neutrals are usually directly earthed.

The 110 kV (sub)transmission network is mostly of the partially grounded ($k_e \leq 1.7$) type, i.e. only a portion of the transformer 110 kV neutrals are earthed at all. Transformer earthing is made in some larger 400/110 kV substations or power plants. This is almost always done via an earthing coil because of the need to limit the earth fault current in the network to a maximum of about 3,5 kA. The earthing of transformer neutrals without earthing coils generally only concerns some of the smallest types of 110/20 kV subtransmission transformers. The 110 kV partially grounded network is mostly meshed, but some parts of it are constructed or used radially. These mostly belong to the regional networks. Fingrid's network is a meshed system.

Only a smallish part of the Finnish 110 kV network is earthed via Petersen coils. This is the network in Northern Finland, mainly Lapland, Fig. 1. This network is naturally isolated from the partially grounded 110 kV Finnish network, as these two cannot be inter-

connected due to their different grounding methods. The Petersen coil grounding concerns only about 15 substations (approximately 10 %) out of all the 110 kV substations if we do not take into account the additional 110/20 kV branch substations, which are for regional feeding of the 20 kV networks only. Also, in the Petersen coil grounded network, Petersen grounding coils have only been constructed at about one third of the substations; all the other substations are not earthed. In total, the Petersen coil grounded network consists of about 1000 km of lines; 200 km belongs to Fingrid and 800 km to regional network owners. One reason for the Petersen coil grounding in that part of the network is the relatively high number of hydro power plants that do not have to be disconnected due to non-permanent faults in the nearby network. In addition, the 110 kV network in Northern Finland is widespread and scattered, so the effect of an outage would always be extremely significant to a few customers in the region. According to experience, about 90 % of the faults are cleared without any line outages at all.

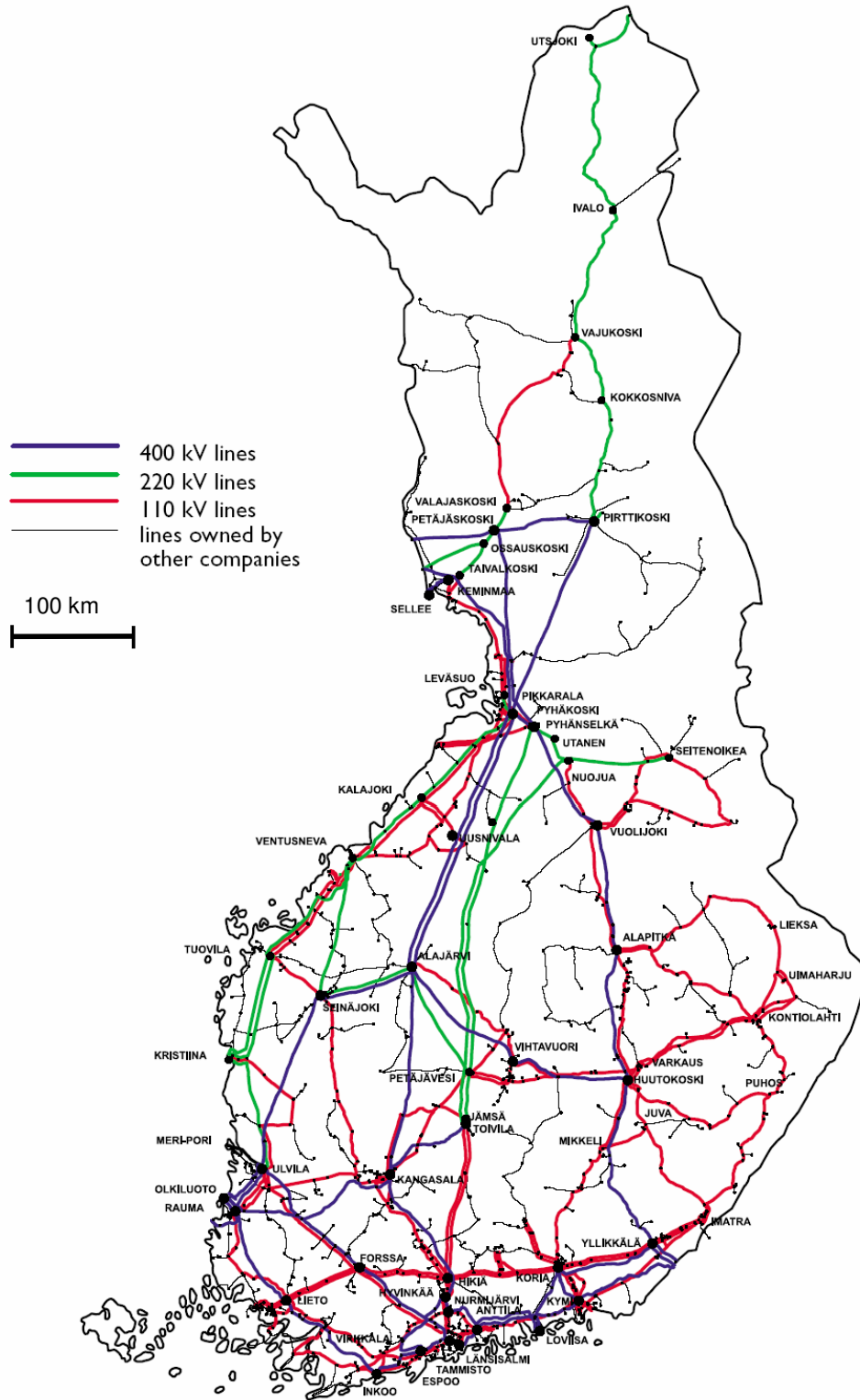


Fig. 1 Transmission grid in Finland on 1.1 2003 , [28]. Fingrid's lines are marked in blue, red and green. The lines of other companies are marked in black.

2.2 Fingrid's fault policy

The Finnish electricity transmission system operator (Fingrid) carries out grid operator services not only in its own network but also in part of the regional 110 kV networks that are interconnected with Fingrid's network. Thus, Fingrid also performs fault clearance and fault location for a major part of the Finnish 110 kV network.

Disturbance recorders

Fingrid today uses disturbance recorders at substations geographically distributed over the whole network, so that fault location can be calculated from the recorded waveforms with sufficient accuracy over most of the network. There are recorders on practically all 400 kV substations but only on some of the 220 kV and 110 kV substations. In some cases protection relays are used for disturbance recording, too. The normal sample frequency is 1 kHz. In some special cases and for this research project, the sampling frequency of some individual recorders was changed to 2.5 kHz. Where the need for a higher sampling frequency is necessary for fault location, e.g. in the Petersen coil grounded parts of the network, Fingrid will consider increasing the sampling frequency to a higher level in all required recorders at the corresponding substations as a consequence of this research project. A new recorder with a sampling rate of 5 kHz has also been installed at one special location.

All three phase voltages are recorded at all substations. About 73-81 % of all network faults are single-phase to ground, [10], [27]. Therefore, the focus has been on recording the earth-fault current ($3I_0$) and not the phase currents. This has led to cost saving in disturbance recorders and their measuring circuits, as only one analogue channel is needed per bay instead of three or four. Only in some special cases and when disturbance recordings are read from protection relays are three phase currents included in the study. This is the main motivation for developing a fault location software application based on earth-fault currents ($3I_0$) instead of phase currents.

Fault location methods

At the 400 kV voltage level travelling wave fault location is the main method. Five devices are installed permanently at substations, suitably distributed over the network to cover as much as possible of the grid.

In the 220 and 110 kV networks, fault location is based on a fault location software application that calculates the fault position using the Power System Simulator for Engineering (PSS/E) software package. The fault voltages and the zero sequence current of the fault are read from the disturbance recordings and fed into this software application,

which then uses a two-step method to calculate the probable fault location. This software application is the reserve system also for 400 kV faults. The accuracy of this method is very high, as the PSS/E simulation is based on an exact electrical model of the Finnish grid taking into account, for example, the prevailing switching situation as well as all parts of the lines or other components that have discontinuities or irregularities in their electrical values. Even the fault resistance is modelled, the dependence of which is built from the measured currents and voltages. Accuracy is also increased if several fault voltages and currents from different substation recordings are used in the calculation instead of only from one substation. Therefore, it is possible to calculate the fault location with a certain degree of accuracy also on branch lines.

The above mentioned fault location software application can be used for normal grounded networks, but not with Petersen coil grounded systems, in which the earth-fault currents are very low because the 50 Hz component is effectively suppressed. Therefore, Fingrid has so far had no effective method for calculating the fault location in Petersen grounded networks; a major motivation for this research project!

Fault types

Faults in the northern Finnish 110 kV network often concern icing on conductors and line poles, which are remote or otherwise difficult to reach due to a harsh environment consisting of a snowy and cold climate. When shield wires are covered with a lot of ice, this has to be manually removed. In the worst cases the shield wire is sometimes broken. Together with some wind, ice-covered heavy shield wires may cause a lot of temporary earth-faults when they touch or move too close to the phase conductors. A fault location system for the Petersen coil grounded network in Northern Finland would be very useful when seeking and removing ice from wires to hinder continuing temporary earth-faults on the same line and also to remove similar permanent faults.

Most earth-faults are initiated at the moment of phase voltage maximum, except for surges, which arise from, for example, lightning strokes.

3 Fault locators

There are several methods for fault location. They use either the fault generated signals themselves or separate signal sources to measure the fault distance. According to fault statistics, the majority (73-81%) of all faults in 110 kV lines are single-phase to ground, [10], [27]. Therefore, fault locators for these faults are most needed. Other faults such as phase to phase, double-phase to ground, etc., are not studied, because their appearance in 110 kV networks is low compared to the single-phase to ground faults. Moreover their location is not so difficult due to the high fault currents.

The aim of Section 3.1 is to provide an overview and comparison of existing fault locators for ground faults (especially single-phase to ground faults). Section 3.2 then reviews the algorithms for ground fault location, which are based on the analysis of low frequency fault transients.

3.1 Division of fault locators

3.1.1 Fault locators using fault generated signals

Fault locators (FL) based on the fault generated signals can be divided, according to Fig. 2, into:

- Conventional fault locators (50Hz)
- Transient fault locators
- Travelling wave fault locators

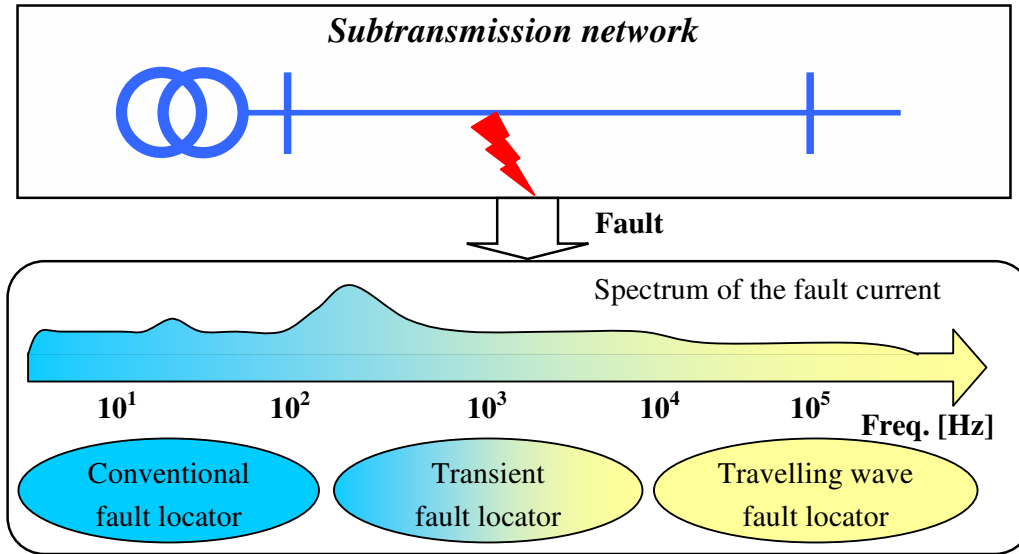


Fig. 2. Fault generated signals and fault locators.

Conventional methods

The conventional fault locators determine the fault position by measuring the post fault impedance from the relay end to the fault point. This is based on the rms voltage and current of the power frequency component. This method is one of the oldest and is still widely used in power systems. The method is analysed in Chapter 4.

Transient based methods

The transient methods are based on the transient signals generated during the fault as a result of the charging or discharging of the network capacitances. More can be found in Chapter 5.

Travelling wave based methods

Travelling wave fault locators are based on travelling waves. They usually work on the detection of a fault generated high frequency transient signal. They require new transducers with a wider frequency band and sophisticated electronic devices. Based on the type of measurement, they can be divided into so-called single-ended (SEM), double-ended (DEM) or multi-ended (MEM) methods. SEM uses the direct and reflected travelling wave from the fault location. Their typical problem is that the reflected wave might not be properly detected at the measurement point (due to the damping in the network, fault impedance, etc.) or might be confused with the wave reflections from the other ends of the network, for example, in the case of a network consisting of 3 ends (a T-branch). Another case is a simple two-ended line, when the fault is behind half of the line from

3. Fault locators

the measurement point of view. When MEM is applied to the network instead of the single-ended approach, the above mentioned reflections have no influence. MEM uses only the first arrival of the wave at each substation. MEM is more accurate, but requires synchronised measurements at all ends of the network. However, travelling wave methods are more accurate than both the conventional and other transient fault location methods. More about the topic can be found in [3], [4], [5].

3.1.2 Fault locators using external signal sources

These fault locators use their own signal sources, i.e. not fault-generated signals. These consist of, for example, an external pulse generator (travelling wave method based on the radar principle) or the bridge methods. They are not in widespread use, however, because they are very slow, require human control, cannot detect non-permanent faults, and the measurements cannot be easily performed in operating networks.

3.2 Low frequency transient based fault location

This type of fault location is based on the detection of the fault path inductance using the ground fault transients. The benefit of using ground fault transients is that they are easily distinguished from the fundamental frequency load currents. The fault distance calculated in this way is largely independent from the fault resistance, too. The independence from the fault resistance and load current makes this method better and more reliable than the conventional method for fault location presented in Chapter 4.

In practice, there are two significant transient components that can be used, the charge and discharge transients. The charge transient is fortunately of high amplitude and relatively low frequency, which makes the method suitable for practical implementation. The discharge transient is of higher frequency and lower amplitude than the charge transient.

In the case of a single-phase to ground fault, the fault loop can be represented by a series connection of the line's symmetrical component impedances, [2]. The fault path inductance L_f is proportional to the fault distance according to the following equation.

$$L_f = \frac{1}{3}(L'_0 + L'_1 + L'_2) \cdot l_f \quad (1)$$

where: l_f is the fault distance and L'_0, L'_1 and L'_2 are the zero-, positive- and negative-sequence inductances of the line per km at the frequency concerned.

In practice, the series connection of the line sequence inductances is affected by the transformer neutral grounding, its phase inductances and also the network configuration (for example, connected lines). The transient method accuracy also depends on the line model. Eq. (1) represents the simplest model (consisting of network series impedances), and does not take into account the network capacitances. This model is also tested in this thesis. The existence of capacitances in the network is the reason for applying a correction factor to the previous model or for using a more complicated model. The model with capacitances included is more complicated, but can be more accurate, [1].

The accuracy also depends on the fault location techniques. There are several methods, such as the **Fourier algorithm** used by Igel [12] and the **differential equation methods** used by Schegner [11] and tested for MV networks in [1]. In this thesis the **wavelet algorithm** is tested, similar to the work in [2] by Hänninen, and comparison is made with a differential equation algorithm.

3.2.1 Wavelet algorithm

The wavelet algorithm (WA) uses the wavelet transform or wavelet filter for the fault path inductance calculation, according to Eq. (2):

$$L_f = \frac{1}{\omega_c} \text{Im} \left[\frac{v_c(t, \omega_c)}{i_c(t, \omega_c)} \right] \quad (2)$$

where ω_c , v_c and i_c are the angular frequency, voltage and current of the charge transient (i.e. wavelet coefficients).

The fault path inductance can then be converted by Eq. (1) into the fault distance. The time-frequency representation of the signal using wavelets is described in more detail in Chapter 6.

3.2.2 Differential equation algorithm

The differential equation algorithm (DEA) computes the fault path inductance by numerically solving the differential equation that describes the fault circuit. In terms of first order modelling the fault circuit can be represented by a simple R-L circuit, Eq. (3).

$$v(t) = R_f i + L_f \frac{di(t)}{dt} \quad (3)$$

where: v and i are the voltage and current of the transient in the faulty phase, R_f and L_f are the resistance and inductance of the fault path, and t is time.

The equation can then be solved by numerical integration because it is easier to solve than the derivatives, as shown in [25]:

$$\int_{t_0}^{t_1} v(t) dt = R_f \int_{t_0}^{t_1} i(t) dt + L_f [i(t_1) - i(t_0)] \quad (4)$$

$$\int_{t_1}^{t_2} v(t) dt = R_f \int_{t_1}^{t_2} i(t) dt + L_f [i(t_2) - i(t_1)] \quad (5)$$

The integrations of the functions in Eq. (4) and (5) for equally spaced samples can be done by the trapezoidal rule:

3. Fault locators

$$\int_{t_0}^{t_1} v(t) dt = \frac{\Delta t}{2} [v(t_1) - v(t_0)] \quad (6)$$

Then the fault path inductance can be computed as a solution of Eqs. (4) and (5) for three samples of voltage and current:

$$L_f = \frac{\Delta t}{2} \left[\frac{(i_{k+1} + i_k)(v_{k+2} + v_{k+1}) - (i_{k+2} + i_{k+1})(v_{k+1} + v_k)}{(i_{k+1} + i_k)(i_{k+2} - i_{k+1}) - (i_{k+2} + i_{k+1})(i_{k+1} - i_k)} \right] \quad (7)$$

where Δt is the sampling time, and v and i are samples of the transient of the faulty phase voltage and current. k is an integer variable. The fault path inductance can then be converted by Eq. (1) into the fault distance.

The differential equation algorithm is not as sensitive to the transient frequency estimation as the wavelet algorithm. The wavelet algorithm includes the transient frequency in its fault location equation, Eq. (2), but it is not seen directly in Eq. (7). Therefore, this algorithm may be more accurate and reliable than the wavelet algorithm. This question arises in cases where the transient is represented by only a few samples. Hence, it is difficult to estimate the transient frequency accurately.

3.3 Literature review

Fault transients have been an object of interest for many years. The charge transient is theoretically studied, for example, in [13], [14]. Fault location based on the charge transient in MV networks (20 kV) has been studied in Finland [1], [2]. However, the method has not yet been applied in the subtransmission networks.

The fault location algorithm requires filtering. There are many filters which might be used for this purpose. The use of the different transformations (Fourier, windowed Fourier and wavelet transform) on the fault transient is thoroughly studied in [15]. All of these techniques have already been applied to fault location based on transients. Fault location algorithms that have already been developed include the Fourier algorithm, [12], and the wavelet algorithm, [2]. A somewhat different approach is provided by the differential equation methods, [11], which are based on solving the differential equation of a model of the line by using the fault transients.

Conventional fault location based on 50 Hz is still very much in use and many researchers continue to investigate new algorithms, for example, [37].

4 Conventional fault location

The conventional fault location method is studied in this chapter. The main purpose is to show the limitations of this technique in typical 110 kV Finnish networks. Conventional fault location is easily applied to radially operated systems with low impedance grounded neutrals, but may be used in networks with isolated neutrals or Petersen coil grounding under some circumstances.

In this chapter the so-called “conventional method” is theoretically analysed with simulated examples in a network with a solidly grounded neutral, Section 4.1. The influence of the fault resistance is then eliminated in the so called “improved conventional method”, Section 4.2. Section 4.3 studies the influence of the type of neutral grounding on the conventional methods. In Sections 4.4 and 4.5 the phase current and zero-sequence currents are used for fault location in real 110 kV networks. The chapter concludes with a discussion, in Section 4.6.

4.1 Conventional method

Conventional fault location (CFL) is based on the measurement of a short circuit loop at fundamental frequency, in solidly grounded networks. The faults are most commonly analysed by symmetrical components, Fig. 3. The model in Fig. 3 is a simplification of a more general symmetrical component model for solidly grounded networks, found for instance in [29]. This model is also valid for non-solidly grounded networks (for example, Petersen coil grounded or isolated neutral), but only under some special circumstances. In subtransmission networks such as the 110 kV system studied in this thesis, the load is expected to be more or less symmetrical, therefore the load impedance is modelled as a positive sequence impedance at the terminal, Fig. 3. This assumption will simplify the derivation of the final equations.

In this study, only single-phase to ground faults in radially operated systems where the neutral is grounded with zero impedance will be analysed.

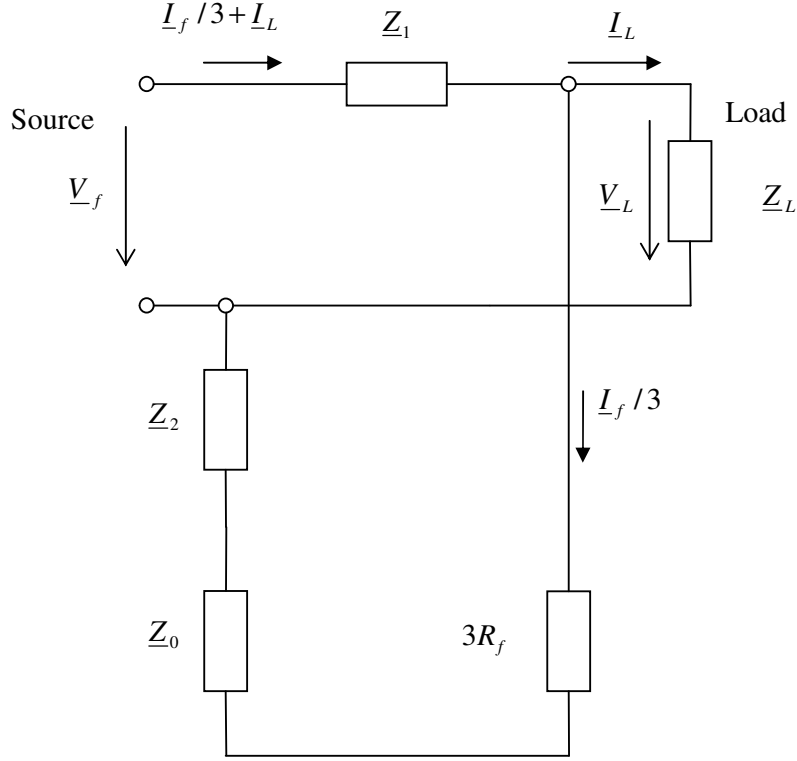


Fig. 3 The symmetrical component model of a radially operated network for the conventional fault location method. This diagram is for single-phase to ground fault analysis. The load is represented by the positive sequence impedance only.

Based on the model shown in Fig. 3, the faulted phase voltage can be estimated from the zero-, positive- and negative- sequence impedances according to Eq. (8), when the fault current \underline{I}_f is flowing through the above mentioned impedances and fault resistance $3R_f$, and the load current \underline{I}_L (which stays symmetrical after the fault) is flowing only through the positive-sequence impedance of the model.

$$\underline{V}_f = l_f \underline{Z}'_1 \left(\underline{I}_L + \frac{\underline{I}_f}{3} \right) + 3R_f \frac{\underline{I}_f}{3} + l_f \underline{Z}'_0 \frac{\underline{I}_f}{3} + l_f \underline{Z}'_2 \frac{\underline{I}_f}{3} \quad (8)$$

Simplified:

$$\underline{V}_f = \frac{1}{3} (\underline{Z}'_0 + \underline{Z}'_1 + \underline{Z}'_2) l_f \underline{I}_f + R_f \underline{I}_f + \underline{I}_L \underline{Z}'_1 l_f \quad (9)$$

4 Conventional fault location

Based on the measured currents \underline{I}_f and \underline{I}_L , and the voltage \underline{V}_f in the substation, the fault distance can be calculated from the following equation, Eq. (10).

$$l_f = \frac{\frac{\underline{V}_f}{\underline{I}_f} - R_f}{\frac{1}{3}(\underline{Z}'_0 + \underline{Z}'_1 + \underline{Z}'_2) + \frac{\underline{I}_L}{\underline{I}_f} \underline{Z}'_1} \quad (10)$$

where:

\underline{V}_f is the fault phase voltage

\underline{I}_f is the fault current

\underline{I}_L is the load current

$\underline{Z}'_0, \underline{Z}'_1$ and \underline{Z}'_2 are the zero-, positive- and negative- sequence impedances of the line per km

R_f is the fault resistance

l_f is the fault distance

4.1.1 Method error

The fault location accuracy mainly depends on the fault resistance and load/fault current ratio as can be seen from Eq. (10).

Fault resistance

The uncertainty in the fault resistance is one of the biggest disadvantages of this method and causes problems if the fault resistance is not close to zero. Nevertheless, low resistance faults (of a few ohms) can sometimes be identified with acceptable error.

The error term due to the fault resistance can be expressed as:

$$\delta_f = \frac{-R_f}{\frac{1}{3}(\underline{Z}'_0 + \underline{Z}'_1 + \underline{Z}'_2) + \frac{\underline{I}_L}{\underline{I}_f} \underline{Z}'_1} \quad (11)$$

The error is linearly dependent on the fault resistance. This is an advantage, because in cases where we can estimate the fault resistance, the necessary correction can be made easily. The fault resistance (resistance of the power arc) can be calculated as shown in [2].

Load and fault current

Other circumstances also lead to very innaccurate fault location, such as when the voltage drop caused by the fault current \underline{I}_f in the line impedances is fully or partially compensated by the voltage drop caused by the load current \underline{I}_L . In this case the denominator of the fault location equation becomes zero, which increases the inaccuracy. Because the line parameters are given, this will depend only on the load and fault current ratio.

The critical ratio of load current to fault current, derived from the denominator of Eq. (10), is:

$$\frac{\underline{I}_L}{\underline{I}_f} = -\frac{\frac{1}{3}(\underline{Z}'_0 + \underline{Z}'_1 + \underline{Z}'_2)}{\underline{Z}'_1} \quad (12)$$

Eq. (12) defines the case where the denominator of Eq. (10) or Eq. (11) is equal to zero. For the studied network (the data is in Appendix A), the critical ratio is $\underline{I}_L / \underline{I}_f = 1.1371 \angle 174.5882^\circ$. The dependence of Eq. (11) for $R_f = 1 \Omega$ is shown graphically in 3D in Fig. 4. This phenomenon is also shown in the simulated examples in the following sub-section, 4.1.2.

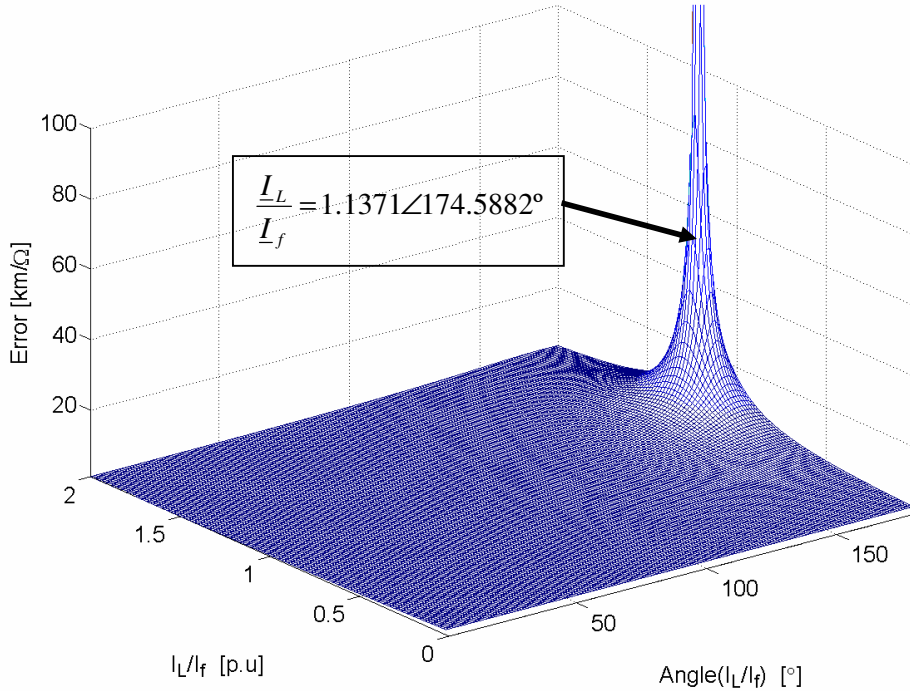


Fig. 4 Error term of the fault location equation with the ratio and the angle of $\underline{I}_L / \underline{I}_f$.

The fault resistance is $R_f = 1 \Omega$. Plotted for the studied network.

At the same time, the numerator of Eq. (10) (i.e. the ratio $\underline{V}_f / \underline{I}_f$) is at its minimum; therefore, the fault location equation Eq. (10) starts to become more sensitive to the fault resistance. The calculation varies with the line parameters, but the example calculation for the studied network (the network data is shown in Appendix A) can be seen in Fig. 5. The minimum of the curve is defined by the symmetrical components of the line.

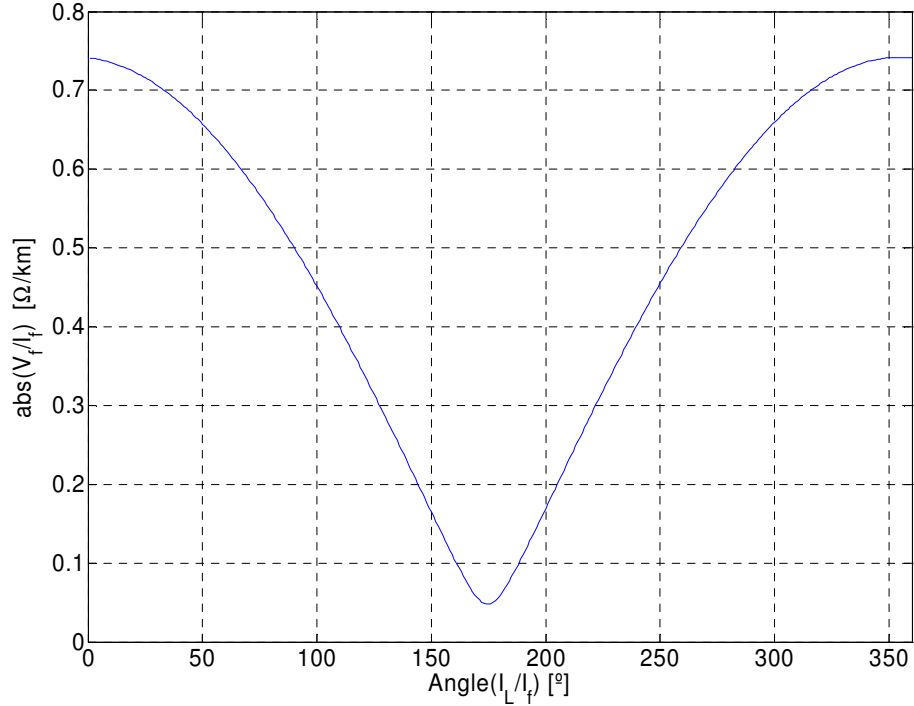


Fig. 5 The variation of $|\underline{V}_f / \underline{I}_f|$ per km in the studied network, when $I_f = I_L$ and the phase angle between the fault current and load current is changed. $R_f = 0 \Omega$.

4.1.2 EMTP/ATP simulations

The fault location accuracy of this conventional fault location method was tested with ground faults in a 110 kV solidly grounded radially operated network using the Electromagnetic Transients Program - Alternative Transient Program (EMTP/ATP). The network details and the simulated data can be found in Appendix A. The simulated network is as in Fig. 101 but without the connected line 3.

For analysis of the fault signals generated by the EMTP/ATP model, a fault locator in Matlab was developed, Chapter 13. This program automatically processes the output of the EMTP/ATP simulation (*.pl4-file) and plots the results using Eq. (10). The reference signal for the vector angle identification was the phase to phase voltage (between

non-faulted phases). The sampling rate in the test was 100 kHz in EMTP/ATP and the signals were subsampled into 2.5 kHz for fault location. It is noteworthy that the load current is measured here as the pre-fault current. Then a (synchronized) measurement of the current is not required on the load side. (This assumption is correct if the load does not change during the fault.)

Load and fault current

The dependence of the fault location accuracy on different load conditions is shown in Fig. 6. The fault resistance is assumed to be zero. The picture shows the situation where the fault and load currents are equal in amplitude (the worst case of fault location due to the phase shift between \underline{I}_L and \underline{I}_f can be seen when the angle is 174°). The reason for the error peak is explained in detail in the previous section. The primary reason is the low value in the denominator of the fault location equation. The low value of the measured current in the substation also has an effect. For comparison, another two cases are plotted with the ratio I_L/I_f equal to 3 or 0.3, Fig. 6. It can be seen that the method works very well if the load and fault current are not equal in amplitude (it is noteworthy that I_L/I_f is usually lower than 1 for networks with solidly grounded neutrals). Therefore, the ratio I_L/I_f is not usually the critical factor in solidly grounded networks. The details from the simulations are in Tab. 13.

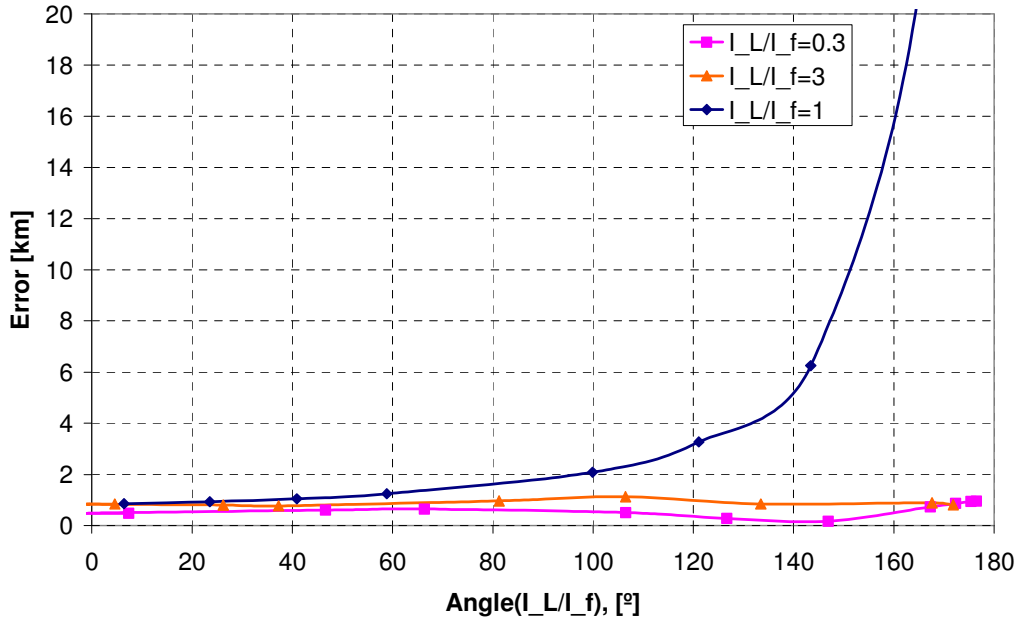


Fig. 6 Error in conventional fault location due to the phase shift between the load and fault current. I_L/I_f is 1, 0.3 and 3. Fault distance $l_f = 25$ km, and $R_f = 0 \Omega$.

Fault resistance

The fault impedance was simulated with a range of fault resistances, 0 -100 Ω . The error in the fault location for the studied case is shown in Fig. 7. Even though the selected range of R_f might not be as high as in a real case, it indicates the influence of increasing fault resistance. Therefore the potential for using this type of conventional fault location method for the "higher impedance" faults that occur in Fingrid's 110 kV networks is very small. The details of the simulations are in Tab. 14.

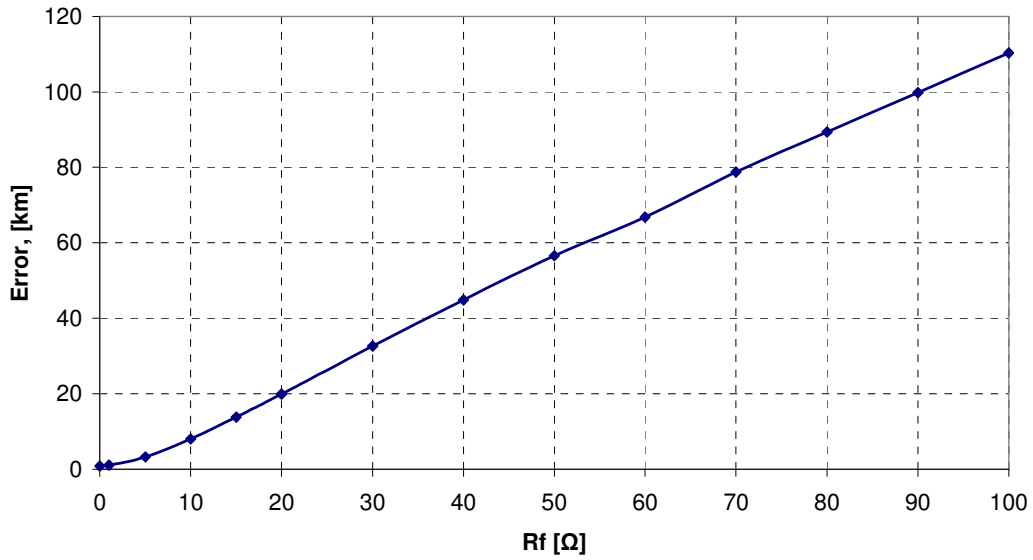


Fig. 7 Error in conventional fault location due to fault resistance; for $I_L / I_f = 3$ and fault distance $l_f = 25$ km.

4.2 Improved conventional fault location

The improved conventional fault location (ICFL) is a reactance based fault location method. The influence of unknown fault resistance on single-phase to ground fault location can be reduced by taking into account only the imaginary parts of the numerator and denominator in Eq. (10):

$$l_f = \frac{\text{imag}\left(\frac{V_f}{I_f} - R_f\right)}{\text{imag}\left(\frac{1}{3}(\underline{Z}'_0 + \underline{Z}'_1 + \underline{Z}'_2) + \frac{I_L}{I_f} \underline{Z}'_1\right)} = \frac{\text{imag}\left(\frac{V_f}{I_f}\right)}{\frac{1}{3}(X'_0 + X'_1 + X'_2) + \text{imag}\left(\frac{I_L}{I_f} \underline{Z}'_1\right)} \quad (13)$$

where the symbols are as in Eq. (10). X'_0 , X'_1 and X'_2 are the zero-, positive- and negative-sequence reactances of the line per km.

4.2.1 Method error

As can be seen from Eq. (13), the method is less dependent on the fault resistance than Eq. (10). (It is assumed that the fault impedance can be substituted by the fault resistance, otherwise the numerator will consist of two imaginary components.) Anyhow, the reduction of the denominator of Eq. (10) into the imaginary part only, Eq.(13), makes the method more sensitive to the angle between the fault and load currents, I_f and I_L . The above mentioned denominator has a zero crossing in the area of interest (for normal R-L load types in series), which means that Eq.(13) is very unstable around this point:

$$\frac{1}{3}(X'_0 + X'_1 + X'_2) + \text{imag}\left(\frac{I_L}{I_f} \underline{Z}'_1\right) = 0 \quad (14)$$

The denominator of Eq. (13) can be plotted with the parameters of the studied network, Fig. 8 (X'_0 , X'_1 , X'_2 and \underline{Z}'_1 can be calculated from the parameters given in Appendix A). As can be seen, the behavior of the equation and its zero crossing depend on the ratio I_L/I_f . This dependence is shown in Fig. 8 for different angles and amplitudes of I_L/I_f . (Note that the curves are valid for any kind of neutral grounding. They depend only on the line parameters and the load-fault current relation.)

For practical application, the range of the ‘‘R-L’’ load phase angle 0-90° and also the ‘‘R-C’’ load angles 0-90° are shown for one case, $I_L/I_f = 3$. This range of load does not hold for all cases. In general, the zero-crossing area can be reached with a normal R-L

4 Conventional fault location

load, because the fault current magnitude and phase depend on the network configuration, neutral grounding, fault resistance, etc. It just so happens that in the particular case under study the load is capacitive. In general, the angle of $\underline{I}_L / \underline{I}_f$ lies within 360 degrees. Therefore, the zero-crossing can be on the both the left and right side of the figure.

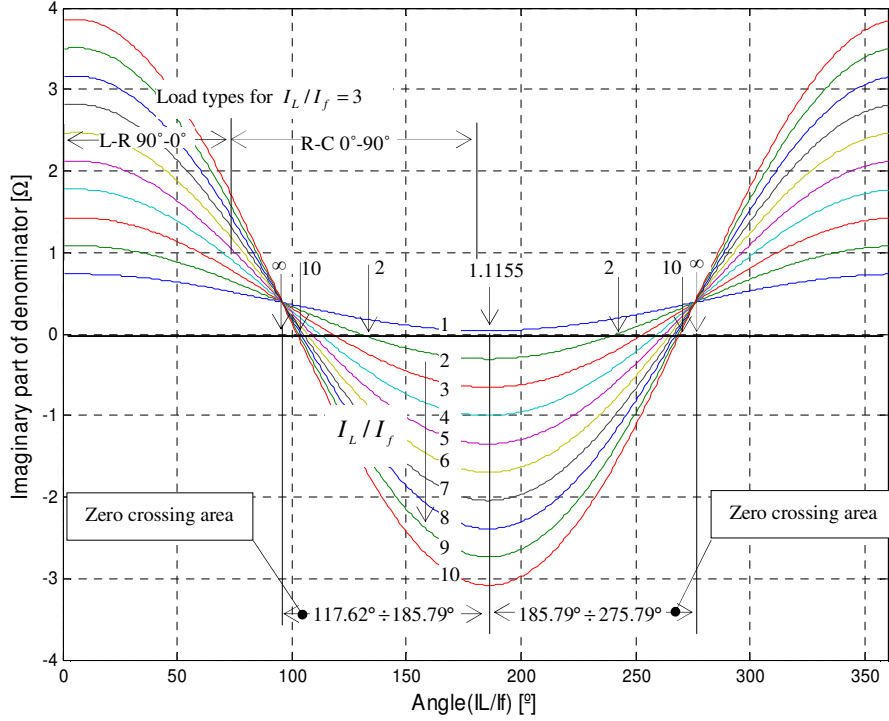


Fig. 8 The imaginary part of the denominator of Eq.(13) for the study network. The different ratios of load to fault current, I_L / I_f , are from 1 to 10.

The phase angle “ $\varphi_0 = \text{angle}(\underline{I}_L / \underline{I}_f) = \varphi_L - \varphi_F$ ” for the zero crossing can be evaluated by solving Eq. (14). Eq. (15) presents the angle φ_0 between the fault and load currents, \underline{I}_f and \underline{I}_L , where fault location would not be possible because of the denominator zero crossing. The development of Eq. (15) from Eq. (14) is shown in Appendix A:

$$\varphi_0 = \varphi_L - \varphi_F = -\left(\text{asin}\left(\frac{\frac{1}{3}(X'_0 + X'_1 + X'_2)}{\underline{I}_L Z'_1}\right) + \varphi_{z1}\right) \quad (15)$$

where φ_L and φ_F are the load and the fault current angle where the denominator zero crossing takes place. φ_{z1} is the angle of the positive-sequence impedance of the line.

4 Conventional fault location

The zero crossing of Eq. (14) moves between two border values, depending only on the ratio I_L / I_f and the network parameters.

Moreover, not only cases where the angle $\varphi_0 = \varphi_L - \varphi_F$, calculated in Eq. (15), will be affected by a denominator zero crossing but also cases where the angle is around this value. From Fig. 8 it can be seen that the affected area is larger for lower rates of I_L / I_f than higher ones, because of the lower growth of the denominator curve of Eq. (13) when crossing the zero point. This can be clearly seen in Fig. 9. In real situations the maximum error (and error distribution) in fault location caused by the zero crossing can be estimated using the measured data.

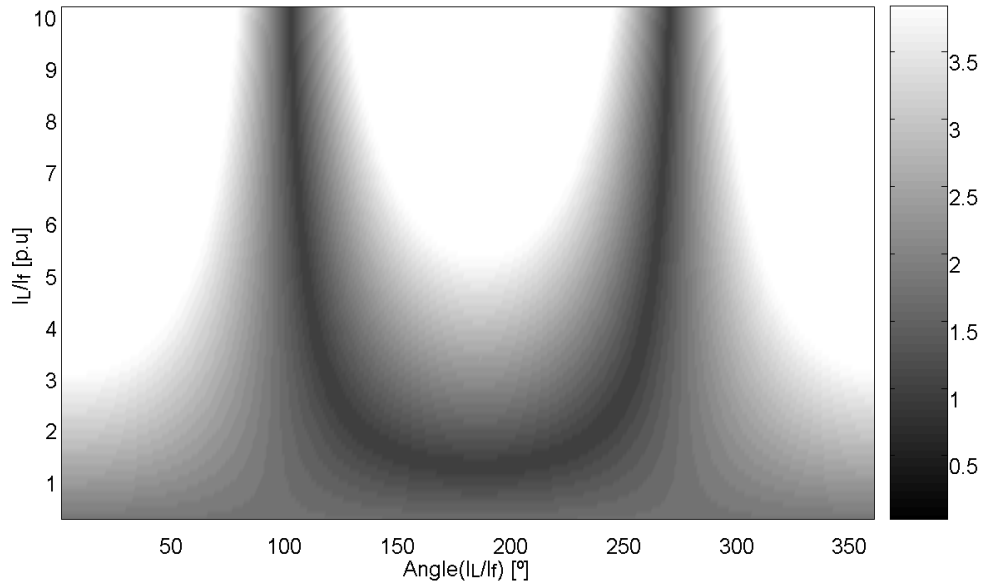


Fig. 9 The absolute value of the imaginary part of the denominator of Eq.(13) for the studied network. The different ratios of load to fault current, I_L / I_f , are from 1 to 10.

The practical influence of the denominator on fault location can be seen from the simulations in Fig. 10 for $I_L / I_f = 3$, and in Fig. 13 for $I_L / I_f = 9$. The ratio I_L / I_f seems to have a strong influence on the affected area. The affected area is much smaller in Fig. 13 than in Fig. 10.

4.2.2 Example of zero-crossing calculation

This calculation example is shown in order to illustrate how to define the border values for the zero crossing region of the denominator in Eq. (13). The parameters of the studied network are given in Appendix A.

Critical value of I_L/I_f

The necessary condition for the possible zero crossing of Eq. (14) can be found when the term under the “asin” in Eq.(15) is equal to 1. This happens at the **critical angle**, φ_{cr} , when $\varphi_{cr} = \varphi_0 = -(\text{asin}(1) + \varphi_{z1})$. For the studied network, this is $\varphi_{cr} = -(90^\circ + \varphi_{z1}) = -174.21^\circ$ (i.e. $\varphi_{cr} = 185.79^\circ$). This value is also shown in Fig. 8 (1.1155). The ratio of I_L/I_f that relates to this zero-crossing is when the argument of “asin” becomes one, $I_L/I_f = \frac{1}{3}(X'_0 + X'_1 + X'_2)/Z'_1$. For the network under study, this is when $I_L/I_f = 1.1155$. If the ratio is below this value there is no zero-crossing caused by any load and there is no significant influence of the phase angle on the fault location itself. In other cases there does exist a zero crossing and hence an increased error area. Therefore, this number is named the **critical value** and is a constant for a given network.

Borders values of φ_0

If I_L/I_f is greater than the critical value there is always a zero-crossing for at least one angle between the load and fault current φ_0 . The maximum value of $\varphi_0 = \varphi_L - \varphi_F$ occurs when the argument of the “asin” of Eq. (15) is equal to zero. This happens at the **border angle** φ_∞ when the load is very big and Eq. (15) can be solved as: $\varphi_\infty = \lim_{I_L \rightarrow \infty}(\varphi_0) = -(\text{asin}(0) + \varphi_{z1}) = k \cdot 180^\circ - \varphi_{z1}$, (where $k = 0, 1, 2, 3, \dots$). This is actually the negative of the angle of the positive-sequence impedance of the line per km, Z'_1 , for $k = 0$. For the studied network, the roots for $k = 0$ and $k = 1$ are: $\varphi_\infty = -\varphi_{z1} = -84.21^\circ$ (i.e. $\varphi_\infty = 275.79^\circ$) and $\varphi_\infty = 180 - \varphi_{z1} = 180 - 84.21^\circ = 95.7861^\circ$. The position of these limits can be seen in Fig. 8, marked for an infinitely high load current (∞). This range defines the zero-crossing area.

Increased error area

When the ratio I_L/I_f becomes greater than the critical value (1.1155), the zero crossing occurs within the interval of $\varphi_\infty = 180 - \varphi_{z1} = 95.7861^\circ$ and $-\varphi_{z1} = 275.79^\circ$. For in-

stance, it can be seen in Fig. 8 that the function for $I_L/I_f = 1$ does not have a zero-crossing, but the zero crossing has already come into existence when this ratio is 2.

In other words, the existence of a zero crossing does not always mean that the method will work incorrectly. This happens only under some unfavorable conditions. An inaccurate fault location occurs if the ratio of the amplitudes of the load and fault currents are greater than the critical value (1.1155 in this studied case) and the angle between them is specific to this ratio, in accordance with Fig. 8. In other cases the method might work with small errors even though the above mentioned ratio is greater than the critical value.

It can be seen that Eq. (15), dependent on I_L/I_f , converges very quickly to the limit values of $\varphi_\infty = 275.79^\circ$ or $\varphi_\infty = 95.7861^\circ$. For higher rates of I_L/I_f the zero-crossing is more or less constant with the angle of I_L/I_f and equal to the border values of φ_∞ , and the error area is smaller. This is generally the case for networks with isolated or compensated network neutrals.

For lower rates of I_L/I_f , the zero-crossing changes with the angle of I_L/I_f even more and the error area is wider. This is usually the case for networks with solidly grounded neutrals.

These effects are seen in both Fig. 8 and Fig. 9 and in the simulated cases shown in Fig. 10 and Fig. 13.

The minimum of the set of curves in Fig. 8, is at the same value of φ_0 equal to the critical angle φ_{cr} . This is because the derivation of Eq. (14) depends only on the positive sequence impedance, not on the ratio of the fault to load current. When the derivation is calculated, it comes to $\varphi_L - \varphi_F + \varphi_{z1} = -90^\circ$ and hence, for the studied case, $\varphi_{cr} = -90^\circ - \varphi_{z1} = 185.79^\circ$.

4.2.3 EMTP/ATP Simulations

Example of zero-crossing simulation

The fault location accuracy of the improved conventional fault location method was tested with ground faults in a 110 kV solidly grounded radially operated network using EMTP/ATP. The network details and the simulated data can be found in Appendix A. The same network as in Fig. 101 was simulated but without the connected line 3. The reference signal for the vector angle identification was the phase to phase voltage (between non-faulted phases). The sampling frequency of the test was 100 kHz in EMTP/ATP and the signals were subsampled into 2.5 kHz for fault location. It should be noted that the load current is measured here as the pre-fault current. This means that a (synchronized) measurement of the load current is not required on the load side. This assumption should be valid if the load does not change during the fault. The results can be seen in Fig. 10.

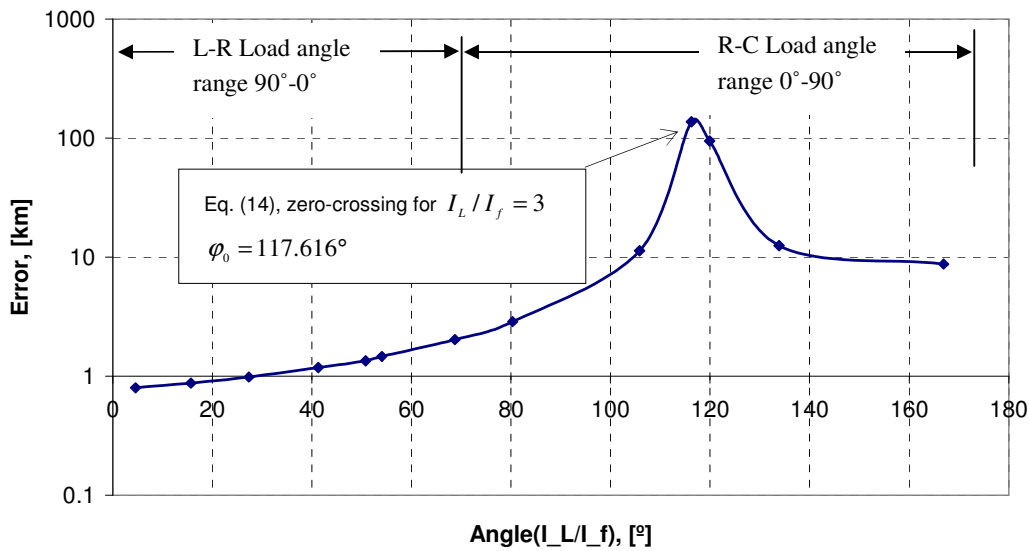


Fig. 10 Error of improved conventional fault location due to phase shift between the load and fault current. For $I_L/I_f = 3$, and fault distance $l_f = 25$ km.

In Fig. 10 the output of the developed fault locator is shown. (The fault locator is basically the same as in Section 4.1, but calculates the imaginary parts of the numerator and denominator for the fault location equation. The fault locator is presented in Chapter 13). Fig. 10 shows the the situation when $I_L/I_f \cong 3$. Simulations clearly show an increased error in fault location under some conditions. Eq. (15) in this case indicates that the highest error occurs at the same place, where $\varphi_0 = 117.6149^\circ$, which can also be seen from the simulated case in Fig. 10. The angle φ_0 represents the capacitive load of

approximately $\varphi_L = 50^\circ(\text{cap})$, i.e. $\cos(\varphi_L) = 0.6428$. The other possible zero-crossing angle, $\varphi_0 = -106.0426^\circ$ (i.e. $\varphi_0 = 253.9574^\circ$), is not reachable, because the passive load angle can only change within 180 degrees. The details are shown in Tab. 15 in Appendix A. $I_L/I_f \cong 3$ is a rather unrealistic case for systems with solidly grounded neutrals. In a real system where $I_L/I_f < 1$, the zero-crossing might not appear at all.

In cases where the load and fault currents do cause a zero-crossing in the fault location equation of the improved conventional fault location method, the conventional method can be used more accurately; compare Fig. 10 and Fig. 6 for $I_L/I_f = 3$.

Nonetheless, fault location is not possible in cases where the fault and load currents cancel each other's voltage drop, as was shown in the previous chapter. In other cases, the fault location accuracy is affected by the denominator of Eq. (13).

Fault resistance

By definition, there should not be any influence from the fault resistance on fault location. However, higher fault resistance causes lower fault currents. The dependence of the error in fault location on fault resistance is shown in Fig. 11.

Nevertheless, the influence is much smaller when compared to the conventional fault location in Fig. 7, which analysed the same data as presented here. The detailed data are shown in Tab. 14.

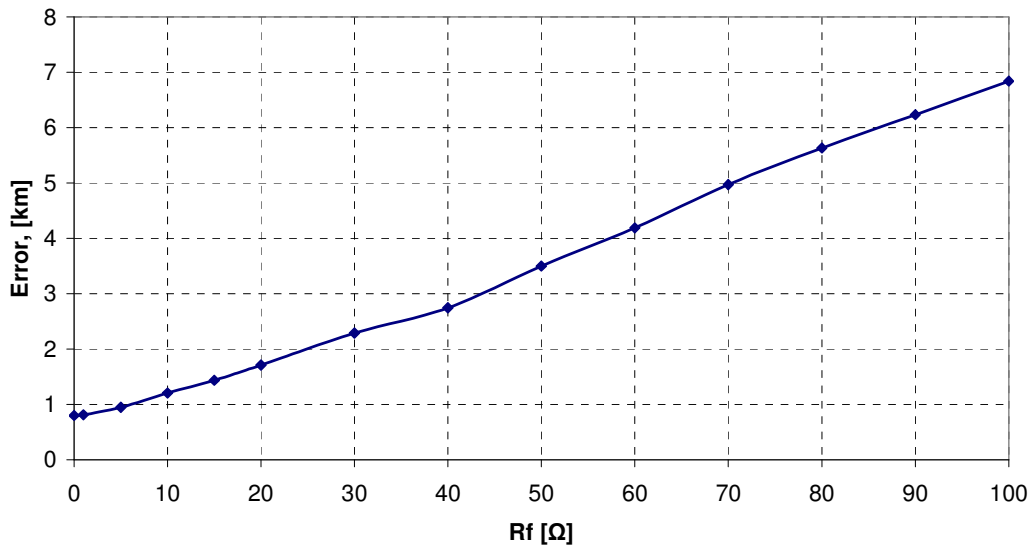


Fig. 11 Error in improved conventional fault location due to fault resistance, for $I_L/I_f = 3$ and fault distance $l_f = 25$ km.

4.2.4 Principle of error estimation

An error estimation of the improved conventional fault location methodology, based on the analyses and simulations provided in the previous chapters, has been designed. The error of the method changes with the load/fault current ratio, as can be seen from the example presented in Section 4.2.2. Even so, the approximate error in the fault location, caused by the low value of the denominator in Eq. (13), can be estimated as indicated in the following figure:

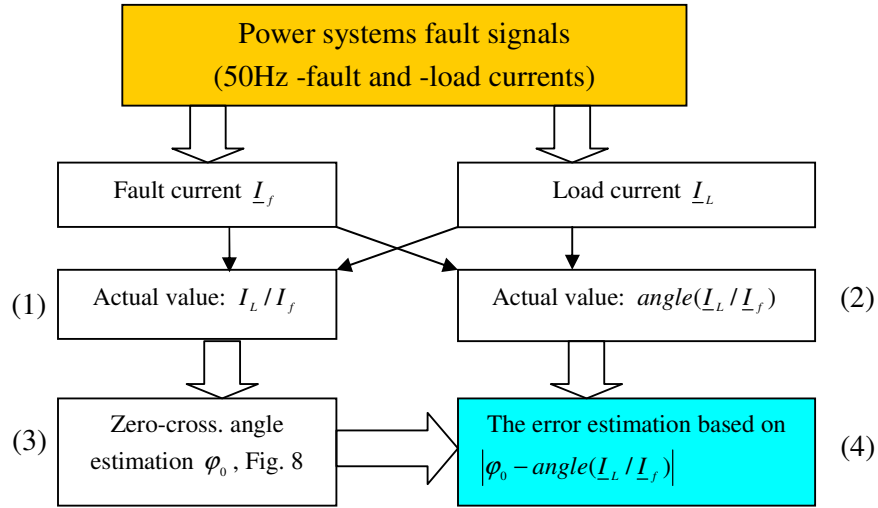


Fig. 12 Principle of fault location error estimation.

The principle of the error estimation involves evaluating the distance in degrees of the actual $angle(I_L / I_f)$ from the zero-crossing angle φ_0 defined by the ratio I_L / I_f :

1. Evaluation of the actual value of I_L / I_f .
2. Evaluation of the actual value of $angle(I_L / I_f)$.
3. Zero-crossing angle calculation φ_0 , based on I_L / I_f , Eq. (15).
4. Comparison of φ_0 with the actual $angle(I_L / I_f)$.
 - a. If the actual angle of the load and fault currents is close to the zero crossing angle φ_0 (when $|\varphi_0 - angle(I_L / I_f)| \rightarrow 0^\circ$) a large error will be indicated.
 - b. When $|\varphi_0 - angle(I_L / I_f)| \gg 0^\circ$, the error is small.

The error evaluated in degrees together with the ratio I_L / I_f provides sufficient information about the accuracy of our fault location, Fig. 9.

It should be noted that in practice there are two zero-crossing angles and therefore two error angles. The closer one is more influential.

4.3 Conventional methods vs. neutral grounding

The conventional fault location methods for the solidly grounded network described in the previous sections, 4.1 and 4.2, can work in networks with all the neutral grounding types (isolated neutral, Petersen coil grounded...), but only for some specific network configurations. The key element in network configuration is to have a good return path for the zero-sequence current to the substation. In cases where the network neutral is not solidly grounded the lines connected to the same substation might help.

The same network is simulated here as in the previous sections. However, one outgoing line (Line 3) of length 55 km is connected to the substation, Fig. 101 in Appendix A. The results are shown in Fig. 13. I_L/I_f was chosen to be 9, because in the case of isolated neutrals or Petersen coil grounded networks the fault current is small. The detailed data are given in Tab. 16.

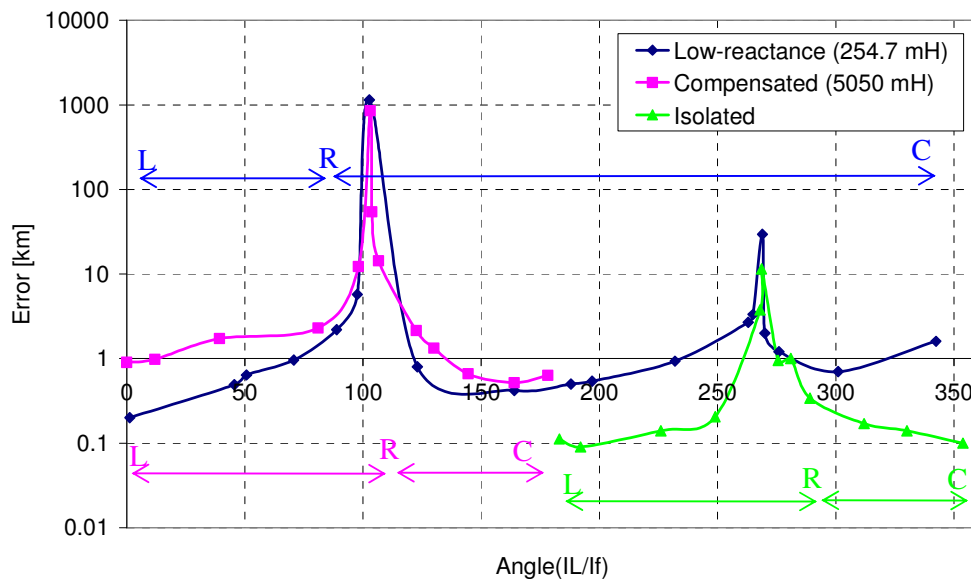


Fig. 13 Error in improved conventional fault location due to phase shift between the load and fault current, for $I_L/I_f = 9$ and fault distance $l_f = 25$ km. Result for different neutral grounding types are shown: low impedance, Petersen coil and isolated. The load conditions are marked as R-resistive, L- inductive and C-capacitive.

The simulation of the studied case for different neutral grounding gave the following results. If the network neutral is grounded with the low impedance reactors (at 50 Hz, 80

Ω), the whole 360 degrees range of $\varphi_L - \varphi_F$ can be reached with the passive load, Fig. 13. This is possible because the phase of the fault current changes as well. In the case of a Petersen coil grounded or isolated neutral network, the fault current angle is almost stable and therefore only a range of 180 degrees is covered, Fig. 13. The conventional methods work similarly for all kinds of neutral arrangements, under the above mentioned conditions.

4.4 Conventional methods vs. real ground faults

The conventional algorithms presented in the previous sections were tested using real ground fault recordings from the Finnish 110 kV network. The recordings are from the Pyhäkoski – Rautaruukki line. This line is radially operated with low reactance grounding. The detailed network data can be found in Appendix A (a diagram of the network is given in Fig. 102 and the network data is in Tab. 17). The phase voltage and current of all three phases were measured along with the zero-sequence current in the Pyhäkoski substation. The sampling frequency was 1 kHz. The exact fault location was measured with a parallel connected travelling wave recorder.

The error of both the conventional and improved conventional algorithms is similar, as shown in Fig. 14. More precise data can be found in Tab. 18 in Appendix A.

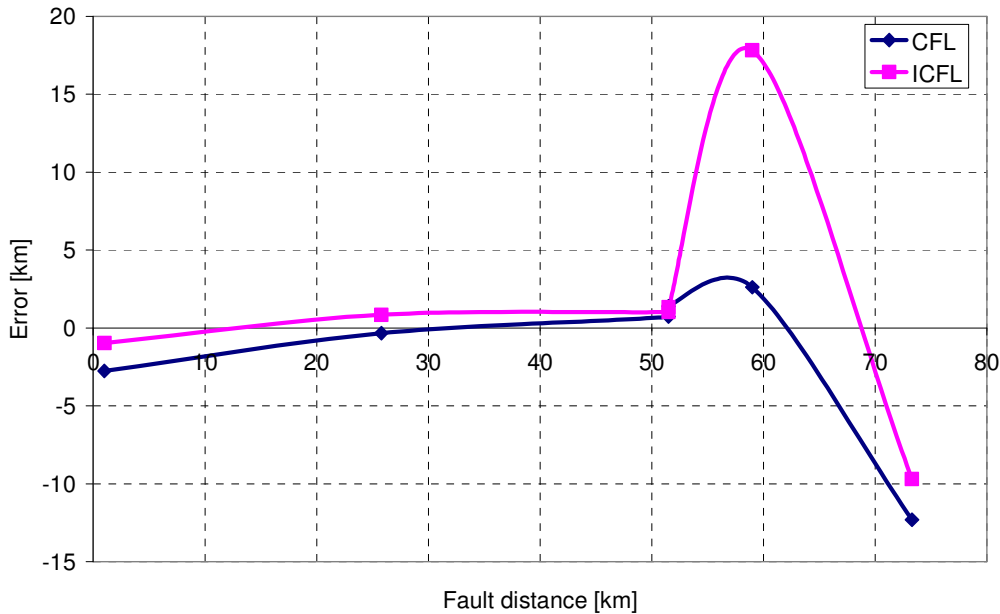


Fig. 14 The error in the conventional (CFL) and improved conventional (ICFL) algorithms. The test data is from the Pyhäkoski – Rautaruukki line.

The fault location was estimated relatively accurately, ± 2 km for the conventional and ± 1 km for the improved conventional fault location methods, for the first 50 km of the line. The fault distance in the last 30 km of the line to the Rautaruukki substation was calculated with much less accuracy. One possible reason is that the line inductances were changed due to a second line that runs parallel to the tested line for 29,358 km, Fig. 102.

4.5 Utilising the zero-sequence current in conventional fault location

The currents of all three phases are not usually measured in the disturbance recorders of Fingrid's 110 kV substations for economic reasons, Chapter 2. The challenge is to use the zero-sequence current instead of the phase currents. The study covered in this section is based on both EMTP/ATP simulations and real fault events.

During the single-phase to ground fault in networks with a solidly grounded neutral, the positive-, negative- and zero- sequence currents are equal to 1/3 of the phase current, Fig. 3. Therefore, it is possible to utilise the zero-sequence current in fault location, at least in theory. The zero-sequence current can be measured in the network as a sum of the phase currents or as a neutral current. The neutral current can only be measured in networks with a neutral grounded via some impedance. Using of this methods it is possible to measure the zero-sequence current under some circumstances. If there are other lines connected to the substation or if the neutral is grounded via a relatively high impedance, the zero-sequence current will not fully return via the measurement point. In such cases only a part of the zero-sequence current is measured and therefore some correction will be needed, [21]. The correction will be based on the lines' total ground capacitance and the grounding coil inductance. If the grounding impedance is a low reactance coil and there are no other outgoing lines from the substation, the circumstances are almost the same as in a solidly grounded network.

Even if all the circumstances mentioned above are ideal for fault location, there will always be some error. The reason is that it is virtually impossible to detect the load conditions (pre-fault current) by measuring only the zero-sequence current. Therefore, such fault location methods are only expected to work if the load current is smaller than the fault current. Otherwise, the load current can be estimated from the power measurement of the line.

4.5.1 EMTP/ATP Simulations

The simulations were performed with the EMTP/ATP software on a radially operated network with a reactance grounded neutral. The size of the reactor was tuned to obtain similar results to those obtained from real faults (500 mH was chosen). The phase voltages and currents were measured in the feeding substation with the neutral current. The sampling frequency of the test was 100 kHz in EMTP/ATP and the signals were sub-sampled into 2.5 kHz for fault location. The parameters of the line match Fingrid's Pyhäkoski – Rautaruukki line. For more details see Appendix A (a schematic representation of the line is given in Fig. 103).

The so-called “improved conventional fault location method” was tested using both phase and zero-sequence currents. The fault distance was 25 km in a network of total line length 81.5 km. The fault resistance was 0 ohms. The simulations were processed by the fault locator detailed in Chapter 13. The fault data was de-noised by a wavelet filter. The influence of the load, known/unknown (unknown when the zero-sequence current is used, known if the phase current is used), is represented by the ratio of load to fault current. The load and fault currents were in phase in the modelled cases. A comparison of the method error is shown in Fig. 15 for both cases. More details and results can be seen in Tab. 20 in Appendix A.

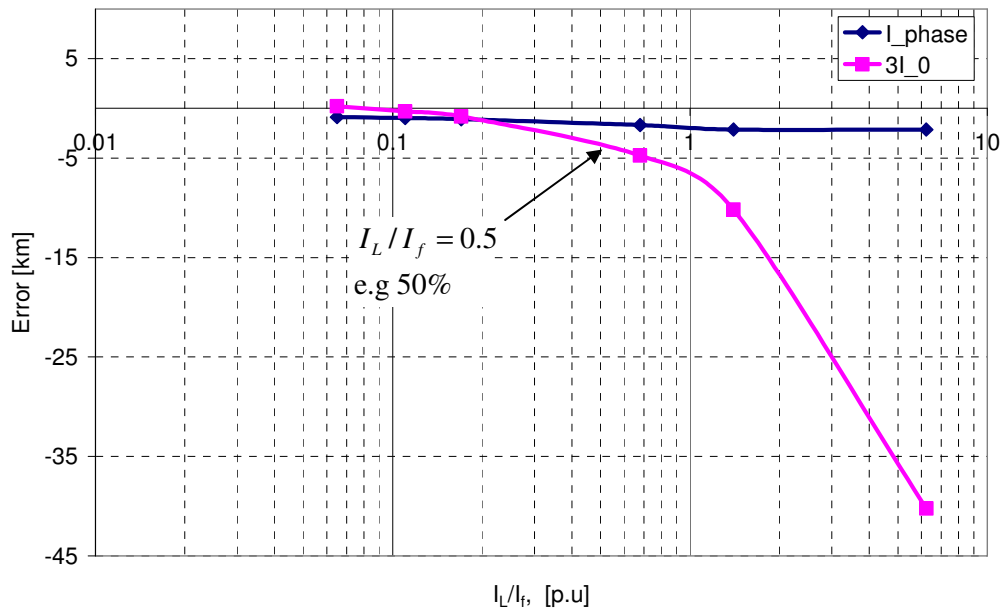


Fig. 15 Error in fault location by the improved conventional method. Utilisation of the phase (I_{phase}) and zero-sequence ($3I_0$) currents are compared. The load (I_L) and fault (I_f) currents are in phase.

From the simulation results, it is clear that fault location using the zero-sequence current will only work when the load current is much lower than the fault current. More precisely, the limit for the load current was identified to be 50% of the fault current in this case. This conclusion might be a bit different if the fault and load currents are not in phase as they were in this case. However, the trend of the curves would probably remain the same.

4.5.2 Real faults from the Pyhäkoski – Rautaruukki line

Similar results can be obtained for real fault cases from the Pyhäkoski – Rautaruukki line. Here only 4 cases are presented out of six available, Section 4.4 (fault distances: 1, 25.8, 51.5 and 51.5 km). The other two yielded such a high degree of error that it would not be illustrative to include them. The error in the so called “improved conventional fault location” is shown in Fig. 16. This figure shows the error for both the phase current and zero-sequence current based methods. The detailed data are in Tab. 18 of Appendix A.

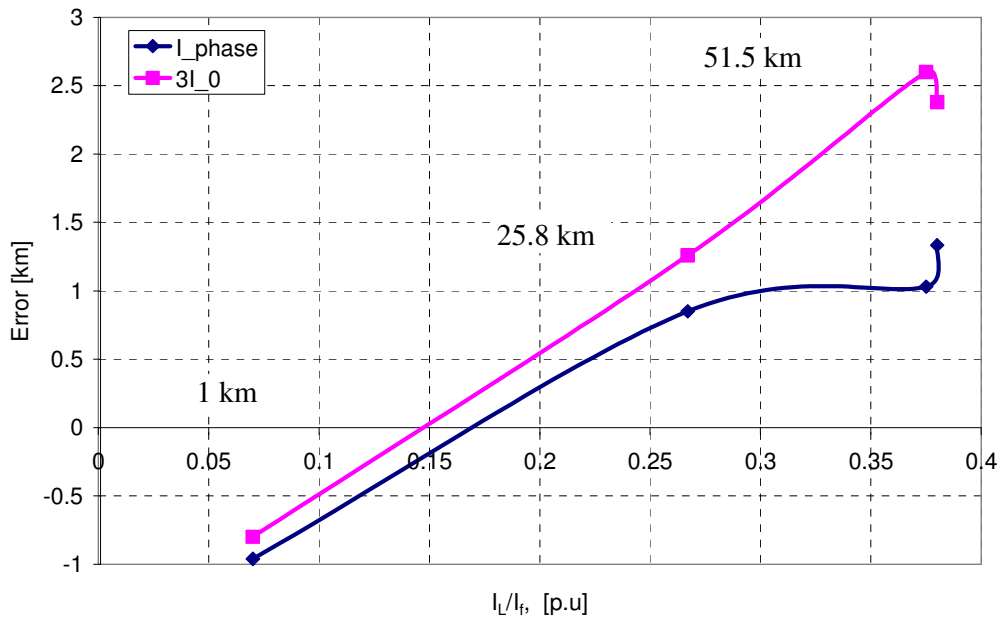


Fig. 16 The error in the improved conventional method. Utilisation of the phase (I_{phase}) and zero-sequence ($3I_0$) currents are compared. Data from the Pyhäkoski – Rautaruukki line.

The figures show similar results to the simulated cases. The fault location error increases with the load/fault current ratio.

4.6 Discussion

Solidly grounded vs. isolated systems

The conventional fault location methodology was examined in this chapter, defined for solidly grounded radially operated systems (or low-reactance grounded networks). The investigation of an isolated neutral network showed that the method can also be applied to this type of network with similar accuracy. The key element is to have enough zero-sequence current flow via the measurement point in the substation. In the case of a solidly grounded network, all three components, the positive, negative and zero sequence components, are equally present and can be measured. However, if the neutral of the transformer is not grounded solidly, the zero-sequence current will return fully or partially via the power lines. The return path for the zero-sequence current would be improved if there are some other outgoing lines or compensation capacitors with grounded neutrals connected to the same busbar as the line under consideration (however, they are not grounded in Finland). In the case of long lines connected to the same busbar, the accuracy of the method would, in the best case, be the same as for a solidly grounded network. In our particular case, the length of the line connected to the same busbar was chosen to improve this path so that the fault location could be made with satisfactory accuracy. The exact correction factor is of a general nature, however, and will be shown for the transient method in Chapter 11.

Correction for improved conventional fault location

The improved conventional fault location method calculated the fault distance more accurately than the conventional fault location method. It has the ability to reduce the influence of the unknown fault resistance. The improvement is remarkable and the method can be considered to be more accurate. However, there is also some weakness in this solution. The fault location equation becomes at some point unreliable, due to the fault location equation denominator's small value. In this chapter the problematic cases have been specified and it is possible to say how accurate our estimation will be directly from the measured signal (from the method's point of view).

Zero-sequence current used for fault location

The zero-sequence current can be measured as a sum of the 3 phase currents or as a current in the neutral of the transformer. These two cases are quite different. In both cases the location would be better if the grounding impedance is lower (the lower the better - the best would be zero) and if the load current is considerably lower than the fault current (the best results would be obtained if the network is unloaded).

The length of the connected line would be an advantage in the first case, where the current sum is measured. But, it would be disadvantageous to measure the neutral current,

4 Conventional fault location

because the neutral current is only part of the total zero-sequence current in the system. The correction will depend on the total network ground capacitance and the reactor size, [21].

5 General study of fault transients

In general, a power transmission system consists of resistances, inductances and capacitances, which exist as lumped parameters but are also distributed over the line, transformers, etc. Such a system will generate transients, which are of a wide spectrum, during every change such as a switching operation or fault.

Fault transients, which can be used for fault location purposes, are studied in this chapter. The spectrum of fault signals can be categorised and the dominant transient components can be identified as in [1]. The typical transients of a fault current are:

Low frequency transients

- Suppression coil current transient (if coil is in use)
- Charge transient

High frequency transients

- Travelling waves
- Discharge transient

The first two transients are of relatively low frequency, which means a maximum level of a few kilohertz. They are described in detail in Sections 5.1 and 5.3 and the discharge transient is covered in Section 5.2. Travelling waves travel in the network at approximately the speed of light in the case of overhead lines. Even if the network is relatively long, a quite high sampling frequency is needed to catch the travelling waves. For overhead lines this is in the range of at least a few hundred kilohertz.

5.1 Charge transient

When an earth fault occurs in a power system, the voltages of the two sound phases rapidly increase, which creates a transient. This transient flows through the transformer primary winding. The simplified situation according to [13] and [14], when the inductance and resistance of the line is neglected, is as shown in Fig. 17. The theory of fault transients covered in this section deals with ungrounded neutral systems. Although other systems exist in Finnish networks, such as compensated and reactance grounded neutrals, the analysis of fault transients in these systems (e.g. Petersen coil systems) is similar to the ungrounded one, because the coil is of relatively high impedance at fault transient frequencies.

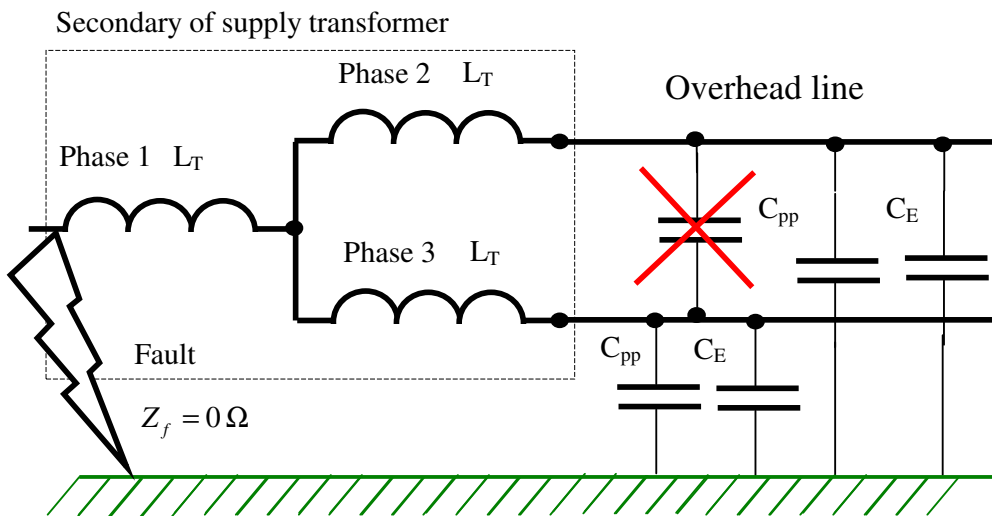


Fig. 17 The lumped model for fault transient study in ungrounded networks.

During a fault in phase 1, the phase to earth capacitance of the faulted phase can be neglected for the purpose of this study (because it is short-circuited by the fault itself). The phase to phase capacitances C_{pp} of the surrounding phases are in parallel with their phase to earth capacitances C_E , as shown in Fig. 17. The capacitance between the unfaulted phases (phases 2-3 in the studied case) can be omitted, since the ends are at the same potential from the transient's point of view (symmetrical system). L_T is the substation transformer inductance.

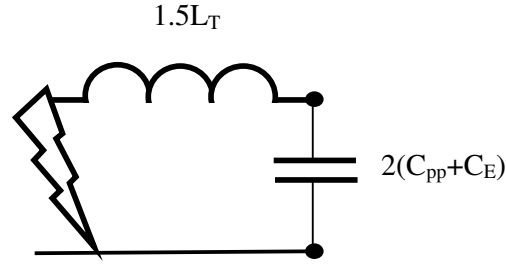


Fig. 18 The circuit for charge transient calculation.

Hence, the frequency of the “charge” transient during undamped conditions is calculated as follows:

$$\omega_c = \frac{1}{\sqrt{L_{eq} C_{eq}}}, \quad L_{eq} = 1.5L_T, \quad C_{eq} = 2(C_{pp} + C_E) \quad (16)$$

where:

ω_c is the angular frequency of the charge transient

L_T is the substation transformer inductance

C_{pp} is the phase to phase capacitance of the line

C_E is the phase to earth capacitance of the line

Note: This example relates only to a fault on the busbar and where the transformer’s inductance is high compared to the line inductance. For a more complex solution the line inductances must be added in series to the transformer’s inductance. Then L_T in Eq. (16) should be substituted by $L_T + L_f$, where L_f is the fault path inductance of the line.

The initial amplitude of the charge transient in an undamped case is calculated by Eq. (17).

$$\hat{i}_c = \frac{v_e}{\omega_c L_{eq}} = v_e \omega_c C_{eq} \quad (17)$$

If the fault happens at the phase voltage maximum, the amplitude of the charge transient is as in Eq. (18):

$$\hat{i}_c = \frac{C_{eq}\omega_c}{3C_E\omega_f} \hat{i}_e \quad (18)$$

where:

ω_f is the fundamental angular frequency

v_e is the instantaneous phase to earth voltage at the fault moment

\hat{i}_e is the uncompensated steady state fault current peak value with zero fault resistance

Influence of the connected lines

If another line (or lines) is connected to the same busbar as the faulted line, the connected line will also contribute to the generation of the fault charge transient. The capacitances of the healthy phases, C_{pp}' and C_E' (phase to faulty phase and phase to ground), of the connected lines are connected in parallel with the healthy phase capacitances of the faulty line, C_E and C_{pp} , shown in Fig. 17. The total equivalent capacitance of the connected line C_{eq}' must be added to the faulted line's equivalent capacitance, i.e. $C_{eq} + C_{eq}' = 2(C_E + C_{pp}) + 2(C_E' + C_{pp}')$. This results in lowering the frequency of the transient and increasing the initial peak value of the fault current transient in relation to Eqs. (16) and (17).

The practical charge transient frequency for 110 kV lines is in the range of 80 to 600 Hz and has a dominant amplitude. For comparison, in medium voltage distribution networks the transient frequency is in the range 100-800 Hz and the amplitude can be 10-20 times higher than the uncompensated fundamental frequency fault current, [1]. It is also easily distinguished from the 50 Hz load current. Therefore, this transient is suitable for fault location.

5.2 Discharge transient

The charge stored in the earth capacitance of the faulty phase is removed during a fault and a “discharge” transient is generated. The discharging of the capacitance takes place at a frequency dictated by the speed of the travelling wave in the line and the fault distance. The situation is clearly illustrated in Fig. 19, where the lattice diagram and the faulted phase voltages are shown for a single-phase to ground fault. The travelling waves caused by the fault are reflected between the fault place and the substation. The amount and polarity of the reflected wave depends on the reflection coefficient. The reflection coefficient is a number between -1 and 1, and for voltage is defined as:

$$\rho_v = \frac{Z_T - Z_C}{Z_T + Z_C} \quad (19)$$

where Z_C is the characteristic impedance of the line and Z_T is the terminal impedance of the line. The reflection coefficient for the current is $\rho_i = -\rho_v$.

The situation in Fig. 19 is idealized; the reflection coefficient for the voltage is 1 at the substation (supposing that the impedance is infinite compared to the line impedance Z_C) and -1 in the fault place (the fault impedance is taken to be zero), [26].

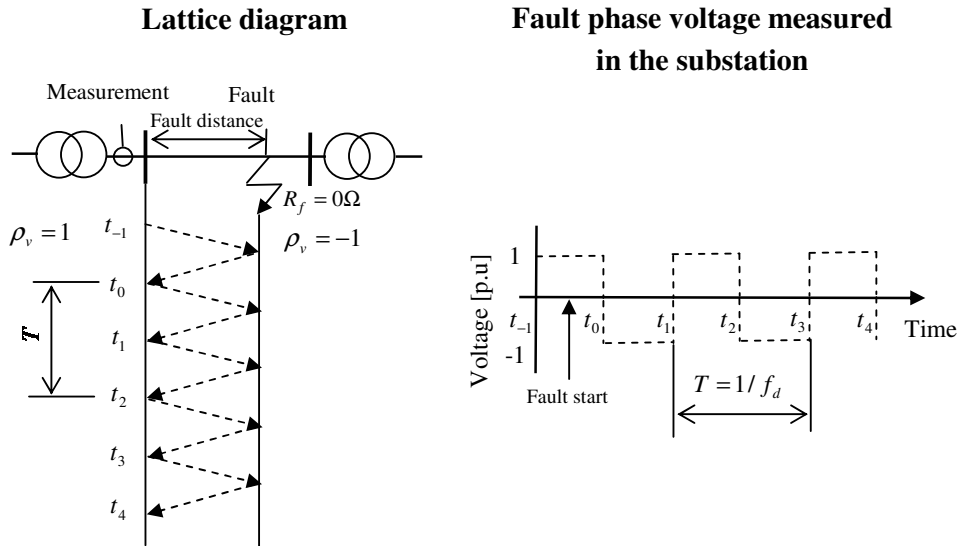


Fig. 19 The lattice diagram for ground fault study (left) with the fault phase voltage in the substation (right).

5. General study of fault transients

The reflections of the travelling waves, shown in Fig. 19 (left), will cause a voltage at the discharge frequency at the measurement point, Fig. 19 (right). The frequency of the discharge transient can be calculated according to [13] as:

$$f_d = \frac{v}{4l_f} \quad (20)$$

where: v is the velocity of the travelling wave and l_f is the fault distance. The discharge frequency calculated according to Eq. (20) exists in a faulted system if there is a perfect reflection at the fault place ($Z_f = 0 \Omega$); otherwise it might be mixed with reflections from the other end of the line.

Influence of the connected line

If another line (or lines) is connected to the same busbar as the faulted line, the connected line will also contribute to the discharging of the capacitance of the faulty line. This means the dominant discharge frequency of the whole system can no longer be calculated according to Eq. (20). This situation is made clear in Fig. 20, where the lattice diagram and the fault phase voltages are shown for a single-phase to ground fault. For simplicity, the reflection coefficient for the voltage is 1 at the substation of the connected line and -1 at the fault location, and the reflection coefficient in the substation with the measurement is taken to be 0. The situation is shown for the connected line length equal to the fault distance. This will cause the total discharge frequency of the network to be half of the value that would occur if there is no connected line.

Based on these facts and experience gained from the EMTP/ATP simulations presented in Chapters 7 and 8, the following equation for the discharge transient frequency f_d can be written:

$$f_d = \frac{v}{4(l_f + l_{cl})} \quad (21)$$

where v is the velocity of the travelling wave in the lines, l_f is the fault distance and l_{cl} , in this case, represents the length of the connected line.

The example shown is only one of the possible network configurations. There might, however, be more than one connected line outgoing from the substation and, what is more, the speed of the travelling waves might differ for the lines. In such cases a more detailed analysis based on the travelling waves must be provided in order to compute the frequency of the discharge transient.

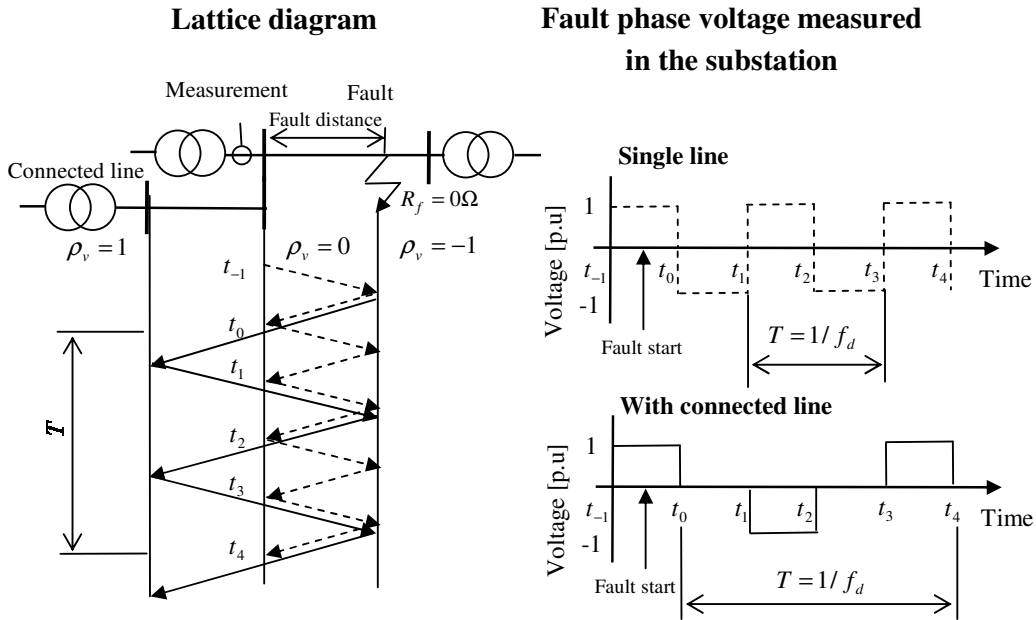


Fig. 20 The lattice diagram for ground fault study in a network with connected lines (left) with the fault phase voltage in the substation (right).

The amplitude of the discharge transient is normally 5-20% of the charge transient. The practical frequency range is 500-2500 Hz for distribution networks, according to [1]. In HV networks the range is wider. The speed of light can be used for approximate calculation of the discharge transient frequencies in HV overhead lines. (More precisely, $v = 1/\sqrt{CL}$ with C and L being the capacitance or the inductance of the line per km). In fact, the frequency of the discharge transient depends only on the fault distance, Eq. (20) or (21). Therefore, the frequency can be very high for faults close to the busbar, but the typical range in 110 kV systems is about 300 Hz -5000 Hz. In practice the frequency of discharge transients is higher than the charge transients.

5.3 Suppression coil current transient

In a compensated neutral network the energising of the compensation coil creates a transient during an earth fault. The transient consists of the supply frequency and a DC component. The suppression coil current transients can be analysed using symmetrical components or using a single phase representation, as shown in Fig. 21. The idea this analysis is based on is the description of the fault impedance loop.

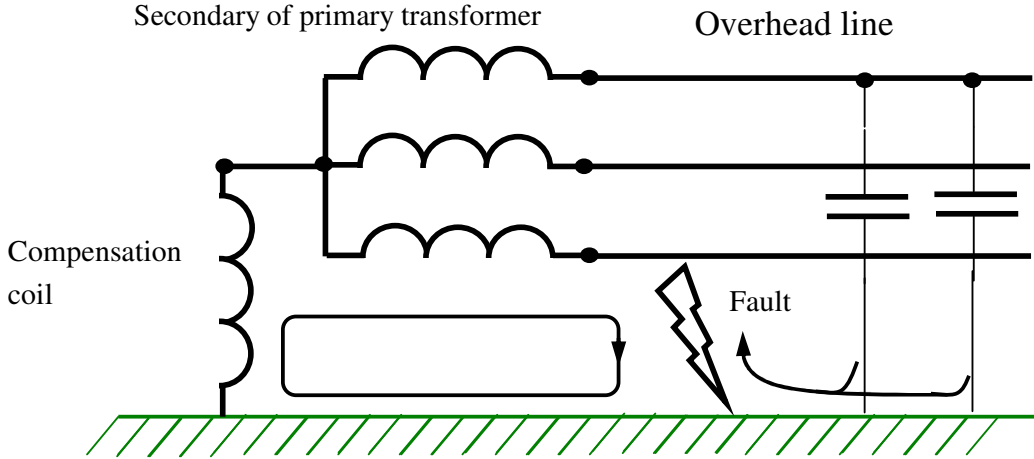


Fig. 21 Transient of the suppression coil current.

The basic solution according to [1] can be obtained from:

$$L_{SC} \frac{di}{dt} + R_{SC} i = \hat{v} \sin(\omega_f t + \varphi) \quad (22)$$

where: ω_f is the fundamental angular frequency, t is time, \hat{v} is the voltage peak value, i is the current, L_{SC} and R_{SC} are the respective sums of the inductances and resistances of the suppression coil, coupling transformer winding, faulty line section (length) and fault, and φ is the initial phase angle.

The solution of Eq. (22) can be expressed as:

$$i = \frac{\hat{v}}{\sqrt{R_{SC}^2 + (\omega_f L_{SC})^2}} \left[\sin(\omega_f t + \varphi - \arctan(\frac{\omega_f L_{SC}}{R_{SC}})) - e^{-\frac{t}{L_{SC}/R_{SC}}} \sin(\varphi - \arctan(\frac{\omega_f L_{SC}}{R_{SC}})) \right] \quad (23)$$

The transient includes two components, an exponentially decaying DC component and a fundamental frequency component. The DC component will appear in situations where the fundamental frequency current is not zero at the fault moment. If this current is equal to zero at the fault initiation, the DC transient will not appear at all. The other extreme is if the fault happens at the current maximum; then the DC component will be maximum, [1]

5. General study of fault transients

In practice this current transient can be highly distorted because of the magnetic core saturation caused by the high DC current. The saturation of the coil depends very much on the initial moment at which the fault occurs. Therefore, this transient can be utilised in fault location if the fault does not appear at a high instantaneous value of the current. If the coil has an air gap in the the steel core, there is no saturation at all.

The saturation of the coil can also be harmful in cases where the charge or discharge transients are used for fault location. The reason is that the saturation of the coil core produces odd numbers of harmonics in the current, which might become mixed up with the actual transients, such as the charge or discharge transient, [1].

6 Signal processing methods

The fault signals that can be used for fault location cover a wide frequency spectrum. Usually the fault signal consists of the 50 Hz wave with some higher or lower frequency components superposed on it. The higher frequency transients typically attenuate quicker than the lower ones.

There are many techniques that can be used for filtering out the fault transients from the measured fault signal. In this chapter the most common ones are represented. More about signal processing can be found in [4], [5], [15], [22], [24] and [30].

For better frequency estimation of the transient, a pre-processing technique can be performed, Section 6.1. Spectrum analysis is presented in Section 6.2. Section 6.3 reviews some of the mathematical transformations used in the time-frequency signal representation. Here the most popular techniques are listed, the windowed Fourier transform and the wavelet transform. Section 6.4 concentrates specifically on wavelet filters.

6.1 Pre-processing of the signal

Sometimes a transient is represented by a limited number of samples and so estimation of its frequency might be difficult. Filtering can be performed in order to detect the frequency of the transient more accurately. For this reason signal pre-processing is applied.

Removing the 50 Hz component with a simple filter

This can be accomplished very easily by filtering:

$$g[n] = f[n] - f[n + N_{50}] \quad (24)$$

where $f[n]$ is the original signal - discrete function of the samples, $g[n]$ is a new signal - discrete function of the samples and N_{50} is the number of samples related to 20 ms (if the system frequency is 50 Hz). The filter's advantage lies in its simplicity, but at the price of a bad side effect. It can partly cancel the other frequencies: DC, 100th 150th 200th ... $k*50^{\text{th}}$ (where $k = 0,1,2,\dots$ etc), as can be seen from the very simple equation.

Removing the 50 Hz with a band pass FIR filter

A digital FIR (finite impulse response) filter is mainly used to remove the 50 Hz signal, which usually has the dominant amplitude and is very close in the frequency domain to the transient itself. It can also remove the higher frequency transients or noise. An example of the “sinc” filter coefficients and the filtered spectrum are shown in Fig. 22. The filter’s lower cutoff frequency is set to $f_{c1} = 100$ Hz and the higher to $f_{c2} = 450$ Hz .

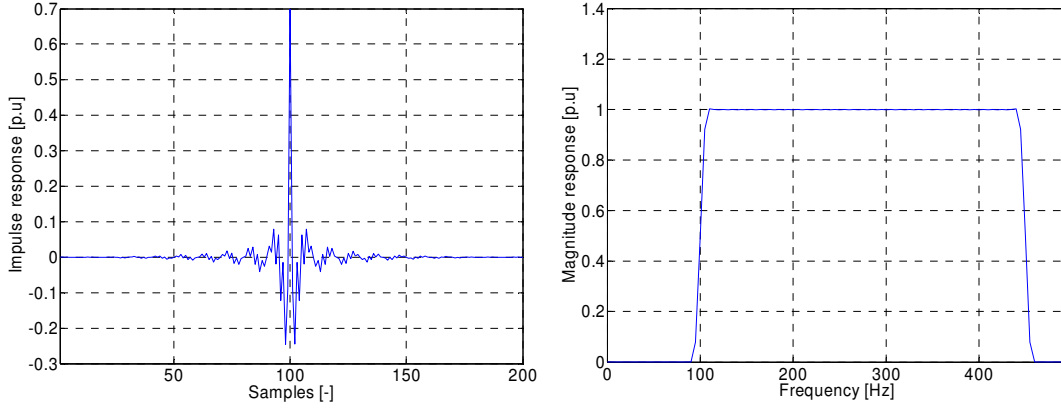


Fig. 22 Example of filter for pre-processing. The filter’s coefficients are represented by 200 samples (left), and the frequency response of the filter (right).

This filter characteristic can be achieved with the coefficients calculated according to Eq. (25), given by the “sinc” function, [22] :

$$h(k) = \frac{\sin(2\pi f_{c2}(k-m))}{\pi(k-m)} - \frac{\sin(2\pi f_{c1}(k-m))}{\pi(k-m)}, \quad \text{if } k \neq m \quad (25)$$

$$h(k) = 2(f_{c2} - f_{c1}), \quad \text{if } k = m$$

In order to reduce the pass-band and stop-band ripples we used the Hamming window, Eq. (26), as presented in [22]. The filter coefficients with the Hamming window applied can be seen in Fig. 22 (left).

$$w(k) = 0.54 - 0.46 \cos(2\pi k / (N-1)) \quad (26)$$

where k and m are the integer variables and N is the number of coefficients.

The filter gives very good frequency resolution as is seen from the frequency response in Fig. 22 (right). However, the time resolution of the filtered signal will strongly depend on the filtered spectrum width. The time resolution will be lower if the filtered frequency band is too narrow.

6.2 Spectrum analysis

For detection of the signal frequency, the Fourier transform (FT) is used. This transform can give the frequency content of the signal but not the time position of its components.

The definition of the FT according to [15] is:

$$FT(f) = \int_{-\infty}^{\infty} x(t) \cdot e^{-j2\pi ft} dt \quad (27)$$

where $x(t)$ is a continuous function of time t , f is the frequency and t is time.

And the discrete version, the discrete Fourier transform:

$$DFT[k] = \frac{2}{N} \sum_{n=1}^{N/2} x[n] \cdot e^{-j \frac{2\pi kn}{N}} \quad (28)$$

where: $x[n]$ is a discrete function of the samples, n and k are the integer variable parameters, and N is the number of samples.

The fault signals are non-stationary signals and the spectrum of such signals gives the correct frequency position of each signal component, but not their amplitude. Because the signals do not exist over the entire analysed period, the amplitude is the mean value over the analysed time interval. The right amplitude can only be achieved if the signal component is so-called stationary. This means that the signal occurs in the analysed window with a stable frequency and amplitude.

6.3 Time-frequency representation of the signal

Mathematical transformations are applied to signals in order to obtain information that would not be readily available in the time-domain signal. There are a number of transformations that can be applied, Fourier, wavelet, and Radon and Hilber, of which the Fourier transform is probably the most popular.

In practice, most of the signals are time-domain signals. This representation is not always the best representation of the signal for other applications. Information that often cannot be readily seen in the time-domain can be seen in the frequency-domain. However, not all information can be seen only in the time-domain or only in the frequency-domain. Therefore, a combination of the two, the time-frequency representation of the signal, is very informative.

For applying the transforms in practice (in digital devices), it is necessary to use their discrete versions. Therefore, these are also presented.

In order to understand which transform is suitable for which signal, all signals can be divided into two types:

- **Stationary signal**
Signals whose frequency content does not change during the analysed period.
- **Non-stationary signal**
Some frequency components exist in a shorter signal time than the analysed period.

Commonly used techniques

In the past, the windowed Fourier transform was in common use. This transform is based on equal windowing for each frequency level. The equal windowing causes disturbance in such signals as the fault transients, mainly because of the existence of frequency components lower than the needed component. This requires a combination of other techniques to remove the lower frequencies.

Nowadays the wavelet transform is very frequently used for signals such as fault transients. The wavelet filtering is based on a multi-resolution analysis that uses small time windows for higher frequencies and wider time windows for lower frequencies. This is naturally suitable for signals like fault transients, because the high frequencies attenuate (die) quickly and the lower transient frequencies are of longer duration, as is shown in [4], [5].

6.3.1 Windowed Fourier transform

The windowed Fourier transform (WFT), also known as the short-term Fourier transform (STFT), gives the time and frequency position of the signal components. The signal is divided into a sufficiently large number of small segments so that each segment of the signal can be assumed to be stationary. The WFT thus gives the frequency spectrum of every window of the signal and so it is possible to locate the time position of shorter frequency components in the signal. The continuous WFT is defined according to [15] by the following equation:

$$WFT_w^x(t, f) = \int_{-\infty}^{+\infty} x(t) \cdot w(t - \tau) \cdot e^{-j2\pi f \tau} d\tau \quad (29)$$

where: $x(t)$ is a continuous function of time, f is the frequency, $w(t - \tau)$ is the window function, t is the time and τ is the translation.

This transform can be displayed in a spectrogram, such as the one in Fig. 23 (left), where the time and frequency domains can be clearly seen. The WFT analyses the signal with the same resolution at both high and low frequencies. In practice, windowing is performed by a window function. The most popular window functions are the Gaussian, rectangular, Hamming, Bartlett and Chebyshev. The Gaussian window function is presented below, [22]. It is defined by:

$$w(t) = \frac{1}{\sqrt{2\pi}\delta} e^{-\frac{t^2}{2\delta^2}} \quad (30)$$

where δ is the standard deviation. In Fig. 23 (right), an example of the Gaussian windowed sinusoidal signal at different frequencies and different time locations is presented for $\delta = 1$. For digital implementation the windowed discrete Fourier transform (WDFT) is used.

To get better resolution in the time or frequency domains we can change the parameters of the windows. A narrow window gives good time resolution, but poor frequency resolution, Fig. 24c. Wide windows give good frequency resolution, but poor time resolution, Fig. 24b. If the window is very narrow, a low frequency signal will appear to be non-periodical in the window and so its spectrum will tend to infinity and disturb the higher frequency components, as shown in Fig. 24d. The resolution also depends on the type of window function. For example, the results using Gaussian windowing are significantly superior to those achieved using rectangular windowing, [5].

6. Signal processing methods

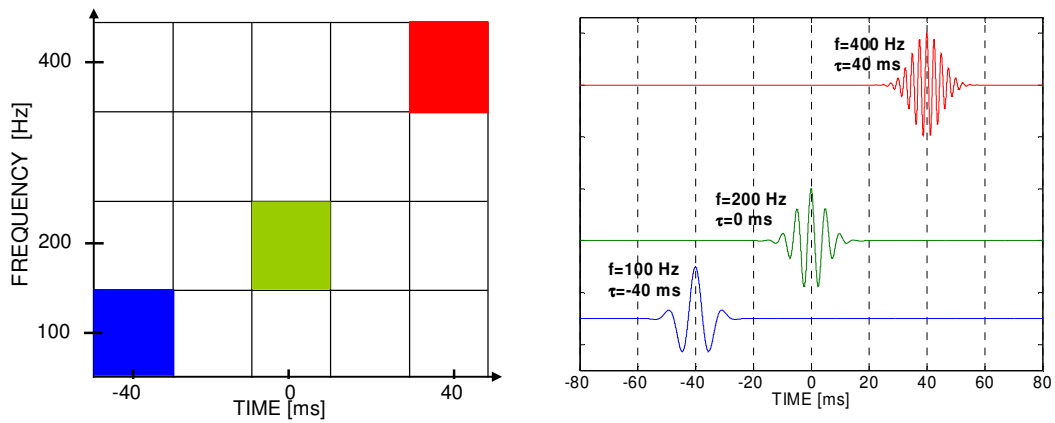


Fig. 23 The time-frequency plane for the WFT (left) and an example of a Gaussian windowed sinusoidal signal at different frequencies and different locations in time, (right).

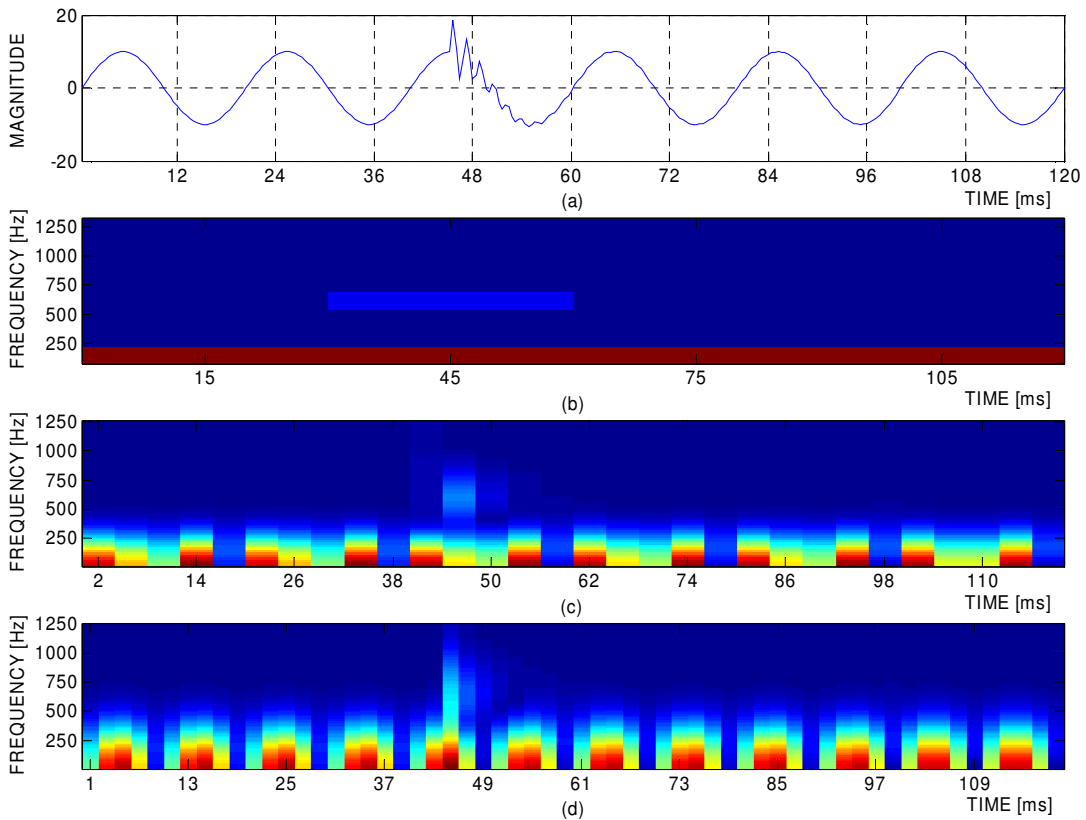


Fig. 24 Input signal ($50\text{ Hz} + 600\text{ Hz}$) and its WDFT. The input signal (a), WDFT with $\tau = 12\text{ ms}$ (b), WDFT with $\tau = 4\text{ ms}$ (c), and WDFT with $\tau = 2\text{ ms}$ (d).

6.3.2 Wavelet transform

The term wavelet means “*small wave*”. The wavelet transform (WT) was introduced by Jean Morlet at the beginning of the 1980s and has undergone rapid development since then in the fields of image processing and acoustic signal analysis. It has the special feature of variable time–frequency localisation, which can be more advantageous when analysing non-stationary signals than WFT. Most of the signals that occur in practice have their most important features in the high frequency range (for example the voice), therefore multi-resolution analysis (MRA) is applied. MRA analyses the signal at different frequencies with different resolutions as it is designed to give good time resolution and poor frequency resolution at high frequencies, but good frequency resolution and poor time resolution at low frequencies, as is shown in Fig. 25 (left). In other words, the WT uses narrow windows at high frequencies and wide windows at low frequencies, which does not make the disturbance characteristic of the WFT, (compare Fig. 26b and Fig. 24d). The continuous WT is defined, according to [15], as:

$$WT_{\psi}^x(a, b) = \frac{1}{\sqrt{|a|}} \int_{-\infty}^{+\infty} x(t) \cdot \psi\left(\frac{t-b}{a}\right) dt \quad (31)$$

The windowing shown in Fig. 25 (left) is performed in practice by scaling and translating a “mother wavelet”. The mother wavelet $\psi(t)$ is a function of two parameters, a -scale and b -translation, according to Eq. (32).

$$\psi_{a,b}(t) = \psi\left(\frac{t-b}{a}\right) \quad (32)$$

b gives the time position of the wavelet, while the parameter a controls its frequency. The mother wavelet $\psi(t)$ must be short and oscillatory, and it must have a zero average and decay quickly at both ends, [15]. There are many families of wavelets, for example, Haar, Daubechies, Meyer, Gaussian, Mexican hat, Morlet, Shannon wavelets, and so on. For example, a Gaussian function used as a Gaussian mother wavelet is defined as:

$$\psi(t) = \frac{1}{\sqrt{2\pi\delta}} e^{-\frac{t^2}{2\delta^2} + j\omega_0 t} \quad (33)$$

where δ is the standard deviation, $t = (t-b)/a$, and ω_0 is the normalized angular frequency of the wavelet. An example of a Gaussian mother wavelet is shown in Fig. 25 (right) for different scales (frequencies) and time locations, for $\omega_0 = 2\pi \text{ rad/s}$ and $\delta = 1$. For the situation where the wavelet occurs at time equals zero, the time is translated by setting $b = 0 \text{ s}$ and the frequency of the wavelet, in this case 200 Hz , is

6. Signal processing methods

achieved by scaling with the value $a = 1/200$ s, in accordance with Eq.(32). For digital implementation, the discrete WT (DWT) is used.

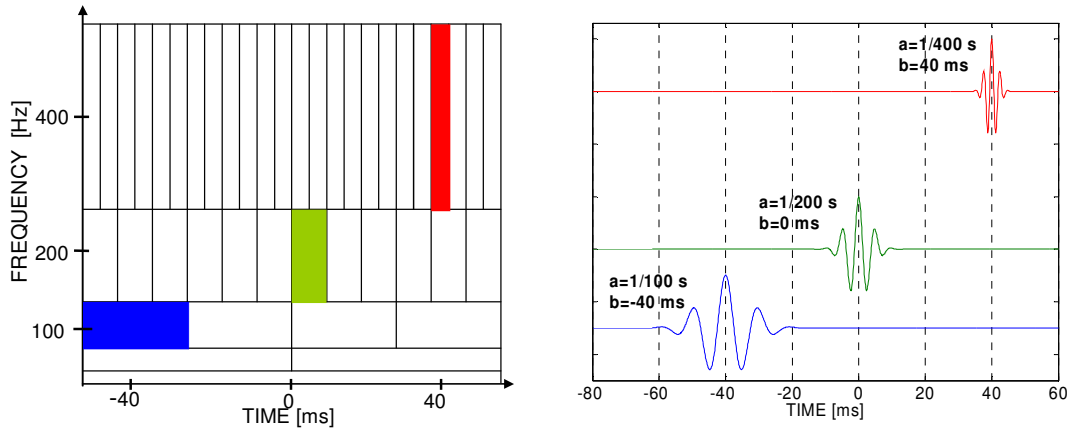


Fig. 25 The time-frequency plane for WT, (left), and the scaled and translated real part of a Gaussian mother wavelet for different scales and different locations in time, (right)

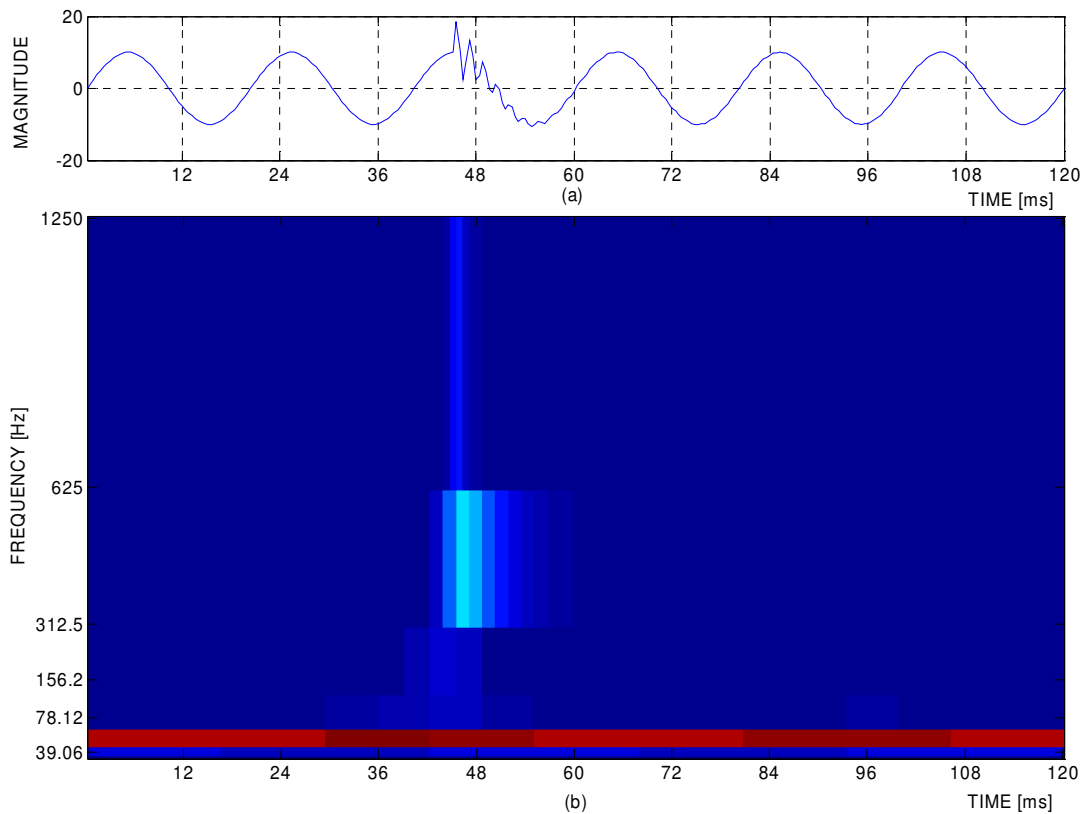


Fig. 26 The input signal (50 Hz + 600 Hz), (a) and its DWT scalogram, (b).

6.4 Wavelet filter

The wavelet transform represents the analysed signal in many frequency scales. However for fault location, only the scale where the transient appears is of interest. Therefore, filtering is more convenient. The wavelet filter can be understood as one scale of the wavelet transform properly designed for the signal.

The wavelet filter's (WF) central frequency must be set. In order to set the wavelet filter at the frequency of the needed frequency component (fault transient), the signal should be pre-processed. Pre-processing can in practice be performed very easily by the DFT. The discrete wavelet transform (DWT) of a discrete signal, according to [15], is:

$$DWT_{\psi}^x[m, k] = \frac{1}{\sqrt{|a|}} \sum_n x[n] \cdot \psi\left(\frac{n-b}{a}\right) \quad (34)$$

where: $x[n]$ is a discrete function of the samples, a is the scale, b is the translation, ψ is the mother wavelet, and k, n , and m are integer variable parameters, with n in this case representing discrete time.

The mother wavelet function is equal to the wavelet filter coefficient.

$$\psi_{a,b}(n) = \psi\left(\frac{n-b}{a}\right) \quad (35)$$

The discrete wavelet filter (DWF), the FIR filter, with the Gaussian wavelet and amplitude correction can be derived as:

$$DWF[n] = \frac{2}{a\sqrt{2\pi}\delta} \sum_n x[n] \cdot e^{-\frac{((n-b)/a)^2}{2\delta^2} + ja_0(n-b)/a} \quad (36)$$

It should be noted that the scaling factor is now calculated from the sampling frequency f_s and the filtered frequency of the charge transient f_c as: $a = f_s / f_c$.

7 Obtaining the fault distance from fault transients

The main issue in this chapter is to show how the fault distance of a single-phase to ground fault can be calculated from the fault generated low frequency transient signals, measured by the voltage and current in the faulted phase. The basic methods of the fault transient's signal processing are described, and possible automatization of the fault distance computation is presented as well. There are many mathematical solutions available for the signal processing, as was shown in Chapter 6. In this basic study the spectrum of the fault transients is analysed by the Fourier transform and the wavelet algorithm (wavelet transformation and wavelet filter), and the differential equation algorithm will be applied to the fault transients in order to calculate the fault distance, for comparison.

The study is conducted using the simulation program EMTP/ATP. The frequency in the EMTP/ATP simulations was 100 kHz and then 2.5 kHz subsampled data was used for the fault location. The studied case is a single-phase to ground fault in a 110 kV un-earthed radially operated network, with fault distance $l_f = 25 \text{ km}$, fault resistance $R_f = 0 \Omega$ and inception angle of the fault voltage (from the zero crossing) in the faulted phase was $\varphi_f = 90^\circ$. The fault happened at time $t_f = 0 \text{ s}$. More details are given in Appendix A.

7.1 Fault transients

Typical single-phase to ground fault transients in the voltage and current of the faulted phase can be seen in Fig. 27. The signals were achieved by ground fault simulation in EMTP/ATP. As was described in Chapter 5, the charge and discharge transients with the travelling waves are generated when a fault appears in the network. All of the above mentioned transient signals plus the 50 Hz component (and possibly the other components) are present in the figure below. In addition to the real transients mentioned above, the EMTP/ATP program can cause some numerical oscillations, especially at the beginning of the simulations, and hence generate signals that never appear in reality.

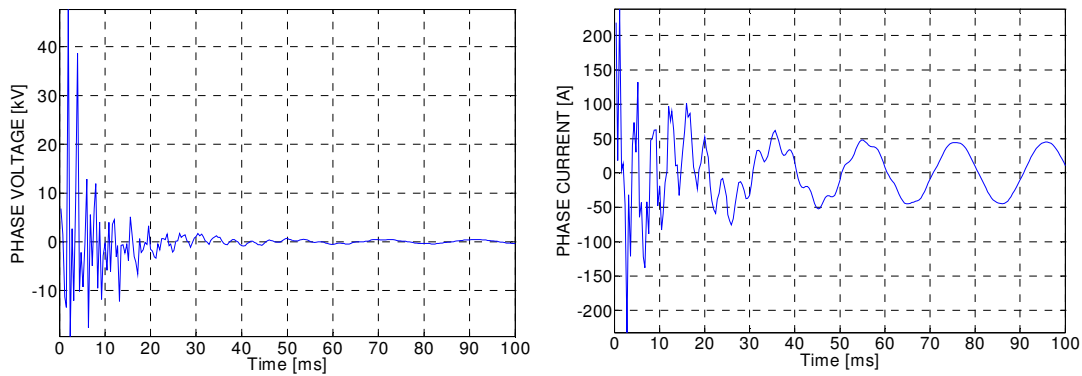


Fig. 27 Typical shapes of the fault current and voltage in the faulted phase. (Study case: $R_f = 0 \Omega$, $l_f = 25 \text{ km}$, $\varphi_f = 90^\circ$ and $t_f = 0 \text{ s}$.)

7.2 Frequency identification of fault transients

The fault current and voltage consist of many frequency components of different time duration. The fault transients are therefore non-stationary signals, such as can be seen in Fig. 27. The spectrum can be calculated by the Fourier transform. The usage of the DFT for spectrum analysis of the non-stationary signals was described in Chapter 6. In Fig. 28, the spectrum of the fault current and voltage is shown (from Fig. 27), as measured in the faulted phase in the studied case. The spectrum was calculated according to Eq. (28).

7. Obtaining the fault distance from fault transients

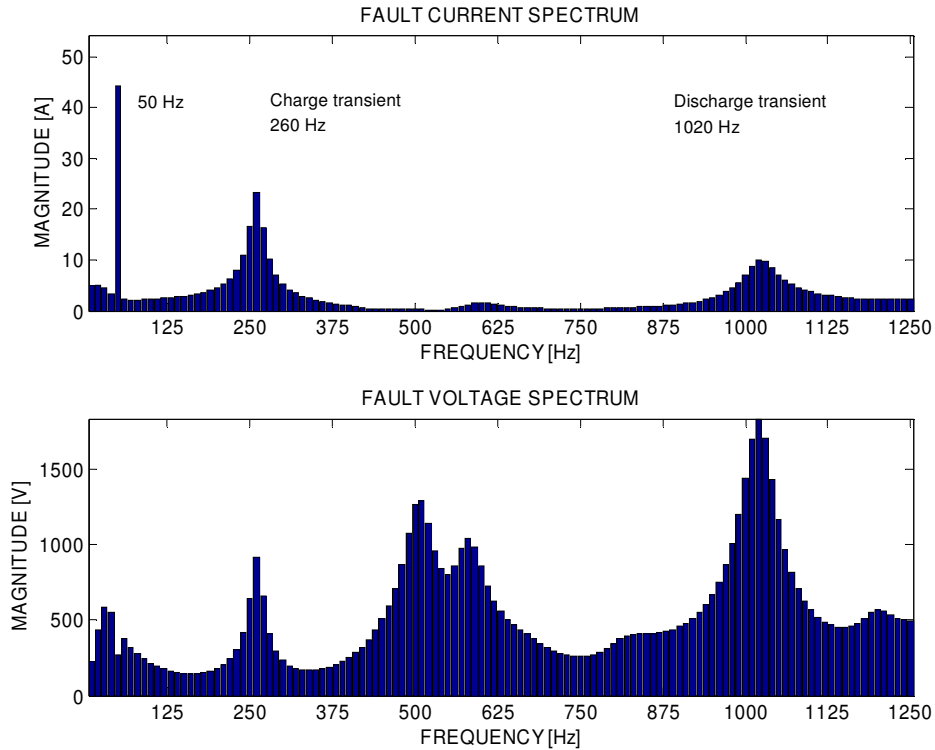


Fig. 28 A typical spectrum of fault current and voltage. (Study case: $R_f = 0 \Omega$, $l_f = 25 \text{ km}$, $\varphi_f = 90^\circ$, and $t_f = 0 \text{ s}$).

The spectrum consists of many components but nevertheless, the charge and discharge transients can clearly be seen. In the studied case the charge transient is 260 Hz and the discharge transient is 1020 Hz. (Note: both frequencies are also affected by connected lines, Sections 5.1 and 5.2.) In general, the situation is much clearer in the fault current spectrum than in the fault voltage spectrum. In the current spectrum one can see the 50 Hz fault current, because the frequency components in the studied time window of 100 ms are of comparable amplitude and time duration. This is not true in the voltage spectrum, because the transients are of higher amplitude than the 50 Hz component itself (the fundamental frequency phase voltage collapses). It can also be seen that the fault voltage transients at higher frequencies are amplified compared to those in the fault current spectrum. This phenomenon is caused by the fault loop inductance (the voltage of an inductor grows linearly with the frequency of its current). The other frequency components, such as the 500 Hz and 600 Hz components, are most probably caused by the connection of the other connected line.

As can be seen from Fig. 27, the charge and discharge transients only exist in the analysed interval, therefore the use of a longer time period does not bring a better frequency resolution, only more bars to the graph (in this case it is 10 Hz/bar). If a longer time pe-

7. Obtaining the fault distance from fault transients

riod is used, the accuracy of the fault location is not affected. This problem will only arise if the window is too small.

7.3 *Fault location algorithms*

A fault signal consists of many frequency components, and so the required transient has to be filtered out. There are many methods available, for example WDFT, DWT, etc, but a satisfactory analysis can be achieved by the wavelet transform or the wavelet filter. The principle differences between the wavelet transform and the wavelet filter are described in Chapter 6. In this chapter the application of both techniques is shown.

The principle of fault location is based on the detection of the fault path inductance using the charge transients. In this chapter the fault path inductance is calculated using the so-called wavelet algorithm, Eq. (2), and the differential equation algorithm, Eq. (7), and is then converted into the fault distance, Eq. (1). The parameters of the zero-, positive- and negative-sequence inductances per km of the studied line are shown in Tab. 9.

7.3.1 *Wavelet algorithm with the wavelet transform*

Filtering

Fig. 29 shows typical examples of fault current and voltage with their wavelet decompositions (calculated for the studied case). The calculation is according to Eq. (34) with the Morlet wavelet, with the parameters $\delta = \sqrt{3/2}$ and $\omega_0 = 5.336$ rad/s given by Eq. (33). The real part of the DWT, which is actually a complex vector, is presented. (Note: the Gaussian wavelet with the setting $\omega_0 = 5.336$ rad/s is the Morlet wavelet, [24].)

The frequency components of the charge transient (260 Hz) and discharge transient (1020 Hz), the 50 Hz fault signals and the others, detected by the DFT (Fig. 28), are clearly separated in Fig. 29. According to the wavelet transform setting and the sampling frequency of 2.5 kHz, each scale of the wavelet decomposition has a different frequency band, as shown in the second column of Tab. 1. The signals will appear in different scales, as is shown in the right side of Tab. 1. The frequency band of scale 1 is <1250-625 Hz> and therefore the discharge transient, which is of frequency 1020 Hz, occurs in that section. The charge transient in this case has a frequency of 260 Hz, so it has to be in scale 4, where the frequency band is <312.5- 156.25 Hz>. The 50 Hz signal will of course occur in scale 16, <78.125- 39.0625 Hz>, as shown in Fig. 29. The original signal for both the voltage and the current can be reconstructed from the wavelet coefficients of all scales 1 to 64. (Note: at the beginning and end of the time window of each scale, there is an error due to the end of the window. However, in the middle of the window the filtering is not affected.)

7. Obtaining the fault distance from fault transients

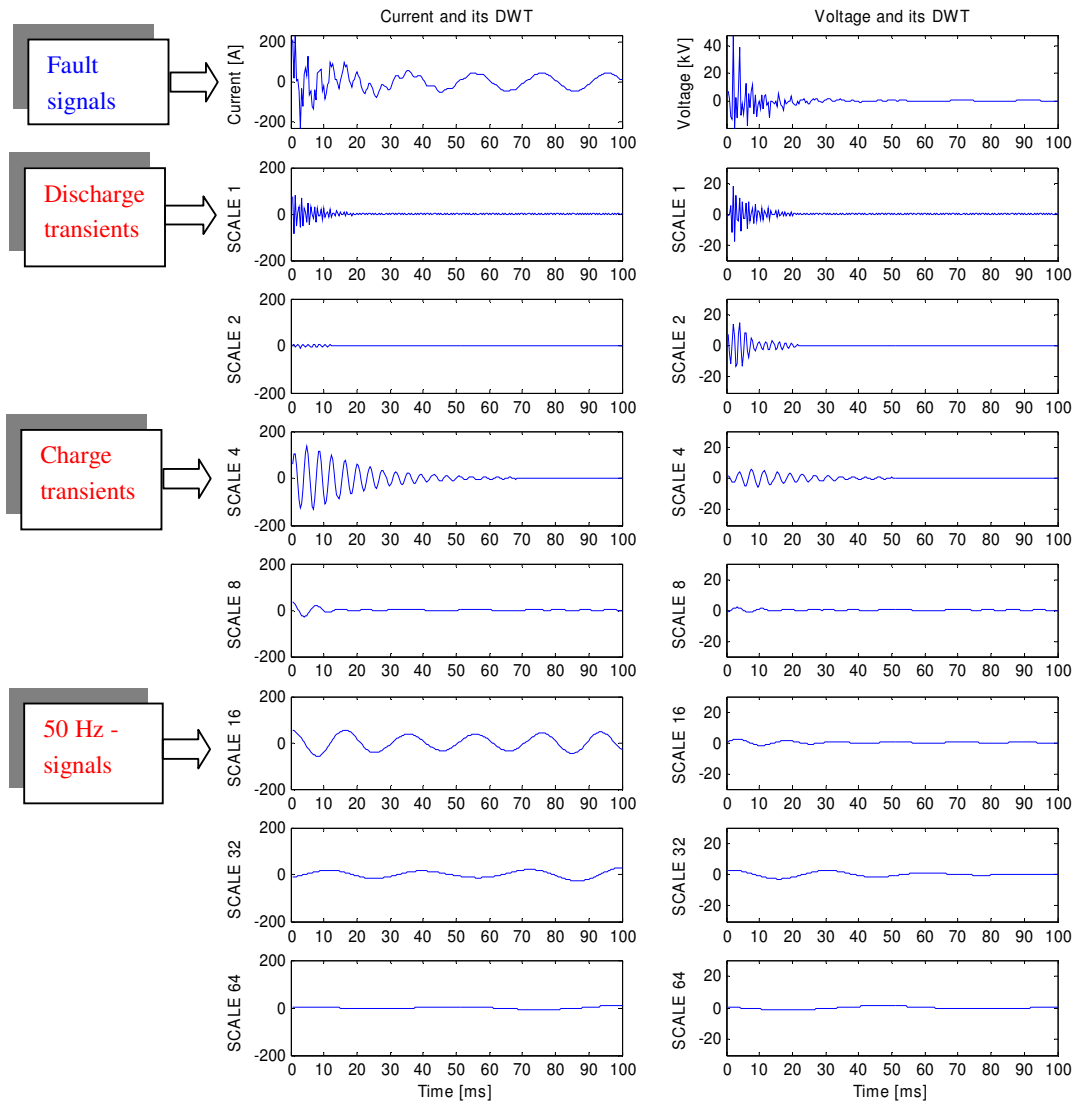


Fig. 29 Fault current and voltage with their wavelet decompositions. (Study case: $R_f = 0 \Omega$, $l_f = 25 \text{ km}$, $\varphi_f = 90^\circ$ and $t_f = 0 \text{ s}$).

Tab. 1 The wavelet transform settings and fault transients for the study case. The sampling frequency is 2.5 kHz.

Wavelet transform properties			Identified signals	
Scale	Filtered freq. band [Hz]	Filtered freq. band [Bar-graph]	Frequency [Hz]	Name
1	1250-625		1020	Discharge transient
2	625-312.5			
4	312.5-156.25		260	Charge transient
8	156.25-78.125			
16	78.125-39.0625		50	50 Hz component
32	39.0625-19.5313			
64	19.5313-9.7656			

Fault location

The fault path inductance is calculated from the transient components of the voltage and current (for the charge transient case under study, it is scale 4 of the signal's DWT, Fig. 29) and the transient frequency itself (in the case of the charge transient, it is 260 Hz, calculated by the DFT, Fig. 28), in accordance with Eq. (2). The inductance can then be converted into a distance using Eq. (1), supposing we know the sequence inductances of the line, and the result can be seen in Fig. 30 (left). For comparison, the fault distance calculated using the discharge transient is shown in Fig. 30 (right).

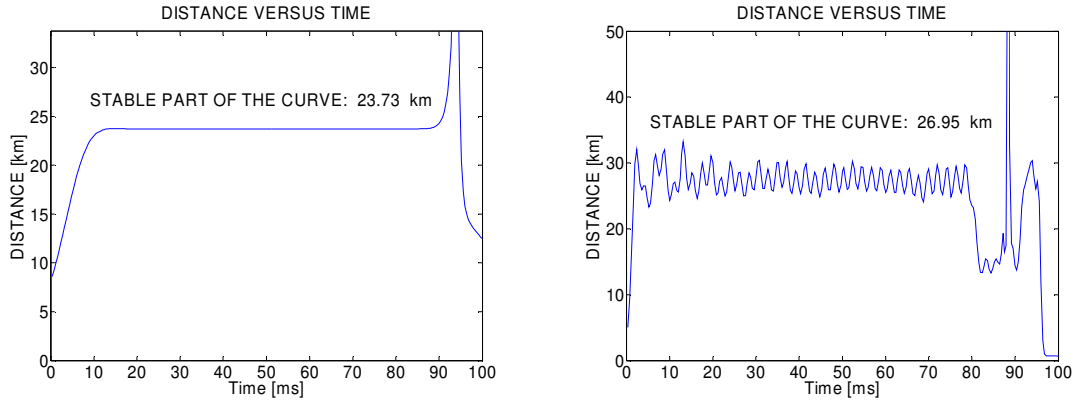


Fig. 30 Estimation of the fault distance by the wavelet algorithm with the wavelet transform, using the charge (left) or discharge (right) transient. (Study case: $R_f = 0 \Omega$,

$$l_f = 25 \text{ km}, \varphi_f = 90^\circ \text{ and } t_f = 0 \text{ s.})$$

7.3.2 Wavelet algorithm with the wavelet filter

Filtering

Use of the wavelet filter for fault location is described here. According to the spectrum analysis the charge transient's frequency is 260 Hz. The wavelet filter is then specifically designed for this frequency, Fig. 31 (top left and right) using the Gaussian wavelet, Eq.(36). The filtered frequency band can also be changed, depending on the neighbouring frequencies. In this case, the closest frequency is the 50 Hz component, which is relatively far from the transient in the frequency domain. (The narrower the frequency band chosen, the worse the time resolution will be; therefore, a compromise must always be chosen.) In this case the frequency bandwidth is $\delta=1$ [p.u], expressed as the standard deviation of the filter response, Fig. 31 (top right).

The original fault current and the filtered fault current are shown in Fig. 31 (bottom left).

7. Obtaining the fault distance from fault transients

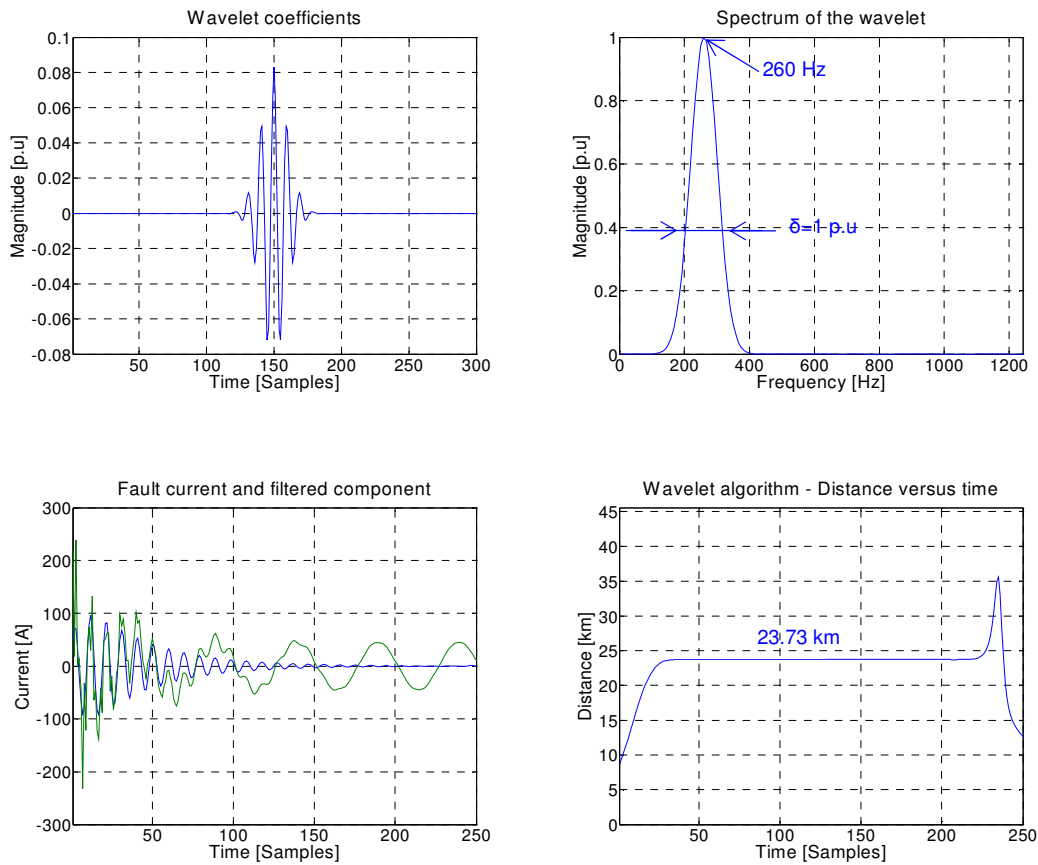


Fig. 31 Wavelet filtering and estimation of fault distance by the wavelet algorithm with the wavelet filter, using the charge transient. (Study case: $R_f = 0 \Omega$, $l_f = 25 \text{ km}$,

$\varphi_f = 90^\circ$ and $t_f = 0 \text{ s}$). 1 sample=0.4 ms.

Fault location

The fault path inductance is calculated from the filtered fault current and voltage charge transient according to Eq. (2) and is then converted into a fault distance using Eq. (1). The fault distance calculated here is about the same as that calculated by the wavelet transform; compare Fig. 31 (lower right) and Fig. 30 (left).

7.3.3 Differential equation algorithm

Here the fault path inductance is calculated according to Eq.(7). The input signal's voltage and current needed for solving the fault location equation are the charge transient voltage and current filtered by the wavelet filter, Section 7.3.2. Then the fault distance can be calculated using Eq. (1), and plotted as in Fig. 32 (left). The detail of the curve is shown in Fig. 32 (right). Results are comparable to those achieved with the wavelet algorithm.

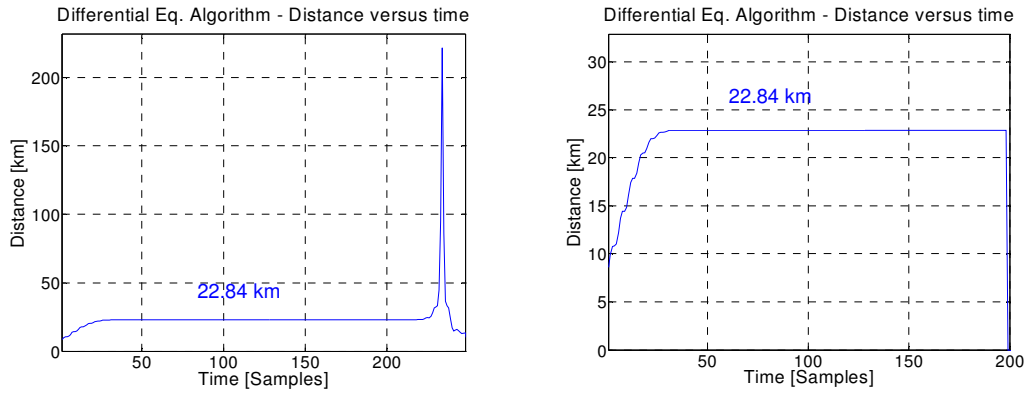


Fig. 32 Estimation of the fault distance by the differential equation algorithm using the charge transient. Presented for the entire time period (left) and in detail (right). (Study case: $R_f = 0 \Omega$, $l_f = 25 \text{ km}$, $\varphi_f = 90^\circ$ and $t_f = 0 \text{ s}$). 1 sample=0.4 ms.

7.4 Automatic fault distance detection

The fault distance calculated by the fault location algorithms is not a single number, but is a time dependent function, Section 7.3. The correct position of the fault can be detected from the stable part of the distance curve, as presented in [2]. A visual estimation of the fault location might be good enough for repair purposes, but if the method is used for protection, a detection algorithm should be designed, because the information about the fault place should be available within a few milliseconds. The detection algorithm is described in the following three steps:

- **Numerical derivation**
The analysed interval can be divided into sub-intervals, where the dispersion of the values over each interval is evaluated.
- **Transient “lifetime” estimation**
The transient “lifetime” can be evaluated as the time in which the current transient is damped by x-dB of its peak value.
- **Decision making**
The fault distance is detected as the mean value of the interval with the smallest dispersion within the current transient lifetime.

Note: The estimated fault distance also depends on the number of intervals used in the detection of the stable part of the distance curve and also on size of the analysed time window, following the occurrence of the fault.

7.5 Discussion

Line modelling

In this study case a simple first order line model has been used. The practical implementation of this model is Eq. (1) in Section 3.2. Normally, the method would not work for isolated network neutral systems, but due to the fact that there is a connected line it was possible to use this model quite accurately, as shown by the simulation results. This issue is studied further in Chapter 11.

Wavelet algorithm versus differential equation algorithm

The simulation results prove that results by both methods are comparable. However, there might be some difference in accuracy for some specific conditions. In a case where the transient is represented by only a few samples, for example, where the sampling frequency is too low or the transient is very much damped, the estimation of the transient frequency might be inaccurate and therefore the wavelet algorithm would fail. This is because the wavelet algorithm uses the transient frequency but the differential equation algorithm does not. In these cases the differential equation algorithm is more reliable, see Section 3.2.

Wavelet filter versus wavelet transform

The fault transients can be filtered out of the fault signals by either the wavelet transform or the wavelet filter. The wavelet transform is very good for visualisation of the signal in different frequency bands, but its application for fault location purposes might be a bit risky in some cases. In practice, the wavelet transform may fail in cases where the transient appears close to the scale border. In a such a case the scale borders should be changed. Therefore, for practical purposes it is more convenient to use the wavelet filter instead. However, the study presented in this thesis has in part been analysed by the wavelet transform, Chapter 8, and by the wavelet filter presented in Chapters 11 and 12, since both techniques are likely to be used in a real application. In addition, this technique is very sensitive to the wavelet type. For fault transient analysis the required accuracy can be achieved with the Gaussian or Morlet wavelets, which were used in this chapter. Using other types might also be advantageous. The Daubechies wavelets are very popular, for example, and they have a very good frequency response over a wide spectrum. A good reference dealing with the application of wavelets to power system transient analysis is [15]. Because both the wavelet transform and the wavelet filter with the two different mother wavelets (Morlet and Gaussian) result in the same fault distance estimation, it can be concluded that the applied signal processing techniques do not contribute to the error in the final fault location.

7. Obtaining the fault distance from fault transients

Sampling frequency

The simulated data were subsampled into 2.5 kHz for the fault location. This frequency is not randomly chosen; it relates to the practice in Finland. The disturbance recorders on the lines where the fault location method can be applied usually operate at a frequency of 2.5 or 5 kHz, Section 2.2.

8 *EMTP/ATP fault transient simulation*

This chapter investigates the sensitivity of ground fault transients on parameters such as the fault distance, fault impedance and the voltage inception angle, and also the impact of the neutral grounding. The same network is studied as in Chapter 7, using the EMTP/ATP program. All simulations presented in this section are processed automatically by the wavelet algorithm with the wavelet transform using the Morlet wavelet (as described in Section 7.3.1). Some results of this study can also be found in [31].

8.1 *Description of the simulated network in EMTP/ATP*

The simulation of the faults presented in this section was carried out using EMTP/ATP. The network is shown in Fig. 33. The network is radially operated and consists of a 220 kV supply network and two connected outgoing 110 kV lines. The 110 kV part of the network is unearthed. The network also consists of the transformers and the terminal loads, which are modelled as resistances. A single-phase to ground fault was simulated in phase A of line 2. The detailed parameters of the network and the fault conditions are shown in Appendix A with the results. The simulations were performed at a frequency of 100 kHz and the data were analysed after subsampling into 2.5 kHz.

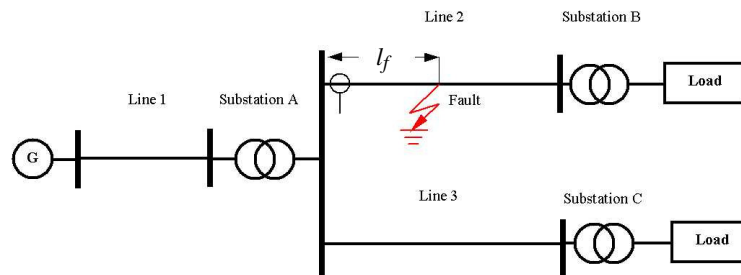


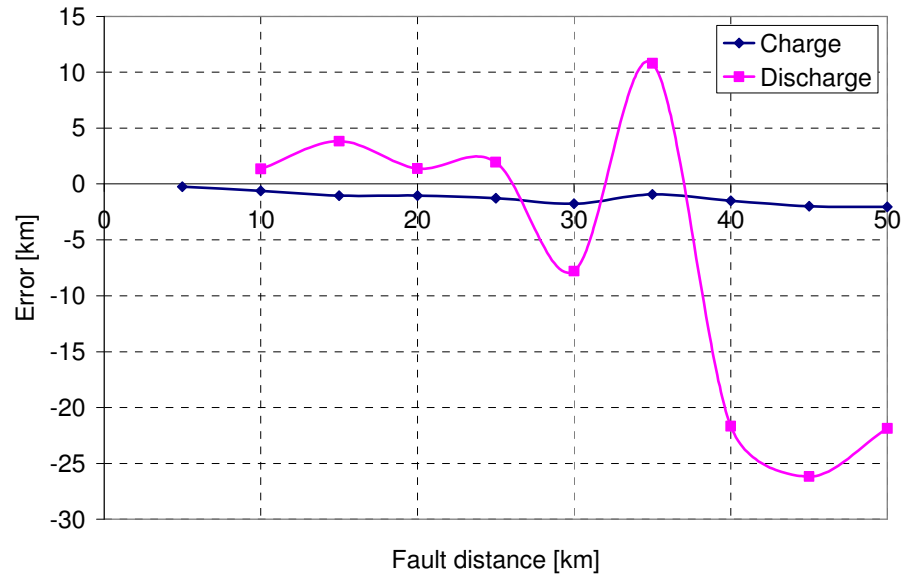
Fig. 33 Schematic diagram of the analysed network.

8.2 *Fault transients versus fault location*

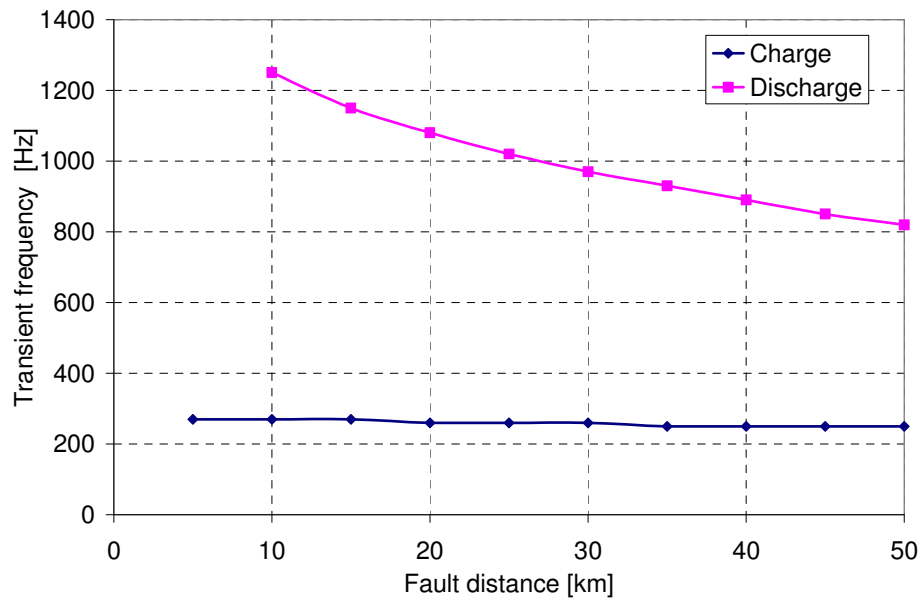
In this section, the fault location algorithm accuracy based on the charge and discharge transients is investigated when the fault distance is varied.

8. EMTP/ATP fault transient simulation

The results of the simulations of the single-phase to ground faults can be seen in Fig. 34. The same fault was simulated over the entire length of the line in steps of 5 km. The fault conditions were: fault resistance $R_f = 0 \Omega$, fault voltage inception angle $\varphi_f = 90^\circ$ and the fault occurred at time $t_f = 0 \text{ s}$. More detailed results are given in Tab. 10, Appendix A.



(a)



(b)

Fig. 34 Transient fault location using charge and discharge transients versus fault distance: (a) the error in the methods, (b) the frequency of the transients. For the studied case: $R_f = 0 \Omega$, $\varphi_f = 90^\circ$ and $t_f = 0 \text{ s}$.

8.2.1 Charge transient

The charge transient is very strong in amplitude (see Fig. 29), which makes it suitable for fault location. The average absolute value of the error in this test was 1.239 km, as can be seen in Fig. 34a. The frequency of the charge transient for a short distance fault (at the beginning of the line) was 270 Hz and for a long distance fault 250 Hz (at the end of the studied line), Fig. 34b. This small variation of frequency in the studied case was caused by the fact that the line inductance was small in comparison to the secondary transformer inductance. Therefore, the accuracy of fault location is mainly determined by the estimation accuracy of the amplitude of the fault transients. The sampling frequency of 2.5 kHz used in this test would be high enough for fault location using charge transients.

In Fig. 35, fault distance estimations are shown for two fault distances, 25 and 35 km.

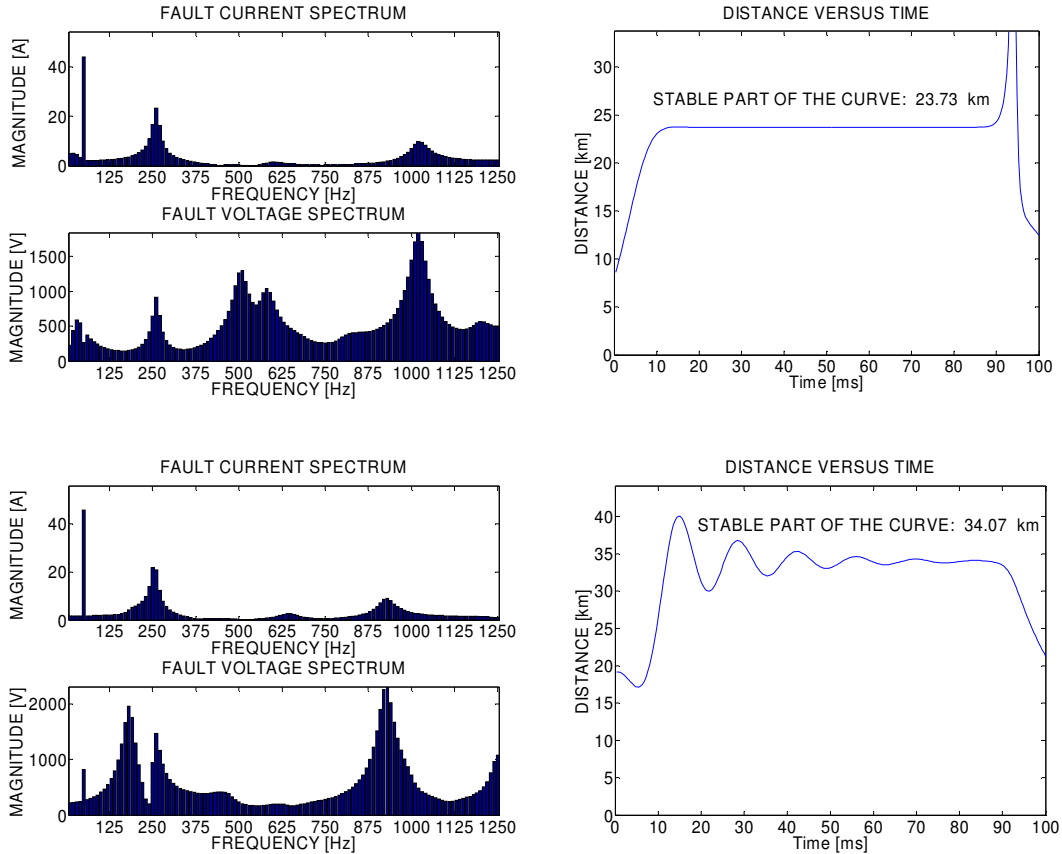


Fig. 35 Fault location sensitivity to the other frequency components. Fault distance estimation using the charge transient for $l_f = 25$ km (upper) and 35 km (lower) with their respective frequency spectrums. For the study case: $R_f = 0 \Omega$, $\varphi_f = 90^\circ$ and

$$t_f = 0 \text{ s}.$$

As can be seen in the figure above, it is sometimes hard to find a stable part of the distance curve for fault detection during the lifetime of the signal. Fortunately, in most of the studied cases such oscillations are near the actual fault distance value, therefore if the mean values are calculated in the intervals (discussed in Section 7.4) this problem is partially eliminated. In this case it is the phase voltage which is causing the oscillation in the fault distance curve; compare the spectrums in Fig. 35. However, this kind of oscillation can be eliminated by a narrower filter frequency band. Note that in this case a wavelet transform with a Morlet mother wavelet was used.

8.2.2 Discharge transients

The discharge transient is not very strong in amplitude and is of shorter duration, which can be seen in Fig. 29. Therefore, it is hardly detectable, but can still be tested for fault location. The simulation results are shown in Fig. 34.

Based on theory, the discharge transient frequency of a single line can be calculated using Eq. (20), which for a fault where $l_f = 25 \text{ km}$ and the speed of light $c = 3 \cdot 10^5 \text{ km/s}$ comes to approximately: $f_d = c/(4l_f) = 3 \cdot 10^5 / (4 \cdot 25 \text{ km}) = 3000 \text{ Hz}$. This is a relatively high value that would not be detected by the sampling frequency of 2.5 kHz used in this test. However, the case in question is rather complicated. One more outgoing line is connected to the same substation (Line 3), with length $l_{cl} = 55 \text{ km}$ as in Fig. 33. Therefore, this line is also discharging, and the dominant discharge frequency will be lower, as described in Section 5.2. For a fault where $l_f = 25 \text{ km}$, the network discharge frequency is approximately $f_d = c/(4(l_f + l_{cl})) = 3 \cdot 10^5 / (4 \cdot (55 + 25)) = 937 \text{ Hz}$.

The average absolute error in the fault estimation was 10.75431 km in this test. The frequency range of the discharge transient for different fault locations varied from 820 Hz for long distance faults (at the end of the line) to more than 1250 Hz for short distance faults (at the beginning of the line). This frequency range of more than 430 Hz is wider than for charge transients (only about 20 Hz), Fig. 34b. The discharging of the faulty line capacitance of the whole network takes place at the frequency given by Eqs. (20) or (21). Because of the low amplitude of the discharge transient the error is high. Note that because the frequency of the discharge transients varies a lot with fault distance, it might be possible to get an approximate value of the fault distance based only on the frequency of the transient, in accordance with Eq. (20) or (21).

In cases where the fault was close to the substation (measurement point), the discharge transients were higher than 1250 Hz, which is half the sampling frequency, and were therefore not detected. It is therefore possible that in some cases a sampling frequency of

2.5 kHz will not be high enough, for example, where the faults are very close to the substation, if the discharge transient is used for fault location.

An example of discharge transient based fault location was shown in Fig. 30. The compared fault distances were calculated using the charge or discharge transient for 25 km, Chapter 7. On the right side of this figure is the distance curve, calculated using the discharge transient. There was much more noise in this curve than occurred with the charge transient, possibly because of the low amplitude of the discharge transient and also because its frequency was close to half the sampling frequency. This noise can be eliminated by using an improved wavelet transform setting. Better results would be expected with a higher sampling frequency. In practice, the sampling frequency must be 4-8 times higher than the processed signal, which in this case would be about 5 kHz.

8.3 Fault transients versus fault conditions

Successful fault distance calculation depends very much on the amplitude of the transient generated during the ground-fault. There are two key factors, the fault resistance and the voltage inception angle of the faulted phase at the beginning of the fault, affecting the transient's amplitude and duration. Detailed data from the simulations are in Tab. 11 and Tab. 12 of Appendix A.

8.3.1 Fault resistance

The fault resistance was a key factor in the conventional fault location method based on the fundamental frequency presented in Chapter 4. In this method, the detection algorithm does not directly include the fault resistance, as can be seen from Eq.(2), but the influence of fault resistance has to be understood from a different point of view. It is important for transient generation. If a fault resistance exists, it attenuates the transient, which causes problems in the detection of the stable part of the inductance if the transient is too short in time and too small in amplitude. This effect can be seen in Fig. 36 where: fault distance $l_f = 25 \text{ km}$, fault voltage inception angle $\varphi_f = 90^\circ$ and the fault occurred at time $t_f = 0 \text{ s}$.

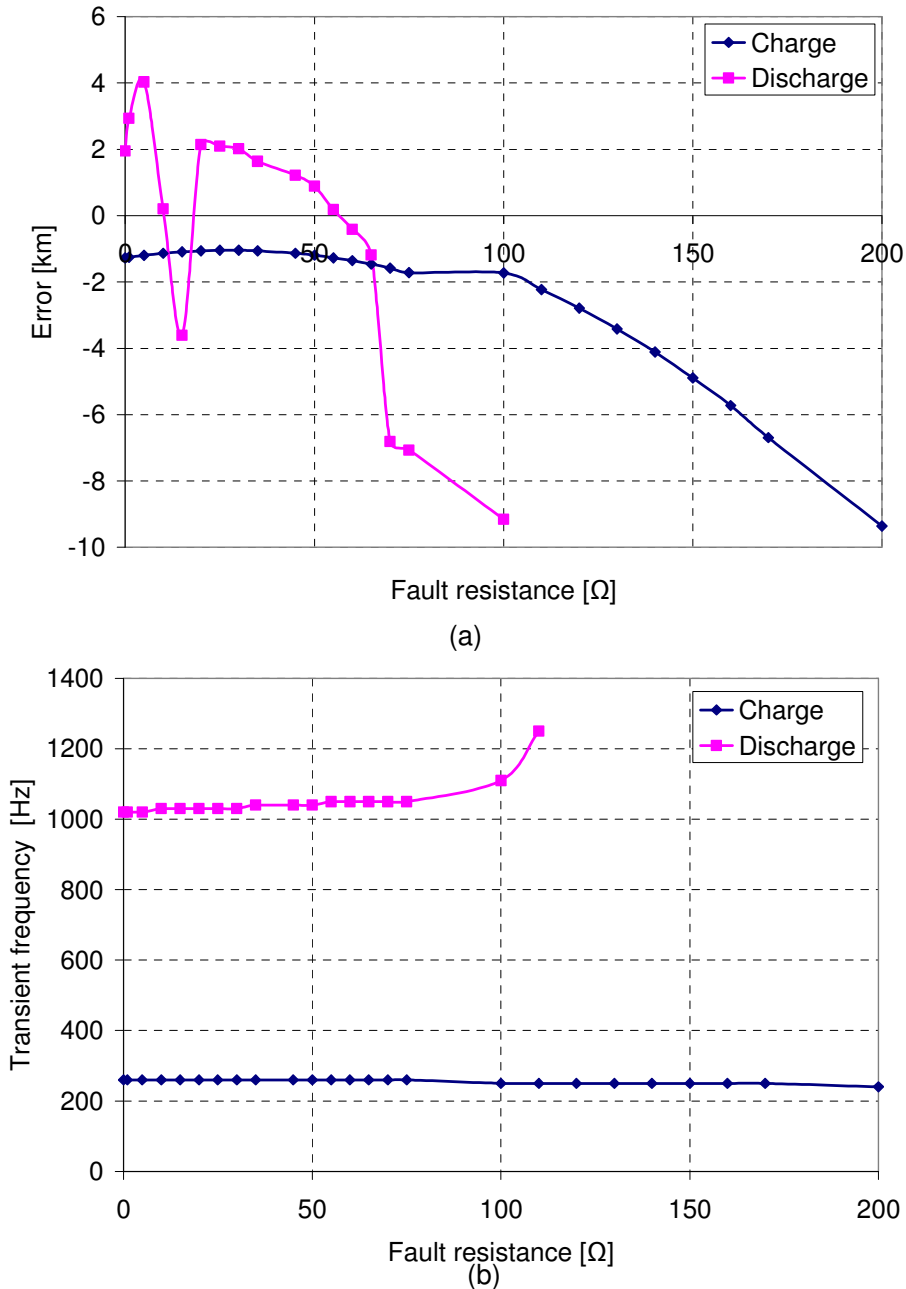


Fig. 36 Transient fault location using charge and discharge transients versus fault resistance: (a) error in the methods, (b) frequency of the transients. Study case:

$$l_f = 25 \text{ km}, \varphi_f = 90^\circ \text{ and } t_f = 0 \text{ s}.$$

Both the charge and discharge transient fault location methods are compared in the same picture. It is clearly seen that fault location using the charge transient has a lower error for a wider range of fault resistance. The fault resistance limit for reliable and accurate fault location is up to 100 Ω, but this also depends on the fault location. The fault resistance limit for correct charge transient detection was about 250 Ω in the studied case.

8. EMTP/ATP fault transient simulation

The damping of fault current transients can be seen when comparing the spectrum diagrams in Fig. 37 for different fault resistances, 0, 20, 50 and 200 Ω .

Fault location using the discharge transient works correctly up to 65 Ω , after which the error starts to increase. When the fault resistance is higher than 110 Ω , the discharge transient is damped so much that it is not detected at all.

Under the conditions for this study, the limit for the charge transient seems to be about 100 Ω . It must be pointed out that this conclusion is not final, and must be understood in the scope of this study. Theoretically, fault location should be possible if the charge transients are detected, in this case up to about 250 Ω . This would be possible with an increased sampling frequency (to keep the same number of samples describing the transient). However, in reality the installed recorders have a fixed sampling frequency, and so from this point of view this study is more realistic, even if the presented values might not be so representative for general use.

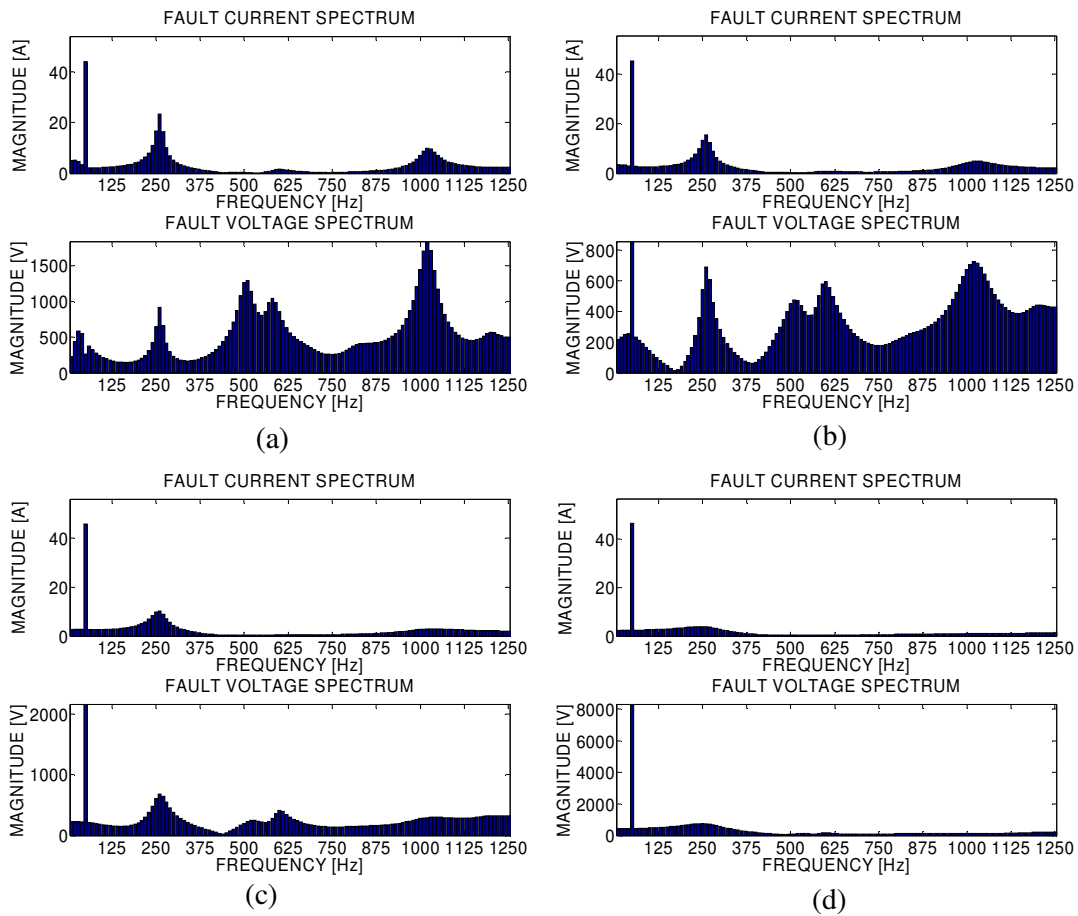


Fig. 37 Spectrum of the fault current and voltage for the study case: $l_f = 25$ km,

$\varphi_f = 90^\circ$ and $t_f = 0$ s for $R_f =$ a) 0 Ω , b) 20 Ω , c) 50 Ω and d) 200 Ω

8.3.2 Fault voltage inception angle

The amount of fault produced transients can also depend very much on the instantaneous value of the phase voltage at the fault initiation instant. This can be numerically estimated by the inception angle of the voltage in the faulted phase. The simulation results are presented in Fig. 38.

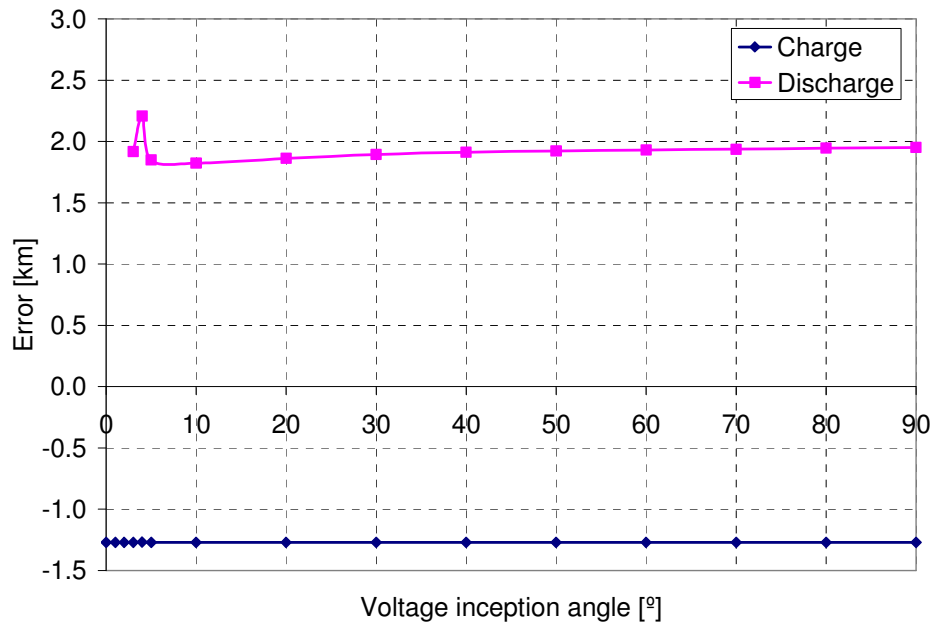


Fig. 38 Transient fault location using the charge and discharge transients versus voltage inception angle. For study case: $R_f = 0 \Omega$, $l_f = 25 \text{ km}$ and $t_f = 0 \text{ s}$.

Fault location depends only slightly on the instantaneous voltage level at the fault instant initiation, when the charge transient is used. This is because the charge transient is generated by the voltage rise in the sound phases. Using the discharge transients there are larger errors (due to the discharge transient not being detected) if the inception angle is lower than 3° . The simulation was performed for the studied case, with fault distance $l_f = 25 \text{ km}$, fault resistance $R_f = 0 \Omega$ and time of fault occurrence $t_f = 0 \text{ s}$. The simulation results are more fully presented in Tab. 12 in Appendix A.

8.4 Fault transients versus neutral grounding type

Fault transients and hence fault location can also be affected by the type of network neutral grounding used. It is wise to investigate how the generation of transients in the networks varies with different grounding. For subtransmission networks, isolated, compensation coil or low-reactance grounded neutral systems are usually employed. In this case the same network was tested, but with a changed grounding impedance. The studied case had the following parameters: $R_f = 0 \Omega$, $l_f = 25 \text{ km}$, $\varphi_f = 90^\circ$ and $t_f = 0 \text{ s}$. The results appear in the following figures.

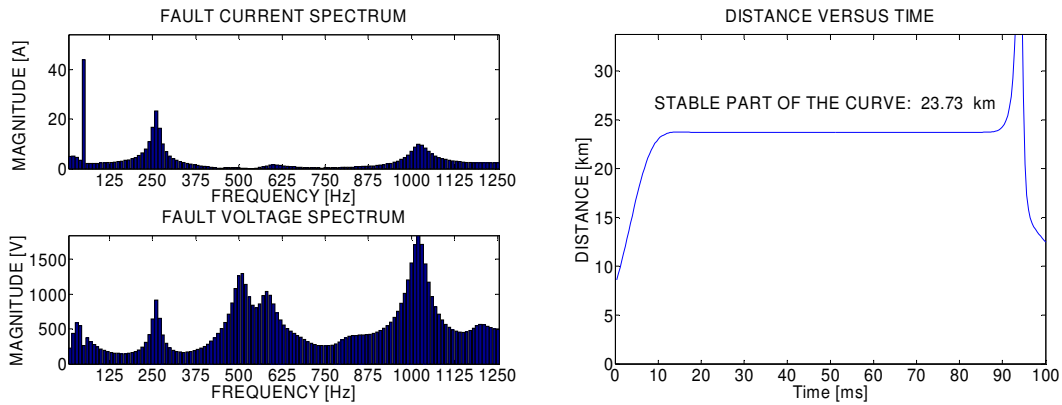


Fig. 39 The fault transient spectrums (left) and fault distance estimation using the charge transient (right) in an isolated neutral network. For the studied case: $R_f = 0 \Omega$,

$$l_f = 25 \text{ km}, \varphi_f = 90^\circ \text{ and } t_f = 0 \text{ s}.$$

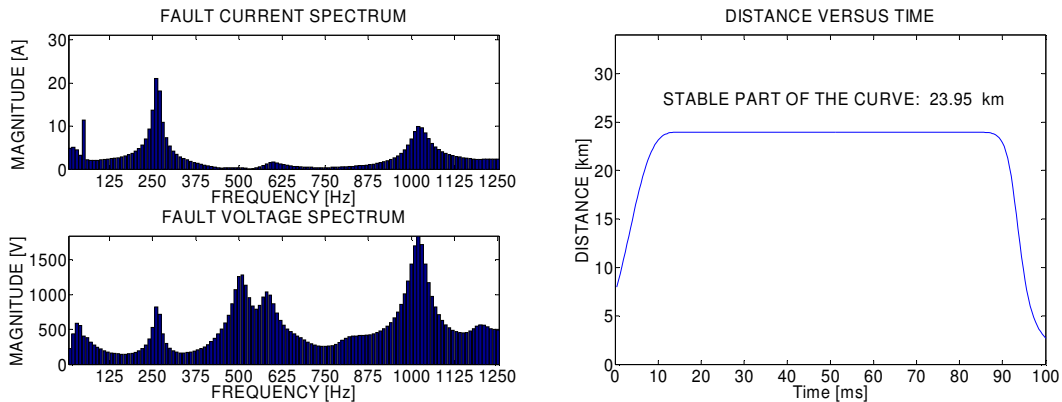


Fig. 40 The fault transient spectrums (left), and fault distance estimation using the charge transient (right) in a compensated network, where: $R_f = 0 \Omega$, $l_f = 25 \text{ km}$,

$$\varphi_f = 90^\circ \text{ and } t_f = 0 \text{ s}. \text{ Petersen coil inductance: } 5050 \text{ mH}.$$

8. EMTP/ATP fault transient simulation

As shown in Fig. 39 and Fig. 40, the fault transient shape does not depend too much on the impedance of the coils in the neutral grounding. The spectrum of the transients in a compensated neutral network is almost the same as in an isolated neutral network. The similarity of the part of the spectrum that contains the transients can be explained by the coil's higher impedance for transient frequencies. It was also found that there is no significant influence on the fault location itself.

The situation is different in a low-reactance grounded network, where the spectrum of the transients is slightly shifted. Nevertheless, this does not cause significant problems in fault location, as can be clearly seen in Fig. 41. Similar results can be achieved in solidly grounded networks.

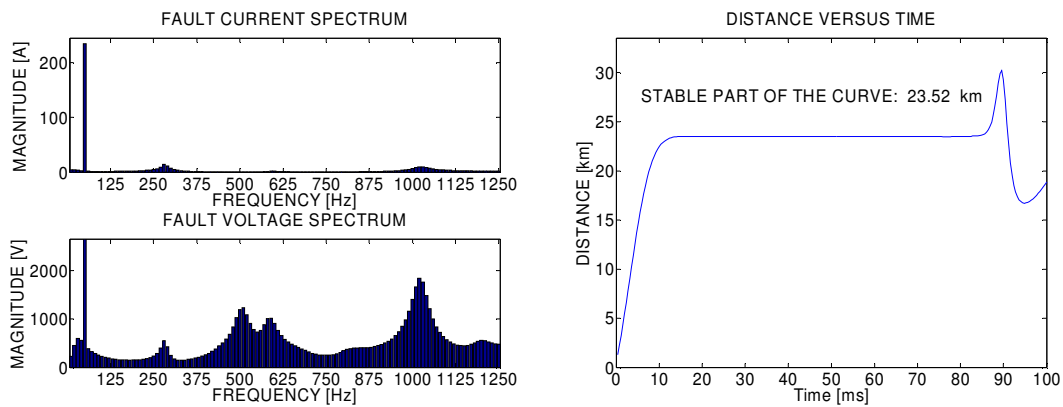


Fig. 41 The fault transient spectrums (left), and fault distance estimation using the charge transient (right) in a low-reactance network, where: $R_f = 0 \Omega$, $l_f = 25 \text{ km}$, $\varphi_f = 90^\circ$ and $t_f = 0 \text{ s}$. Low-reactance coil inductance: 600 mH .

Considering all the studied grounding methods, it can be concluded that there is no significant difference in fault transient generation and hence fault location caused by the grounding impedance.

8.5 Double-ended method

A simple double-ended method has been tested. A network 100 km long with an isolated neutral was tested in EMTP/ATP. This method requires measurement from both ends of the line but synchronisation is not required. The method is, in fact, based on two single-ended methods. The fault distance was measured from each end and the average of these two, referred to one line end, was calculated.

This method proved to be relatively accurate, Fig. 42. The problematic areas were the ends of the line. However, in the middle the accuracy was good. The inaccurate regions increase with the fault resistance, as shown in Fig. 42. For very high fault impedances the accurate region was confined to just the middle of the line, rendering the algorithm useless for such faults. However, the simplicity of the algorithm is an advantage.

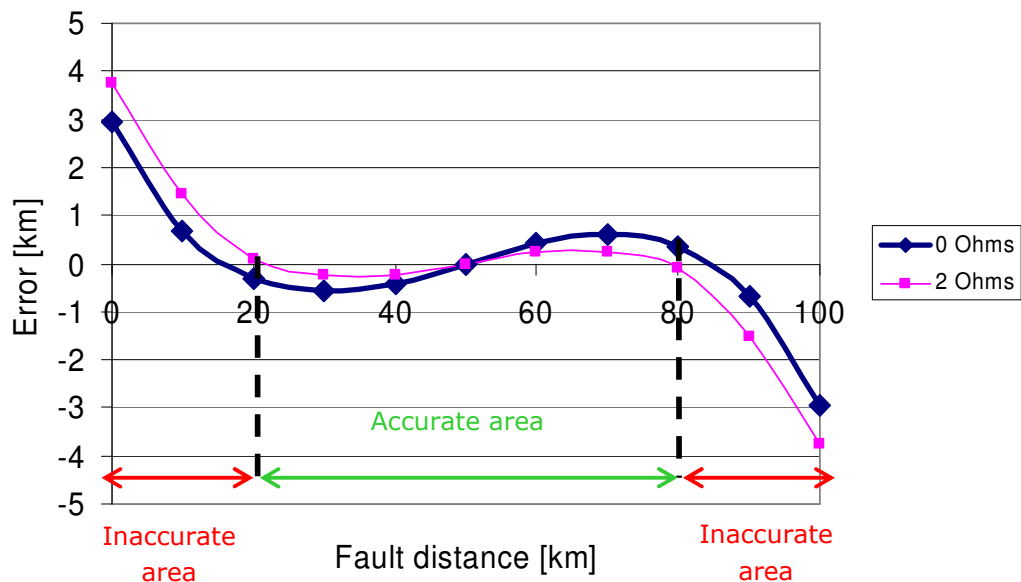


Fig. 42 The double ended method. The fault resistance was 0 or 2 Ohms.

The inaccurate area covered the beginning and end of the line, where the fault location error was higher than in the middle of the line. However, the relative error per km was acceptable along the line for low fault resistances.

8.6 Discussion

Charge transient versus discharge transient

In principle it is possible to use both transients, the charge and discharge transients, for fault location. However, the charge transient is more suitable, mainly because of its higher amplitude and lower frequency compared to the discharge transient.

Connected line influence

First, the connected lines make the necessary return path for the fault transient current in the case of the studied network, which has an isolated neutral. This issue will be studied more fully in Chapter 11. Then Eq. (1) for the first order line model is valid. Secondly, both charge and discharge transient frequencies are greatly affected by the existence of connected lines. The connected lines lower both of the frequencies that would occur in a single line, Chapter 5.

Fault conditions

Finally, there seems to be a problem with fault location when the fault resistance exceeds a few hundred ohms. The exact limit for general use would be difficult to estimate from any study. However, the results in this chapter indicate that the method can be used for faults with higher impedance than the conventional methods, Chapter 4. Under the studied conditions, the limit when using the charge transient seems to be about 110 Ω . However, the accurate area can be increased, mainly by a higher sampling rate, but only up to the limit where the transient is totally damped. This value in our study then becomes about 250 Ω for the charge transient. For a realistic estimation, real fault cases must be processed.

The inception angle of the voltage does not significantly affect the generation of the charge transient, because it is generated by the voltage rise of the healthy phases.

Fault transients versus neutral grounding type

Although the transients may only be slightly affected by the impedance of the neutral grounding, as seen in the simulated cases, the fault location will only be accurate where we have a low impedance return path for the zero-sequence current; for example, a line connected to the same substation (the studied case). The situation would be very different in the case of a single line (no other lines connected to the same busbar). Then the impedance of the neutral grounding will play a key role in fault location accuracy (the lower the better), because it is the only way for the zero-sequence current to close via the measurement point in the substation. These issues will be explored further in Chapter 11.

Sampling frequency

The entire study in this chapter was performed with a 2.5 kHz sampling frequency, mainly to enable practical application of the results in the real Finnish subtransmission system. The study showed that this value would be high enough for fault location purposes. Increasing the sampling frequency would primarily enable an increase in the allowable fault resistance to the possible maximum. However, because in reality the transients do not always last as long as those generated in the simulations, it would also be wise to utilise a higher sampling frequency. Further, as there are other error sources affecting the method accuracy that cannot be reduced, it would be prudent to reduce the influence of the sampling frequency to the minimum. A sampling rate of 10 kHz would be relatively safe for this kind of fault location application.

9 Modelling of the 110 kV instrument transformers for transients

Instrument transformers have a guaranteed ratio at 50 Hz, but it is necessary to investigate how they transmit signals at transient frequencies and in transient situations for the purpose of fault location. This can be performed by measurement of the transformer ratio. The modelling is important for the fault simulations and for the analysis of real fault signals as well. When developing a fault locator using a simulation program, it is wise to pass the fault signal through the instrument transformer model in order to include the error of the measurement. The output is then more realistic, and can be used for fault distance computation with the measurement error included. In real cases, when we process real fault signals, it is then possible to make corrections based on the model frequency (transient) response.

In general, the modelling of a voltage transformer for transients is more complicated than the modelling of a current transformer. The voltage transformer may have a resonance point in the frequency range of the low frequency transients, which can cause inaccurate measurement at these frequencies. Current transformers on the other hand do not usually have any non-linearities in transmission in the transient frequency range. In the context of this study, i.e. in this chapter, the term low frequency transients means the frequency range of ground fault signals, where the maximum is limited to 5 kHz.

There are many modelling methods used for instrument transformers. Basically, they can be divided into lumped and distributed parameter models. Some approaches are based on a mathematical analysis of the measurements performed on the transformer or on the physical construction of the transformer as well. It is difficult to make a model that is valid over the entire frequency spectrum, especially with low degrees of freedom in the model. Only the most complicated models, based on distributed parameters, which also take into account the geometry of the transformer, can fully satisfy this requirement. In any case, the construction details of the transformer are not always available to the end user. It is also much easier to build a model for the specific frequency range we are interested in. In this case very good results can be achieved with lumped models. There are many methods for constructing such models, but the most common method is based on the classical model calculated from open and short circuit measurements at 50 Hz (to estimate the lumped resistances and inductances). Capacitances are usually added to these standard models in order to generate the resonance points and

there are various methods covering how to estimate them, [1], [6], [7]. In this thesis a new approach is developed, also published in [32]. All the model element parameters are calculated from measurements performed on real instrument transformers. Simulations of this model were performed in EMTP/ATP and the necessary signal processing was conducted in Matlab.

9.1 Voltage transformer

In this section a lumped model of a voltage transformer is constructed. There were three voltage transformers measured (with internal names PT1, PT2 and PT3), the basic parameters of which are given in Appendix B. The transformers behaved similarly in the range of low frequency transients, and therefore only one of them, PT1, was modelled. The model accuracy was tested in EMTP/ATP and then compared with the real transformer.

9.1.1 The model's backbone

For the modelling of instrument transformers up to 10 kHz it is clear that we can use a lumped model. PT1 consists of two secondary windings. The simplest lumped parameter model of a voltage transformer with two secondary windings is shown in Fig. 43. For this model we need the results from open and short circuit measurements on a real voltage transformer. The parameters of this model were calculated from measurements provided by Fortum (an energy company in the Nordic countries) with a network analyser.

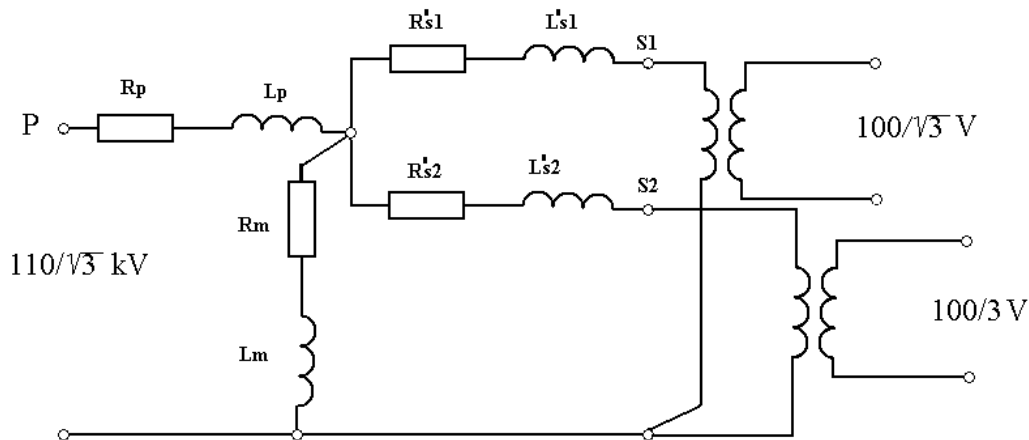


Fig. 43 The linear 50 Hz model of a 110 kV voltage transformer.

9. Modelling of the 110 kV instrument transformers for transients

Recalculated data from the network analyzer (at 50 Hz) are shown in Tab. 2. It can be seen that there was no big difference between the short circuit and open circuit measurement performed from the primary side of the investigated voltage transformer (PT1).

Tab. 2 Short and open circuit impedances of the voltage transformer (PT1), calculated from Fortum's measurements.

Measurement	f [Hz]	Impedance	Values	Unit
Short circuit, P-S1	50	Z_{ps1}	$1.9259 + 0.98281j$	$k\Omega$
Open circuit, P	50	Z_p	$30.950 + 25.167j$	$k\Omega$

The ratio between the absolute values of the impedances shown in Tab. 2 is only about 18, which means that the primary windings of the transformer form the dominant part of the short circuit impedance. The model response is similar to the real transformer when the short circuit impedance is divided between the primary and secondary with a ratio of 90 % on the primary to 10 % on secondary side, as shown in Tab. 3.

Tab. 3 Division of the short-circuit impedance of PT1 to the model's primary and secondary.

From Tab. 2	Ratio	Primary	Secondary S1
$L_{ps1} = 3.13$ H	90% to 10%	$L_p = 2.8170$ H	$L_{s1}' = 0.313$ H
$R_{ps1} = 1.9259$ $k\Omega$		$R_p = 1.7333$ $k\Omega$	$R_{s1}' = 192.59$ Ω
for $\omega_f = 314$ rad / s			

The transformer model's vertical branch can be easily calculated from the open circuit impedance, as shown in Tab. 4.

Tab. 4 The open circuit recalculation for PT1.

Measured values	From Tab. 2	Calculated
Imag. part	25.167j $k\Omega$	$L_m = 80.1497$ H
Real part	30.950 $k\Omega$	$R_m = 30.950$ $k\Omega$
for $\omega_f = 314$ rad / s		

The second secondary winding S2 has similar parameters to the winding S1. Because of the symmetry of the transformer model, the coil S2 can be assumed to have the same parameters as S1.

9.1.2 Calculation of the equivalent model capacitances

The capacitances of the voltage transformer windings are of course distributed, but for the low frequency analysis we are interested in, they can be taken as lumped. Six significant capacitances can be identified for a voltage transformer with two secondary windings, as PT1 is. The six capacitances in the transformer consist of the capacitance between each winding and the body of the transformer and the capacitances between the windings themselves. These lumped capacitances inside the voltage transformer are shown in Fig. 44. The model with implemented capacitances is shown in Fig. 45. The capacitances needed for the modelling of the transformer cannot be measured directly, because they are inside the transformer and cannot be disconnected during testing. Thus, each measurement does not directly measure the required capacitance in isolation, but the overall capacitance between the connection points. A more detailed analysis shows that these capacitances appear to be connected in the real transformer in a 4-corner symmetrical network (polygon), especially at high frequencies, as shown in Fig. 46 (the impedance of the virtual transformer capacitors will be so low at higher frequencies, that the transformer really becomes a capacitance polygon). To estimate the value of each capacitance a total of six measurements are needed.

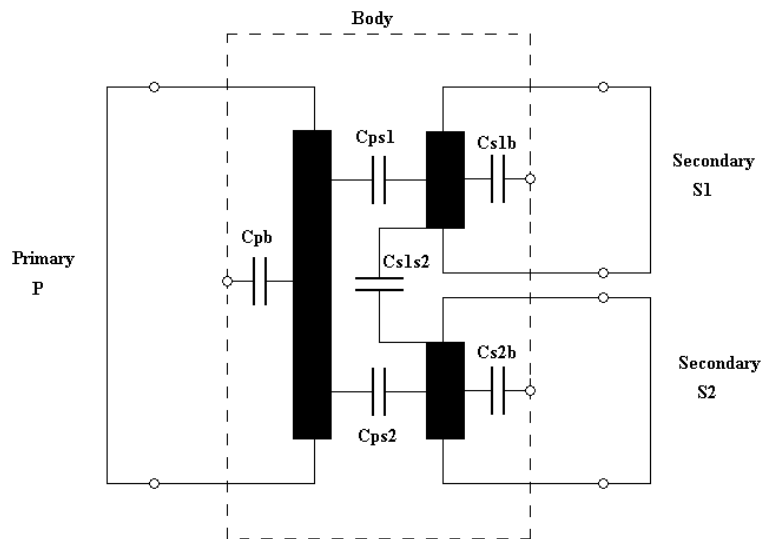


Fig. 44 Assumed lumped capacitances in a voltage transformer.

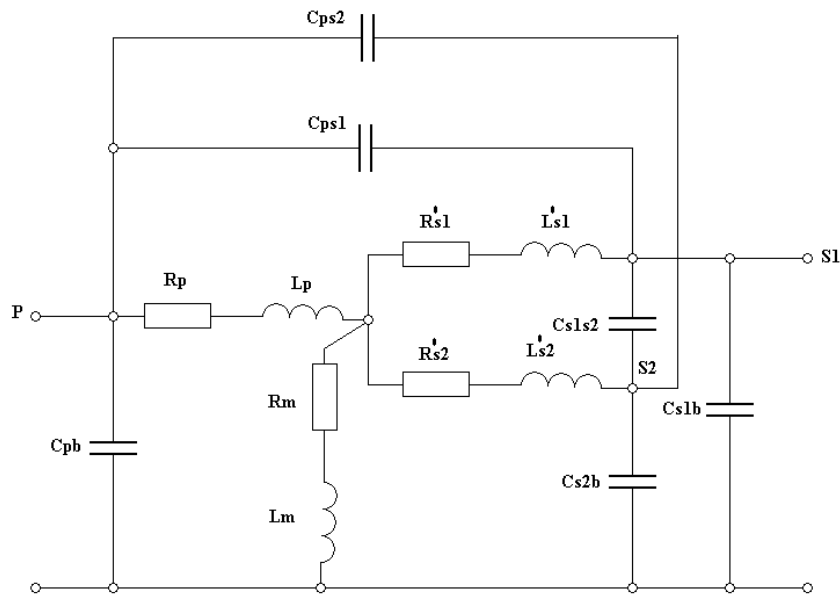


Fig. 45 Capacitances in the model.

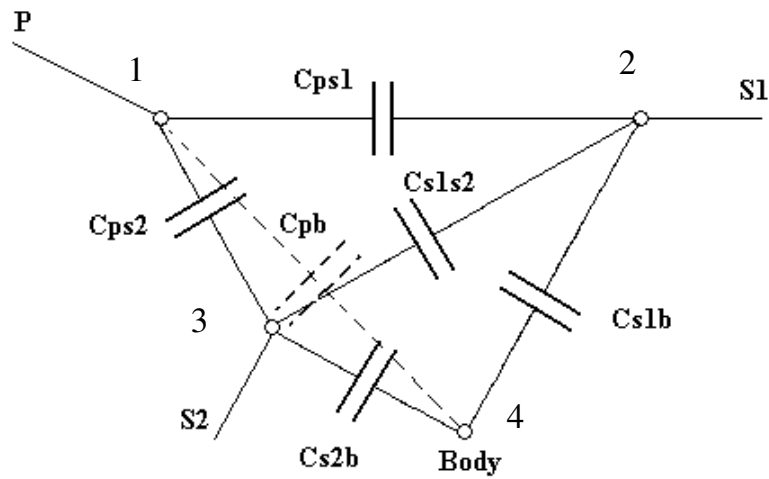


Fig. 46 Connections of the capacitances in the transformer at higher frequencies.

9.1.2.1 Capacitance measurement description

During the six required capacitance measurements, all windings of the transformer were short-circuited as shown in Fig. 44. An impulse of shape 1,2/50 μs and a voltage level of a few hundreds volts were applied to the transformer. During the tests the impedance (or voltage and current) was measured. The connections were between the windings and between each winding and the body of the transformer (note: in these measurements the primary was disconnected from the body). The measurement circuits and results are shown in Appendix B.

When analysing the measurements, the spectrum of the measured voltage and current was first calculated, using Eq. (28). The frequency dependent capacitance was then calculated from the measured voltage and current spectrum as follows:

$$C(\omega) = \frac{1}{\omega} \text{imag}\left(\frac{\text{DFT}(i)}{\text{DFT}(v)}\right) \quad (37)$$

where ω is the angular frequency, $\text{DFT}(v)$ is the spectrum of the voltage and $\text{DFT}(i)$ is the spectrum of the current.

9.1.2.2 Recalculation of the capacitance network

The basic idea behind the calculation of all six capacitances inside the capacitance network shown in Fig. 46 was to use all possible combinations of measurements (6) between the corners of the polygon (1, 2, 3, 4) or, in practice, between the windings of the transformer, primary (P), secondary (S1), secondary (S2) and the body of the transformer, as shown in Fig. 44.

For example, the capacitance C_{ps1} between the primary and secondary can be calculated using the measured capacitance between points 1-2 in Fig. 46 and all known capacitances from inside the capacitance network, as presented in Eq. (38). The detailed development of this equation can be found in Appendix B.

$$C_{ps1} = C_{12} - \frac{C_{pb}C_{s1b}}{C_{pb} + C_{s1b} + C_{s2b}} - \frac{(C_{ps2} + \frac{C_{pb}C_{s2b}}{C_{pb} + C_{s1b} + C_{s2b}})(C_{s1s2} + \frac{C_{s2b}C_{s1b}}{C_{pb} + C_{s1b} + C_{s2b}})}{(C_{ps2} + C_{s1s2} + \frac{C_{s2b}C_{s1b} + C_{pb}C_{s2b}}{C_{pb} + C_{s1b} + C_{s2b}})} \quad (38)$$

9. Modelling of the 110 kV instrument transformers for transients

where:

C_{pb} is the capacitance between primary winding (P) and body (b) of transformer

C_{s1b} is the capacitance between secondary (S1) and body (b) of transformer

C_{s2b} is the capacitance between secondary (S2) and body (b) of transformer

C_{s1s2} is the capacitance between secondary (S1) and secondary (S2) of transformer

C_{ps1} is the capacitance between primary winding (P) and secondary (S1) of transformer

C_{ps2} is the capacitance between primary winding (P) and secondary (S2) of transformer

C_{12} is the measured capacitance between primary (P) and secondary (S1) of transformer and other measured capacitances

C_{13} is the measured capacitance between primary (P) and secondary (S2) of transformer

C_{14} is the measured capacitance between primary (P) and body (b) of transformer

C_{24} is the measured capacitance between secondary (S1) and body (b) of transformer

C_{34} is the measured capacitance between secondary (S2) and body (b) of transformer

C_{23} is the measured capacitance between secondary (S1) and secondary (S2) of transformer

The capacitances inside the polygon are unknown (only the measured capacitances, C_{12} , C_{13} , C_{14} , C_{24} , C_{34} , and C_{23} , are known). Nevertheless, a solution similar to Eq. (38) can be written for each internal capacitance shown in Fig. 46. Hence the systems of six equations can be solved using a suitable numerical method (in this case the ‘‘Gauss-Seidel iteration method’’ was used, [8]). The solution of this system of equations with measured capacitances for the measured voltage transformer (PT1) can be seen in Tab. 5.

Tab. 5 Measured and calculated values of the capacitances in the voltage transformer (PT1).

Measured capacitances of voltage transformer PT1			Calculated capacitances with Gauss-Seidel iteration method		
Name	Value	Unit	Name	Value	Unit
C_{12}	1.1	nF	C_{ps1}	0.5371	nF
C_{13}	1.1	nF	C_{ps2}	0.5371	nF
C_{23}	2.8	nF	C_{s1s2}	2.4754	nF
C_{14}	0.6	nF	C_{pb}	0.4144	nF
C_{24}	0.5	nF	C_{s1b}	0.1121	nF
C_{34}	0.5	nF	C_{s2b}	0.1121	nF

9.1.3 Model analysis with EMTP/ATP

The model of the voltage transformer shown in Fig. 45, with the parameters calculated for PT1 as shown in the previous sections, was simulated in EMTP/ATP. The simulated model diagram can be seen in Fig. 47.

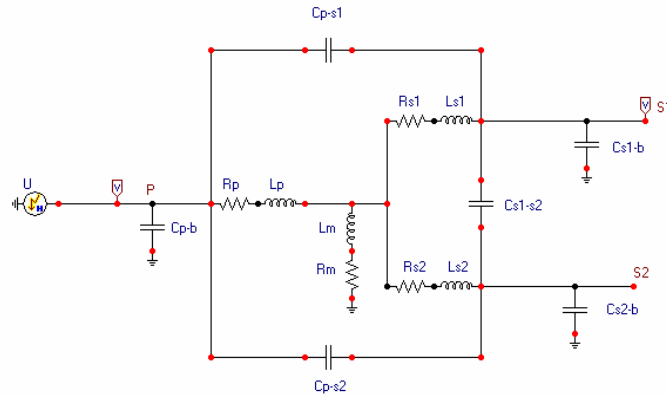


Fig. 47 The EMTP/ATP model of the voltage transformer with impulse generator and measurement voltage probes on the primary (P) and secondary (S1).

The frequency response of transformer PT1 was first measured. The transfer function of the primary (P) to secondary (S1) of the real transformer (PT1) is shown in Fig. 48. It is, in fact, the response of the transformer to an impulse of a few hundreds volts with shape 1,2/50 μ s. The results are shown in the four curves in Fig. 48. Starting from the top, there is an applied impulse to the primary winding (P) with the response measured on the secondary (S1) after multiplying by 1000 (so that both impulse and response can be seen in one picture). Below, the spectrum of both the impulse and the response is shown. Finally, the last two curves are the rated ratio of the transformer with the phase angle of the transformer as a function of frequency. The first resonance point of the transformer was detected at 2600 Hz.

The model of Fig. 47 was actually tested in the same way as the real transformer (using the connection indicated in Fig. 47, with the same impulse shape 1,2/50 μ s and amplitude that were applied to the real transformer). By applying the same measurement to the model, we obtained the results shown in Fig. 49. The figure consists of the same set of curves as Fig. 48. The main resonance frequency of the model was 2600 Hz.

In Fig. 50, the measured transfer function of PT1 is compared with its model. The figure structure is slightly different. In every curve the simulated and measured transformers are compared; starting from the top: applied impulses, responses, ratios, and phase angles. As is clearly seen, the responses of the model and the transformer are quite similar

9. Modelling of the 110 kV instrument transformers for transients

and oscillate at the same main frequency of 2600 Hz with the same attenuation (they cover each other). The model fits with the real transformer quite well up to 5 kHz. However, the error in the model was a little higher around the nonlinear point at 2600 Hz.

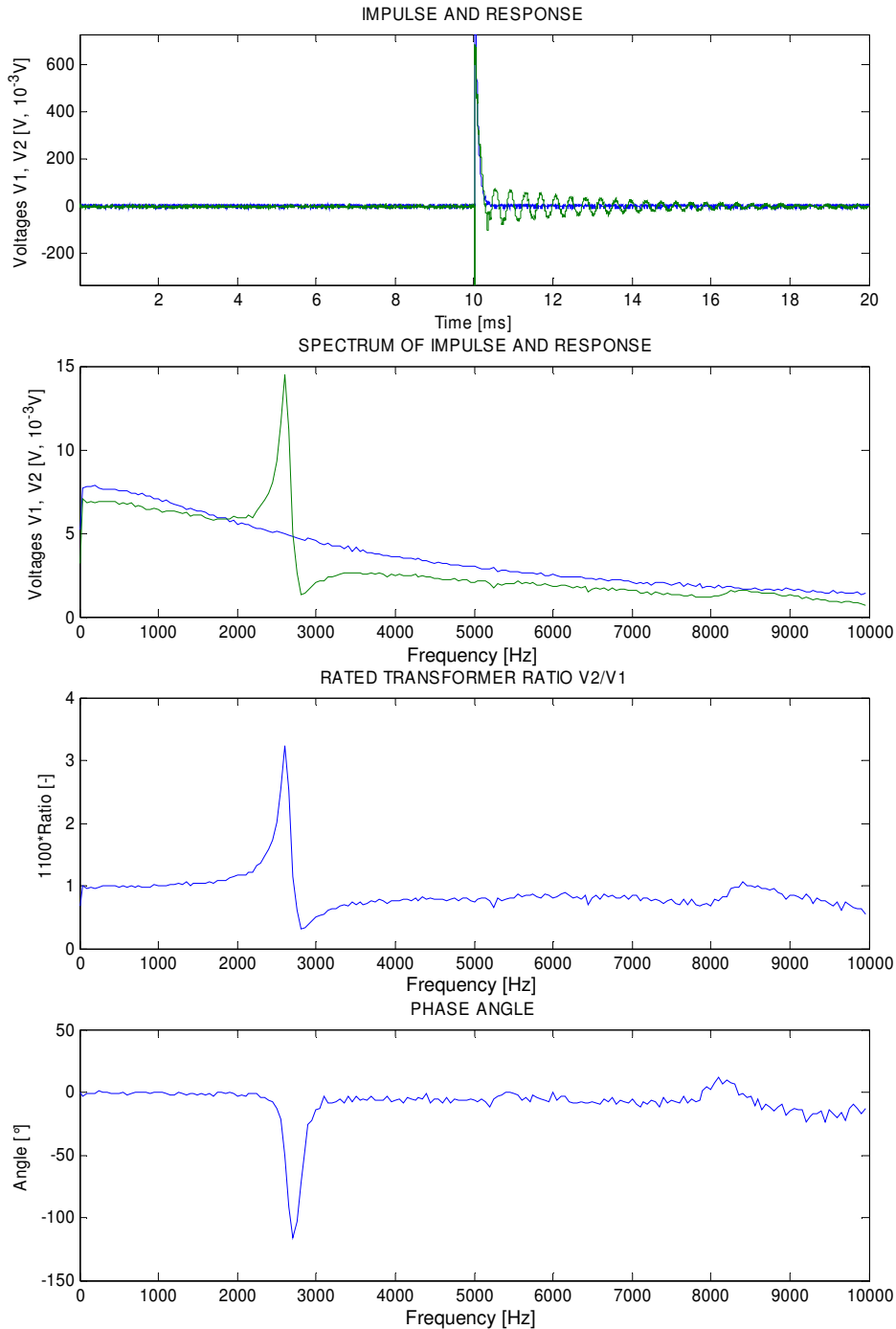


Fig. 48 The measured ratio of the voltage transformer, (PT1). Measured connection: primary (P) to secondary (S1). Applied impulse 1,2/50 μ s. (V2 – green color)

9. Modelling of the 110 kV instrument transformers for transients

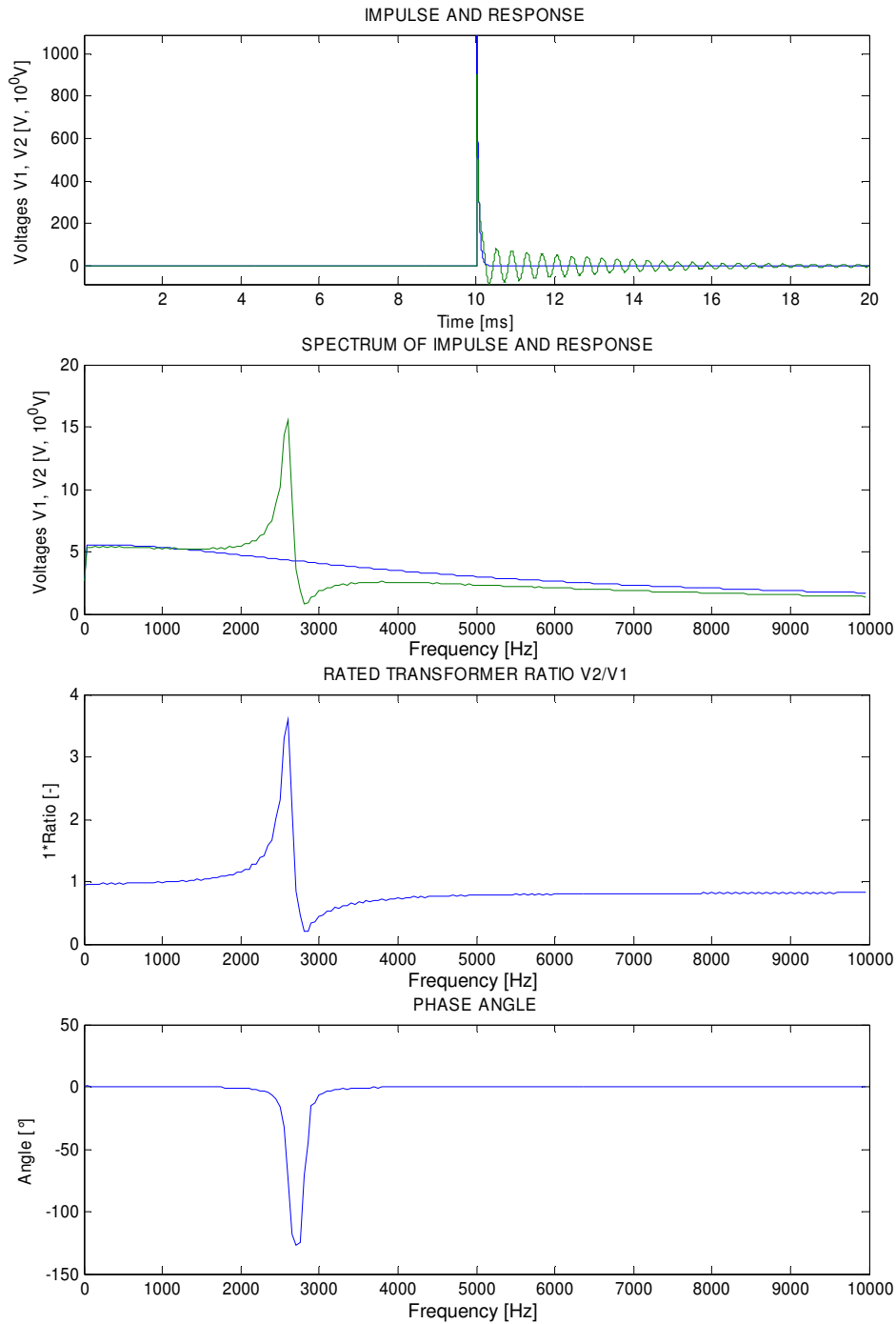


Fig. 49 The simulated ratio of the PT1 voltage transformer model. Measured connection: primary (P) to secondary (S1). Applied impulse 1,2/50 μ s. (V2 – green color)

9. Modelling of the 110 kV instrument transformers for transients

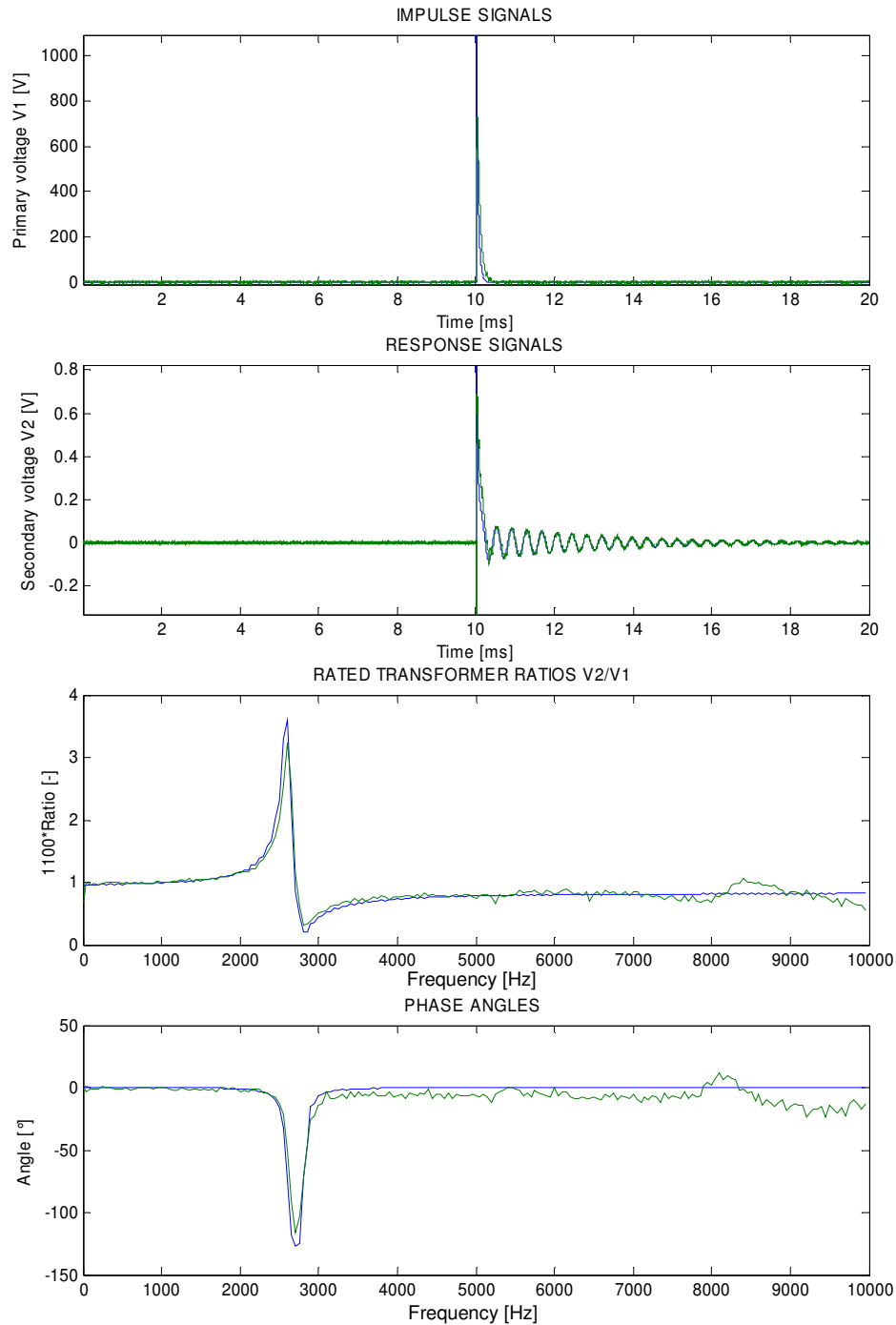


Fig. 50 Comparison of the measured ratio of the voltage transformer (PT1) and its model. Measured connection: primary (P) to secondary (S1). Applied impulse 1,2/50 μ s. (Measured signals – green color, simulated signals – blue color)

9.1.4 Analysis of the impact of the model components on the frequency response

Each element of the model has an impact on its final frequency response and so it is very important to study the properties of the model. The “back-bone” of the model was built according to the classical lumped model for 50 Hz. The non-linearity of the core was not considered in the model. To get the frequency response of the model similar to the original response of the transformer, the capacitances were added. Therefore, their impact on the model frequency response is investigated. It is important to know the connection between each capacitance and resonance or shape change in the model, i.e. which capacitance causes which resonance or shape change in the model.

The model without the capacitances gave the correct ratio at 50 Hz, as expected. The capacitances added between the windings themselves, and between the windings and the ground (which are of “nF” size) are of a high impedance at 50 Hz, as an approximate calculation shows:

$Z = 1/\omega_f C = 1/(314 \cdot 10^{-9}) = 3.1847 \text{ M}\Omega$. Thus, these capacitances do not influence the model at 50 Hz, which should be the case. This was proved by the EMTP/ATP simulations, as well.

The capacitance on the primary side, $C_{pb} = 0.4144 \text{ nF}$, does not have any impact on the model frequency response. When varying this capacitance, or even if we do not include this capacitance at all, the model responses will not be changed.

The capacitance between the primary and the secondary, for example, $C_{ps1} = 0.5371 \text{ nF}$, is connected directly across the whole short circuit impedance. This capacitance together with the short circuit impedance generates the frequency response:

$f = 1/(2\pi\sqrt{L_{ps1}C_{ps1}} = 1/(2\pi\sqrt{3.13 \cdot 0.5371 \cdot 10^{-9}}) = 3.8817 \text{ kHz}$. When adding the capacitance of the secondary to ground, $C_{sb} = 0.1121 \text{ nF}$, this resonance point will change to $f = 3,55 \text{ kHz}$. When the model is completed with the capacitances of the second secondary winding C_{ps2} and C_{s2b} , the system will have a resonance frequency at 2600 Hz.

The value of the capacitance, $C_{s1s2} = 2.4754 \text{ nF}$, did not make any difference to the frequency response. Only extremely high capacitance values ($> 0.1 \text{ F}$, which is not realistic) can change the transformer model response.

9. Modelling of the 110 kV instrument transformers for transients

In conclusion, the main impact on the final response is given by the capacitances between the primary and secondary windings, and between the secondary windings and the ground.

9.2 Burden of the voltage transformer

The frequency response of the voltage transformer shows that a PT is suitable for the transmission of fault signals without any significant influence. This is only true, however, when the transformer, or the transformer model presented in Section 9.1, is not loaded. Therefore, to investigate the effect of loading on the transformer, a burden representing the cable connection between the secondary of the PT and the substation building was connected to the model. The typical capacitance of a secondary cable is 20 nF. This capacitance value was obtained from a measurement in a real substation, where cables for measurement and protection, 75 m long, are connected to the PT secondary; the relevant data are presented in Appendix B. To be used in the model, the capacitance must be referred to the primary side of the transformer. The influence on the frequency response of the PT1 model can be seen in Fig. 51.

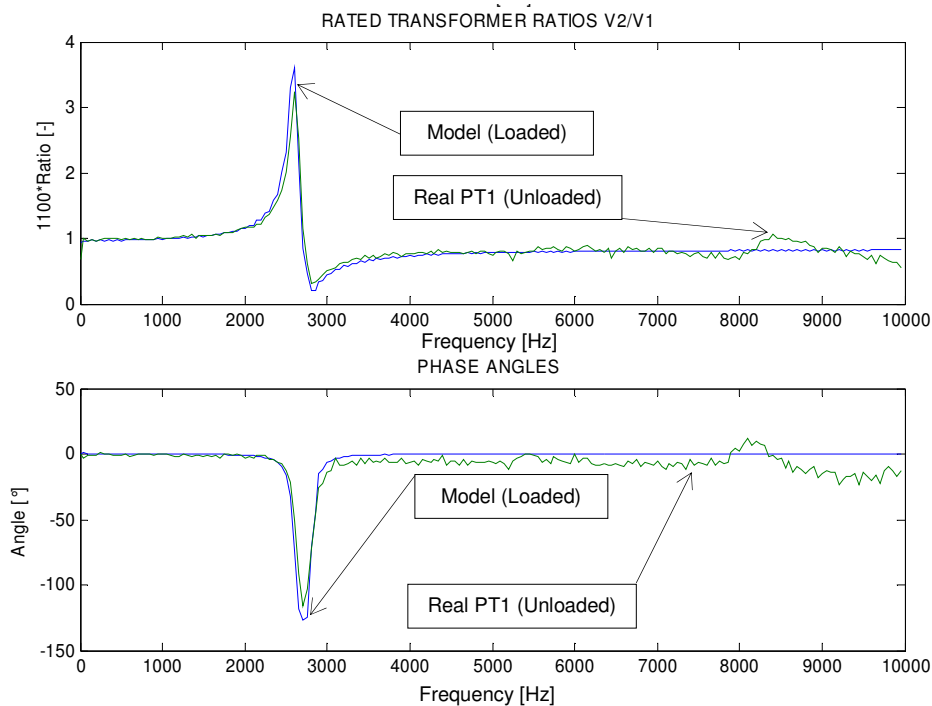


Fig. 51 The simulated and measured frequency response of PT1. The secondary of the model was loaded with a cable of capacitance 20 nF. The real PT1 was unloaded. Measured connection: primary (P) to secondary (S1). Applied impulse: 1,2/50 μ s.

As can be seen, the loaded model of the voltage transformer with the secondary cable connected has almost the same frequency response as the unloaded real voltage transformer PT1. Therefore, it can be concluded that the secondary burden of the transformer (mainly the capacitance of the cable) does not significantly influence the frequency re-

sponse of the voltage transformer model. Hence, it can be assumed that a real transformer will behave similarly, and so no correction is needed for fault transients.

9.3 Current transformer

A current transformer's transfer function was measured. The measured transformer is CT4 (ratio $80/2=40$, 0.5%, 60VA, 5A; the detailed parameters are in appendix B). The measurement comprised two different approaches, an impulse test and an AC measurement. The impulse test was used to measure the resonance of the transformer, Fig. 52, and the AC measurement was used to precisely measure the frequency range of interest. The results are shown in Fig. 53 and Fig. 54. It is clear that the transformer ratio error is less than about 3.5% up to 1 kHz. The main resonance point of CT4 was at 320 kHz.



Fig. 52 Impulse measurement of CT4 in the HV laboratory, HUT, Finland.

9. Modelling of the 110 kV instrument transformers for transients

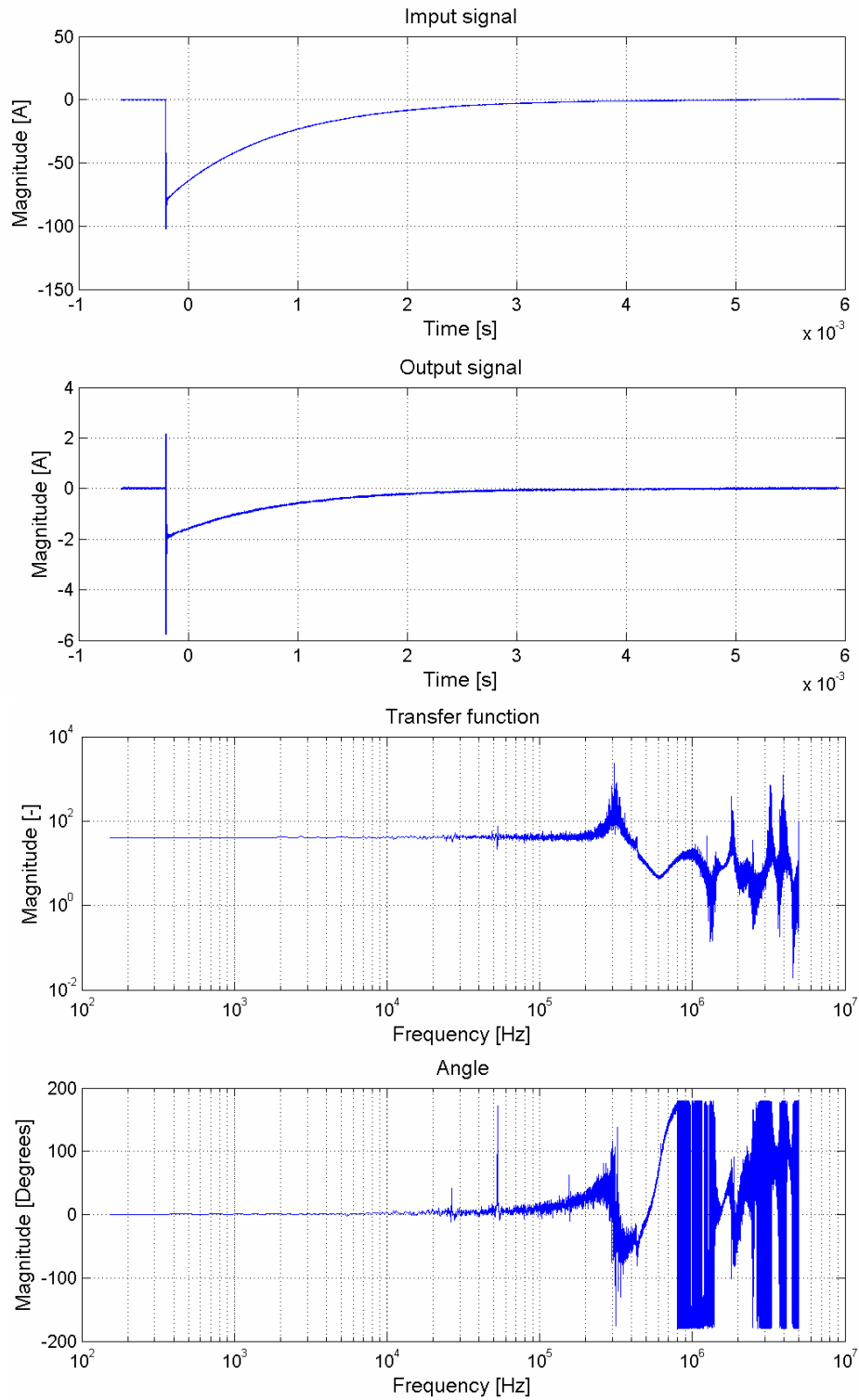


Fig. 53 The transfer function of CT4 measured with an impulse generator.
Measured connection: primary (P) to secondary (S1).

9. Modelling of the 110 kV instrument transformers for transients

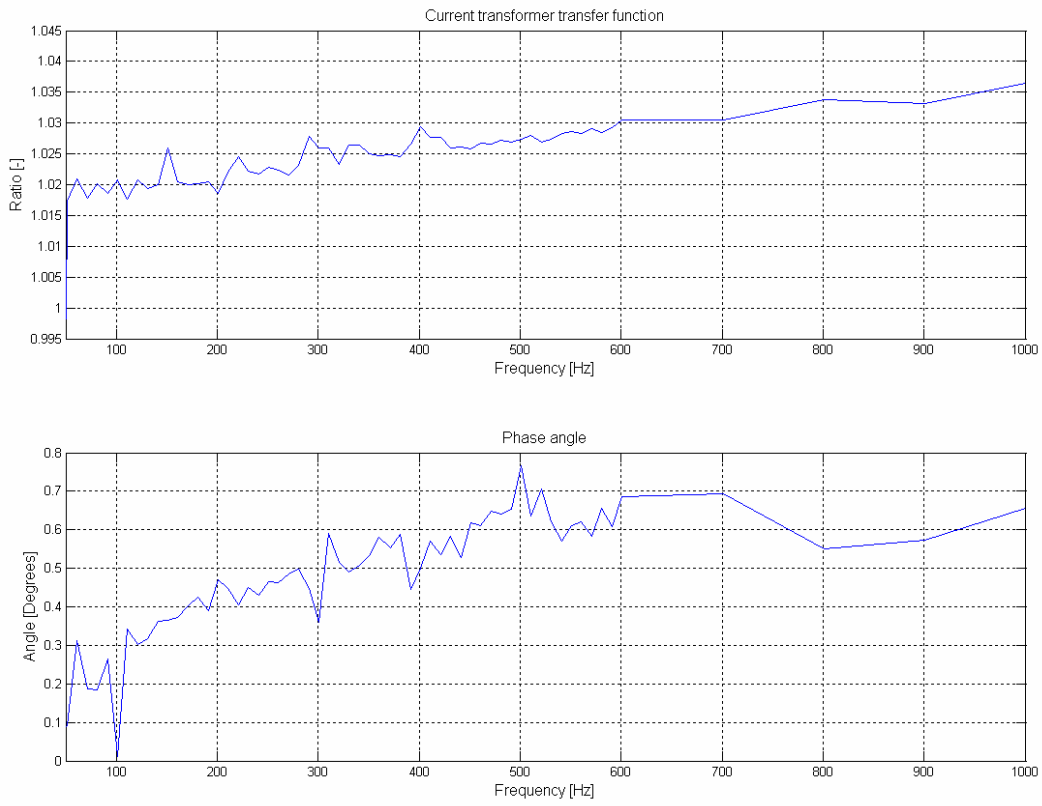


Fig. 54 The transfer function of CT4 measured with an AC generator. The measured frequency range was from 50 Hz to 1 kHz. (The 50-600 Hz range was measured in steps of 10 Hz, and the 600-1000 Hz frequency range in steps of 100 Hz).

10 Line reactances at transient frequencies

Ground fault transients propagate through the network. After passing through the network they can be measured in the substation and used for fault location purposes. On their way to the substations these transients are affected by the network itself. Moreover, the line parameters might vary.

Line parameters such as the resistances, inductances and capacitances per km of all the sequence components are not constants. For the transient based method only the sequence inductances are important. The zero- positive- and negative- sequence inductances of the line vary with many of the parameters. The dependence on frequency is very important, because in practice the fault transient frequency can be as high as 1000 Hz. Moreover, the zero-sequence impedance of the line can also change due to the influence of the ground, if the current returns via the ground. The study conducted in this chapter uses the Carson method.

HV subtransmission lines usually have overhead ground wires situated above the phase conductors and they are grounded at each tower in order to protect the line from lightning. The existence of these overhead ground wires has a significant influence on both the fault generated transient propagation along the network and the line parameters. Therefore, all fault signals returning to the source can actually propagate through both the ground and the overhead ground wires, depending on the tower dimensions, wire parameters, ground parameters and fault signal parameters. The overhead ground wires are considered to be conductors with more stable electrical parameters than the ground. The exact division of the returning current between the two can be obtained by studying the zero-sequence impedance of the line. The study related in this chapter was conducted with various methods derived from the Carson formula.

The standard method proposed by Carson, [19], is probably the most commonly used method for the calculation of the frequency-dependent line parameters considering an earth return. However, Carson's formula does not provide a closed-form solution. It expresses the impedance by means of an improper integral that has to be expanded into an infinite series for computation. The complicated impedance solution has several times been simplified by reducing the infinite series to a finite number. A similar solution was simultaneously proposed by Pollaczek [35], [36]. There are also completely different approaches based, for example, on a layer model of the ground or on FEM (the finite element method). A study in [20] compares the different methods used for calcula-

10. Line reactances at transient frequencies

tion of the frequency-dependent impedance of overhead transmission lines. The methods studied were Carson's, Gary's and FEM. From their analysis it can be seen that the results obtained from the various methods are only slightly different.

Sections 10.1 and 10.2 present the theoretical background relevant to the following sections. In Sections 10.3 and 10.4, the propagation of a transient is investigated using both a reduction factor and a matrix based model. Both are based on Carson's ground simplification, presented in [17] and [18]. Sub-section 10.4.1 investigates the effect of counterpoises on zero-sequence current propagation. These sections primarily study the rate of penetration of the zero-sequence current into the ground. The sections subsequently study the impact of the overhead ground wire material on zero-sequence current propagation and line parameter calculation accuracy. The line parameters for various frequencies, ground resistivities and different overhead ground wire materials are also calculated using the original Carson formula in Section 10.5. A typical 110 kV line structure (3-phase network with two return overhead ground wires) is studied.

10.1 Zero-sequence impedance of the line

The transmission system becomes unbalanced when a ground fault occurs. If the phase currents are not balanced (as during the fault), there will be a return current in the overhead grounded neutral wires and in the ground. The ground return current will spread out under the line, seeking the lowest impedance return path, [17]. An unbalanced power system can be described in terms of symmetrical components, proposed by Fortescue [16]. The ratio of how the return fault currents are divided between the ground and the overhead ground wire will affect the zero-sequence impedance of the line.

In Fig. 55, a network model for zero-sequence impedance estimation is shown. If the supply zero-sequence voltage \underline{V}_0 is sinusoidal, then the phases will have equal “zero-sequence” currents \underline{I}_0 . Part of this current returns via the overhead ground wires \underline{I}_{ogw} and the rest via the ground, \underline{I}_{gr} . The ground wires are grounded at every tower. They are connected to the ground through the tower footing resistance. The large number of such parallel connections to ground per km (in 110 kV lines the number is about 5) allows us to assume that the ground wires and the ground are electrically in parallel and are connected at the ends of the section of the circuit being considered, [18]. Therefore, the same voltage \underline{V}_{nN} can be assumed over both of them, as indicated in Fig. 55. The zero-sequence impedance can be calculated as: $\underline{Z}_0 = \underline{V}_0 / \underline{I}_0$.

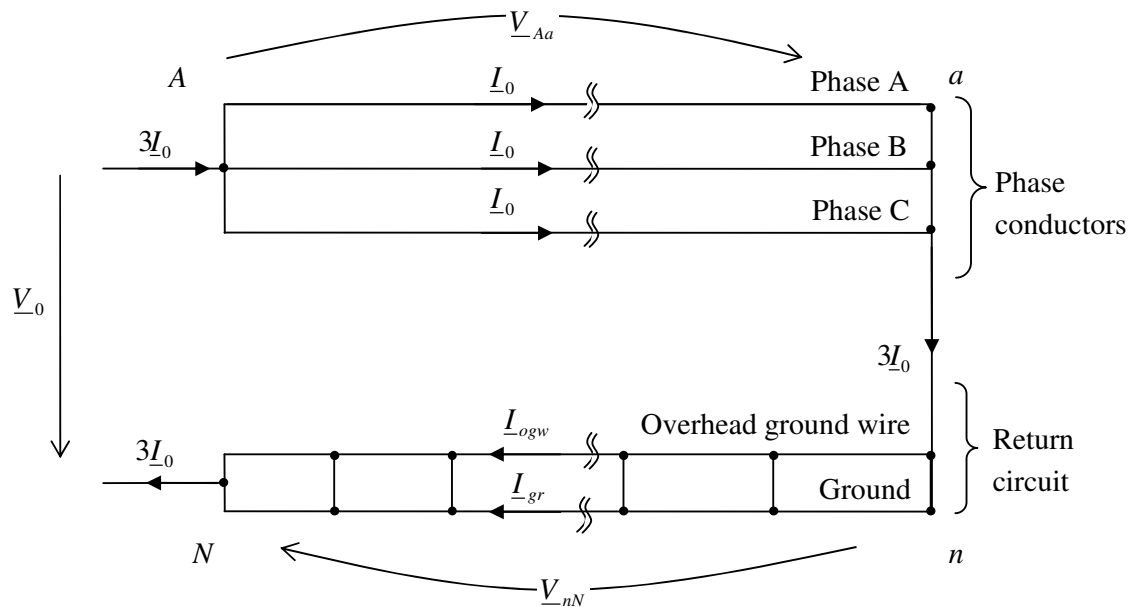


Fig. 55 The model of an overhead line used for estimation of the zero-sequence impedance.

10.2 Self and mutual inductance of a conductor

Let us consider the situation of a conductor in a group of conductors where the sum of the currents in all the conductors is zero. Such a group of conductors is shown in Fig. 56. Conductors 1, 2, 3, ..., n carry the currents $\underline{I}_1, \underline{I}_2, \underline{I}_3, \dots, \underline{I}_n$. The distances of the other conductors from conductor 1 are $D_{12}, D_{13}, \dots, D_{1n}$. By solving this problem as in [18] we get an equation, Eq. (39), for all the flux linkages ψ_1 of conductor 1 in a group of conductors, provided the sum of all the currents is zero.

$$\underline{\psi}_1 = \frac{\mu_0}{2\pi} \left(\underline{I}_1 \ln\left(\frac{1}{r_1'}\right) + \underline{I}_2 \ln\left(\frac{1}{D_{12}}\right) + \underline{I}_3 \ln\left(\frac{1}{D_{13}}\right) + \dots + \underline{I}_n \ln\left(\frac{1}{D_{1n}}\right) \right) = L_1 \underline{I}_1 + M_{12} \underline{I}_2 + M_{13} \underline{I}_3 + \dots + M_{1n} \underline{I}_n \quad (39)$$

Hence the equation can be extended and the components $L_1, M_{12}, M_{13}, \dots, M_{1n}$ can be understood as the self and mutual inductances of conductor 1 with the others, as shown in Eq. (39). The currents are instantaneous values or complex rms values. $r_1' = r_1 e^{-1/4}$ is the equivalent radius of conductor 1 (of radius r_1) for non bundled conductors (note: the internal inductance of the conductor is taken into account by the term $e^{-1/4}$). μ_0 is the permeability of free space.

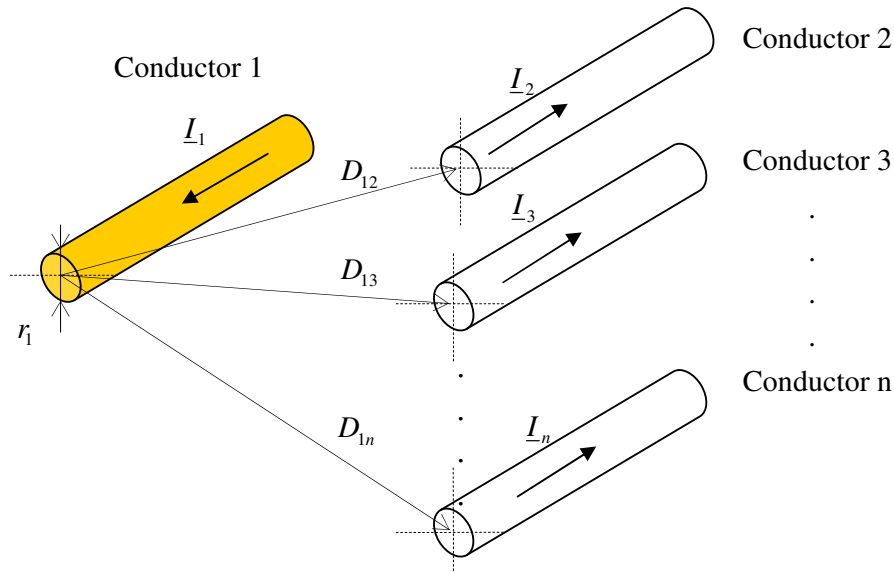


Fig. 56 Cross-sectional view of a group of n -conductors carrying currents whose sum is zero.

10.3 Reduction factor

A section of a transmission line is shown in Fig. 57 on the right. It consists of three single-phase conductors, two return overhead ground conductors and the ground as well, represented by a fictional ground conductor placed at Carson's distance, $D_e = 685.5\sqrt{\rho/f}$ (the 1st term approximation of the Carson series), [19], and with a resistance $R_{gr} = \mu_0\omega l/8$, where μ_0 is the permeability of free space, ω is the angular frequency, l is the length of the analysed line section, ρ is the ground resistivity and f is the frequency.

The picture assumes that the zero-sequence current I_0 flows equally in each phase (as in Fig. 55). Three times the zero-sequence current returns via both the overhead ground wires I_{ogw} and the fictional ground wire $I_{gr} = 3I_0 - I_{ogw}$. The method for solving the zero sequence impedance of such a network is presented in [18]. It is based on the transformation of the three-phase system (Fig. 57 right) into a single phase system (Fig. 57 left) in order to simplify the solution. The three-phase system of wires can be reduced to a single "composite phase wire – a" and the two overhead ground wires to a single "composite overhead ground wire – g". The ground is represented by a "fictional ground conductor". A more detailed solution of this problem is given in Appendix C.

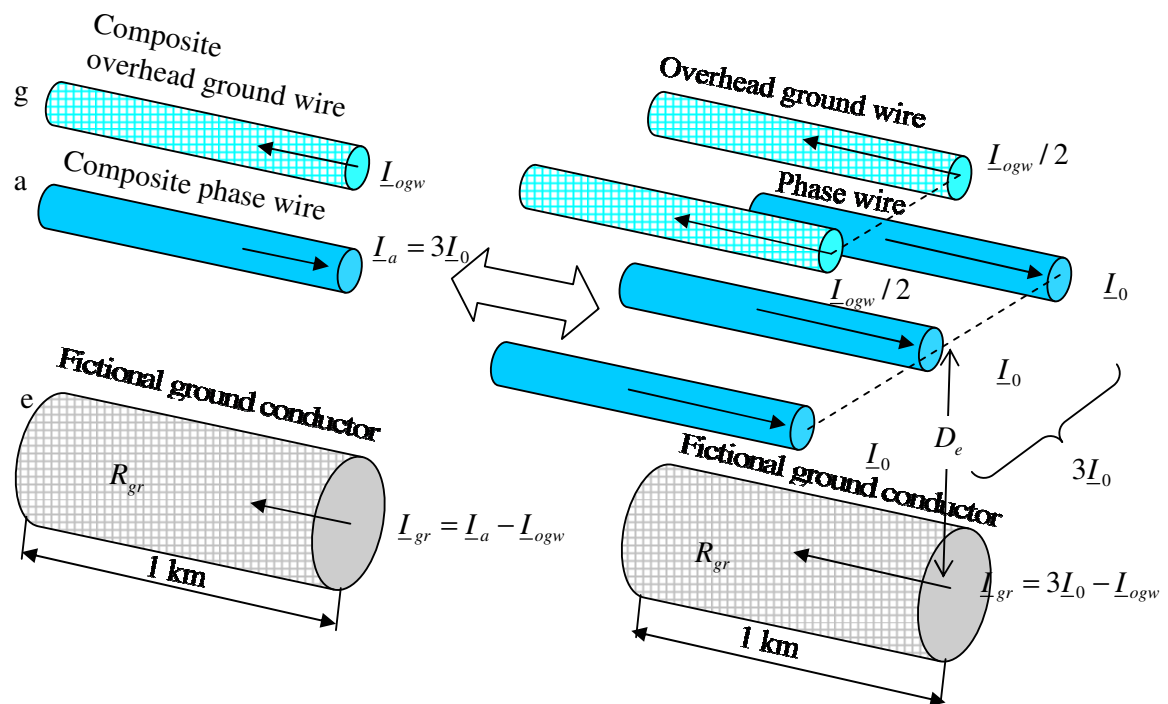


Fig. 57 Transformation between the single- and three-phase systems with ground conductors.

10. Line reactances at transient frequencies

The basic equation describing the zero-sequence impedance of 3-phase overhead lines with two overhead ground return wires and the ground represented as a single conductor according to [18] is:

$$\underline{Z}_0 = 3\left(\underline{Z}_{aa} - \frac{\underline{Z}_{ag}^2}{\underline{Z}_{gg}}\right) \quad (40)$$

where:

\underline{Z}_{aa} is the self-impedance of the phase conductor-ground loop

\underline{Z}_{gg} is the self -impedance of the overhead ground conductor-ground loop

\underline{Z}_{ag} is the mutual impedance between the “phase conductor-ground loop” and the “overhead ground conductor-ground loop”

Detailed calculations of the impedances \underline{Z}_{aa} , \underline{Z}_{gg} and \underline{Z}_{ag} can be found in Appendix C.

The division of $3\underline{I}_0$, the tripled zero-sequence current, into the ground wires \underline{I}_{ogw} and ground \underline{I}_{gr} is expressed by means of the reduction factor k_u , which shows the amount of $3\underline{I}_0$ flowing in the ground \underline{I}_{gr} :

$$k_u = \frac{\underline{I}_{gr}}{3\underline{I}_0} = \frac{\underline{Z}_{ag} - \underline{Z}_{gg}}{\underline{Z}_{gg}} = \frac{R_{ogw}/n_0 + j\omega(M_{ag} - L_{gg})}{R_{ogw}/n_0 + R_{gr} + j\omega L_{gg}} \quad (41)$$

where:

R_{ogw} is the resistance per km of the overhead ground wire

n_0 is the number of the overhead ground wires

M_{ag} is the mutual inductance between the “phase conductor-ground loop” and the “overhead ground conductor-ground loop”

L_{gg} is the inductance of the overhead ground conductor-ground loop

The behaviour of the reduction factor and the zero-sequence inductance per km for a typical Fingrid 110 kV tower is graphically represented in Fig. 58 (a) and (b) (the parameters of the studied network are given in Appendix C), which shows the situation when the phase wires and overhead ground wires are made of aluminum and their rela-

10. Line reactances at transient frequencies

tive permeability is $\mu_r = 1$. Although in practice there is some steel for reinforcement, the difference in the calculated result will not be significant. In the case of overhead ground wires completely made of steel, the relative permeability would be $\mu_r = 50$ and the resistivity much higher, and then the result will change a lot, Fig. 58 (c) and (d).

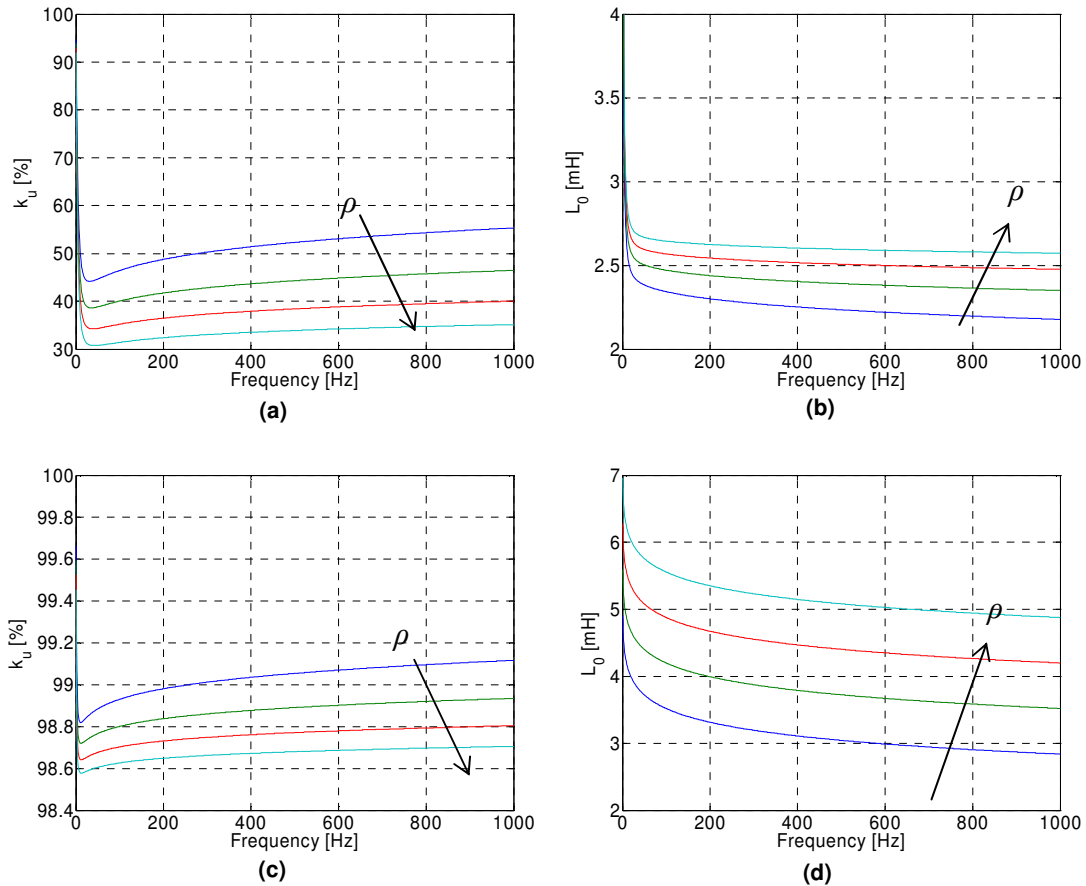


Fig. 58 The frequency dependence of the reduction factor and zero-sequence inductance for typical 110 kV overhead lines with two overhead ground wires made of aluminium, (a) and (b), and steel, (c) and (d). The calculation is made for $\rho = 10, 10^2, 10^3$ and $10^4 \Omega m$. The arrows indicate an increase in the ground resistance.

The penetration of the zero-sequence current into the ground at transient frequencies is very much dependent on the ground resistivity and also on the material the overhead ground wires are made of. The zero-sequence current tends to flow via the overhead ground wire rather than the ground when aluminum is used. If steel is used, the majority of the zero-sequence current tends to flow in the ground. This is partly because the overhead ground wires are of high impedance due to their higher resistance, but is mainly due to the higher inductance caused by the higher conductor permeability.

10.4 Matrix method

The reduction factor was calculated in the previous section using a simplification of the ground but in this section a different approach is presented. The method of modelling the zero-sequence impedance of a line section is based on the assumption that the ground can be substituted by a system of equivalent wires, with the appropriate resistances and inductances, at Carson's distance $D_{kk'}$ from the overhead wires (instead of in the ground). This type of analysis method can be found for instance in [17].

The model can be seen in Fig. 59. The overhead conductors of phases a, b and c, also numbered 1, 2 and 3, and the return overhead ground wires n1 and n2, also numbered 4 and 5, are situated on a tower. This system of wires has corresponding ground representatives (which are also shown in Fig. 59) to substitute the influence of the ground itself. This is a rather complicated approach. In practice, one wire placed in the ground would be enough.

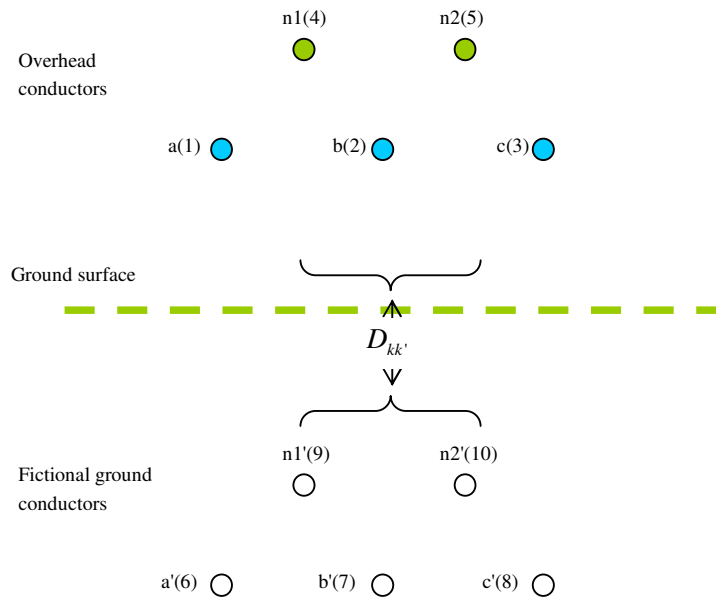


Fig. 59 Three-phase transmission line with two overhead ground conductors and the ground replaced by ground return conductors.

Each of the ground conductors a', b', c', n1' and n2' has a GMR (geometric mean radius) $D_{k'k'} = D_{kk}$ (r' for non-bundled conductors) the same as the original conductors, and all conductors in the ground have the same resistance $R_{k'k'} = n_{grw} (\mu_0 \omega l / 8)$, where μ_0 is the permeability of free space, ω is the angular frequency and l is the length of the analysed line section. n_{grw} is the number of the wires representing the ground (5 in this model). All the ground return conductors are the same distance $D_{kk'}$ from their respec-

10. Line reactances at transient frequencies

tive overhead conductors [17]. According to Carson's theory, the distance is $D_{kk'} = 685.5\sqrt{\rho/f}$ (approximated by using only the 1st term of the Carson series), where ρ is the ground resistivity and f is the frequency.

Note: the original method described in [17] gives the expression $R_{k'k'} = \mu_0\omega l/8$ for each wire in the ground. However, this causes the total zero-sequence resistance to be too low. Therefore the total ground resistance of all wires in the ground should be equal to $\mu_0\omega l/8$. This is corrected by n_{grw} , such that $R_{k'k'} = n_{grw}(\mu_0\omega l/8)$.

The circuit model for the zero-sequence impedance estimation of the line section with, for example, a length of 1 km is shown in Fig. 60. The model includes the resistance and inductance of each wire and, moreover, all mutual inductances between all wires. The tripled zero-sequence current flowing in the phases, $3\underline{I}_0$, returns through the ground \underline{I}_{gr} and overhead ground wire \underline{I}_{ogw} , as shown in the model.

10. Line reactances at transient frequencies

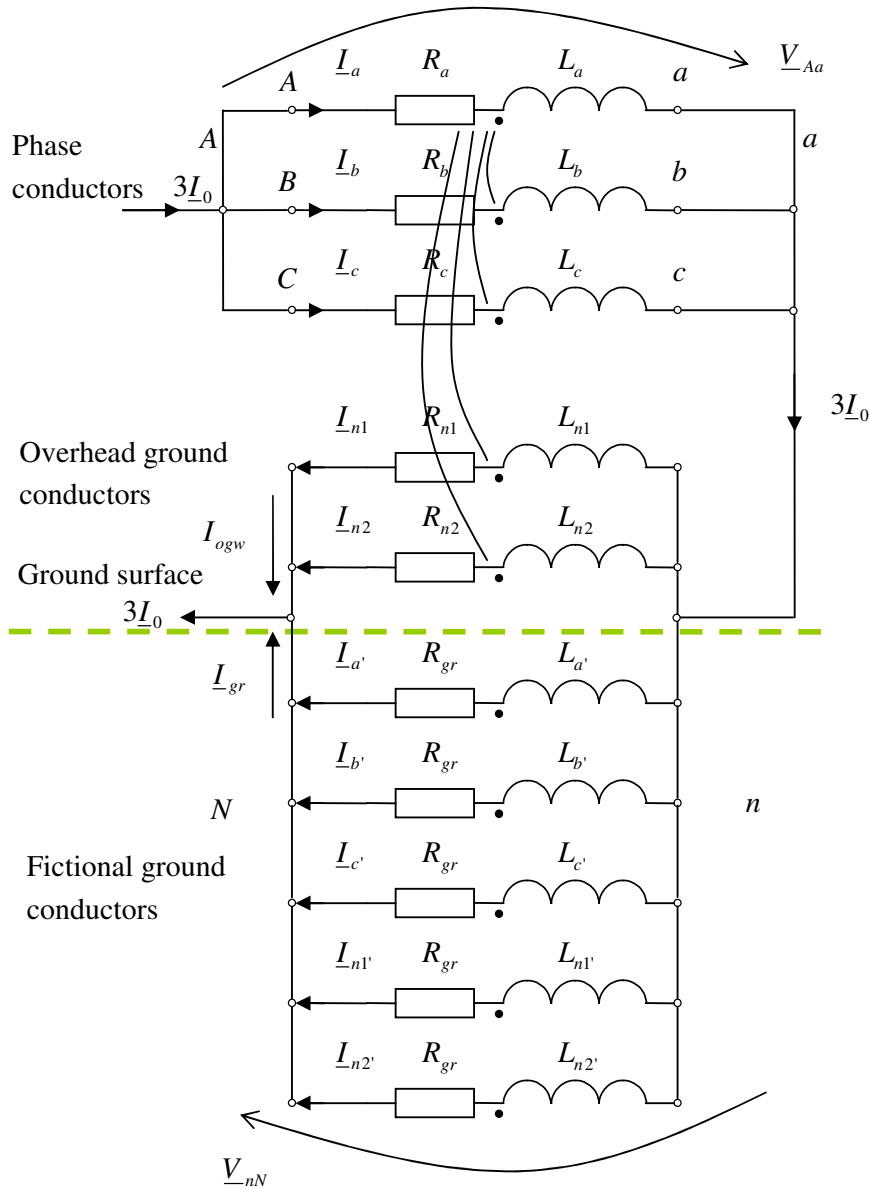


Fig. 60 Circuit for estimating the zero-sequence impedance and current of a three-phase transmission line with two overhead ground conductors.

To describe the voltage drops V_{Aa} over the phase conductors and V_{nN} over the ground wires, and the ground in the circuit shown in Fig. 60, we can write the following matrix equation:

10. Line reactances at transient frequencies

The matrix solution:

$$\begin{bmatrix} \underline{V}_{Aa} \\ \underline{V}_{Ab} \\ \underline{V}_{Ac} \\ \underline{V}_{nN} \\ \underline{V}_{nN} \\ \underline{V}_{nN} \\ \underline{V}_{nN} \\ \underline{V}_{nN} \\ \underline{V}_{nN} \\ \underline{V}_{nN} \end{bmatrix} = j\omega \begin{bmatrix} \frac{R_a}{j\omega} + L_a & M_{ab} & M_{ac} & -M_{an1} & -M_{an2} & -M_{aa} & -M_{ab'} & -M_{ac'} & -M_{an1'} & -M_{an2'} \\ M_{ba} & \frac{R_b}{j\omega} + L_b & M_{bc} & -M_{bn1} & -M_{bn2} & -M_{ba} & -M_{bb'} & -M_{bc'} & -M_{bn1'} & -M_{bn2'} \\ M_{ca} & M_{cb} & \frac{R_c}{j\omega} + L_c & -M_{cn1} & -M_{cn2} & -M_{ca} & -M_{cb'} & -M_{cc'} & -M_{cn1'} & -M_{cn2'} \\ -M_{a1a} & -M_{a1b} & -M_{a1c} & \frac{R_{n1}}{j\omega} + L_{n1} & M_{a1n2} & M_{a1a'} & M_{a1b'} & M_{a1c'} & M_{a1n1'} & M_{a1n2'} \\ -M_{a2a} & -M_{a2b} & -M_{a2c} & M_{a2n1} & \frac{R_{n2}}{j\omega} + L_{n2} & M_{a2a'} & M_{a2b'} & M_{a2c'} & M_{a2n1'} & M_{a2n2'} \\ -M_{a'a} & -M_{a'b} & -M_{a'c} & M_{a'n1} & M_{a'n2} & \frac{R_{a'}}{j\omega} + L_{a'} & M_{a'b'} & M_{a'c'} & M_{a'n1'} & M_{a'n2'} \\ -M_{b'a} & -M_{b'b} & -M_{b'c} & M_{b'a1} & M_{b'a2} & M_{b'a'} & \frac{R_{b'}}{j\omega} + L_{b'} & M_{b'c'} & M_{b'a1'} & M_{b'a2'} \\ -M_{c'a} & -M_{c'b} & -M_{c'c} & M_{c'a1} & M_{c'a2} & M_{c'a'} & M_{c'b'} & \frac{R_{c'}}{j\omega} + L_{c'} & M_{c'a1'} & M_{c'a2'} \\ -M_{n1a} & -M_{n1b} & -M_{n1c} & M_{n1n1} & M_{n1n2} & M_{n1a'} & M_{n1b'} & \frac{R_{n1}}{j\omega} + L_{n1} & M_{n1n1'} & M_{n1n2'} \\ -M_{n2a} & -M_{n2b} & -M_{n2c} & M_{n2n1} & M_{n2n2} & M_{n2a'} & M_{n2b'} & M_{n2c'} & \frac{R_{n2}}{j\omega} + L_{n2} & M_{n2n2'} \end{bmatrix} \begin{bmatrix} \underline{I}_a \\ \underline{I}_b \\ \underline{I}_c \\ \underline{I}_{n1} \\ \underline{I}_{n2} \\ \underline{I}_{a'} \\ \underline{I}_{b'} \\ \underline{I}_{c'} \\ \underline{I}_{n1'} \\ \underline{I}_{n2'} \end{bmatrix} \quad (42)$$

where M_{km} are the mutual inductances between two conductors and ω is the angular frequency. All matrix elements are calculated in Appendix C.

The matrices in Eq. (42) can be rewritten as:

$$\underline{[V]} = \underline{[Z]} \cdot \underline{[I]} \quad (43)$$

where $\underline{[V]} = [\underline{V}_{Aa} \ \underline{V}_{Ab} \ \underline{V}_{Ac} \ \underline{V}_{nN} \ \underline{V}_{nN} \ \underline{V}_{nN} \ \underline{V}_{nN} \ \underline{V}_{nN} \ \underline{V}_{nN} \ \underline{V}_{nN}]^T$ is the matrix of the voltage drops, $\underline{[I]} = [\underline{I}_a \ \underline{I}_b \ \underline{I}_c \ \underline{I}_{n1} \ \underline{I}_{n2} \ \underline{I}_{a'} \ \underline{I}_{b'} \ \underline{I}_{c'} \ \underline{I}_{n1'} \ \underline{I}_{n2'}]^T$ is the matrix of the currents in each wire and $\underline{[Z]}$ is the impedance matrix according to Eq. (42). The solution for the unknown currents is:

$$\underline{[I]} = \underline{[Y]} \cdot \underline{[V]} \quad (44)$$

where $\underline{[Y]} = \underline{[Z]}^{-1}$ is an admittance matrix. The currents in the 4th and 5th rows of the matrix equation, Eq. (44), are the currents in the overhead ground wires, $\underline{I}(4) = \underline{I}_{n1}$ and $\underline{I}(5) = \underline{I}_{n2}$, shown in Eq. (45), and the summation of the currents in both the ground and the ground wires caused by the voltage V_{nN} is 3 times the zero-sequence current itself, Eq. (46).

$$\underline{I}_{ogw} = [\underline{I}(4) + \underline{I}(5)] = [\underline{Y}(4) + \underline{Y}(5)] \cdot \underline{[V]} \quad (45)$$

10. Line reactances at transient frequencies

$$\begin{aligned}
 3\underline{I}_0 &= [\underline{I}(4) + \underline{I}(5) + \underline{I}(6) + \underline{I}(7) + \underline{I}(8) + \underline{I}(9) + \underline{I}(10)] \\
 &= [\underline{Y}(4) + \underline{Y}(5) + \underline{Y}(6) + \underline{Y}(7) + \underline{Y}(8) + \underline{Y}(9) + \underline{Y}(10)] \cdot [\underline{V}]
 \end{aligned} \tag{46}$$

Finally, the voltage drop, which is equal over the ground wires and the ground, can be eliminated. Thus we can now estimate the return current in the overhead ground wire as:

$$\frac{\underline{I}_{ogw}}{3\underline{I}_0} = \frac{[\underline{Y}(4) + \underline{Y}(5)]}{[\underline{Y}(4) + \underline{Y}(5) + \underline{Y}(6) + \underline{Y}(7) + \underline{Y}(8) + \underline{Y}(9) + \underline{Y}(10)]} \tag{47}$$

and the return current in the ground as:

$$\frac{\underline{I}_{gr}}{3\underline{I}_0} = \frac{[\underline{Y}(6) + \underline{Y}(7) + \underline{Y}(8) + \underline{Y}(9) + \underline{Y}(10)]}{[\underline{Y}(4) + \underline{Y}(5) + \underline{Y}(6) + \underline{Y}(7) + \underline{Y}(8) + \underline{Y}(9) + \underline{Y}(10)]} \tag{48}$$

The return current in the ground for a typical 110 kV Finnish line, according to Eq. (48), can be plotted as in Fig. 61a. (The parameters of the line appear in Appendix C.)

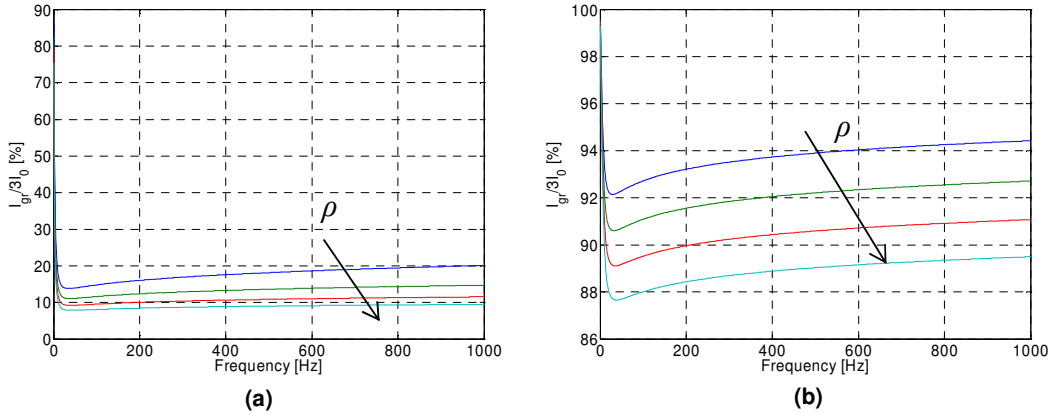


Fig. 61 The frequency dependence of the current penetrating into the ground for typical 110 kV overhead lines with two overhead ground wires made of aluminium (a) and steel (b). The calculation is made for $\rho = 10, 10^2, 10^3$ and $10^4 \Omega m$. The arrows indicate increasing ground resistance.

In Fig. 61a, approximately 15% of the fault transients return via ground, which in other words means that 85% of the fault transients return via the overhead ground wire. This result is a bit different from that shown in Fig. 58a, where the reduction factor was used.

When the overhead ground wires are made of steel the zero-sequence currents tend to return via the ground, Fig. 61b, consistent with the calculation by the reduction factor, Fig. 58c. Steel wires on the top of the line can cause significant changes in the fault transient return path. If they are made of steel (the steel wire is modelled as a conductor

10. Line reactances at transient frequencies

with a higher relative permeability, $\mu_r = 50$, and higher resistance than aluminium) they have a higher inductance at transient frequencies, as indicated in Fig. 61b. Around 90% of the zero-sequence current penetrates into the ground for all shown frequencies.

This result basically highlights the practical limitation of the transient based ground fault location method described in this thesis. When the overhead ground wires are constructed from steel, their inductance will be higher (in comparison to the aluminium wires) and the dominant part of the zero-sequence current will flow through the ground. The ground is an unstable conductor with continuously changing impedance, strongly dependent on frequency and soil resistivity, which tends to decrease the reliability of the method.

The line parameter calculations

The symmetrical components of the line can be easily calculated with this approach as well. The impedance matrix in Eq. (42) can be used if the designated polarity of the impedances is removed. The matrix accounts for the different current directions in the phase wires and the ground.

The number of equations, ten for a 10×10 matrix, can be reduced to 3 (a 3×3 matrix) if it is supposed that the voltage drop over the ground and the ground wires, \underline{V}_{nN} , is the same. Then the last equation (row 10) can be subtracted from the other equations. The details of this matrix manipulation are shown in Appendix C.

The line parameters are calculated for typical 110 kV lines (parameters in Appendix C). The accuracy is almost as good as when using the original method proposed by Carson, which can be seen by comparison with Section 10.5.

10. Line reactances at transient frequencies

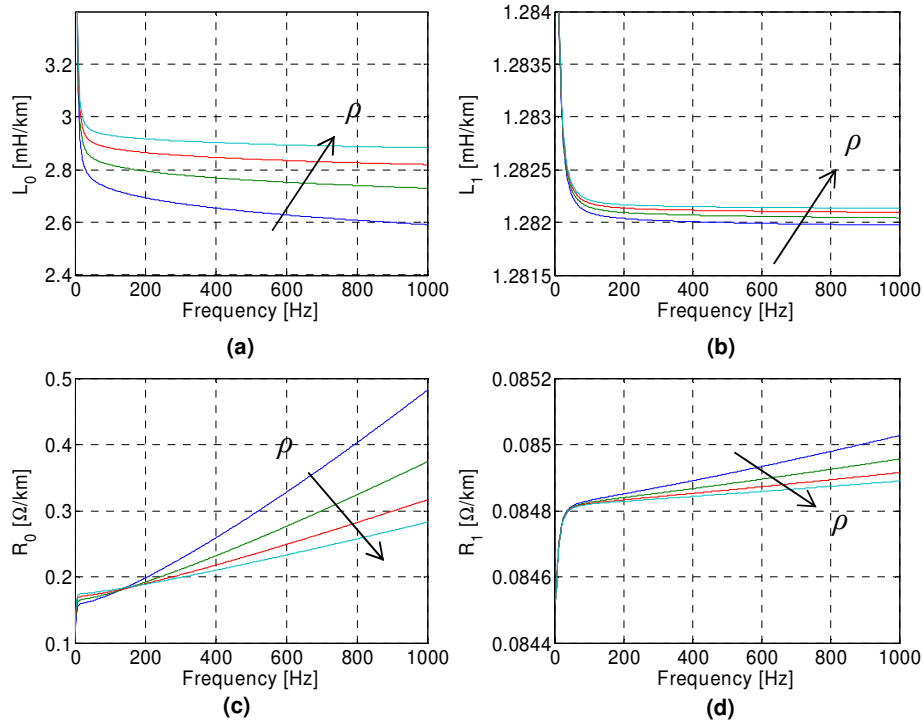


Fig. 62 The symmetrical components of typical 110 kV overhead lines with two ground wires made of aluminium . The calculation is made for $\rho = 10, 10^2, 10^3$ and $10^4 \Omega m$. The arrows indicate ground resistance growth.

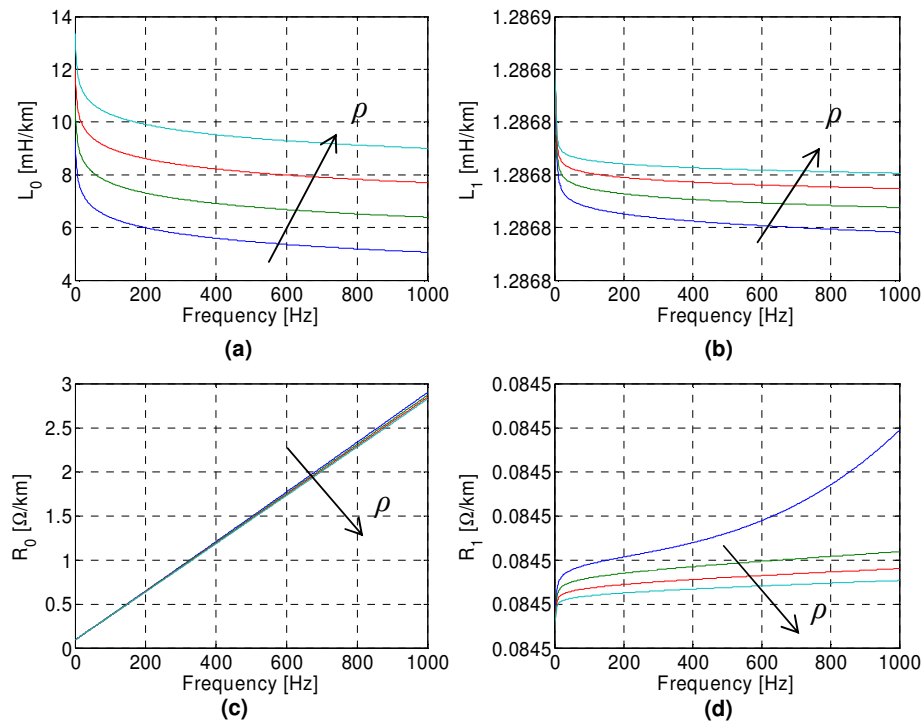


Fig. 63 The symmetrical components of typical 110 kV overhead lines with two ground wires made of steel . The calculation is made for $\rho = 10, 10^2, 10^3$ and $10^4 \Omega m$. The arrows indicate an increase in ground resistance.

10.4.1 The effect of counterpoises

The ground resistivity in Finland is very high. Therefore, in order to increase the ground conductivity counterpoises are installed in some line sections. The counterpoises are situated along the line under the ground surface and are also connected to each tower and its overhead ground wires. This situation is symbolically illustrated in Fig. 64b.

Modelling principle

The model presented in Fig. 59 is rather complicated but it can be simplified without any serious impact on the accuracy of the calculation. Because the distance between the images (situated in the ground) is very small in comparison to their depth (in the frequency range used), all ground images can be represented by one wire, without causing significant error, Fig. 64a.

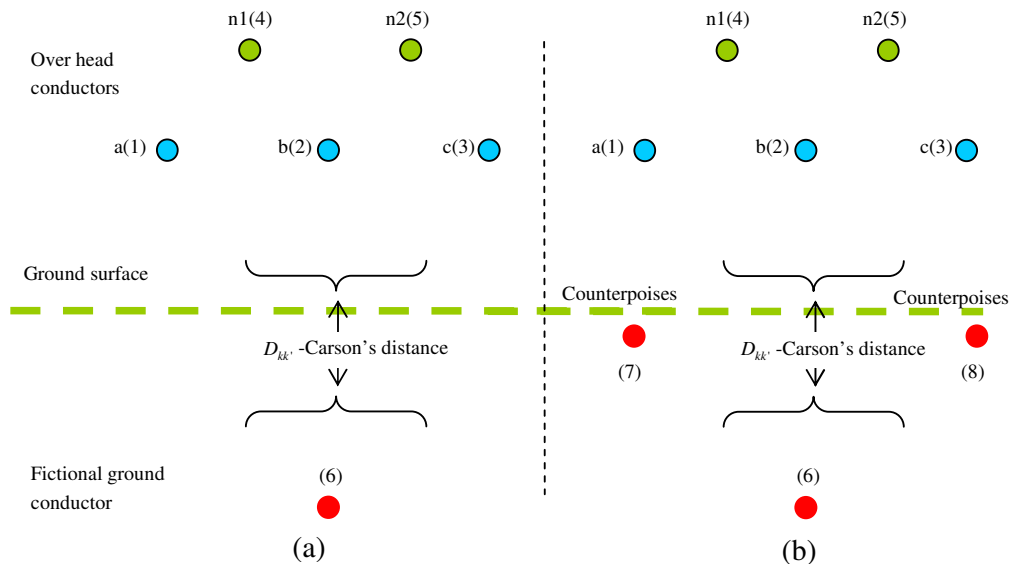


Fig. 64 Three-phase transmission line with two overhead ground conductors and with ground replaced by one ground return conductor for (a) a normal line, (b) a line with counterpoises.

If all ground conductors are replaced with only one wire, rows 6, 7, 8, 9 and 10 in the impedance matrix, Eq. (42) will be replaced with only one row, the 6th one. (Note: the matrix size will become 6×6 instead of 10×10). Hence the current in the ground can be estimated using Eq. (49).

$$\frac{\underline{I}_{gr}}{3\underline{I}_0} = \frac{\underline{Y}(6)}{\underline{Y}(4) + \underline{Y}(5) + \underline{Y}(6)} \quad (49)$$

The meaning of the symbols in Eq. (49) is the same as in Section 10.4.

10. Line reactances at transient frequencies

An example calculation was made for a typical 110 kV line and various ground resistivities, $\rho = 10, 10^2, 10^3$ and $10^4 \Omega\text{m}$, and frequencies up to 1 kHz. All the necessary parameters for the calculations are given in Appendix C. The counterpoises are placed one meter below the surface along the line. For easy calculation the counterpoises, which are made of aluminium of the same radius as the top wires, are situated directly below the phase conductors a(1) and c(3), one meter below the surface, Fig. 64b. However, in practice the counterpoises are made of copper. The wires are not bundled.

The impact of the counterpoises is huge. The counterpoises reduce the current in the ground so much that even if the overhead ground wires are made of steel only a small fraction of the current will penetrate into the ground. Compare Fig. 65, where the overhead ground wires are made of aluminium, with Fig. 66, where they are made of steel.

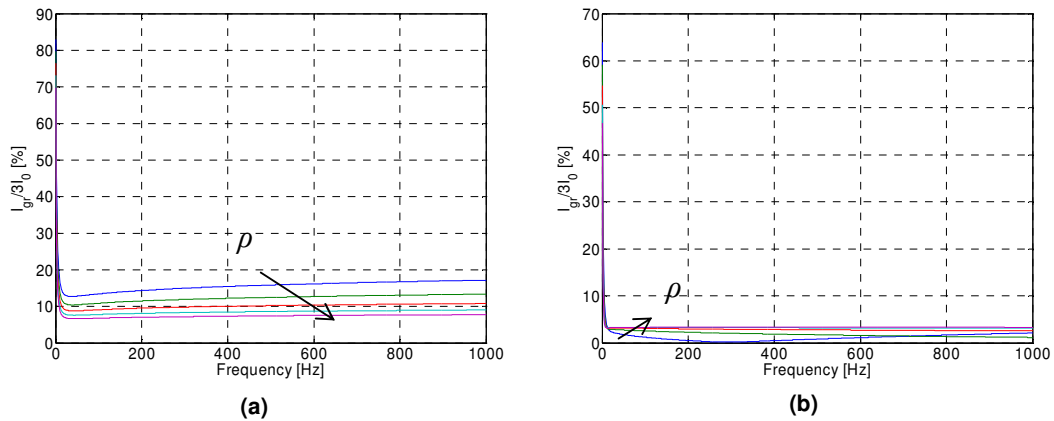


Fig. 65 The frequency dependent ground current. Overhead ground wires made of aluminium: (a) with no counterpoises, (b) with counterpoises. The calculation is made for $\rho = 10, 10^2, 10^3$ and $10^4 \Omega\text{m}$; the arrows show the ground resistance growth.

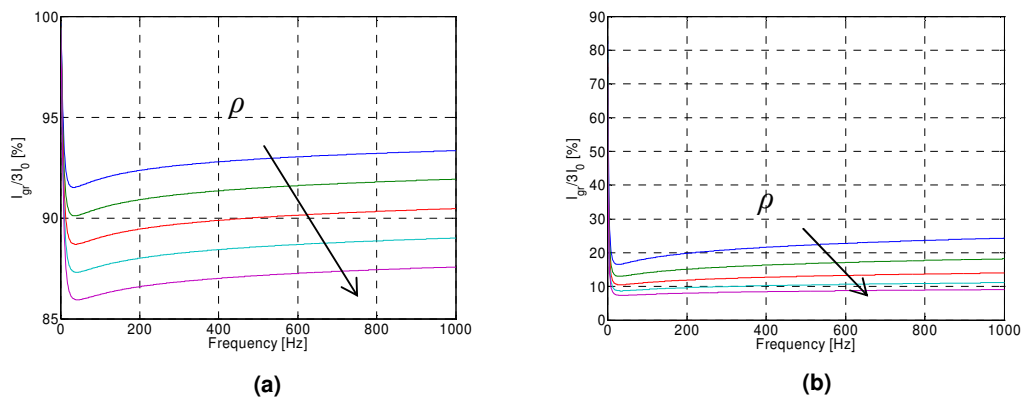


Fig. 66 The frequency dependent ground current. Overhead ground wires made of steel: (a) with no counterpoises, (b) with counterpoises. The calculation is made for $\rho = 10, 10^2, 10^3$ and $10^4 \Omega\text{m}$; the arrows show the ground resistance growth.

10. Line reactances at transient frequencies

The counterpoises cause the current in the ground to be reduced even though the top wires are made of steel. The existence of counterpoises improves the reliability of the transient based fault location method, particularly when steel top wires are used. The effect of the counterpoises can be used in networks where they are already installed. Otherwise it would be more economical to change the overhead ground wires than to bury the counterpoises.

10.5 Line parameter calculation by the Carson formula

One of the most precise methods for line parameter calculation is based on Carson's formula, [19]. The impedance matrix's series and mutual impedances (of the line) can be calculated as:

$$\underline{Z}_{ii} = \underline{Z}_{int} + \underline{Z}_{ext} + \Delta\underline{Z}_g \quad (50)$$

$$\underline{Z}_{ij} = \underline{Z}_{ij} + \Delta\underline{Z}_{gm} \quad (51)$$

where: \underline{Z}_{int} is the internal impedance of the conductor, \underline{Z}_{ext} is the external impedance (reactance) of the conductor, and $\Delta\underline{Z}_g$ and $\Delta\underline{Z}_{gm}$ are the earth correction terms in Carson's formula, [19]. A detailed description of how to build the series impedance matrix is given in Appendix C.4.

Once the impedance matrix has been built for all the conductors (a 5×5 matrix), the ground conductors in the impedance matrix are eliminated, resulting in a 3×3 matrix, which is then symmetrically transformed. The reduction of the overhead ground wires is possible because their electrical potential is zero. Details of this transformation are given in Appendix C. If the symmetrical impedances are calculated, the resistances and inductances can be plotted as a function of frequency and ground resistivity, Fig. 67. These components were calculated for a typical 110 kV Finnish line (for a tower construction, the dimensions are given in Appendix C.). The calculation was made for the frequency range 1-1000 Hz and ground resistances $\rho = 10, 10^2, 10^3$ and $10^4 \Omega\text{m}$. However, this calculation does not take into account the skin effect of the conductors. The calculation used the first 100 terms of the infinite Carson series.

10. Line reactances at transient frequencies

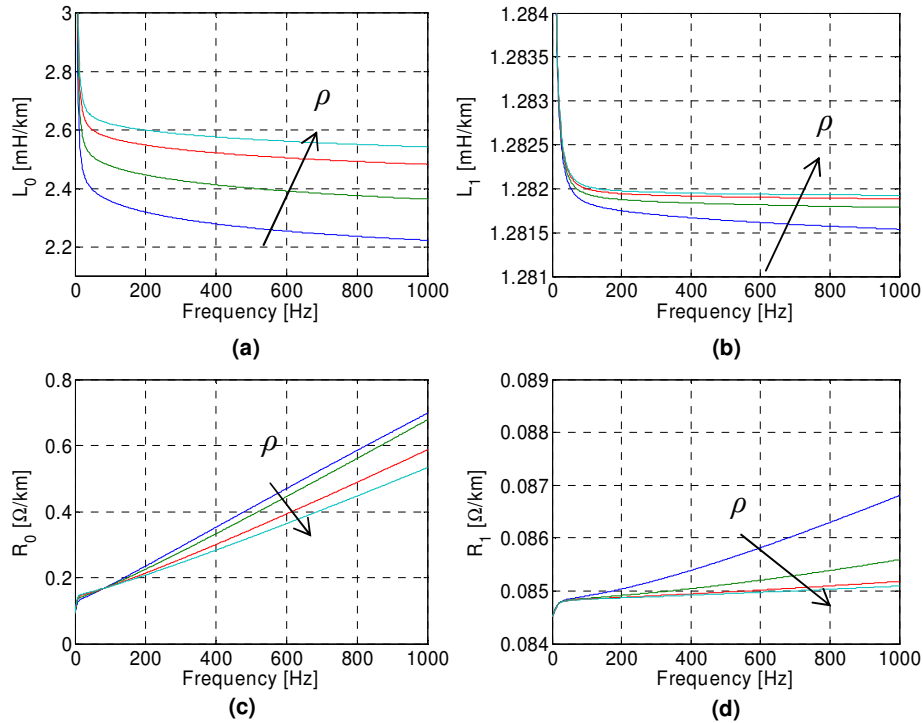


Fig. 67 The symmetrical components of typical 110 kV overhead lines with two ground wires made of aluminium . The calculation was made for $\rho = 10, 10^2, 10^3$ and $10^4 \Omega m$; the arrows show the direction of ground resistance growth

Zero-sequence resistances have a tendency to grow with the frequency, Fig. 67c. This is natural behavior because of the ground. If the skin effect is included in the conductors this value will be higher. However, for frequencies under 1000 Hz the difference will not be seen. The zero-sequence resistance increases with ground resistivity up to approximately 100 Hz and decreases with higher ground resistivity for higher frequencies.

A more important conclusion from this analysis concerns the behaviour of the line inductances. Both components, the zero- and the positive-sequence inductances, decrease with frequency. The zero sequence inductance changes more than the positive, as Fig. 67a shows. This stronger relationship is caused by the ground inductance. With higher frequencies the returning ground current penetrates less into the ground. Therefore, the total area occupied by the “flowing current” becomes smaller, hence the mutual and self inductances of the ground are also reduced.

The positive- and negative- sequence inductance of the line should not be affected by the ground resistivity. However, some small variation can be seen in the presented figures.

10. Line reactances at transient frequencies

For comparison, the overhead ground wires were substituted by steel wires. Naturally, the zero-sequence components increase. The positive sequence components stay about the same.

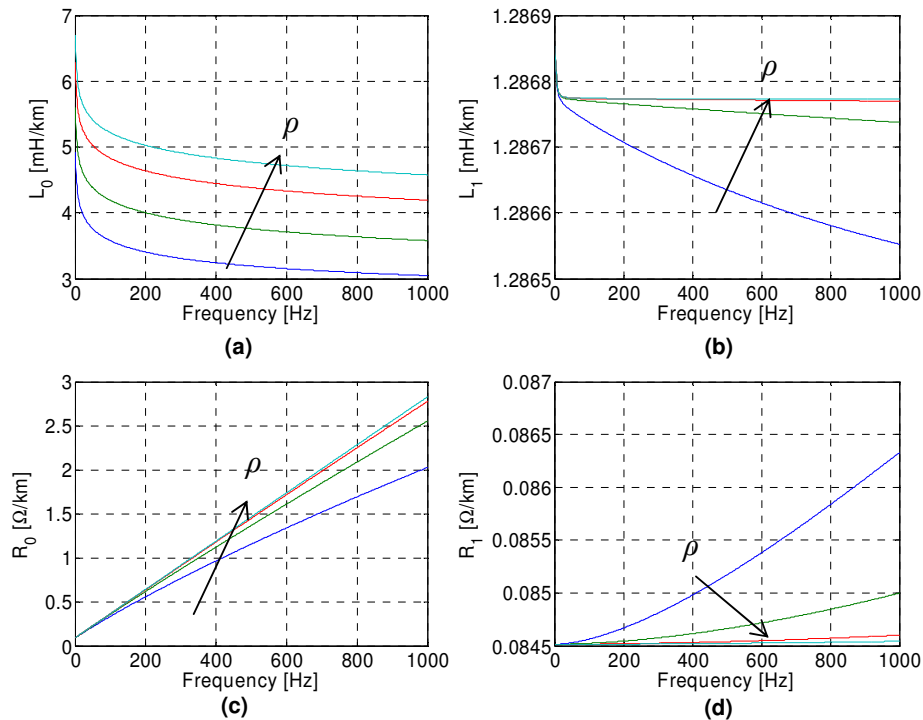


Fig. 68 The symmetrical components of typical 110 kV overhead lines with two ground wires made of steel. The calculation was made for $\rho = 10, 10^2, 10^3$ and $10^4 \Omega$ m; the arrows indicate an increase in the ground resistance.

A comparison of the Carson method with the simplified approaches presented in the previous sections, 10.3 and 10.4, (compare Fig. 58b and Fig. 58d for the reduction factor, and Fig. 62 and Fig. 63 for the matrix method) shows that the symmetrical components of the line can be calculated accurately for frequencies up to 1 kHz with either method.

10. Line reactances at transient frequencies

However, for fault location purposes the sum of all the sequence inductances and their frequency dependence is important. This is shown in Fig. 69. Because the positive and negative sequence inductances do not vary much with frequency, the zero-sequence inductance has the most influence.

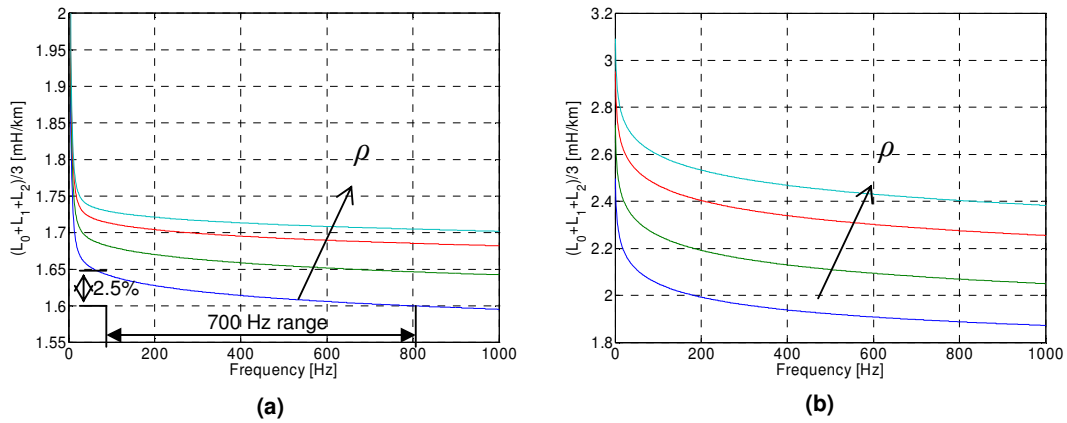


Fig. 69 The fault path inductance of the line per km of typical 110 kV overhead lines with two ground wires made of aluminium (a) and steel (b). The calculation is made for $\rho = 10, 10^2, 10^3$ and $10^4 \Omega m$; the arrows indicate growth in the ground resistance.

The variation of the fault path inductance at the transient frequency is about $2.5\%/700 \text{ Hz} = 0.0036\%/ \text{Hz}$. Because the transients are usually higher than 100 Hz it is not so important to deal with inductances below 100 Hz. In reality, the range of the transient frequency does not change very much in a given network configuration. The range is about 100-300 Hz, which can cause a maximum inductance error of 1%, according to the results shown in Fig. 69 for an overhead ground wire made of aluminium (with 5% steel). The influence of ground resistivity on line parameters is much stronger. The variation of the line parameters with ground resistivity is about 5% at transient frequencies if the overhead ground wires are made of aluminium. In cases where the top wires are made of steel, the variation is greater, 25%.

10.6 Discussion

Zero-sequence current return path

The ground is an unstable conductor with parameters that change with the soil resistivity and frequency. Therefore, it would be best from the fault location point of view that the transients return via the ground wire. The various methods in this chapter have shown that the zero-sequence current at transient frequencies tends to return to the source via the overhead ground wire rather than via the ground. This is true in a normal line, where the overhead ground wires are made of aluminium. In cases where the overhead ground wires are made of steel the zero-sequence current mostly returns via the ground. This can be improved by installing counterpoises along the line. This solution is very effective but impractical, because of the high cost of installation. The replacement of the overhead ground wires is therefore more reasonable.

Conductor material

Normally, the conductors used for the phase and ground wires in Finland are made of aluminium reinforced with a steel wire in the middle (FerAl). Due to the skin effect, the current flows in the aluminium part and so the relative permeability can be considered to be 1. The analysis performed for aluminium conductors in this chapter is therefore valid for FerAl cables as well. In some special cases the ground wires might also be made of steel. In steel wires both the resistivity and the relative permeability are much higher than for aluminium.

Line parameter variation

The line parameters are relatively stable with frequency in the range of the transient frequencies. The maximum error caused by the line parameters due to variations in the transient frequencies was identified to be around 1 % for a line where the overhead ground conductors are made of aluminium and 5% in the case of steel. However, the dependence with ground resistivity is much greater, approximately 5% if the overhead ground wires are made of aluminium and 25% for steel. Due to the fact that the ground resistivity in Finland is in the range $10^0 - 10^5 \Omega\text{m}$ and varies along the line, the variation of line parameters in a typical line is highly significant.

Model comparison

The reduction factor seems to be in good agreement with the original Carson method, but the matrix model gives a higher error when calculating the line parameters. The difference is in the ground modelling. The current in the ground estimated by the matrix model is smaller than it is in reality.

11 Correction factors

The fault location algorithms are based on the assumption that the fault loop can be represented by a series connection of the zero-, positive- and negative-sequence inductances and resistances of the faulted line. This assumption has been made in both the conventional fault location method, Chapter 4, and the transient based fault location presented in Chapter 3. However, in practice this is only correct in networks with solidly grounded neutrals (or low impedance grounding). In the case of networks with isolated neutral or Petersen coil grounding, some correction that takes into account the line and phase capacitances is required.

Section 11.1 closely focuses on the comparison of the two different line models and also studies the influence of the other lines connected to a substation where the network neutral is isolated. A correction factor for fault location in a network with an isolated neutral is computed in Section 11.2. In Section 11.3 the impact of network neutral grounding is studied. Section 11.4 summarises the most influential error sources in the fault location method.

11.1 Ground fault studies using symmetrical components and line models

Modelling by means of symmetrical components is the most commonly used method for studying ground faults. In this section the model of a ground fault is designed and compared to a line model. The aim of this simulation was to compare the fault calculation using the line model, Fig. 71, with its symmetrical component model, Fig. 70. The line model is the distributed transposed Clark line model. Both were studied in EMTP/ATP and were then analysed in the fault locator presented in Chapter 13. The results are given in Tab. 21, Tab. 22 and Tab. 23 in Appendix A.

11.1.1 EMTP/ATP modelling of the network

The faults were simulated in a 110 kV unearthened radially operated network. The line parameters are the same as for Fingrid's Pyhäkoski – Rautaruukki line, Tab. 17. The fault distance varies between 10 and 100 km in a 100 km long line. The model also includes a connected line, i.e. a line connected to the substation. The length of this connected line is 0, 70 and 300 km. The Clark line model of the network can be seen in Fig.

71, and the symmetrical component model in Fig. 70. The position of the generator, which operates at power frequency, can be located in the positive sequence network or, as is shown here, at the fault location. Note that in the simulations the circuit in Fig. 70 is modelled so that each 10 km of the faulty line represents one pi-section. The faulty line then consists of ten connected pi-sections. The connected lines are modelled as one pi-section for the 70 km line and three for the 300 km line, each segment having 100 km.

The symmetrical component model, Fig. 70, generates charge transients similar to those for the Clark line model, Fig. 71. The results can then be compared.

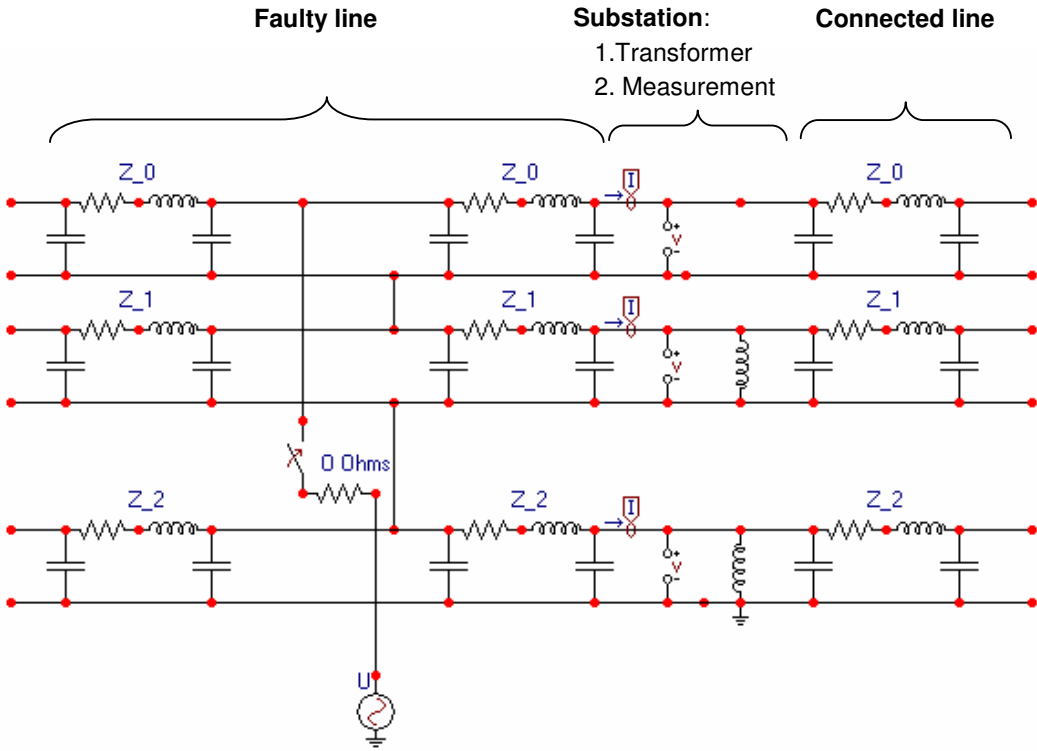


Fig. 70 Model of the network with single-phase to ground fault, using symmetrical components.

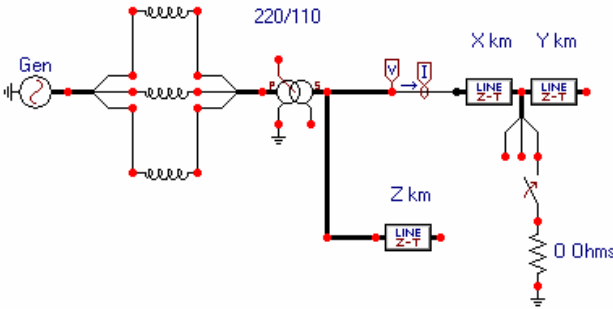


Fig. 71 Schematic diagram of the network; modelled with the distributed transposed Clark line model.

11.1.2 Correction factor definition

The fault distance can be computed with a correction factor C_f :

$$C_f = \frac{l}{l'} \quad (52)$$

where l is the exact fault distance and l' is the calculated fault distance.

11.1.3 Comparison of the Clark network model with the symmetrical component model

The first case is without a connected line. As the simulations show, both models give exactly the same results along the line (10-100 km). The correction factors calculated for both are almost the same, in the range 1.1 to 2.3, Fig. 72. The correction factor is not a constant along the line. It decreases with the fault distance and is strongly dependent on the fault position.

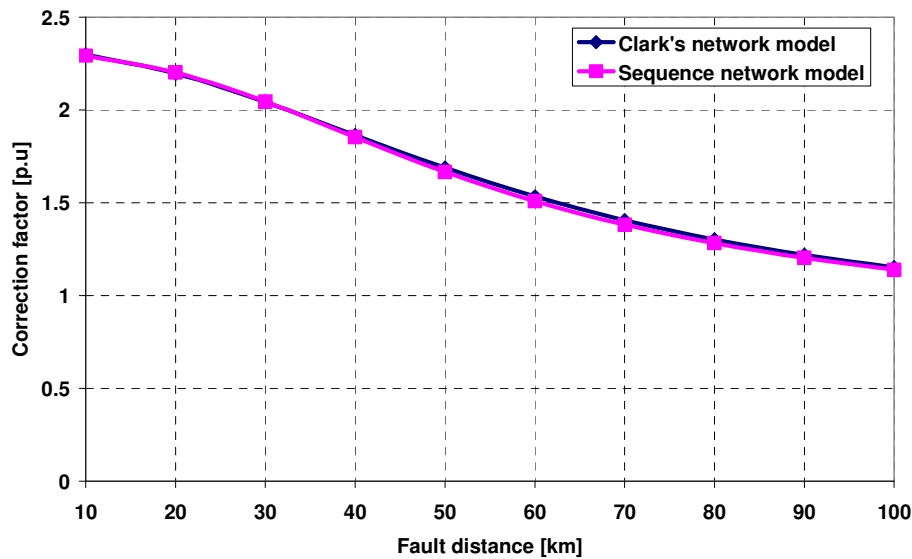


Fig. 72 Correction factors for fault location using the charge transient calculated for the symmetrical component model and Clark line model by the wavelet algorithm with wavelet filter. The length of the connected line is 0 km.

Next a connected line of 70 km was added to the feeding busbar. Again there is a strong correlation between the correction factors of the two models, Fig. 73. However, the correction still depends on the fault distance. It is in the range 1.6 to 1.05, which is smaller than in the previous case.

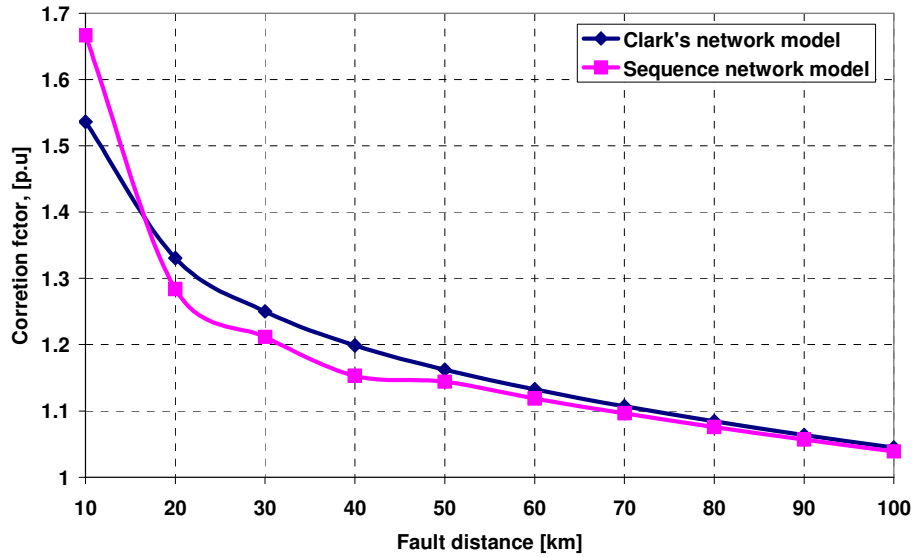


Fig. 73 Correction factors for fault location using the charge transient calculated for both the symmetrical component and Clark line models by the wavelet algorithm with wavelet filter. The length of the connected line is 70 km.

Finally, a connected line of length 300 km was added. Both models gave very close results. Surprisingly, the correction factor is almost equal to one and does not depend much on fault position. This is different to the previous cases. So, for long connected lines the correction is not needed for any place in the network because it is almost equal to one.

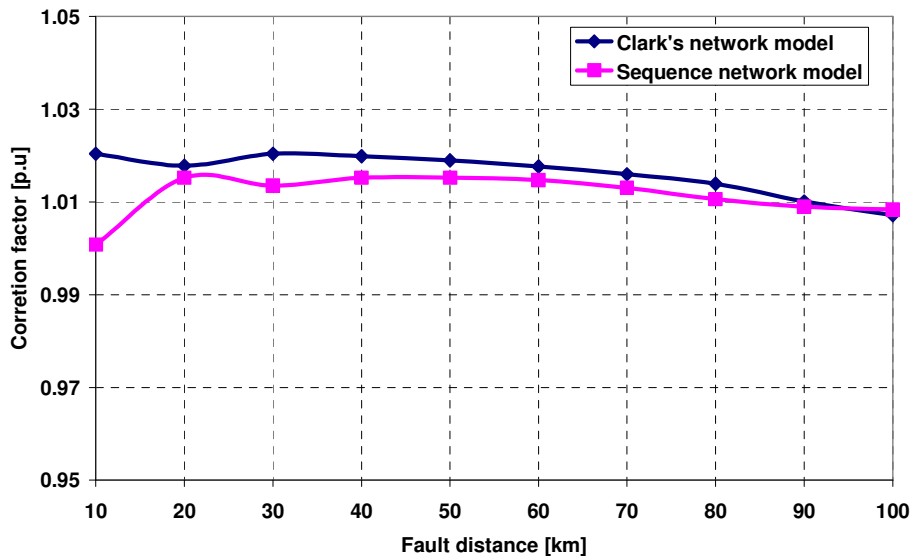


Fig. 74 Correction factors for fault location using the charge transient calculated for the symmetrical component and Clark line models by the wavelet algorithm with wavelet filter. The length of the connected line is 300 km.

11.2 Evaluation of a correction factor for transient based fault location

The accuracy of transient based fault location in a network with an isolated neutral varies due to several factors. Some influential parameters are defined by the line, power transformer, measurement, load condition, etc. The network configuration and fault position are investigated in this section. The aim is to show under which circumstances the method works accurately and under which conditions inaccurately. The critical area where the correction factor is needed is shown and its calculation is proposed. The study was made over a large number of faults. Altogether 1100 faults were simulated.

What follows is an example of how fault location in a network with an isolated neutral can vary with fault distance and the length of the connected line. The example is taken from the previous section. The calculated correction factors are plotted in Fig. 75. It is clear that the correction factor decreases with the length of the connected line. For a long line it will reach 1. In practice this is achieved by a connected line of 300 km, as seen from the example. However, for shorter lines the correction factor is higher than 1 and varies with the fault position. It is essentially this phenomenon that is analysed in this section.

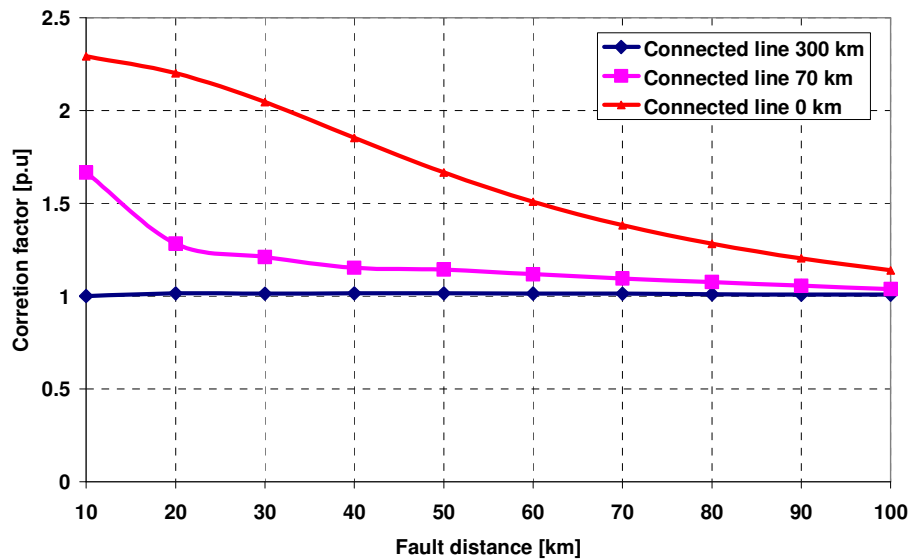


Fig. 75 Correction factors for fault location using the charge transient calculated for both models, the symmetrical component model and the Clark line model, by the wavelet algorithm with wavelet filter. The length of the connected line is 0, 70 and 300 km.

11.2.1 Data acquisition

The ground faults were simulated in EMTP/ATP and then processed by the fault locator developed in Chapter 13. Both of them are controlled automatically by Matlab without any human intervention. Therefore, it was possible to perform a large number of simulations.

11.2.2 EMTP-ATP model

The faults were simulated in a 110 kV network, Fig. 71. The line parameters match those of Fingrid's Pyhäkoski – Rautaruukki line, Tab. 17. Several cases were simulated. The length of lines x , y and z were changed by the program and the fault distances calculated.

11.2.3 Error source

The error source in a network can be understood from its symmetrical component model, Fig. 70. The most influential parts are:

1. Fault distance
2. Line behind the fault
3. Connected lines

The correction idea is based on the symmetrical component model. If the network parameters do not change over the line, the division of the current between the two line sections will be a function of their lengths only. Therefore, a correction factor might also be based on this principle.

Fault distance

The faults were simulated at the end of the line, which means the fault distances were also the length of the line. This distance was varied from 0 to 200 km. There were no connected lines. The distances y and z were equal to zero, Fig. 71. The error in the fault location in such cases grows linearly with the fault distance (line length), Fig. 76. The approximate analytical solution for the error is:

$$\delta_1 = 1.5 + \frac{x}{8} \text{ [km]} \quad (53)$$

where x is the fault distance. In this particular case there is no path for the zero-sequence current to be closed via the transformer since the network has an isolated neutral. Therefore, the fault distance must be corrected by $3/2$. Eq. (53) already includes this term.

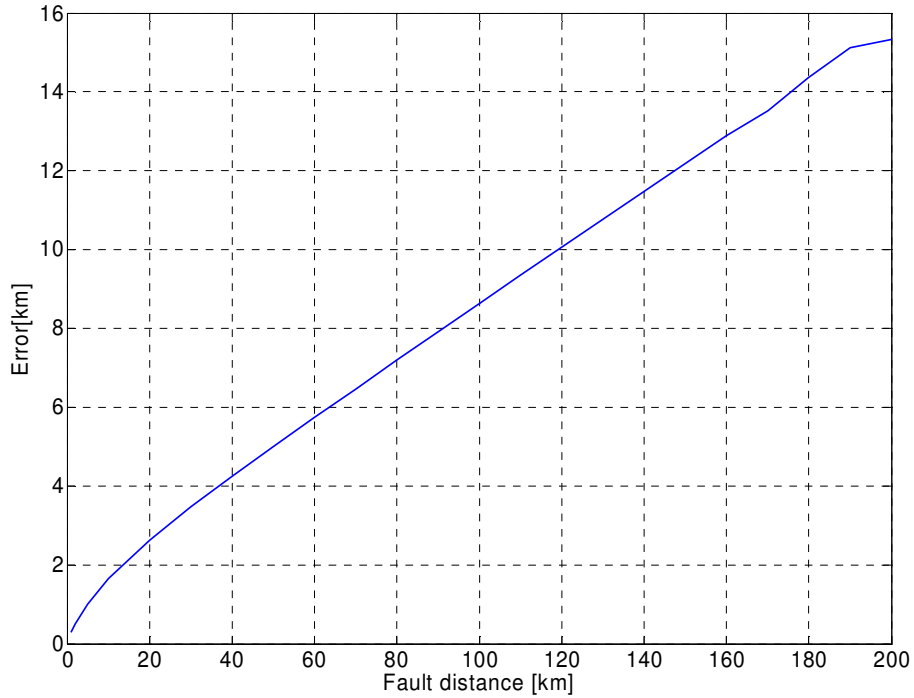


Fig. 76 Error in the fault location using the charge transient versus fault distance. The computation was made by the wavelet algorithm with the wavelet filter. The fault was simulated at the end of the line. There were no connected lines.

Line behind the fault

It was recognised from experiences with simulations that the length of the line behind the fault (from the fault point to the other end of the line) has an important impact on fault location. Therefore, this phenomenon is now treated independently. The fault simulations were performed for a network similar to that in Fig. 71, where $z=0$ km.

The main impact on fault location is given by the zero-sequence part of the line behind the fault. This is obvious from the symmetrical component model in Fig. 70, because it is an isolated network. (The positive and negative sequence inductances of the lines are connected via the low impedances of the transformer, but the zero sequence inductance of the line is not connected if there are neither connected lines nor low grounding impedance. Moreover, some zero-sequence current will flow to the part of the line behind the fault instead of the fault section). The longer the line connected behind the fault, the less the zero-sequence current that will flow to the faulted line section and the greater the error in the fault location, Fig. 77(solid lines).

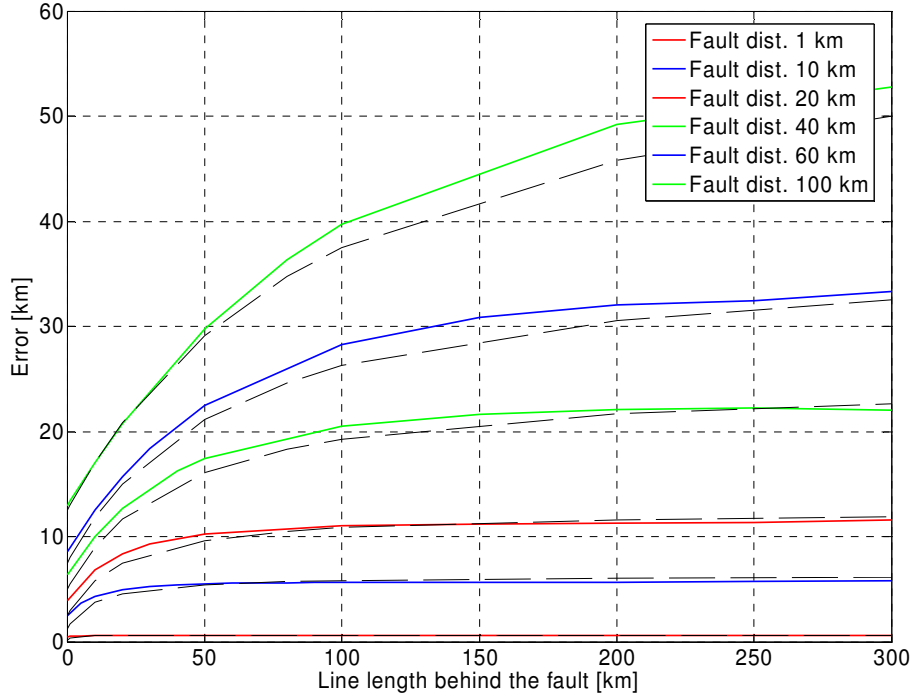


Fig. 77 Error in the fault location using the charge transient with the line length behind the fault. The computation was made by the wavelet algorithm with the wavelet filter. There were no connected lines. Error from simulations (solid lines), the correction (dashed lines).

A fault transient will divide into two parts at the fault point: one goes to the supply substation via the faulted line section and the other goes to the line section behind the fault, Fig. 70. The error in the fault location is a parallel combination of the two parts of the line, x and y , together with the error δ_1 , caused by the fault distance:

$$\delta_2 = \delta_1 + \frac{\frac{x}{2} \frac{y}{2}}{\frac{x}{2} + \frac{y}{2}}, [\text{km}] \quad (54)$$

where x is the fault distance and y is the line length behind the fault, according to Fig. 71. The accuracy of this estimation is relatively high. A comparison of the simulated and calculated error is in Fig. 77 (compare the solid and dashed lines).

Connected lines

There is a lack of zero-sequence current measurement in the case of an isolated network, as mentioned earlier. The calculated fault distance can be corrected by a correction factor equal to $3/2$. However, in a case where there are connected lines, there exists a path for the zero-sequence current to return via the measurement point and be measured as well, Fig. 71. So, the correction can no longer be $3/2$. In order to simulate only the influence of the connected line, the fault was placed at the end of the line. The error in the fault location decreases with the length of the connected line, Fig. 78 (solid lines).

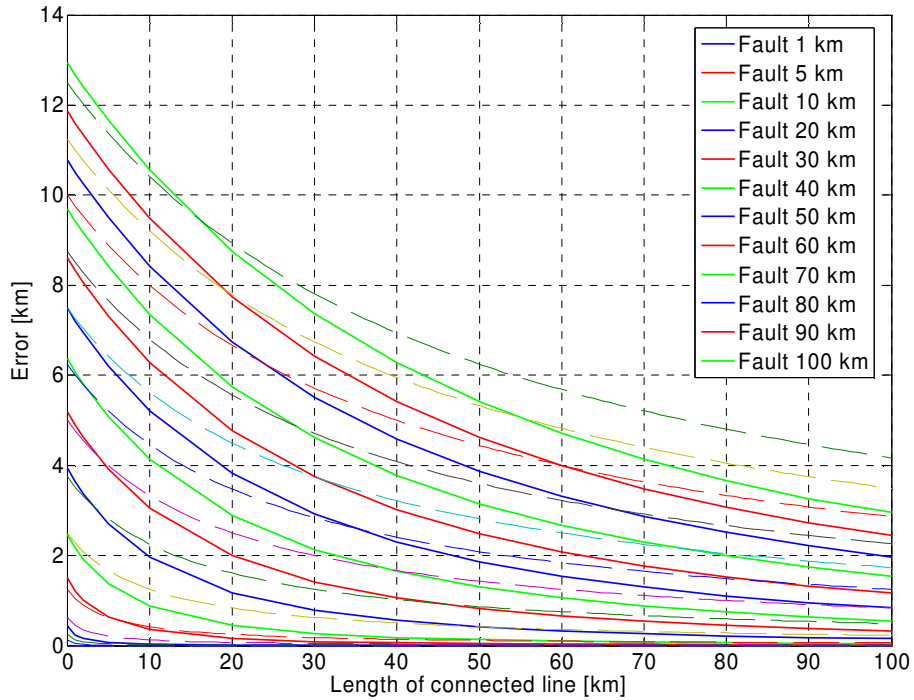


Fig. 78 Error in the fault location using the charge transient versus the length of connected line. The computation was performed using the wavelet algorithm with the wavelet filter. The fault was simulated at the end of the line. Error from simulations (solid lines), the correction (dashed lines).

The error term in the case of connected lines is:

$$\delta_3 = \frac{\frac{x}{2}}{z + \frac{x}{2}} \text{ [p.u]} \quad (55)$$

where x is the fault distance and z is the length of the connected lines. A comparison between the error from the simulations and the calculated errors is shown in Fig. 78

(compare the solid and dashed lines). In this particular case the fault distance was also the length of the faulty line. In a real case there is always some part of the line behind the fault point. Therefore, instead of x , the fault distance, the length of the entire fault line must be considered in Eq. (55), i.e. $x \rightarrow x + y$.

11.2.4 Comparison of designed correction factor with simulations

The fault location accuracy was studied for a large number of fault cases. Altogether some 1100 faults were simulated in EMTP/ATP and then processed by the fault locator. The error in this fault location method is now compared to the error calculated by the correction factors proposed in the previous section.

The ground faults were studied in a network of length 100 km, Fig. 71. The part of the line behind the fault is always $100 - x$, where x is the fault distance. The fault distance was varied from 5 to 95 km in steps of 5 km in the simulations. A connected line of length 5-300 km (with steps of 5 km) was added to the line. The impact of the connected lines is similar to the previous section – the error exponentially decreases, Fig. 79. The error dependence on fault distance is somewhat different from the previous case, however. This phenomenon is due to the fixed line length. There is increased noise in fault location for very long connected lines caused by the low frequency resolution in that area. The transient frequency changes less for long connected lines. Therefore, in order to reduce this noise a higher sampling frequency would be required (in this case it was 2.5 kHz).

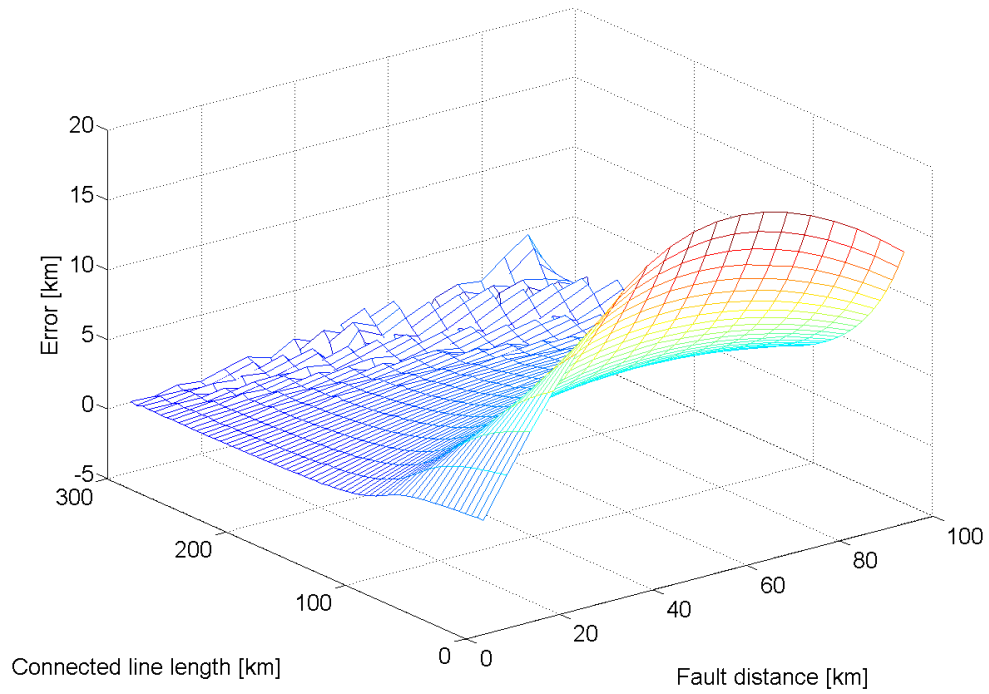


Fig. 79 Error in the fault location with length of connected line and fault distance. The graph contains 1080 simulated faults.

The estimation of the error is:

$$\delta_f = \delta_2 \delta_3 \text{ [km]} \quad (56)$$

The difference between the estimated error according to Eq. (56) and the error of the simulated cases is very small; compare Fig. 80 to Fig. 79. The increased inaccuracy is only for the shorter connected lines, see Fig. 81.

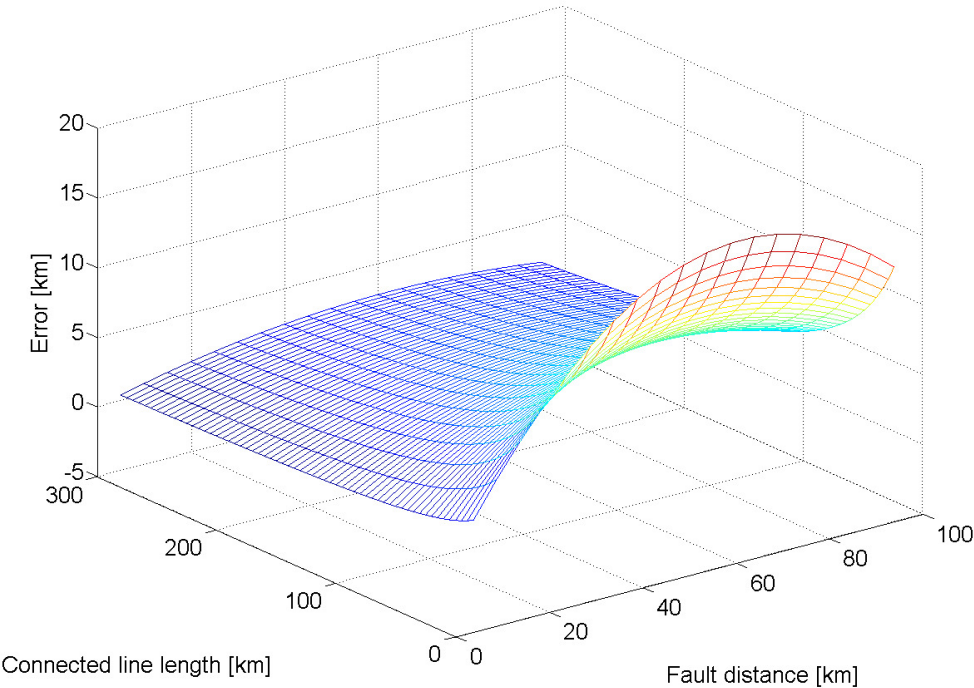


Fig. 80 Error correction term in Eq. (56) versus length of connected line and fault distance.

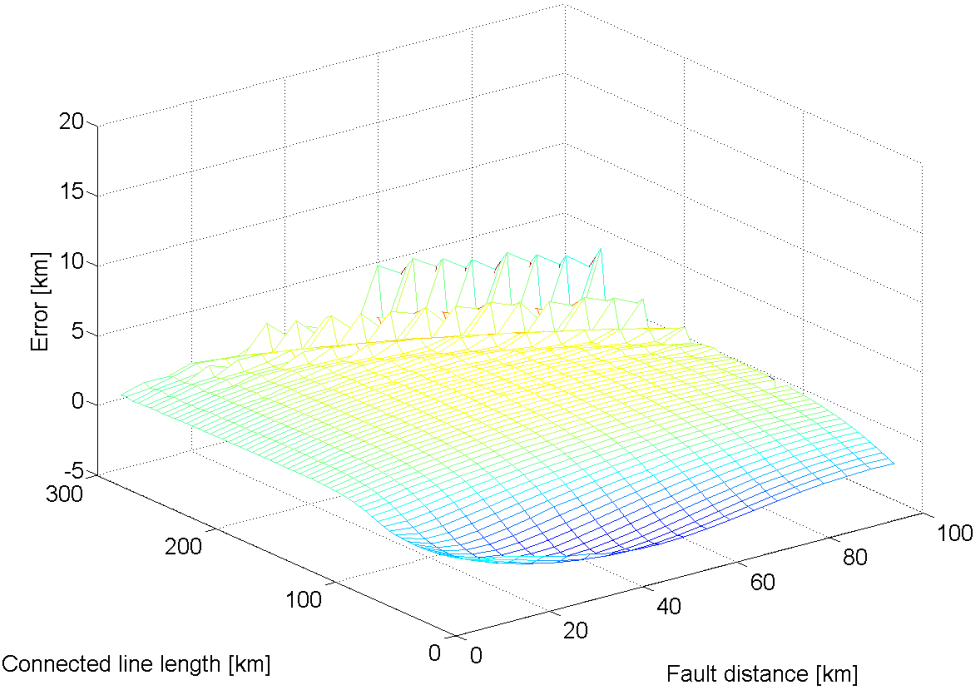


Fig. 81 The remaining fault location error after the application of Eq. (56) versus length of connected line and fault distance.

11.3 Impact of the neutral grounding on fault location accuracy

The analysis in the previous section was performed in a network with an isolated neutral. For comparison, the influence of compensation or low-reactance grounding is shown in this section. The same network that was used in the previous section is analysed here, with a connected line of length 300 km. The results computed by the two different methods, the wavelet algorithm, Fig. 82, and differential equation algorithm, Fig. 83 show very small errors. As seen from the pictures the accuracy of computation does not depend on the impedance of the neutral grounding at all. The error in both methods is comparable for isolated, compensated or low reactance grounded network neutrals. The generated transients are almost independent of the neutral grounding as was also shown in Section 8.4. The neutral grounding is important for the fundamental frequency, but not for the transients, mainly because of their higher frequency, Section 5.1. However, in this test the frequency of the transient varied between 150 and 110 Hz and was low because of the long connected line.

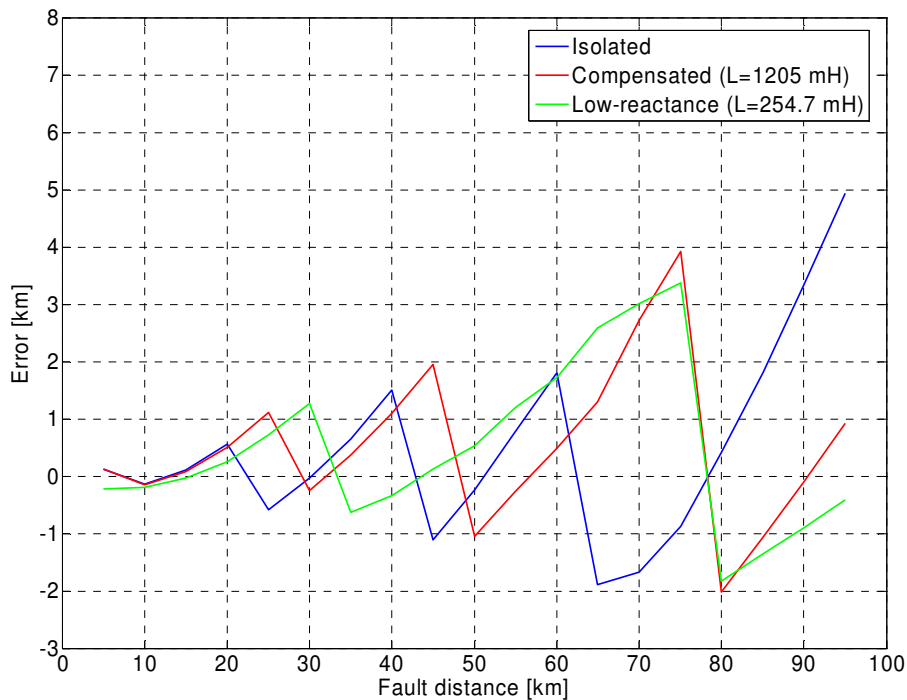


Fig. 82 Error in the fault location using the charge transient versus the fault distance. The computation was made by the wavelet algorithm with the wavelet filter. The different types of neutral grounding form the parameters.

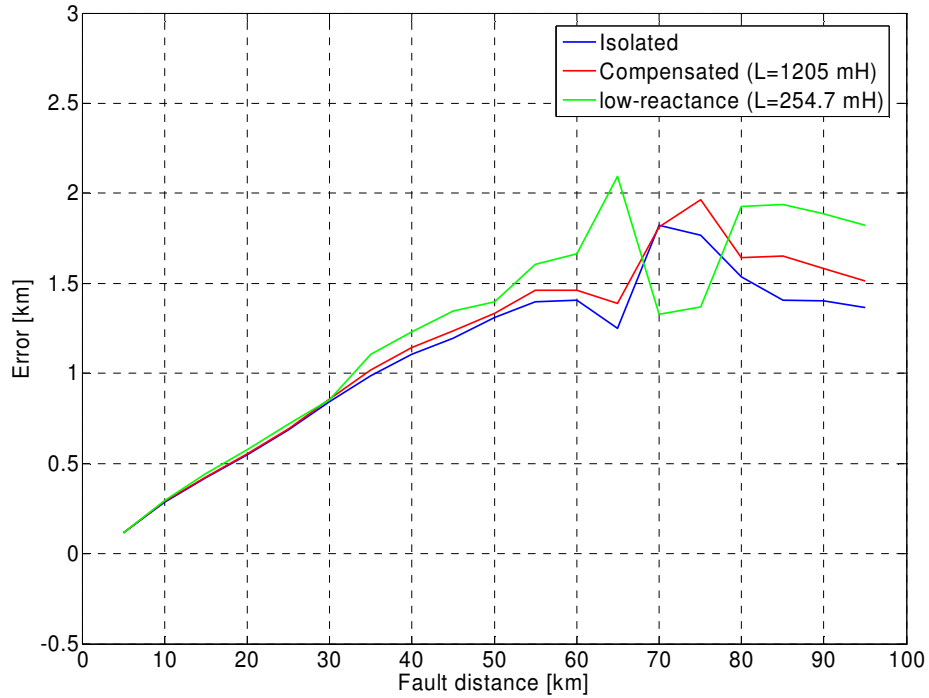


Fig. 83 Error in the fault location using the charge transient versus the fault distance. The computation utilised the differential equation algorithm. The different types of neutral grounding form the parameters.

By comparing the two figures it can be seen that the wavelet algorithm is more sensitive to the transient frequency estimation than the differential equation algorithm. However, the oscillation of the error is around zero, and its variation can be radically decreased by a higher sampling rate.

11.4 Error estimation for the transient based ground fault location

There are many factors influencing fault location accuracy based on transients. Estimation of the error of the most influential factors is shown in Tab. 6.

Tab. 6 Error estimation for transient based ground fault location.

Source of error	Estimated maximum error	Comment
Measurement		
Current transformer	3.5%	Fig. 54 up to 1 kHz
Voltage transformer	4%	Fig. 48 up to 1 kHz
Sampling frequency *)	5%	Fig. 82 for 2.5 kHz for WA
Signal processing	0%	Discussion, Section 7.5
Fault conditions		
Fault resistance***)	0%	Fig. 36 up to 100 Ω
Connected lines and line sections behind the fault	4.5%	Fig. 81 for shorter connected lines
Line model inductance**)		
with frequency	1%	Fig. 69a for 100-300 Hz
with ground resistivity	5%	Fig. 69a at 200 Hz
Sum	23%	
Geometric mean value	10%	

Note:

*) The presented value of 5% is for the wavelet algorithm. A slightly lower value of 2% applies to the differential equation algorithm, Fig. 83

***) The values are presented for the most typical line construction in Finland (e.g. overhead ground conductors made of aluminium).

***) The fault resistance is not a primary source of error. It simply damps the signal. In the studied case the error in fault location was the same for fault resistances in the range 0 to 100 Ω . In this range the error was determined by other factors.

In the worst scenario the error arises from the maximum error of each contributor, and would be as much as 23%. However, this is highly unlikely, because each element does not always have the maximum error and the error sources may cancel each other to some extent. Therefore, the geometric mean value is more informative. This value is around 10%. It must be stressed that even this value is overestimated. Most likely, better results would be achieved with a higher sampling frequency (see the discussion in Section 8.6). Connected lines, which almost always exist in Finnish 110 kV networks, also improve the results.

11.5 Discussion

Comparison of models

In this chapter the two different models for ground faults were compared, the line model (distributed transposed Clark line model) in EMTP/ATP and the symmetrical component model. The two models gave very close results for different fault conditions. The error in both models has probably the same reason. Therefore, it is possible to base the correction factor on the symmetrical component analysis, which then should also apply to the line model.

Correction factor

A ground fault in a network with an isolated neutral was simulated. In a single line a correction will always be needed because of the lack of a zero-sequence measurement in the substation. The existence of connected lines makes the necessary path for the zero-sequence current in the substation, which improves the fault location. The same applies for all signals including the 50 Hz component; refer to the discussion in Chapter 4.

The study of a large number of ground faults has been performed in this chapter. The area that can be accurately estimated by the fault location algorithms without any correction has been identified. This applies in networks with long connected lines (more than 100 km if the faulted line is 100 km) and shorter line sections behind the fault. Secondly, a correction factor based on a symmetrical component representation of the network has been proposed, the accuracy of which is satisfactory.

There are several outgoing lines from most of the substations at the 110 kV level in Finland. Therefore, the faulty line would probably have enough length of connected lines and hence the correction factors will be low for Finnish conditions.

Different neutral treatment

The network neutral mainly affects the fundamental frequency component. The charge transient generation, theoretically described in Section 5.1 for an isolated network, can also be generated in networks with other neutral configurations. The charge transient seems to be the same and hence the fault location accuracy is about the same for low-reactance and compensated network neutrals as in an isolated network.

Error in the transient based fault location method

The error in transient based ground fault location for Finnish 110 kV lines using the charge transient is about 10 %.

12 Transients in real networks

The ground fault charge transients from a real network are presented in this chapter. The fault location methods were applied to fault transients recorded in 400 kV, 110 kV and 20 kV lines.

The signal processing is performed in two steps as described in Chapter 7. First the pre-processing is done in order to detect the transient frequency more accurately and then the wavelet filter is applied.

1. Digital band-pass FIR filter
2. Charge transient frequency detection
3. Wavelet filter

Then the two methods of fault location are applied.

1. Wavelet algorithm
2. Differential equation algorithm

All signal processing and fault distance estimation were performed by the fault location program that will be presented in Chapter 13.

12.1 Faults in the 110 kV Pyhäkoski – Rautaruukki line

All data used were recorded in Fingrid's 110 kV network with the neutral grounded via low reactance reactors. The sampling frequency was 1 kHz. Altogether, 6 cases were processed. Not all the faults were permanent; therefore the exact positions of the faults were calculated by a travelling wave fault locator connected in parallel with the transient recorder. The faults occurred in the Pyhäkoski - Rautaruukki branch, Fig. 102 in Appendix A. Some results from this analysis have also been presented in [33].

A case from 1.9 2002, where the fault distance was 25.8 km, is shown in the following figures as an example. Fig. 84, shows the recorded phase voltages and currents. As can be clearly seen the fault current was of high magnitude. There was a charge transient of very short duration starting from 200 ms and lasting about 20 ms.

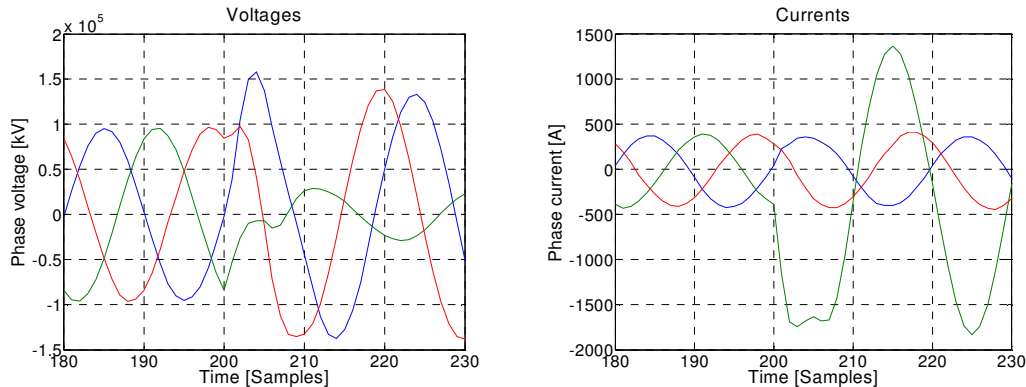


Fig. 84 The recorded single-phase to ground fault: phase voltages (left) and currents (right). Case: 1.9 2002.

The frequency of the charge transient was 166.6 Hz. The wavelet algorithm gave the result shown in Fig. 85. The exact fault distance was taken from the stable part of the fault distance curve where the transient exists. The results of the differential equation algorithm applied to the example signals are also shown in Fig. 85. As can be seen, the stable part of the curve indicates the fault distance. Detailed data can be found in Appendix A.

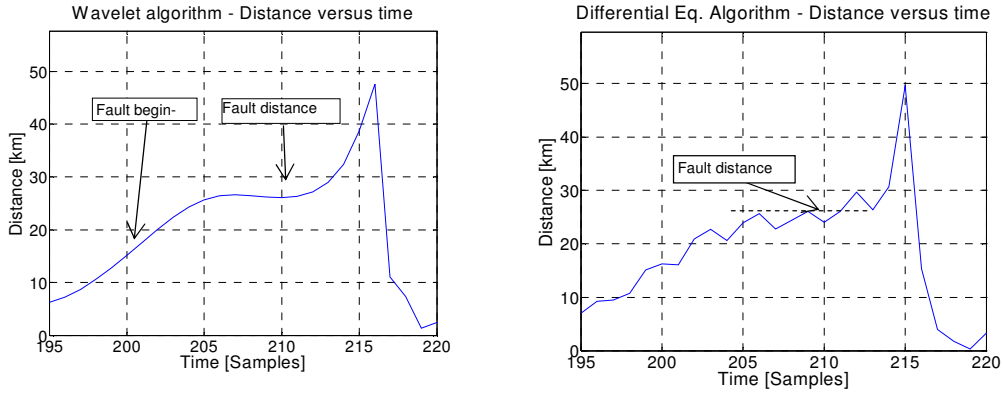


Fig. 85 Fault distance curve for the wavelet algorithm (left), and differential equation algorithm (right). Case: 1.9 2002.

A comparison of both methods can be better seen in Fig. 86. Both methods work very well up to 50 km of the line length. Similar behavior can be seen in Fig. 14 in Chapter 4, where the same recording was analyzed by the conventional methods. The sudden change in accuracy might therefore be caused by the parallel line, which runs parallel to the faulty line for approximately 30 km, see the schematic diagram of the network in Fig. 102 in Appendix A.

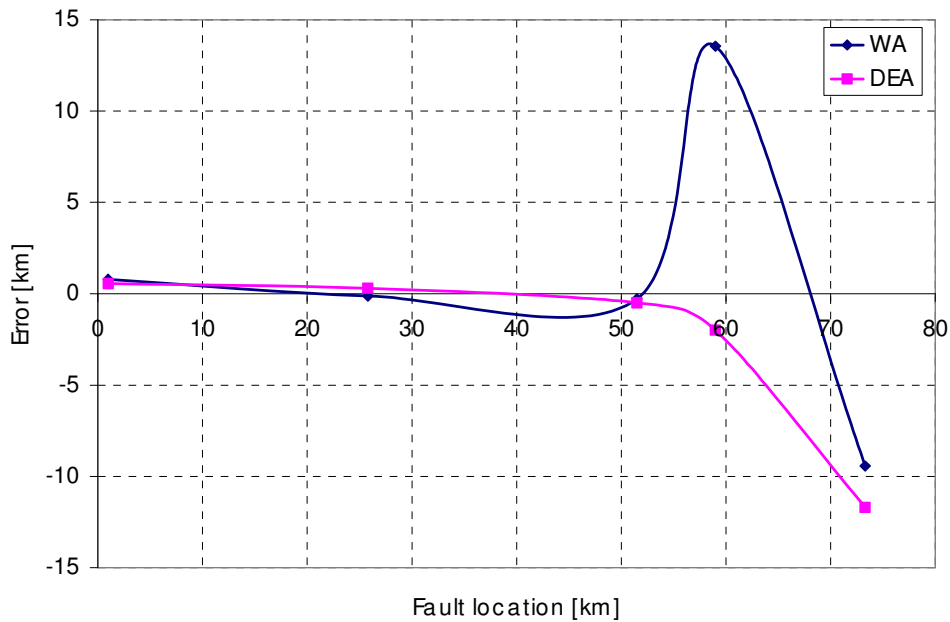


Fig. 86 Transient based fault location using the charge transient. Wavelet algorithm (WA), Differential equation algorithm (DEA).

12.2 Faults in the 400 kV Alapitkä – Huutokoski line

Single-phase to ground faults were recorded in the 400 kV Fingrid network. The fault distance in study case 270703 was 28.1 km. This network is solidly grounded with numerous connected lines. The sampling frequency was 12.8 kHz. The phase voltages and currents, and neutral current were measured in the Alapitkä substation.

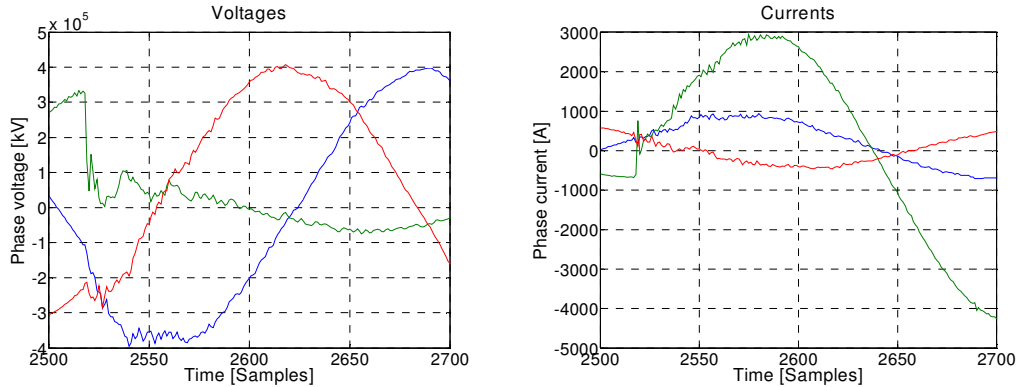


Fig. 87 The fault voltage (left) and current (right). The frequency of the fault transient was 512 Hz. The exact fault distance was 28.1 km

The fault distances calculated using the charge transient with the wavelet algorithm using the phase and neutral currents are in following figures.

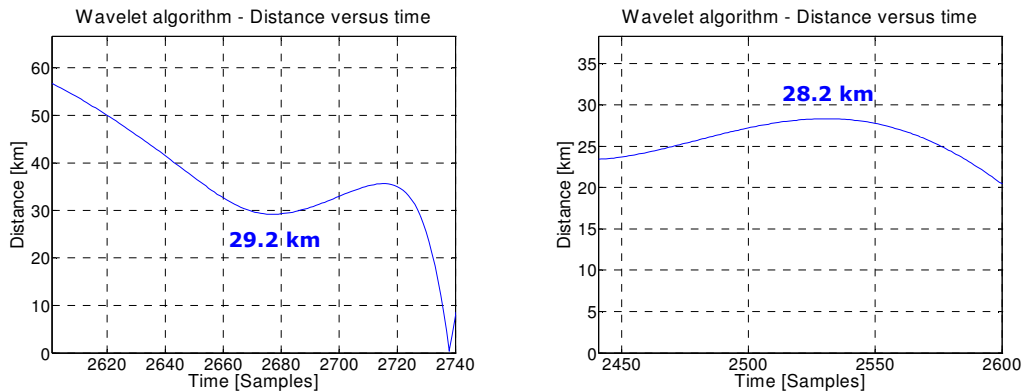


Fig. 88 The fault distance calculated using the phase current (left) and the neutral current (right). The fault distances were calculated by the wavelet algorithm. The exact fault distance was 28.1 km.

For comparison, the conventional method in this case located the fault as follows:

1. Phase current: 28.09 km
2. Neutral current: 29.9 km

12.3 Faults in MV networks

MV network faults are presented in this section. Faults artificially made for study purposes were recorded in Vaasan Sahko Oy (VSOY) and Lounais-Suomen Sahko Oy (LSS) on 11 and 12 December and 19 and 20 June, 1990 by Matti Lehtonen. The 20 kV networks consist of overhead lines and have isolated, compensated or partially compensated network neutrals. The sampling frequency of the recordings was 20 kHz.

As an example, one single-phase to ground fault from an isolated neutral network, with fault distance 14.2 km (RTN45), will be presented. The fault voltage and current are shown in Fig. 89 and the results are given in Fig. 90.

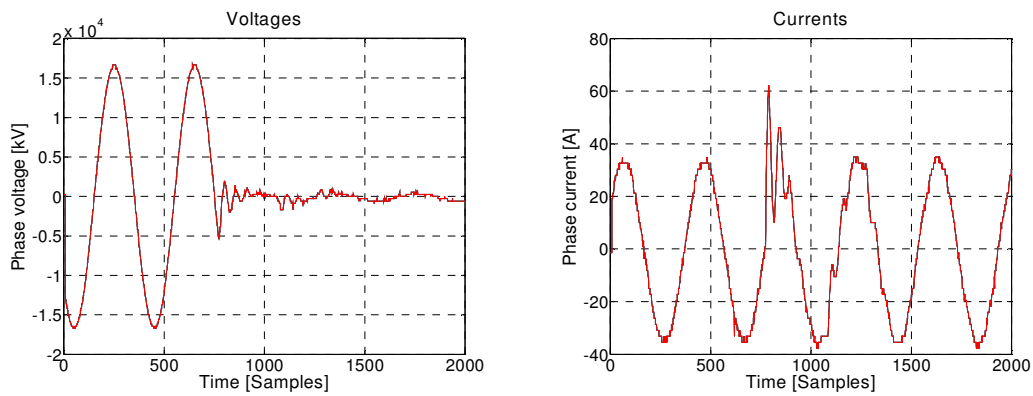


Fig. 89 The fault voltage (left) and fault phase current (right). Case RTN45, fault distance 14.2 km, $R_f=0 \Omega$. Isolated neutral network

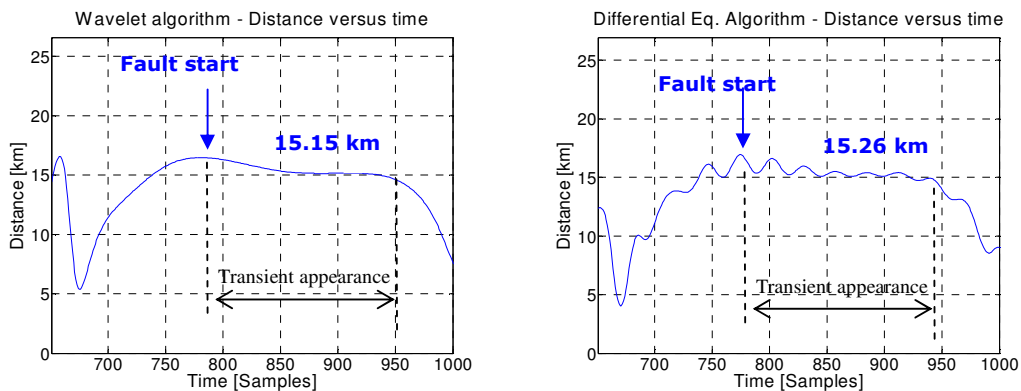


Fig. 90 The fault distance calculated using the charge transient with the wavelet algorithm and the differential equation algorithm. Case RTN45, fault distance 14.2 km, $R_f=0 \Omega$. Isolated neutral network

The charge transient of 371 Hz is of strong amplitude. The network has many connected lines, so there is a sufficient path for the zero-sequence current to be closed via the measurement point (even if the network neutral is isolated). The calculated fault distance is relatively accurate. More statistics from similar networks are presented in the following figures. The processing was made with the fault location program that will be shown in Chapter 13.

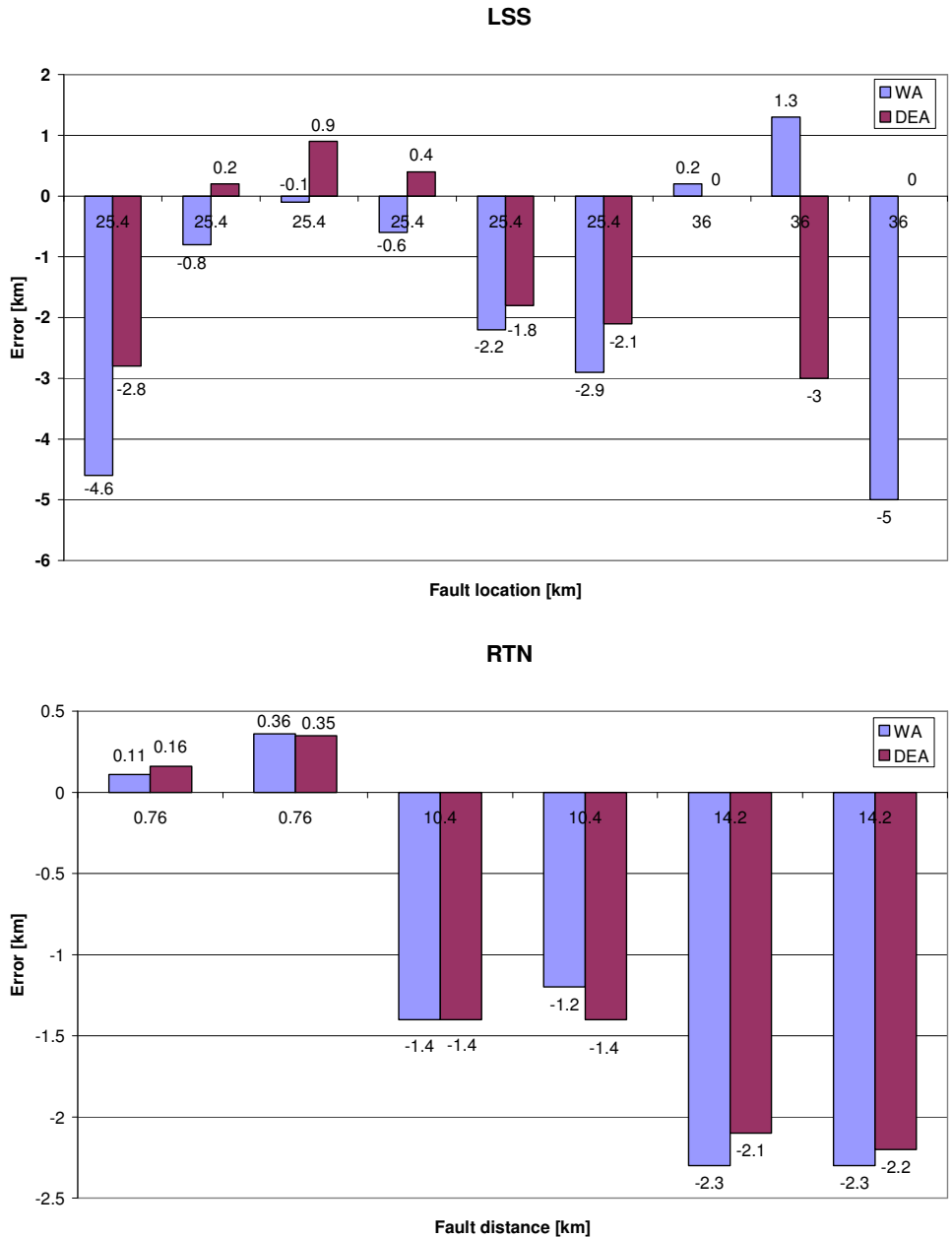


Fig. 91 Fault statistics from the MV network, showing the errors in the wavelet and differential equation algorithms. The LSS faults are from a partially compensated network. The RTN faults at 0.76 and 10.4 km occurred in a compensated network. The fault at 14.2 km was in an isolated network

12.4 Discussion

The location of ground faults at different voltage levels has been analysed in this chapter.

Faults on 110 kV and 400 kV lines

The single-phase to ground faults from the 110 kV and 400 kV networks are from networks with reactor grounding and solidly grounded neutrals, respectively. Therefore, these two can be compared quite reasonably. In these networks the accuracy is relatively high. In the case of a 400 kV line there are also many connected lines, which is favourable for fault location.

Ground faults in MV networks

The real “ground faults” were recorded in MV networks with an isolated, compensated or partially compensated neutral. The network has a lot of connected lines. The transients in an MV network are of relatively high amplitude. Therefore, fault location is easier. The reason is that the zero- and positive- sequence capacitances of the lines per km are much greater in MV networks than in HV networks.

Using the neutral current

In the case of a 400 kV fault, using the neutral current for fault location is almost as accurate as using the phase current.

Conventional method

In addition to the wavelet algorithm, the conventional methods were used for the 400 kV faults and some of 110 kV ground faults were calculated in Chapter 4. The accuracy is comparable, mainly because of the high ground fault currents due to the neutral grounding type.

13 Fault location program

A practical output of this research has been the development of a fault location program with a graphical user interface. The program was written in Matlab 7 and can also work outside matlab using the Matlab runtime version. A block diagram of the program with the basic data flow is shown in Fig. 92.

Data reading

The program can process both the EMTP/ATP simulations and the real fault recordings from Fingrid's recorders and can cope with various sampling frequencies, time lengths and data structures.

Transient methods

The frequency estimation of the fault transients was made with the Fourier transform following completion of the pre-processing. The pre-processing was performed with the sinc filter presented in Section 6.1. The transient based methods with the wavelet and differential equation algorithms based on the wavelet filter were implemented as described in sub-sections 7.3.2 and 7.3.3. The automatic detection of the fault distance works on the principle proposed in Section 7.4. The program preprocessing window can be seen in Fig. 95, the wavelet filter in Fig. 96 and the fault distance window in Fig. 97.

Conventional methods

The conventional and improved conventional methods, according to the descriptions in Sections 4.1 and 4.2 and the error estimation in Chapter 4.2.4, are programmed into the fault locator. The conventional algorithm window is shown in Fig. 98, with the de-noising wavelet based filter presented in Fig. 99.

Program settings

The line parameter calculations were made by a developed line constant program that uses the Carson formula presented in Chapter 10.5. The settings for the data reading and line parameters can be made for both the EMTP/ATP simulation and the real recorders. A recorder organizer allows the user to save the program settings for future use. The above mentioned settings can be seen in Fig. 100.

13. Fault location program

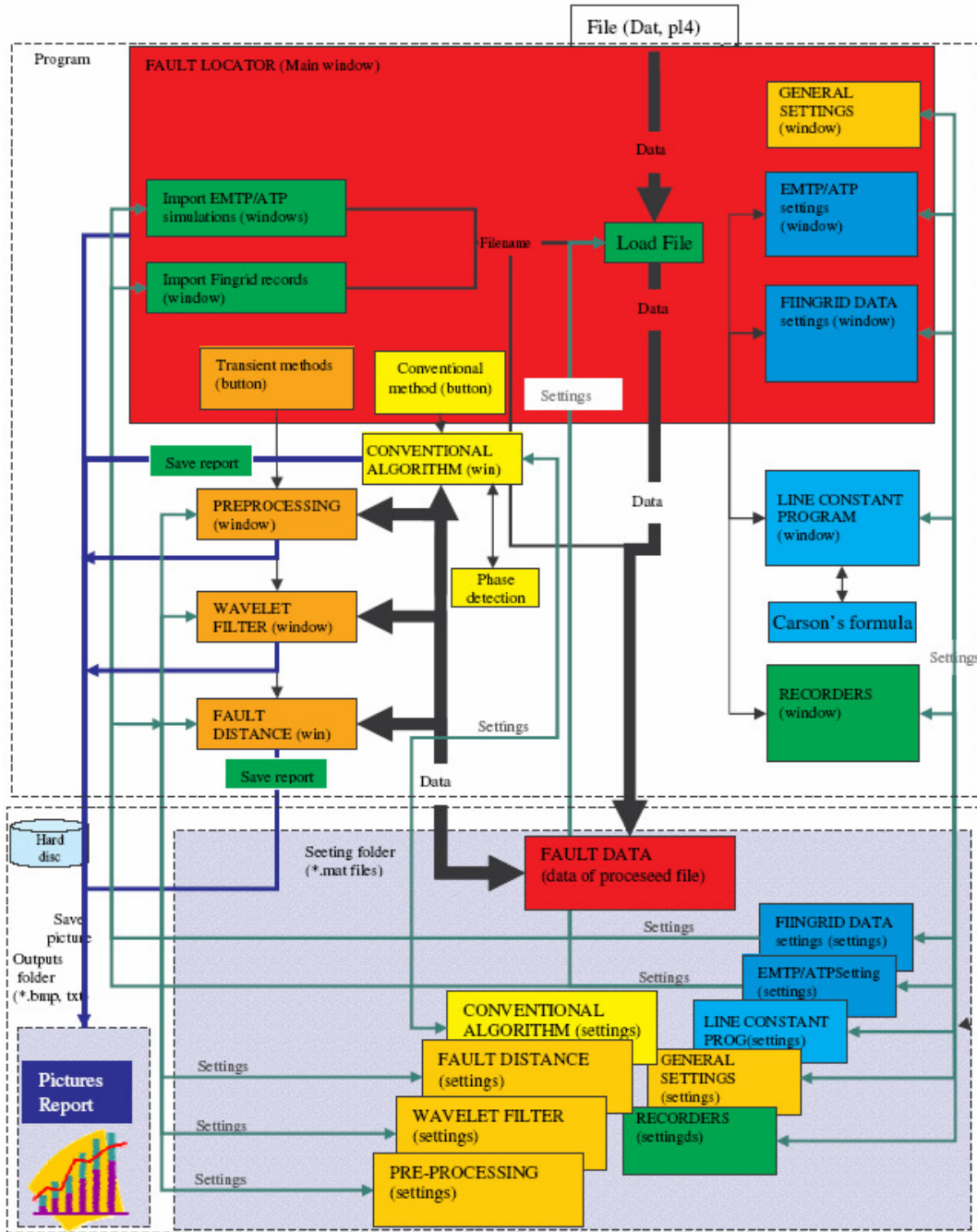


Fig. 92 Block diagram of the fault location program and basic data flow.

13. Fault location program

Main window

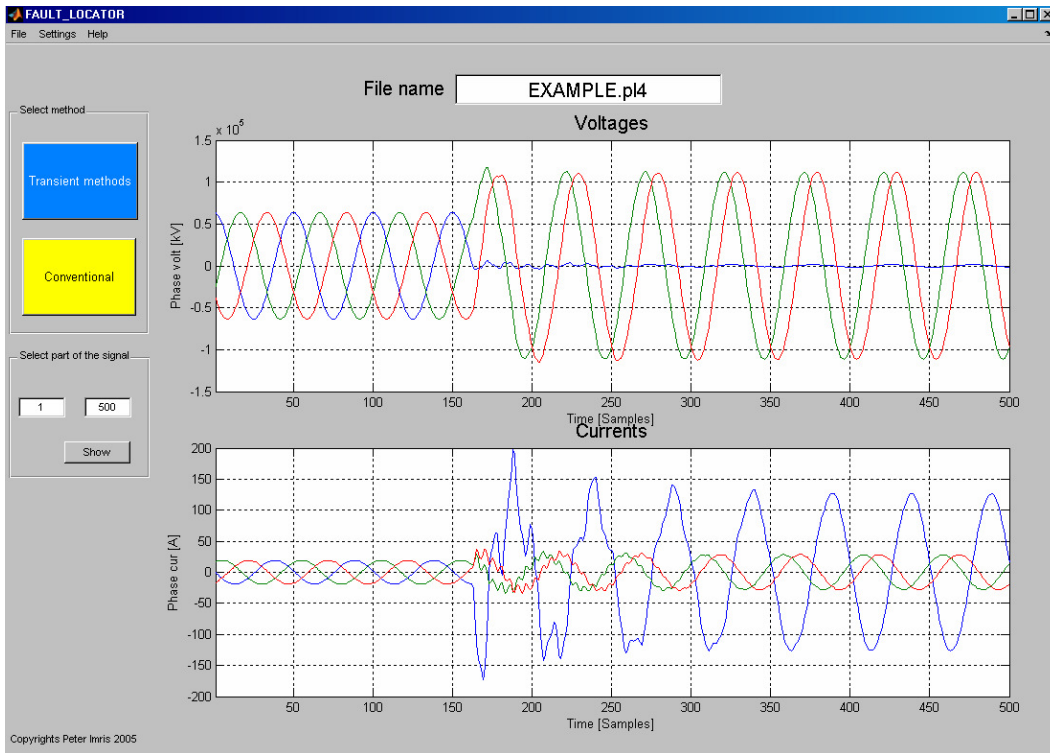


Fig. 93 The main window of the fault locator.

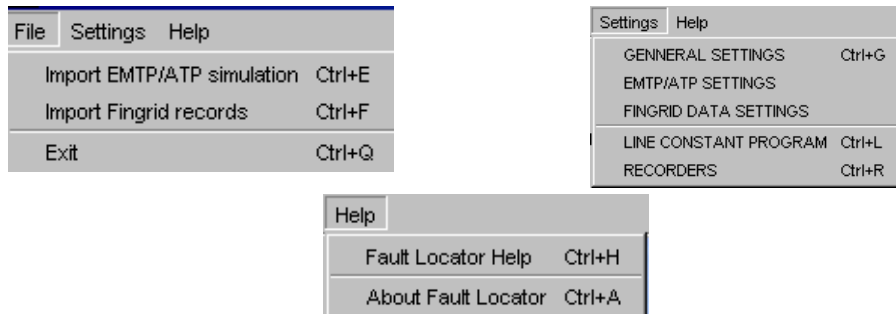


Fig. 94 Menu bar of the main window

13. Fault location program

Transient fault location

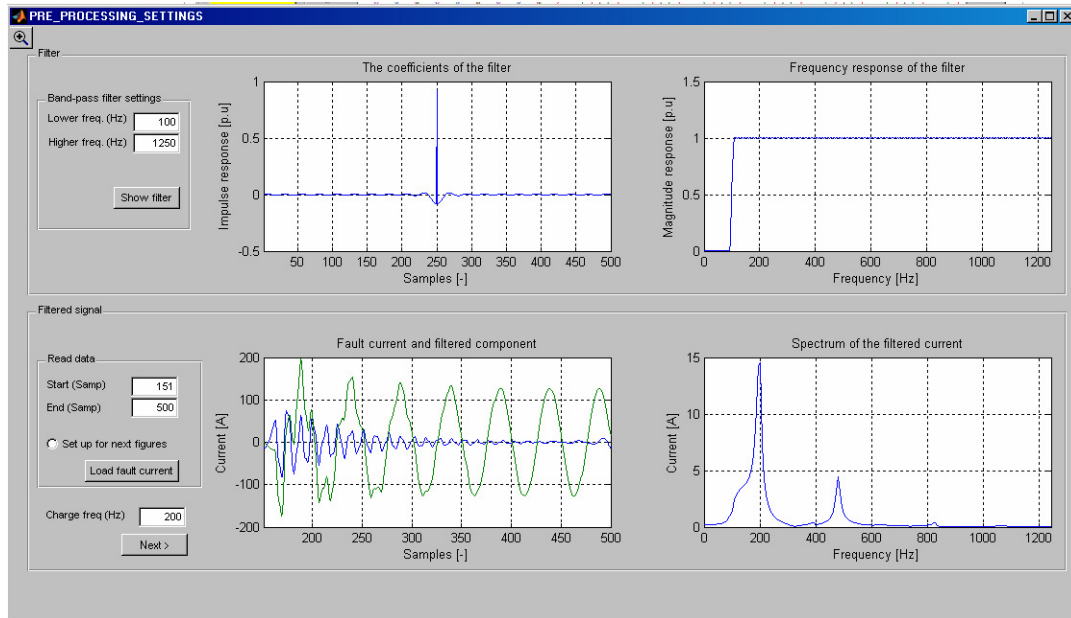


Fig. 95 The pre-processing.

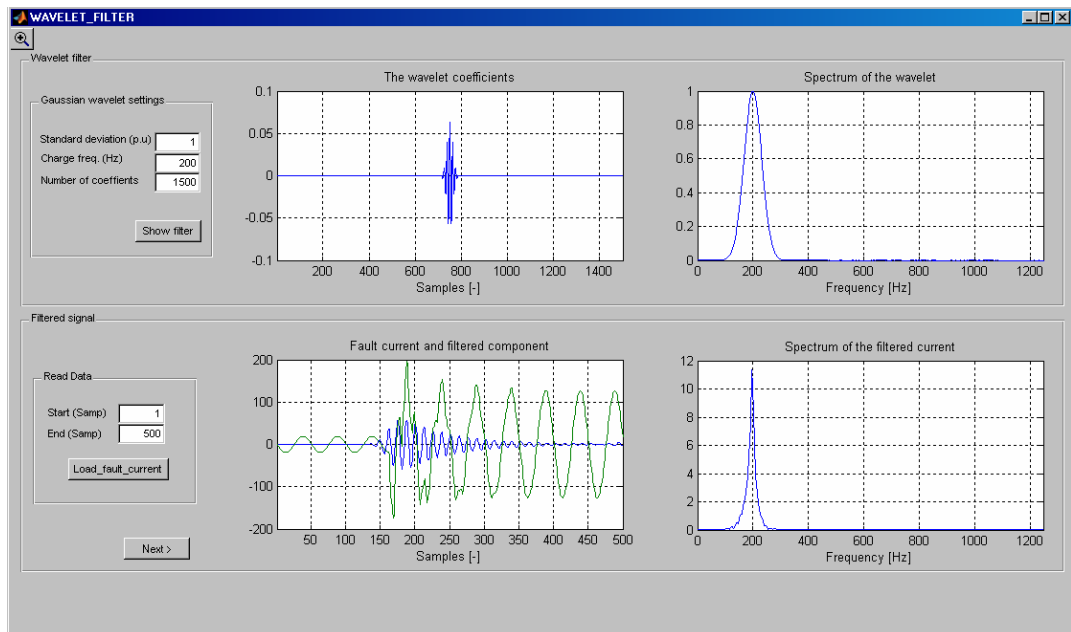


Fig. 96 The wavelet filter.

13. Fault location program

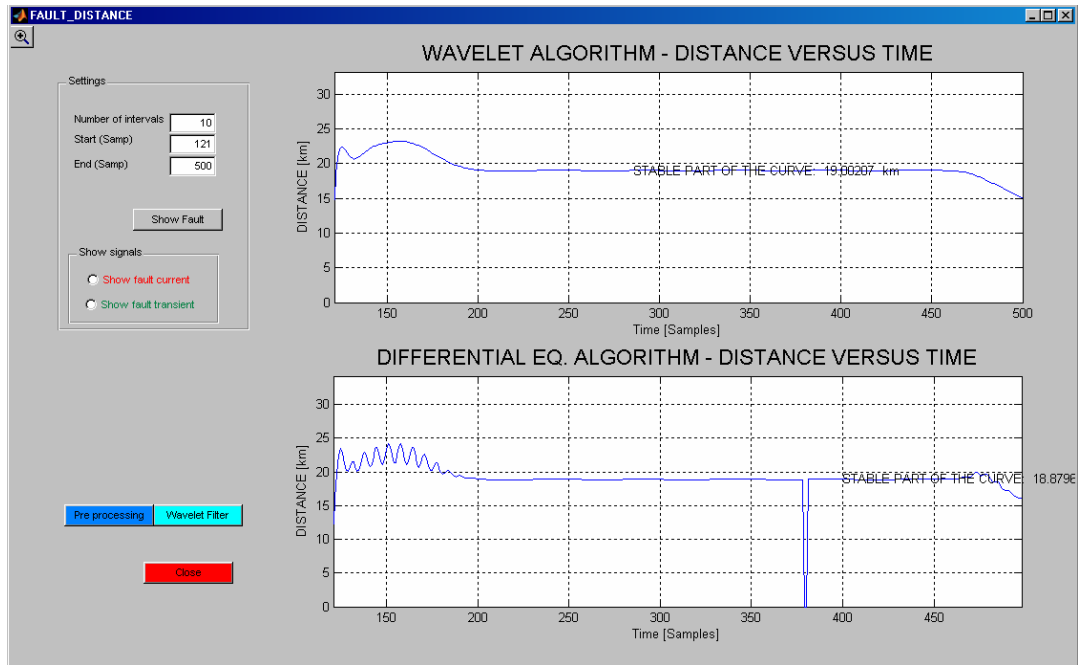


Fig. 97 Transient based fault location algorithms.

13. Fault location program

Conventional fault location

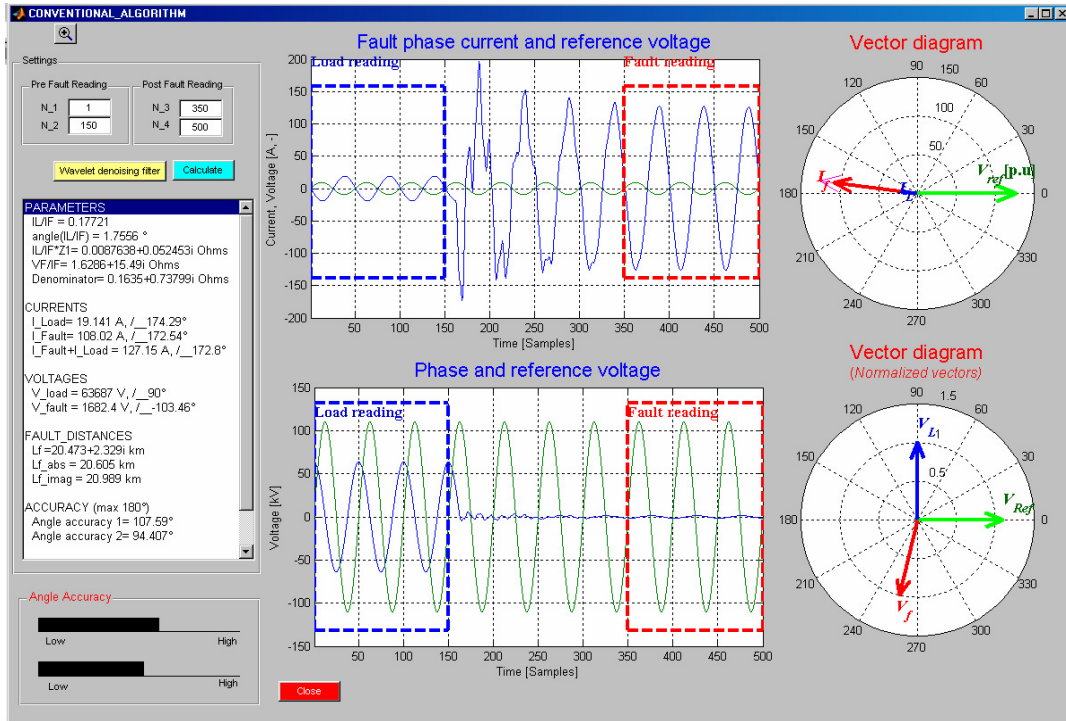


Fig. 98 Conventional algorithm.

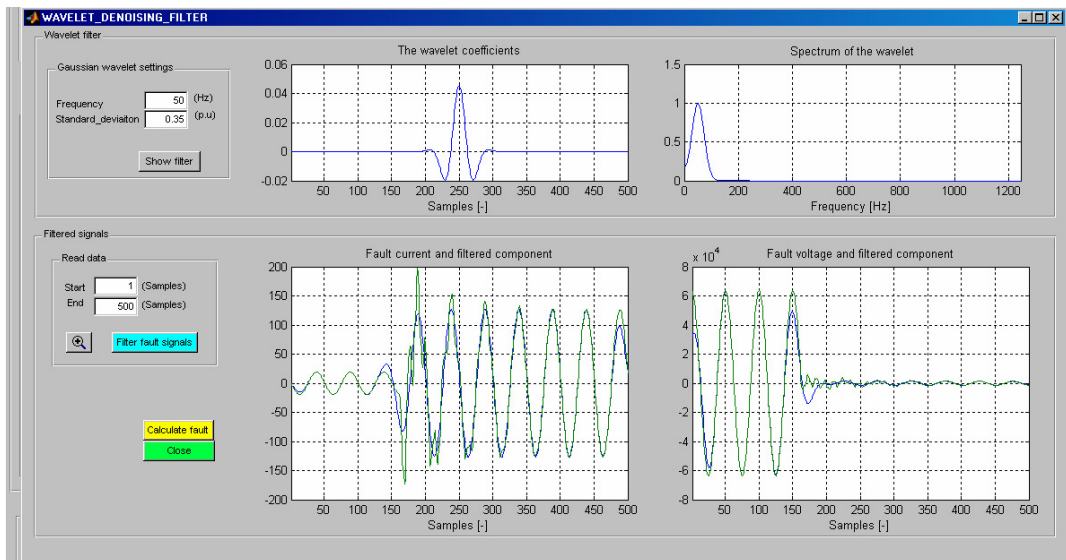


Fig. 99 Wavelet de-noising filter for conventional fault location.

13. Fault location program

Settings

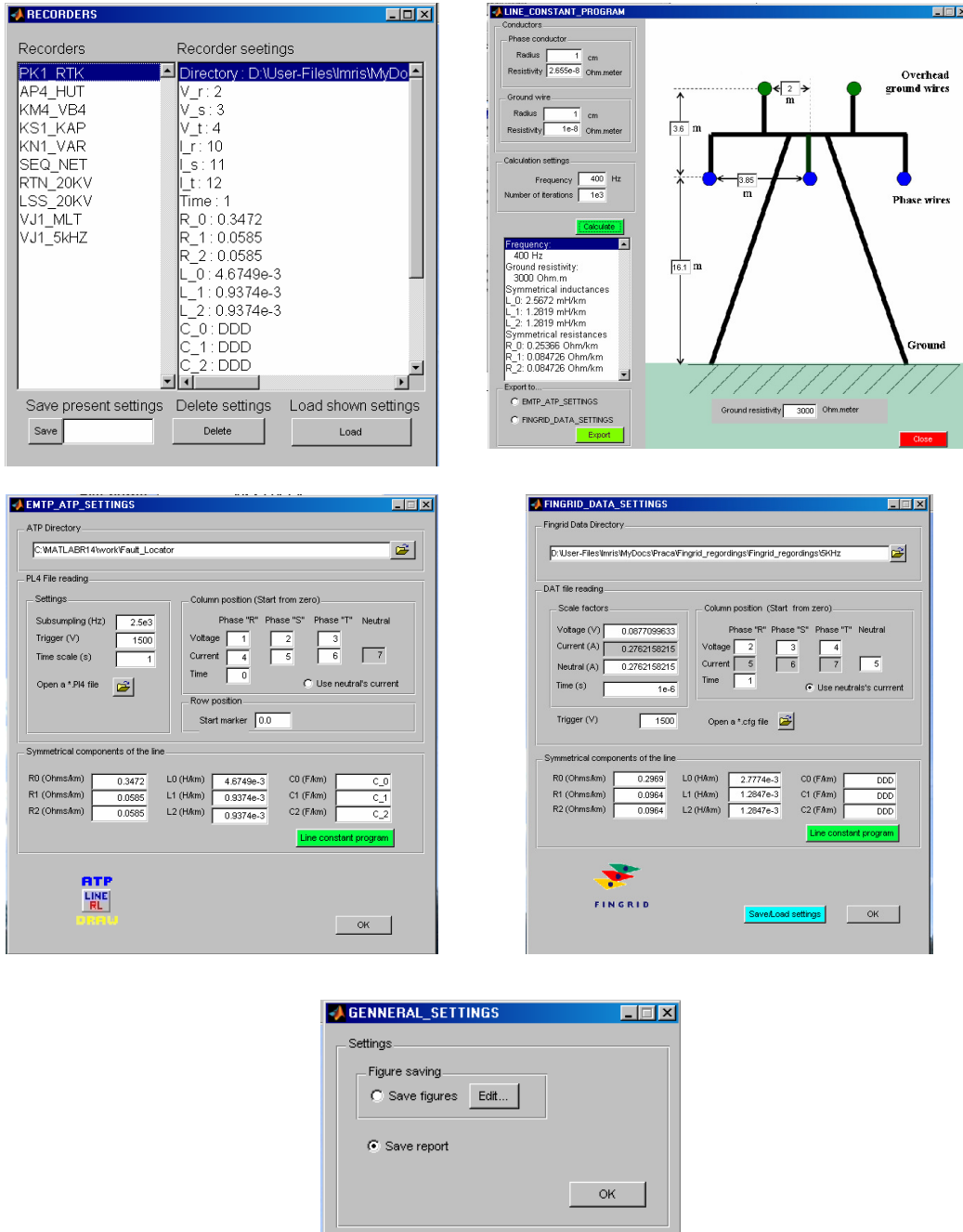


Fig. 100 Main settings for the program. Recorder organiser (top left). Line constant program (top right), settings for the EMTF/ATP files (middle left) and for the Fingrid recorded data (middle right). The general settings (lower)

14 Conclusions

This thesis deals with transient based ground fault location and conventional fault location methods in subtransmission networks. Based on the analysis and study of the different issues, the following conclusions can be made:

Conventional methods

- The conventional fault location method has limitations, mainly due to the load current and fault resistance. Reducing the influence of the fault resistance means that the fault location method will have a more limited usage under certain conditions, caused by the unfavourable relation between the load and fault current. This area was identified and an error estimation algorithm has been developed.
- The use of the current sum instead of the fault phase current is only reasonable if the load current is much smaller than the fault current.
- If the network neutral is not grounded solidly, a connected line(s) can improve the accuracy by increasing the zero-sequence current flow via the measurement point.

Transient methods

- A sampling frequency of 2.5 kHz would be high enough for fault location based on charge transients. However, the higher sampling frequency, the more reliable the fault location. Discharge transient fault location would require a sampling rate of approximately 5 kHz.
- Fault location based on charge transients works for a wider range of different fault conditions than discharge transient fault location and conventional fault location.
- The wavelet filter is suitable for fault transient filtering. The wavelet transform and windowed Fourier transform can be used but they are not so convenient.

14. Conclusions

- Fault transient signals can be measured by conventional CTs and PTs almost as accurately as the 50 Hz signals. The capacitance of added secondary cables connected to the substation building does not move the resonance point of PTs into the fault transient's spectrum. A new method of PT model parameter estimation was developed and the model can be used for the correction of measured signals from both simulations and real fault recordings.
- The line parameters in transient frequencies are almost constant with frequency; the dependency with ground resistivity is much stronger. Analysis of the propagation of fault transients showed that the fault transients return via the overhead ground wire rather than the ground. This makes the transient less dependent on the unstable ground resistivity. In the case of steel overhead ground wires, counterpoises must be used to reduce the portion of the transient that returns via the ground.
- The transient based fault location method can be used in networks with solidly grounded neutrals. Application of the method in a network with some grounding impedance (Petersen coil, low-reactance or isolated) depends on the existence of a return path to the substation. The zero-sequence current in the measurement point is increased by connected lines or by compensation capacitors placed on the busbar (with a grounded neutral). The longer the connected lines and the shorter the line section behind the fault, the more precise the fault location will be. However, this phenomenon was mathematically described and the critical area can be corrected by the method proposed.
- The transient based method inherently works with the phase current; however, the current sum can be used instead.
- The main conclusion of this work is that transient based fault location can be applied to Fingrid's 110 kV subtransmission networks. The developed fault location application was tested and verified using both simulated and real power system fault data. Since there is no big difference in the charge transients between the various types of high impedance grounded networks, the transient based method works similarly in ungrounded, Petersen grounded and low-reactance coil grounded systems. The main limitations of the method are related to the fault resistance, overhead ground wires made of steel, low sampling frequency and network configuration.

References

- [1] Lehtonen, Matti. Transient analysis for ground fault distance estimation in electrical distribution networks, Espoo 1992, Technical Research Centre of Finland, VTT Publications 115. 182p+app. 92p
- [2] Hänninen, Seppo. Single phase earth faults in high impedance grounded networks. Characteristic, indication and location. Espoo 2001. Technical Research centre of Finland, VTT Publication 453. 78p.+app.61p.
- [3] Imris, Peter; Lehtonen, Matti; Fault location in underground distribution networks using travelling waves, The 44th International Scientific Conference of Riga Technical University, Riga, Latvia, October 9-11, 2003, pp. 227-232.
- [4] Imris, Peter; Lehtonen, Matti; A comparison of different signal processing techniques for travelling wave fault location, The 44th International Scientific Conference of Riga Technical University, Riga, Latvia, October 9-11, 2003, pp. 220-226.
- [5] Imris P. Fault location in underground distribution networks using travelling waves, Univeristy of Zilina, Master's thesis, Zilina, Slovakia 2002, 91p.
- [6] Samesima, M.I.; de Oliveira, J.C.; Dias, E.M.; Frequency response analysis and modeling of measurement transformers under distorted current and voltage supply, Power Delivery, IEEE Transactions on , Volume: 6 , Issue: 4 , Oct. 1991, Pages:1762 – 1768
- [7] Bak-Jensen, B.; Ostergaard, L.; Estimation of the model parameters in equivalent circuit models of potential transformers, Power Engineering Society 1999 Winter Meeting, IEEE , Volume: 2 , 31 Jan-4 Feb 1999, Pages:1053 - 1058 vol.2
- [8] Erwin Kreyszig, “Advanced Engineering Mathematics”, 8th edition, John Wiley & Sons, Inc., 1999.

References

- [9] J. Lewis Blackburn, "Symmetrical components for power systems engineering", Marcel Dekker, Inc., 1993.
- [10] Jarmo Elovaara, Yrjö Laiho, "Sähkölaitostekniikan Perusteet", Otatieto Oy, 1988.
- [11] Schegner, P.: Digitaler Erdschlußuniversalschutz. Konzept und erste Realisierung. Dissertation, Universität des Saarlandes, Saarbrücken, 1989, 186 pp.
- [12] Igel, M.: Neuartige Verfahren für den Erdschlußdistanzschutz in isoliert und kompensiert betriebenen Netzen. Signale und Algorithmen im Frequenzbereich. Dissertation, Universität des Saarlandes, Saarbrücken, 1990, 181 pp.
- [13] Pundt, H.: Untersuchungen der Ausgleichsvorgänge bei Erdschluß in Hochspannungsnetzen mit isoliertem Sternpunkt und induktiver Sternpunktterdung als Grundlage zur selektiven Erdschlußerfassung. Dissertation, TU Dresden, 1963, 167 pp. + app.
- [14] Willheim, R., Waters, M.: Neutral earthing in high-voltage transmission. Elsevier Publishing Co., New York, 1956, 669 pp.
- [15] Robertson, D.C.; Camps, O.I.; Mayer, J.S.; Gish, W.B.; Wavelets and electromagnetic power system transients, *Power Delivery, IEEE Transactions on, Volume: 11*, Issue: 2, April 1996, Pages:1050 – 1058.
- [16] C. L. Fortescue; "Method of Symmetrical Coordinates Applied to the Solution of Polyphase Networks" AIEE Transactions, Vol. 37, 1918, pp. 1027-1140.
- [17] Glover J. D., Sarma M., "Power system analysis and design", PWS publishers, Boston, 1987.
- [18] Stevenson W., D., JR., "Elements of power system analysis", McGRAW-HILL publishing company LTD., London 1955.
- [19] Carson, J.R., Wave propagation in overhead wires with ground return. Bell System Technical Journal, Vol. 5, 1926. pp. 539-54.

References

- [20] Yaw-Juen Wang, Shi-Jie LIU. A review of methods for calculation of frequency-dependent impedance of overhead power transmission lines. Proc. Natl. Sci. Coun. ROC(A), Vol.25, No.6, 2001, p. 329-338.
- [21] Lakervi, E; Holmes E,J; Electricity distribution network design. Short Run Press Ltd., Exeter. 1998, second edition, IEE power engineering series 21.
- [22] Stearns Samuel D., Digital Signal Processing with examples in Matlab, CRC Press LLC, 2000 N.W. Corporate Blvd., Boca Raton, Florida 33431., pp. 112-124
- [23] Imris, Peter, and Lehtonen, Matti, "Transient based earth fault location in 110 kV subtransmission networks", *15th Power Systems Computation Conference, PSCC 2005*, Liege, Belgium, August 22-26, 2005, 4 p.
- [24] G.Strang and T.Nguyen, "*Wavelets and Filter Banks*", Wellesley-Cambridge Press,1996.
- [25] A. G. Phadke and J. S. Thorp, *Computer Relaying for Power Systems*, Research Studies Press Ltd., 1988.
- [26] Grainger, John, J., Stevenson, William D, jr., "Power system analysis", McGraw-Hill, 1994
- [27] "Fault statistic 2004", <http://www.nordel.org/>, link available on 20.6 2006: <http://195.18.187.215/2/LIPOBGPBIHCMFOIADNJDKHFFPDB19DBKCN9DW3571KM/docs/DLS/2005-00486-01-E.pdf>
- [28] "Living adjacent to a transmission line", Fingrid publication. Link available on 20.6 2006: <http://www.fingrid.fi/attachments/english/publications/LivingAdjacent.pdf>
- [29] Lehtonen, Matti; Hakola, Tapio: Neutral Earthing and Power System Protection. Earthing Solutions and Protective Relaying in Medium Voltage Distribution Networks. Kirjapaino FRAM Oy. 1996. 118 p.

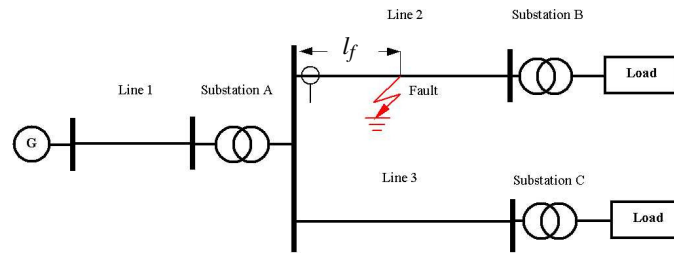
References

- [30] Ingrid Daubechies, "Ten Lectures on Wavelets", CBMS-NSF Regional Conference Series in Applied Mathematics Vol. 61 (SIAM, Philadelphia, 1992).
- [31] Imriš, P.; Lehtonen, M.; "Transient based Ground Fault Location using Wavelets", The 4th IASTED International Conference on POWER AND ENERGY SYSTEMS, Rhodes, Greece, June 28-30, 2004, pp. 507-511
- [32] Imris, Peter and Lehtonen, Matti, "Modelling of a voltage transformer for transients", *2005 IEEE PowerTech'2005*, St. Petersburg, Russia, June, 27-30, 2005, Paper 201, 5 p.
- [33] Imris, Peter, and Lehtonen, Matti, "Transient based earth fault location in 110 kV subtransmission networks", *15th Power Systems Computation Conference, PSCC 2005*, Liege, Belgium, August 22-26, 2005, 4 p.
- [34] H. W. Dommel, "EMTP Theory Book", BPA, Portland, August 1986.
- [35] Pollaczek, F. (1926) Über das feld einer unendlich langen wechselstromdurchflossenen Einfachleitung. *Elektrische Nachrichten Technik*, **3**(9), 339-359.
- [36] Pollaczek, F. (1931) Sur le champ produit par un conducteur simple infiniment long parcouru par un courant alternatif. *Revue Générale d'Électricité*, **29**(22), 851-867.
- [37] Izykowski, J.; Molag, R.; Rosolowski, E.; Saha, M.M.; "Accurate location of faults on power transmission lines with use of two-end unsynchronized measurements" *IEEE Transactions on Power Delivery*, Volume 21, Issue 2, April 2006 Page(s):627 - 633

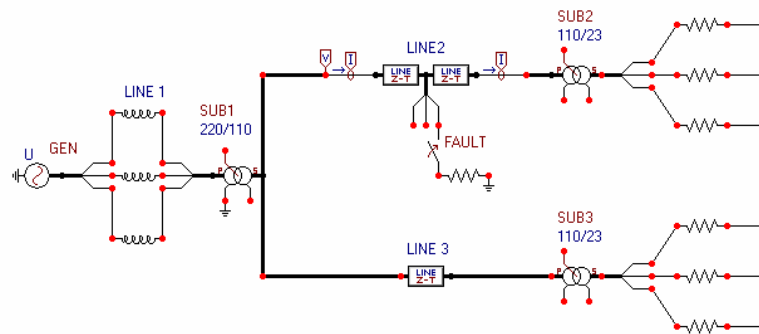
Appendices

A Fault simulations

A.1 Parameters of the simulated network



(a)



(b)

Fig. 101 The analysed network: (a) schematic diagram and (b) EMTP/ATP model

Tab. 7 Parameters of the network.

Type of the network	Network		Three phase load	Busbar
	Voltage [kV]	Frequency [Hz]	R [Ω]	C _B [μ F]
Three phase, ungrounded, radial	220 and 110	50	300	0

Tab. 8 Parameters of the transformers.

Transformer	I_{0M} [A]	F_0 [WB-turn]	R_m [M Ω]	V_{rp} [kV]	R_p [Ω]	L_p [mH]	V_{rs} [kV]	R_s [Ω]	L_s [mH]	Cou- pling
A	3.55	50	10	234	0.966	310	117	0.216	54	Yy
B,C	1	50	1	117	0.216	50	23	0.0216	10	Yy

Tab. 9 Parameters of the lines.

LINE	I_n [A]	Volt- age Level [kV]	Length [km]	Symmetrical components						L [mH]
				$R_{0'}$ [Ω /km]	$R_{1'}$ [Ω /km]	$L_{0'}$ [mH/km]	$L_{1'}$ [mH/km]	$C_{0'}$ [μ F/km]	$C_{1'}$ [μ F/km]	
1	900	220	-	-	-	-	-	-	-	40
2	775	110	50	0.16	0.035	1.5	1.1	0.0063	0.0095	-
3	775	110	55	0.16	0.035	1.5	1.1	0.0063	0.0095	-

A.2 Simulation results

A.2.1 Transient fault location

Tab. 10 Transient fault location versus fault distance.

$R_f=0 \Omega$, $\phi_f=90^\circ$, $t_f=0$ s Time window=100 ms, Maximum transient damping -30 dB, $f_s=100$ kHz/2.5 kHz								
Fault distance [km]	Charge transient				Discharge transient			
	l_f [km]	Frequency [Hz]	Freq. Shift [Hz]	Error, δ_f [km]	l_f [km]	Frequency [Hz]	Freq. Shift [Hz]	Error, δ_f [km]
5	4.752658	270	0	-0.247342	not detected			
10	9.404958	270	0	-0.595042	11.34887	1250	0	1.34887
15	13.967120	270	0	-1.032880	18.83920	1150	-100	3.83920
20	18.969280	260	-10	-1.030720	21.37917	1080	-170	1.37917
25	23.728880	260	-10	-1.271120	26.94968	1020	-230	1.94968
30	28.225210	260	-10	-1.774790	22.21482	970	-280	-7.78518
35	34.072750	250	-20	-0.927250	45.79534	930	-320	10.79534
40	38.518660	250	-20	-1.481340	18.34387	890	-360	-21.65613
45	43.008390	250	-20	-1.991610	18.82752	850	-400	-26.17248
50	47.962000	250	-20	-2.038000	28.13722	820	-430	-21.86278
Absolute error				1.239009	10.75431			

Tab. 11 Transient fault location versus fault resistance

<i>$l_f=25$ km, $\varphi_f=90^\circ$, $t_f=0$ s, Time window=100 ms, Maximum transient damping -30 dB, $f_s=100$kHz/2.5 kHz</i>								
Fault resistance [Ω]	Charge transient				Discharge transient			
	l_f [km]	Frequency [Hz]	Freq. Shift [Hz]	Error, δ [km]	l_f [km]	Frequency [Hz]	Freq. Shift [Hz]	Error, δ [km]
0	23.72888	260	0	-1.27112	26.94968	1020	0	1.94968
1	23.74518	260	0	-1.25482	27.93547	1020	0	2.93547
5	23.80399	260	0	-1.19601	29.02801	1020	0	4.02801
10	23.86447	260	0	-1.13553	25.20060	1030	10	0.20060
15	23.90951	260	0	-1.09049	21.39500	1030	10	-3.60500
20	23.93964	260	0	-1.06036	27.13825	1030	10	2.13825
25	23.95509	260	0	-1.04491	27.09390	1030	10	2.09390
30	23.95590	260	0	-1.04410	27.01637	1030	10	2.01637
35	23.94055	260	0	-1.05945	26.63512	1040	20	1.63512
45	23.86685	260	0	-1.13315	26.22083	1040	20	1.22083
50	23.80677	260	0	-1.19323	25.88271	1040	20	0.88271
55	23.73026	260	0	-1.26974	25.18722	1050	30	0.18722
60	23.64296	260	0	-1.35704	24.59035	1050	30	-0.40965
65	23.53812	260	0	-1.46188	23.81772	1050	30	-1.18228
70	23.41726	260	0	-1.58274	18.19077	1050	30	-6.80923
75	23.28218	260	0	-1.71782	17.93536	1050	30	-7.06464
100	23.26866	250	-10	-1.73134	15.84724	1110	90	-9.15276
110	22.77035	250	-10	-2.22965	13.69684	1250	230	-11.30316
120	22.21048	250	-10	-2.78952				
130	21.58071	250	-10	-3.41929				
140	20.89017	250	-10	-4.10983				
150	20.10456	250	-10	-4.89544				
160	19.27679	250	-10	-5.72321				
170	18.30567	250	-10	-6.69433				
200	15.64059	240	-20	-9.35941				

Not detected discharge transient

Tab. 12 Transient fault location versus voltage inception angle.

<i>$l_f=25$ km, $R_f=0$ Ω, $t_f=0$ s, Time window 100 ms, Maximum transient damping -30 dB, $f_S=100$kHz/2.5 kHz</i>						
Voltage inception Angle ϕ_f [°]	Charge transient			Discharge transient		
	l_f [km]	Frequency [Hz]	Error, δ_f [km]	l_f [km]	Frequency [Hz]	Error, δ_f [km]
0	23.72870	260	-1.27130			
1	23.72883	260	-1.27117	Not detected discharge transient		
2	23.72908	260	-1.27092			
3	23.72909	260	-1.27091	26.91696	1020	1.91696
4	23.72973	260	-1.27027	27.20588	1020	2.20588
5	23.72903	260	-1.27097	26.84813	1020	1.84813
10	23.72868	260	-1.27132	26.82296	1020	1.82296
20	23.72892	260	-1.27108	26.86102	1020	1.86102
30	23.72900	260	-1.27100	26.89302	1020	1.89302
40	23.72888	260	-1.27112	26.91203	1020	1.91203
50	23.72884	260	-1.27116	26.92250	1020	1.92250
60	23.72876	260	-1.27124	26.92978	1020	1.92978
70	23.72895	260	-1.27105	26.93600	1020	1.93600
80	23.72883	260	-1.27117	26.94446	1020	1.94446
90	23.72888	260	-1.27112	26.94968	1020	1.94968

A.2.2 Conventional fault location

Tab. 13 Conventional fault location in solidly grounded network. Influence of $\underline{I}_L / \underline{I}_f$.

$l_f = 25\text{km}, R_f = 0\Omega, \text{simulated time } 1\text{ s}, t_f = 0.45\text{s}, f_s = 100\text{kHz}/2.5\text{ kHz}$							
Parameters				Conventional fault location			
$\underline{I}_L/\underline{I}_f$ [p.u]	Angle ($\underline{I}_L/\underline{I}_f$) [°]	Re (VF/IF) [Ω]	Im (VF/IF) [Ω]	Re (Denomin) [Ω]	Im (Denomin) [Ω]	Fault distance [km]	Abs (Error) [km]
$\underline{I}_L/\underline{I}_f=1$							
1	6.421	2.276	18.943	0.073	0.734	25.86	0.857
1.012	23.513	-0.434	18.733	-0.03	0.722	25.93	0.932
1.044	40.897	-3.123	17.875	-0.132	0.684	26.05	1.053
1.096	58.848	-5.694	16.263	-0.227	0.616	26.25	1.247
0.983	99.914	-7.156	9.815	-0.264	0.363	27.09	2.088
1.036	121.11	-7.164	6.45	-0.249	0.233	28.27	3.273
1.079	143.45	-5.764	2.962	-0.176	0.11	31.25	6.251
1.095	166.41	-2.745	0.07	-0.049	0.029	48.05	23.047
1.095	172.13	-1.748	-0.443	-0.013	0.018	81.16	56.162
1.094	175.54	-1.122	-0.698	0.009	0.014	80.74	55.743
1.093	176.67	-0.944	-0.807	0.016	0.012	60.01	35.008
$\underline{I}_L/\underline{I}_f=0.3$							
0.296	7.378	2.003	12.468	0.074	0.49	25.49	0.486
0.34	-2.081	2.532	12.818	0.093	0.504	25.49	0.486
0.304	46.635	0.199	11.958	0.008	0.467	25.61	0.607
0.31	66.372	-0.513	11.285	-0.017	0.44	25.65	0.646
0.303	106.53	-0.916	9.36	-0.027	0.368	25.51	0.513
0.31	126.66	-0.699	8.375	-0.016	0.332	25.28	0.278
0.314	146.91	-0.123	7.508	0.008	0.302	24.83	0.169
0.317	167.27	0.752	6.894	0.042	0.283	24.26	0.739
0.318	172.36	1.006	6.796	0.051	0.28	24.14	0.863
0.318	175.42	1.162	6.746	0.057	0.279	24.06	0.938
0.318	176.44	1.215	6.732	0.059	0.278	24.04	0.963
$\underline{I}_L/\underline{I}_f=3$							
2.959	4.585	3.411	36.486	0.098	1.414	25.85	0.848
3.182	-0.492	5.976	38.253	0.197	1.485	25.84	0.838
3.194	26.198	-6.971	37.018	-0.31	1.426	25.81	0.806
3.518	37.248	-13.3	37.254	-0.561	1.429	25.77	0.767
2.956	81.26	-22.86	18.016	-0.917	0.645	25.97	0.968
2.906	106.5	-23.35	7.301	-0.915	0.2	26.13	1.131
3.075	133.46	-20.74	-3.373	-0.768	-0.27	25.85	0.846
2.94	167.6	-12.89	-10.02	-0.242	-0.58	25.89	0.892
2.972	171.85	-12.59	-10.6	-0.172	-0.61	25.82	0.816

A Fault simulations

Tab. 14 Conventional and improved conventional fault location in solidly grounded network. Influence of the fault resistance. Studied case $I_L / I_f = 3$.

$I_L / I_f = 3$, $l_f = 25\text{km}$, simulated time 1 s, $t_f = 0.45\text{s}$, $f_s = 100\text{kHz}/2.5\text{kHz}$												
Rf	Parameters						Conventional FL		Improved Conventional FL			
	I_L/I_f [p.u]	Angle (I_L/I_f) [°]	Re (VF/IF) [Ω]	Im (VF/IF) [Ω]	Re (Denomin) [Ω]	Im (Denomin) [Ω]	Fault distance [km]	Abs (Error) [km]	Angle Accuracy1 [°]	Angle Accuracy2 [°]	Fault distance [km]	Abs (Error) [km]
0	2.959	4.585	3.411	36.486	0.098	1.414	25.85	0.848	110.95	113.3	25.798	0.798
1	2.967	2.556	6.284	36.545	0.135	1.416	26.07	1.073	108.85	115.3	25.812	0.812
5	3.046	-5.32	17.765	36.972	0.28	1.425	28.24	3.244	100.38	122.6	25.946	0.946
10	3.066	-14.09	31.386	36.383	0.439	1.388	33	8.002	91.456	131.2	26.206	1.206
15	3.042	-21.4	43.482	35.072	0.559	1.327	38.8	13.799	84.326	138.7	26.434	1.434
20	3.051	-27.46	54.657	34.003	0.657	1.273	44.92	19.924	78.197	144.7	26.707	1.707
30	3.004	-36.46	73.944	31.636	0.778	1.159	57.61	32.605	69.549	154	27.287	2.287
40	3.003	-42.92	91.42	29.833	0.86	1.075	69.84	44.84	63.103	160.5	27.742	2.742
50	2.988	-47.4	106.86	28.755	0.907	1.009	81.56	56.562	58.739	165.1	28.499	3.499
60	3.075	-51	122.78	28.371	0.97	0.972	91.78	66.776	54.479	168.1	29.188	4.188
70	2.969	-53.48	134.95	27.392	0.963	0.914	103.7	78.737	52.8	171.3	29.971	4.971
80	2.96	-55.67	148.03	26.904	0.979	0.878	114.4	89.372	50.687	173.6	30.63	5.63
90	2.95	-57.48	160.64	26.484	0.991	0.848	124.8	99.799	48.951	175.5	31.232	6.232
100	2.94	-59.02	173.21	26.163	1	0.822	135.3	110.329	47.492	177.1	31.839	6.839

Tab. 15 Conventional and improved conventional fault location in solidly grounded network. Influence of the angle (I_L / I_f). Studied case $I_L / I_f = 3$.

$I_L / I_f = 3$, $l_f = 25\text{km}$, $R_f = 0\Omega$, simulated time 1 s, $t_f = 0.45\text{s}$, $f_s = 100\text{kHz}/2.5\text{kHz}$												
Parameters						Conventional fault location		Improved Conventional fault location				
I_L/I_f [p.u]	Angle (I_L/I_f) [°]	Re (VF/IF) [Ω]	Im (VF/IF) [Ω]	Re (Denomin) [Ω]	Im (Denomin) [Ω]	Fault distance [km]	Abs (Error) [km]	Angle Accuracy1 [°]	Angle Accuracy2 [°]	Fault distance [km]	Abs (Error) [km]	
2.959	4.585	3.411	36.486	0.098	1.414	25.85	0.848	110.95	113.3	25.798	0.798	
2.942	15.699	-1.637	36.057	-0.099	1.393	25.84	0.836	122.19	102.4	25.875	0.875	
3.033	27.376	-7.027	35.496	-0.311	1.366	25.83	0.826	133.17	89.99	25.982	0.982	
3.083	41.302	-13.02	32.942	-0.545	1.258	25.83	0.832	146.73	75.7	26.179	1.179	
3.38	50.809	-18.28	32.054	-0.753	1.217	25.79	0.785	154.29	64.25	26.345	1.345	
3.047	54.052	-17.36	28.884	-0.713	1.092	25.85	0.85	159.74	63.21	26.462	1.462	
3.102	68.742	-21.79	23.706	-0.883	0.877	25.88	0.877	174.03	48.12	27.031	2.031	
3.054	80.345	-23.54	18.658	-0.945	0.67	25.92	0.924	174.02	36.86	27.864	2.864	
2.978	105.82	-23.97	7.513	-0.942	0.207	26.05	1.053	147.97	11.96	36.272	11.272	
3.031	116.26	-23.47	3.11	-0.909	0.019	26.04	1.037	137.94	1.121	161.78	136.78	
2.928	119.9	-22.22	1.949	-0.851	-0.03	26.2	1.195	133.49	1.725	-69.29	94.29	
3.006	133.85	-20.23	-3.21	-0.745	-0.26	26	1.002	120.15	16.28	12.532	12.468	
3.11	166.94	-13.32	-10.32	-0.272	-0.63	24.41	0.595	87.829	50.13	16.258	8.742	

Tab. 16 Conventional and improved conventional fault location with different network neutral arrangements. Influence of the angle (I_L / I_f). Studied case

$$I_L / I_f \approx 9.$$

Reactance grounded network neutral with 80 Ohms (254.7mH)																				
Load	L					R					C									
	45mH	14.0 35mH	15.0 30 mH	19.0 15mH	21.0 1000µF	21.0 1000µF	22.0	22.0 700µF	21.0 300µF	17.0 150µF	15.0 120µF	13.0 116µF	10.0 100µF	60 95µF	60 94µF	5.90 92µF	5.60 92µF	5.0 94µF	3.10 90µF	95µF
IL/IF [p.u]	9.25	8.9	9.12	9.17	8.8	9.6	9.21	9.6	9.6	8.7	9.6	9.07	9.46	8.9	8.02	8.15	9.5	7.9	9.2	
Angle IL/IF [°]	1.32	45.56	50.7	70.7	88.8	97.6	103	123	164	188	197	232	263	265	269	270	276	301	342	
CA [km]	25.3	25.3	25.4	25.3	25.4	25.3	25.3	25.2	24.5	24.5	24.34	23.67	23.58	23.5	23.4	23.4	24	23	23.4	
ICA [km]	25.2	25.49	25.6	26	27.2	30.73	1173	25.8	24.6	24.5	24.46	24.088	22.32	21.88	54.5	27	26	24	23.4	
Ang. accuracy1	92.4	137	141	162	179.7	171	166	145	104	81.3	72	37.2	6.12	4.16	0.29	2.99	6	32	73.5	
Ang. accuracy2	101	57.4	52	32.1	14.2	4.84	0	21	62	81.03	94	128.6	160.3	161.5	164	167	172	163	120	
abs(ErrorCA)	0.2	0.49	0.64	0.96	2.2	5.73	1148	0.8	0.42	0.5	0.54	0.932	2.68	3.32	29.5	2	1.2	0.7	1.6	
abs(ErrorCA))	0.3	0.3	0.35	0.3	0.4	0.3	0.3	0.2	0.5	0.5	0.66	1.33	1.42	1.5	1.59	1.6	1.5	1.7	1.6	

Compensated (5050 mH)																				
Load	L					R					C									
	90°	80°	60°	20°	15°	11°	10°	10°	7°	10°	20°	40°	70°	88°	90°	88°	90°	88°	90°	88°
IL/IF [p.u]	7.5	7.95	8.78	8.89	9.13	8.917	9.1	8.94	8.76	8.7	8.7	8.69	9.43	10.26	11.13	10.26	11.13	10.26	11.13	
Angle IL/IF [°]	0	11.97	39.3	81	98.04	103	104	107	123	130	144.5	164	178.3	358	358	178.3	358	178.3	358	
CA [km]	26.01	25.95	26	25	25.51	25.47	25.5	25.4	25.2	25.04	24.8	24.5	24.45	24.33	24.72	24.33	24.72	24.33	24.72	
ICA [km]	25.9	25.98	26.7	27.3	37.22	-825	-29.3	10.6	22.9	23.68	24.343	24.48	24.37	24.75	24.75	24.37	24.75	24.37	24.75	
Ang. accuracy1	92	104.2	131	172	170.7	185.6	165	162	146	138.4	123.85	104.66	91.29	87.85	103.7	91.29	87.85	104.66	103.7	
Ang. accuracy2	104	91.87	63.8	22	4.76	0.066	1.01	3.64	19.4	26.9	41.406	61.78	76.25	103.7	76.25	103.7	76.25	103.7	103.7	
abs(ErrorCA)	0.9	0.98	1.72	2.3	12.22	850	54.3	14.4	2.13	1.321	0.657	0.52	0.63	0.63	0.63	0.52	0.63	0.63	0.63	
abs(ErrorCA))	1.013	0.95	0.96	0.01	0.506	0.474	0.48	0.39	0.16	0.043	0.2	0.55	0.87	0.87	0.87	0.55	0.87	0.87	0.87	

Isolated																				
Load	L					R					C									
	88°	80°	50°	30°	12.5°	11°	5°	0°	0°	10°	30°	50°	80°	80°	80°	80°	80°	80°	80°	80°
IL/IF [p.u]	10.3	10.37	10	9.9	9.7	9.6	9.52	9.47	9.36	8.87	8.3	7.63	7.63	7.63	7.63	7.63	7.63	7.63	7.63	
Angle IL/IF [°]	183	192	226	249	268	268.6	276	281	289	312	330.1	353.8	353.8	353.8	353.8	353.8	353.8	353.8	353.8	
CA [km]	25.11	25.09	25.1	25	24.9	24.91	24.9	24.9	24.9	24.86	24.84	24.8	24.8	24.8	24.8	24.8	24.8	24.8	24.8	
ICA [km]	25.11	25.09	25.1	25.2	26.77	36.48	24	24	24.7	24.83	24.86	24.9	24.9	24.9	24.9	24.9	24.9	24.9	24.9	
Ang. accuracy1	87	77.89	44.1	20.8	1.45	0.53	6.54	11.1	20	42.64	62.017	86.36	86.36	86.36	86.36	86.36	86.36	86.36	86.36	
Ang. accuracy2	80	88.75	123	146	165.4	166.2	173	177	174	151.8	133.4	110.42	110.42	110.42	110.42	110.42	110.42	110.42	110.42	
abs(ErrorCA)	0.112	0.09	0.14	0.2	3.77	11.48	0.95	1	0.34	0.17	0.14	0.1	0.1	0.1	0.1	0.1	0.1	0.1	0.1	
abs(ErrorCA))	0.112	0.088	0.05	0.05	0.1	0.09	0.12	0.09	0.11	0.12	0.16	0.2	0.2	0.2	0.2	0.2	0.2	0.2	0.2	

Note:
 CA - conventional fault location algorithm
 ICA - improved conventional fault location algorithm

A.3 Pyhäkoski – Rautaruukki faults

A.3.1 Real faults

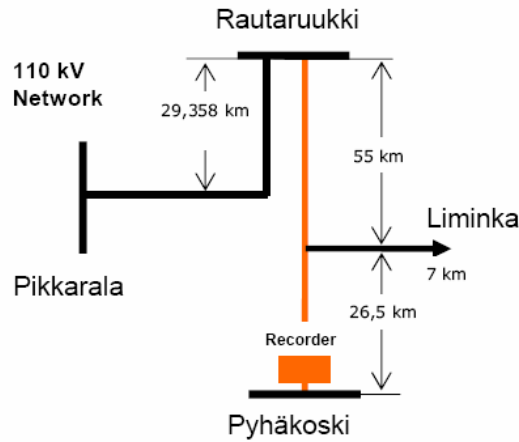


Fig. 102 Schematic layout of the Pyhäkoski – Rautaruukki line.

Tab. 17 Parameters of the Pyhäkoski – Rautaruukki line

Symmetrical components of the line						Other parameters		
R_0' [Ω/km]	R_1' [Ω/km]	R_2' [Ω/km]	L_0' [H/km]	L_1' [H/km]	L_2' [H/km]	Length [km]	Voltage level [kV]	Neutral
0.34	0.0585	0.0585	4.67E-3	9.37E-4	9.37E-4	8.15E+1	110	Low-reactance

Tab. 18 The conventional and improved conventional fault location methods for real faults from the Pyhäkoski – Rautaruukki line. $f_s=1$ kHz.

I_L/I_f [p.u.]	l_f [km]	Phase currents (I_{phase})			Zero-sequence current ($3I_0$)		
		CFL		ICFL	CFL		ICFL
		Distance [km]	Distance [km]	Error [km]	Distance [km]	Distance [km]	Error [km]
0.07	1	3.76	1.96	-0.96	3.7	1.8	-0.8
0.267	25.8	26.137	24.95	0.85	25.662	24.54	1.26
0.375	51.5	50.778	50.47	1.03	47.86	48.9	2.6
0.38	51.5	50.107	50.166	1.334	48.08	49.12	2.38
0.382	59	56.38	41.185	17.815	55.16	56.195	2.805
0.49	73.3	85.6	83	-9.7	66.9	66.94	6.36

Note:

CFL- Conventional fault location algorithm Eq. (10)

ICFL improved conventional fault location algorithm Eq. (13)

A Fault simulations

Tab. 19 Transient based methods using the charge transient. Calculated fault distances of single-phase to ground faults. $f_s=1$ kHz.

Date of fault	Exact Fault distance [km]	Wavelet algorithm		Differential equation algorithm	
		Fault distance [km]	Error [km]	Fault distance [km]	Error [km]
30.06.2002	59	45,65	13,35	61	-2
27.07.2002	1	0,21	0,79	0,45	0,55
01.09.2002	25,8	25,92	-0,120	26,1	0,3
04.10.2002	73,3	82,73	-9,43	85	-11,7
19.05.2003	51,5	51,79	-0,29	52	-0,5
22.05.2003	51,5	50,48	1,02	50	1,5

A.3.2 Simulated faults

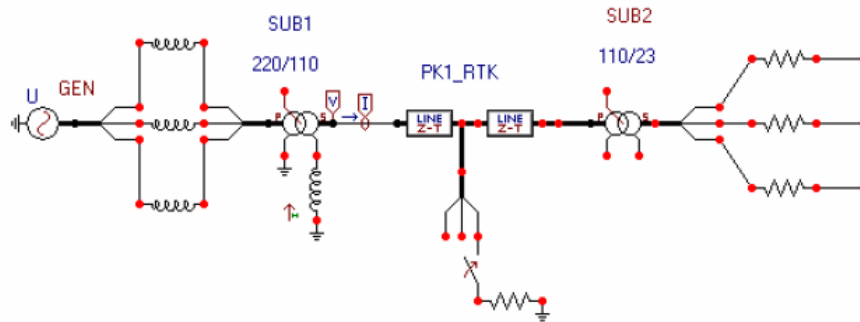


Fig. 103 Schematic representation of the simulated network. The line parameters are the same as in Tab. 17.

Tab. 20 Conventional and improved conventional fault location on the simulated Pyhäkoski – Rautaruukki line.

$l_f = 25\text{km} \cdot R_f = 0\Omega \cdot f_s = 100\text{kHz}/2.5 \text{ kHz}$							
Phase currents					I_0 current ($3I_0$)		
I_{L/I_f} [p.u] $\text{angl}(I_{L/I_f})=0$	Load, X , [mH]	CFL	ICFL		CFL	ICFL	
		Distance [km]	Distance, [km]	Error [km]	Distance [km]	Distance, [km]	Error, [km]
0.065	6000	25.87	25.87	-0.87	24.79	24.79	0.21
0.11	4000	25.97	25.98	-0.98	25.303	25.304	-0.304
0.17	3000	26.068	26.086	-1.086	25.811	25.814	-0.814
0.68	1000	26.623	26.685	-1.685	29.772	29.741	-4.741
1.4	500	27.042	27.131	-2.131	35.114	35.174	-10.174
6.23	100	27.178	27.125	-2.125	64.63	65.23	-40.23

Note:

CFL- Conventional fault location algorithm Eq. (10)

ICFL improved conventional fault location algorithm Eq. (13)

A.4 Developing of the equation for improved conventional fault location

Eq. (14) can be developed into Eq. (15) as follows:

$$\frac{1}{3}(X'_0 + X'_1 + X'_2) + \text{imag}\left(\frac{I_L}{I_f} \underline{Z}'_1\right) = 0 \quad (57)$$

$$-\frac{1}{3}(X'_0 + X'_1 + X'_2) = \text{imag}\left(\frac{I_L}{I_f} \underline{Z}'_1\right) \quad (58)$$

$$-\frac{1}{3}(X'_0 + X'_1 + X'_2) = \text{imag}\left(\frac{I_L}{I_f} \underline{Z}'_1 \cdot e^{j(\varphi_L - \varphi_F + \varphi_{z1})}\right) \quad (59)$$

$$-\frac{1}{3}(X'_0 + X'_1 + X'_2) = \frac{I_L}{I_f} \underline{Z}'_1 \cdot \sin(\varphi_L - \varphi_F + \varphi_{z1}) \quad (60)$$

$$\varphi_0 = \varphi_L - \varphi_F = \text{asin}\left(\frac{-\frac{1}{3}(X'_0 + X'_1 + X'_2)}{\frac{I_L}{I_f} \underline{Z}'_1}\right) - \varphi_{z1} \quad (61)$$

And finally the zero-crossing angle of term $\underline{I}_L / \underline{I}_f$ can be calculated as:

$$\varphi_0 = \varphi_L - \varphi_F = -\left(\text{asin}\left(\frac{\frac{1}{3}(X'_0 + X'_1 + X'_2)}{\frac{I_L}{I_f} \underline{Z}'_1}\right) + \varphi_{z1}\right) \quad (62)$$

All symbols are as in Section 4.2.

A.5 Correction factor

Tab. 21 Correction factors for fault location using the charge transient calculated for both models, the symmetrical component model and Clark line model, by the wavelet algorithm with wavelet filter. No parallel line connected.

Parallel line length 0 km $R_f = 0\Omega, f_s = 100\text{kHz}/2.5\text{ kHz}$										
fault dist.[km]	Network model					Symmetrical component model				
	Freq. [Hz]	WA		DEA		Freq. [Hz]	WA		DEA	
Dist. [km]		CF [p.u]	Dist. [km]	CF [p.u]	Dist. [km]		CF [p.u]	Dist. [km]	CF [p.u]	
10	460	4.37	2.28	4.35	2.298	360	4.37	2.28	4.36	2.29
20	470	9.21	2.17	9.1	2.19	372	9.15	2.18	9.08	2.20
30	470	14.9	2.013	14.68	2.04	379	14.7	2.04	14.66	2.04
40	460	21.77	1.83	21.46	1.86	372	21.5	1.86	21.58	1.85
50	440	30	1.66	29.6	1.68	352	29.95	1.66	29.99	1.66
60	420	39.1	1.53	39.1	1.53	326	39.98	1.50	39.76	1.50
70	390	49.85	1.40	49.78	1.40	299	51.18	1.36	50.62	1.38
80	360	61.86	1.29	61.4	1.30	279	62.26	1.28	62.35	1.28
90	340	73.1	1.23	73.77	1.22	259	74.28	1.21	74.78	1.20
100	310	87.8	1.138	86.78	1.15	239	87.57	1.14	87.8	1.138

Tab. 22 Correction factors for fault location using the charge transient calculated for both models, the symmetrical component model and Clark line model, by the wavelet algorithm with wavelet filter. Parallel line length 70 km.

Parallel line length 70 km $R_f = 0\Omega, f_s = 100\text{kHz}/2.5\text{ kHz}$										
fault dist.[km]	Network model					Symmetrical component model				
	Freq. [Hz]	WA		DEA		Freq. [Hz]	WA		DEA	
Dist. [km]		CF [p.u]	Dist. [km]	CF [p.u]	Dist. [km]		CF [p.u]	Dist. [km]	CF [p.u]	
10	430	6.62	1.51	6.51	1.53	352	6.1	1.63	6	1.66
20	400	15.77	1.26	15.03	1.33	326	15.68	1.27	15.58	1.28
30	360	24.3	1.23	24	1.25	292	24.62	1.22	24.76	1.21
40	330	33.45	1.19	33.37	1.19	259	34.23	1.16	34.69	1.15
50	300	43.38	1.15	43.02	1.16	233	44.29	1.128	43.7	1.14
60	280	52.77	1.13	52.97	1.13	213	54.38	1.10	53.62	1.11
70	260	62.97	1.11	63.23	1.11	199	63.72	1.09	63.844	1.09
80	240	74.31	1.07	73.78	1.08	186	73.9	1.08	74.36	1.07
90	230	83.45	1.07	84.61	1.06	173	85.2	1.05	85.16	1.05
100	210	97.44	1.02	95.7	1.04	159	98.02	1.02	96.25	1.03


Tab. 23 Correction factors for the fault location using the charge transient calculated for both the symmetrical component and Clark line models by the wavelet algorithm with wavelet filter. Parallel line length 300 km.

Parallel line 300 km											
$R_f = 0\Omega, f_s = 100\text{kHz}/2.5\text{kHz}$											
	Network model					Symmetrical component model					
	WA			DEA			WA			DEA	
fault dist. [km]	Freq. [Hz]	Dist. [km]	CF [p.u]	Dist. [km]	CF [p.u]	Freq. [Hz]	Dist. [km]	CF [p.u]	Dist. [km]	CF [p.u]	
10	140	10.19	0.981	9.8	1.020	108	9.992	1.0008	9.992	1.0008	
20	140	19.4	1.03	19.65	1.017	104	20	1	19.7	1.015	
30	130	30.1	0.99	29.4	1.020	100	29.4	1.020	29.6	1.013	
40	130	38.44	1.040	39.22	1.019	96	39.2	1.020	39.4	1.015	
50	120	50.37	0.99	49.07	1.018	92	49.23	1.015	49.25	1.015	
60	120	58.32	1.028	58.96	1.017	88	59.6	1.006	59.13	1.014	
70	110	71.96	0.97	68.9	1.015	84	70.4	0.994	69.1	1.013	
80	110	79.7	1.003	78.9	1.013	80	81.87	0.977	79.16	1.010	
90	100	93.08	0.966	89.1	1.010	80	89.3	1.007	89.2	1.008	
100	100	102	0.980	99.29	1.007	76	101	0.990	99.17	1.008	

B Modelling of instrument transformers


B.1 Parameters of the measured transformers

B Modelling of instrument transformers

Nameplate of transformer		
Name:	PT1	
Voltage level:	110 kV	


ASEA		Voltage transformer						
Made in Sweden Fabrique en Svedo								
A	1a	Type	EMFC 145	No.	7150192			
		Rules	IEC 186		145	kV	50	Hz
	1n	Rated insul. Level	275- 650 kV					
		Mass incl. Oil	570 kg	Year	1979	Vf	1.9	
				Mass of oil	90			kg
	2a							
		A-N	1a-1n	2a-2n				
	2n							
		$110000/\sqrt{3}$	$100/\sqrt{3}$	$100/3$				V
								V
		Output	300	400	100			VA
		Class	0.5	1	3P			
N								

B Modelling of instrument transformers

Nameplate of transformer		
Name:	PT2	
Voltage level:	110 kV	


GEC ALHSTOM						
Berlin		T&D		Made in Germany		
JÄNNITEMUUNTAJA						
Type	UET 123		V	110000 / $\sqrt{3}$ A-N		
No.	97/768187		V	100 / $\sqrt{3}$	100 / $\sqrt{3}$	
	123/230/550		VA	300	120	
kV	1.9 U_n 30s		Cl.	0.2/3P	3P	
	50Hz	IEC 186	lth	25	25 8 h	
ULOS ASENNETTAVA				a-n	d-n	
KULJETUS PYSTYASENNOSAA			Oil	Technol US-3000P 50kg		
			Weight	325 kg		

B Modelling of instrument transformers

Nameplate of transformer		
Name:	PT3	
Voltage level:	110 kV	


ASEA		Voltage transformer					
Made in Sweden Fabrique en Svedo							
A	1a	Type	EMFC 145	No.	6504 073	50	Hz
		Rated insul. Level	275- 650 kV	Rules	IEC 186		
	1n	Nimel lisjänni tekerroin 1.9/30 S					
	2a	A-N	1a-1n	2a-2n			
		$110000/\sqrt{3}$	$100/\sqrt{3}$	100/3			V
							V
							V
		Output	300	300	150		VA
		Class	0.5	3P	3P		
N	2n						

B Modelling of instrument transformers

Nameplate of transformer		
Name:	CT1	
Voltage level:	110 kV	

Virtamuuntaja						
ASEA	IMBD 145 A3	N.	7715 677			
Made in Sweden Fabrique en Svedo						
	Rated insul. Level	275- 650	kV	145	kV	50 Hz
Standard	SFS 2874			Kuormituskerroin		1,2
P1-P2	1	1	2.3		I _{th}	I _{dyn}
	S1-S2	S1-S3	S1-S2		kA/s	kA
400	200/5	400/5	400/5	A	32/1	80
800	400/5	800/5	800/5	A	35/1	90
Output	60	60	60	VA		
Class	0.2 Fs5	0.2Fs5	10P20			
R 75Ω	0.2	1.0	0.35		Sisätaakka	
P1						P2
Core	1	S1	S2			S3
Core	2	S1				S2
Core	3	S1				S2
Core						
Core						


B Modelling of instrument transformers

Nameplate of transformer		
Name:	CT2	
Voltage level:	110 kV	

ARTECHE		Current transformer					
Type		CTE-123			Voltage	kV	123
No.		1992/924038-1			Freq.	Hz	50
Standard		SFS-2874			Ins.lev.	kV	230/550
Oil type		SHELL DIALA G			Ith	kA	31.5
Oil weight	kg	30			Idyn	kA	80
Prim. Current	A	200-400			Cont.load	%	120
Core No.		1	2	3	Weigh	kg	330
Sec. current	A	1	1	1	Water resistant, Do not Open, Transport in vertical position.		
Output	VA	10	10	10			
Class		0.2	10P20	10P20			
Coeff.		5					
Int. load	Ω						
Time constant	ms						

No.		924038-1							
		1S1		1S2 2S1		2S2 3S1		3S2	
B-ST		1S1-1S2		2S1-2S2		3S1-3S2			
A		1		1		1			
VA		10		10		10			
CL-KL		0.2		10P20		10P20			
Fs		5							


B Modelling of instrument transformers

Nameplate of transformer		
Name:	CT3	
Voltage level:	110 kV	

ARTECHE		Current transformer					
Type		CTE-123			Voltage	kV	123
No.		1992/924037-1			Freq.	Hz	50
Standard		SFS-2874			Ins.lev.	kV	230/550
Oil type		SHELL DIALA G			Ith	kA	31.5
Oil weight	kg	30			Idyn	kA	80
Prim. Current	A	150-300			Cont.load	%	120
Core No.		1	2	3	Weith	kg	330
Sec. current	A	1	1	1	Water resistant, Do not Open, Transport in vertical position.		
Output	VA	10	10	10			
Class		0.2	10P20	10P20			
Coeff.		5					
Int. load	Ω						
Time constant	ms						

No.		924037-1					
		1S1	1S2	2S1	2S2	3S1	3S2
B-ST		1S1-1S2		2S1-2S2		3S1-3S2	
A		1		1		1	
VA		10		10		10	
CL-KL		0.2		10P20		10P20	
Fs		5					

B Modelling of instrument transformers

Nameplate of transformer		
Name:	CT4	
Voltage level:	110 kV	

Strömberg				Laji-typ	
				KOTU 110 J2	
				N.o 593861	
	1	2	3	110/260	kV
A	4*100	4*100	4*100	50	Hz
A	5	5	5	I term	I dyn
VA	60	60	60	kA	kA
lk	0.5	0.5	1	4*10	4*25
kl					
n	<3	<3	>10		

B.2 Lists of performed measurements

Tab. 24 List of the measurements performed on the voltage transformers.

List of measurements- Voltage transformers			
Impulse tests	LCR-meter	Network analyser	Signal generator
-Ratio, (P-S1, P-S2)	-Capacitance meas-	-Impedances (all com-	-Ratio
-Open circuit, (P, S1, S2)	urements	binations of open and	-Open circuit meas-
-Short circuit, (P-S1, P-S2,)		short circuit measure-	urements
-Capacitance, (P-B, S1-B, S2-		ments, plus capacitance	
B, P-S1, P-S2, S1-S2)		measurement)	
Wave shape:			
all tests			
-1,2/50			
some tests:			
-250/2500			
-20/2500			

Tab. 25 List of the measurements performed on the current transformers.

List of measurements- Current transformers		
Impulse tests	Network analyser	Signal generator
-Ratio, (P-S1, P-S2, P-S3)	-Impedances (All combina-	-Ratio
-Open circuit, (P, S1,S2)	tions of open and short cir-	-Open circuit measurements
-Short circuit, (P-S1S2S3, S1-P, S2-P,	cuit measurements, plus	
S3-P)	capacitance measurement)	
-Capacitance, (P-S1, P-S2, P-S3, S1-		
S2, S1-S3, S2-S3, P-B, S1-B, S2-B,		
S3-B)		
-Test of voltage divider		
Wave shape:		
all tests		
-1,2/50		
some tests:		
-250/2500		
-20/2500		

B.3 Capacitance measurements of PT1

In this measurement a voltage wave was applied to the transformer in order to measure the impedances and hence the capacitance. The capacitances were calculated from the imaginary part of the measured impedances. The values were estimated from the most stable part of the capacitance curve (in each measurement there is a stable part between approximately 10 kHz and 1 MHz).

Estimated capacitances and the main resonance points for each connection:

Tab. 26 Capacitance measurement, overview.

Connection	Estimated capacitance [nF]	Main resonance [MHz]
P-S1	1.1	1,600
P-S2	1.1	1,700
S1-S2	2,8	0.950
P-b	0.6	2,200
S1-b	0.5	1,820
S2-b	0.5	1,885

Capacitance P-S1

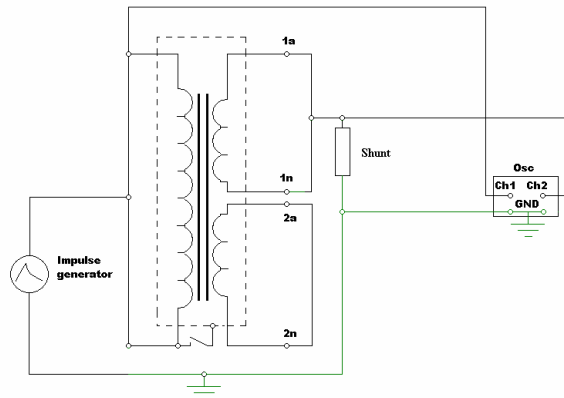


Fig. 104. Schematic diagram of the measurement setup

Tab. 27 Oscilloscope

	Measurement parameters	Probes	Input of Osc.
Channel 1	V	100:1	100:1, DC
Channel 2	I	1:1	1:1, DC

Tab. 28 Shunt.

T&M RESEARCH PRODUCTS, INC., 129 RHODE ISLAND NE, ALBUQUERQUE, NEW MEXICO 87108		
W-1T-5-1STUD	0,4905 Ω,	8532

Tab. 29. Measurement record

Sampling Frequency	Name of shown file	Comments
50 MHz	002	9.07 2003

Comments: The capacitance was estimated from the stable part of the capacitance curve to be:
 $C = 1.1 nF$

The main resonance point is: $f_1 = 1.6 MHz$

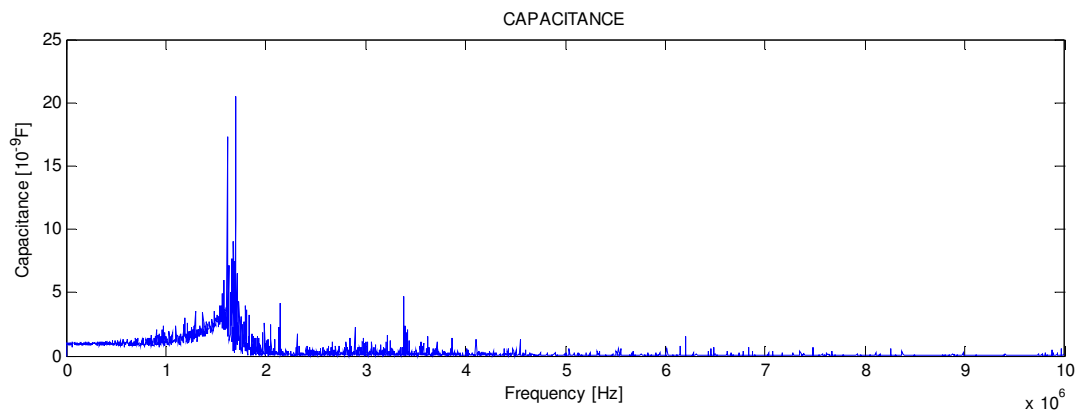


Fig. 105 The capacitance of the connection. PT002A, 50 MHz, 9.07 2003

Capacitance P-S2

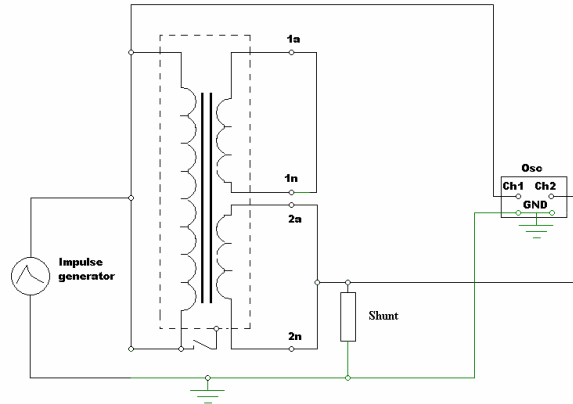


Fig. 106. Schematic diagram of the measurement setup

Tab. 30 Oscilloscope

	Measurement parameters	Probes	Input of Osc.
Channel 1	V	100:1	100:1, DC
Channel 2	I	1:1	1:1, DC

Tab. 31 Shunt

T&M RESEARCH PRODUCTS, INC., 129 RHODE ISLAND NE, ALBUQUERQUE, NEW MEXICO 87108		
W-1T-5-1STUD	0,4905 Ω,	8532

Tab. 32. Measurement record

Sampling Frequency	Name of shown file	Comments
1 MHz	003	9.07 2003

Comments: The capacitance was estimated from the stable part of the capacitance curve to be:
 $C = 1.1 nF$

The main resonance point is: $f_1 = 1.7 MHz$

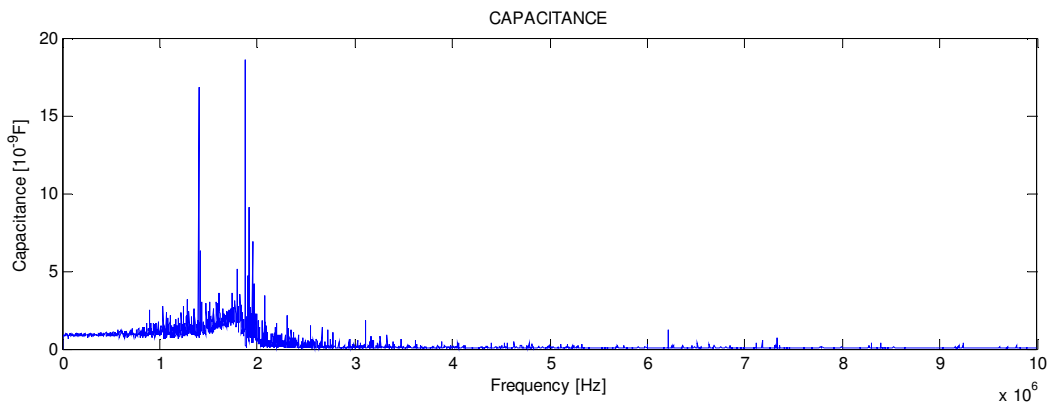


Fig. 107 The capacitance of the connection. PT003A, 1MHz, 9.07 2003

Capacitance S1-S2

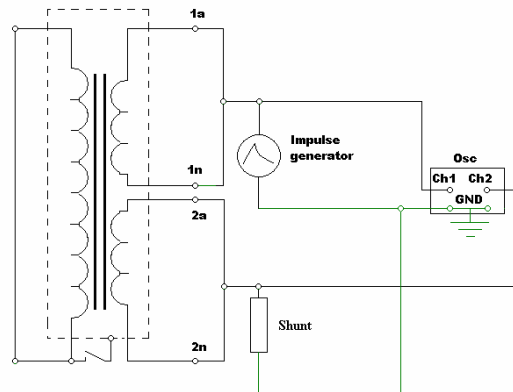


Fig. 108. Schematic diagram of the measurement setup

Tab. 33 Oscilloscope

	Measurement parameters	Probes	Input of Osc.
Channel 1	V	100:1	100:1, DC
Channel 2	I	1:1	1:1, DC

Tab. 34 Shunt.

T&M RESEARCH PRODUCTS, INC., 129 RHODE ISLAND NE, ALBUQUERQUE, NEW MXICO 87108		
W-1T-5-1STUD	0,4905 Ω,	8532

Tab. 35. Measurement record

Sampling Frequency	Name of shown file	Comments
5 MHz	037	17.07 2003

Comments: The capacitance was estimated from stable part of the capacitance curve to be:
 $C = 2.8 \text{ nF}$

The main resonance point is: $f_1 = 0.95 \text{ MHz}$

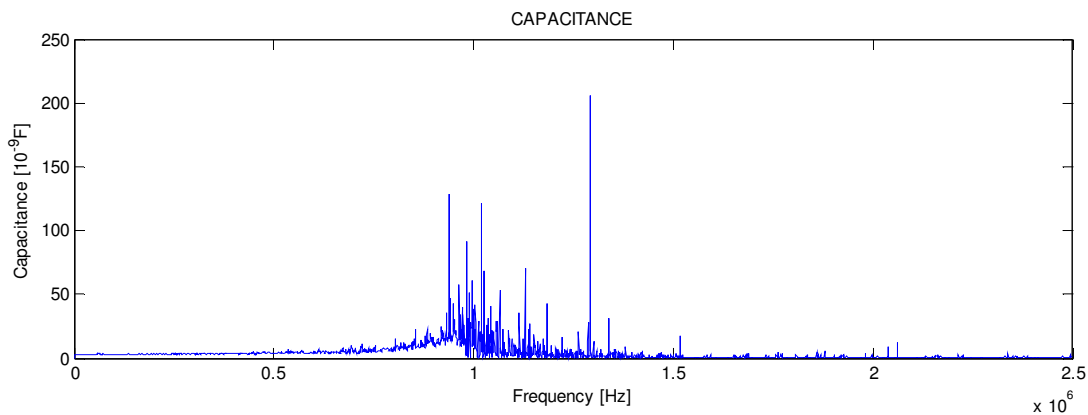


Fig. 109 The capacitance of the connection. 037A, 5 MHz, 17.07 2003

Capacitance P-B

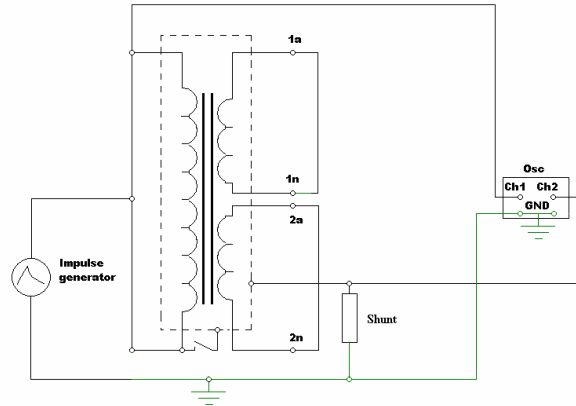


Fig. 110. Schematic diagram of the measurement setup

Tab. 36 Oscilloscope

	Measurement parameters	Probes	Input of Osc.
Channel 1	V	100:1	100:1, DC
Channel 2	I	1:1	1:1, DC

Tab. 37 Shunt

T&M RESEARCH PRODUCTS, INC., 129 RHODE ISLAND NE, ALBUQUERQUE, NEW MEXICO 87108		
W-1T-5-1STUD	0,4905 Ω,	8532

Tab. 38. Record from measurement

Sampling Frequency	Name of the file	Comments
10 MHz	002	9.07 2003

Comments: The capacitance was estimated from stable part of capacitance curve to be: $C = 0.6 \text{ nF}$
 The main resonance point is: $f_1 = 2.2 \text{ MHz}$

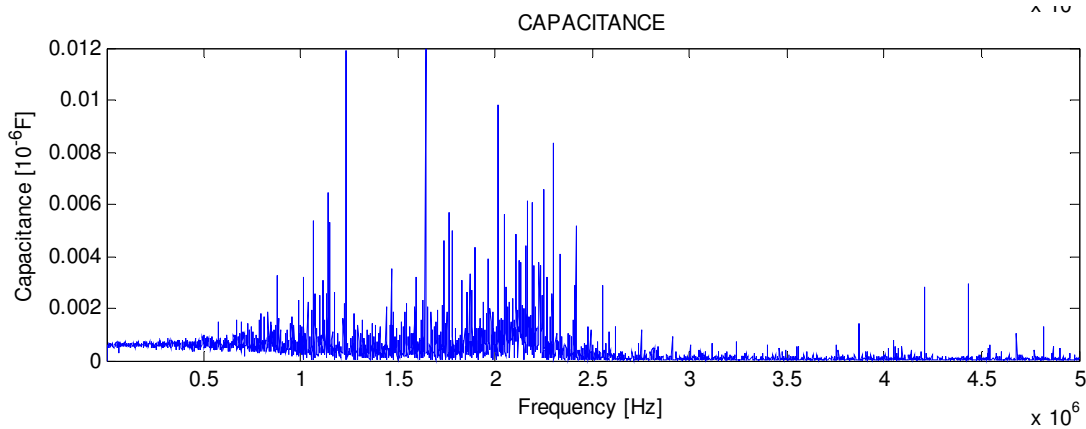


Fig. 111 The capacitance of the connection. 002A, 10 MHz, 9.07 2003

Capacitance S1-B

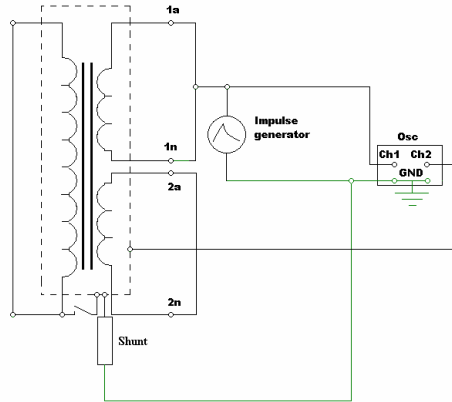


Fig. 112. Schematic diagram of the measurement setup

Tab. 39 Oscilloscope

	Measurement parameters	Probes	Input of Osc.
Channel 1	V	100:1	100:1, DC
Channel 2	I	1:1	1:1, DC

Tab. 40 Shunt

T&M RESEARCH PRODUCTS, INC., 129 RHODE ISLAND NE, ALBUQUERQUE, NEW MEXICO 87108		
W-1T-5-1STUD	0,4905 Ω,	8532

Tab. 41 Measurement record

Sampling Frequency	Name of shown file	Comments
10 MHz	003	9.7 2003

Comments: The capacitance was estimated from the stable part of capacitance curve to be:
 $C = 0.5 nF$

The main resonance point is: $f_1 = 1.82 MHz$

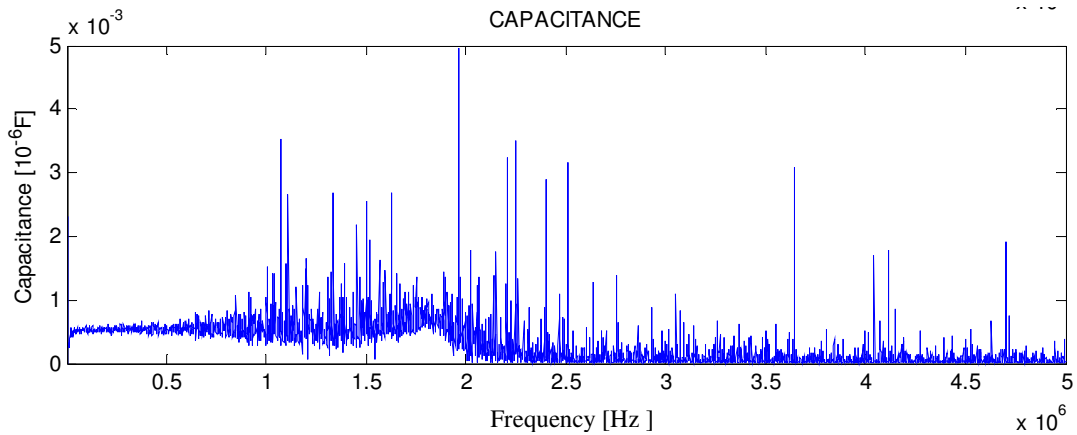


Fig. 113 The capacitance of the connection. 003, 10 MHz, 9.07 2003

Capacitance S2-B

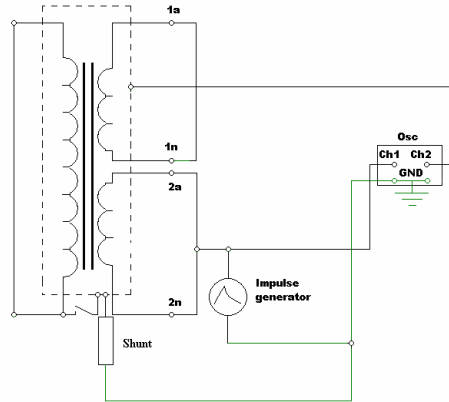


Fig. 114. The Schematic diagram of the measurement setup

Tab. 42 Oscilloscope

	Measurement parameters	Probes	Input of Osc.
Channel 1	V	100:1	100:1, DC
Channel 2	I	1:1	1:1, DC

Tab. 43 Shunt

T&M RESEARCH PRODUCTS, INC., 129 RHODE ISLAND NE, ALBUQUERQUE, NEW MXICO 87108		
W-1T-5-1STUD	0,4905 Ω,	8532

Tab. 44. Record from measurement.

Sampling Frequency	Name of the file	Comments
10 MHz	002	9.7 2003

Comments: The capacitance was estimated from stable part of capacitance curve to be: $C = 0.5 \text{ nF}$
 The main resonance point is: $f = 1,885 \text{ MHz}$

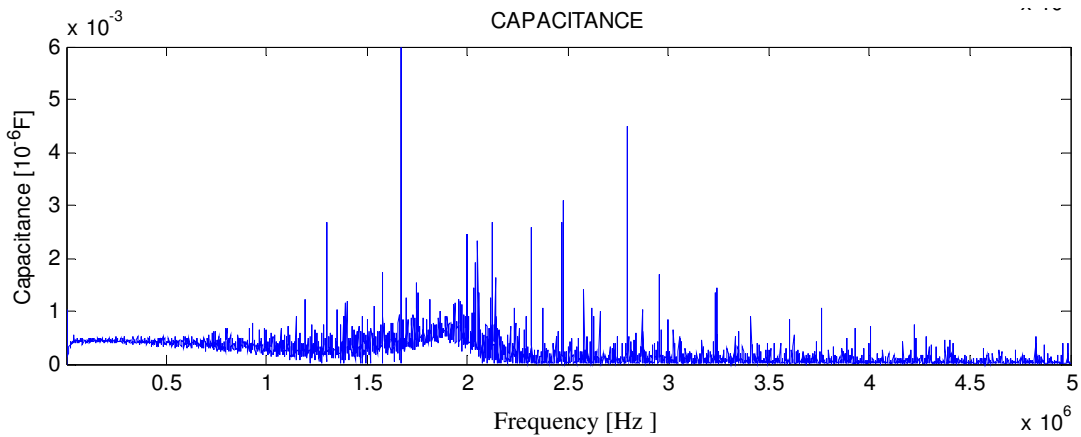


Fig. 115 The capacitance of the connection. 002A, 10 MHz, 9.07 2003

B.4 Detailed calculation of the PT's capacitances

The calculation of the capacitance C_{ps1} , shown in Fig. 46, uses the capacitance C_{12} , measured between the points 1-2, and the other capacitances shown in the same figure. The calculation starts with a Wye-Delta network transformation. The Wye capacitance network (Y: 1-4, 2-4, 3-4) from Fig. 46 must be transformed to a Delta network (which is in parallel with a Delta, Δ : 1-2, 2-3, 3-1). If the Wye-Delta transformation, shown in [9], is developed for capacitances, it can be written as:

$$SUM = C_{s2b} + C_{s1b} + C_{pb} \quad (63)$$

$$C_{ps1}' = C_{pb} C_{s1b} / SUM$$

$$C_{ps2}' = C_{pb} C_{s2b} / SUM \quad (64)$$

$$C_{s1s2}' = C_{s2b} C_{s1b} / SUM$$

Now both the Deltas are in parallel, therefore for the parallel capacitances we can write:

$$C_y = C_{ps2} + C_{ps2}' \quad (65)$$

$$C_x = C_{s1s2} + C_{s1s2}'$$

For the capacitances in series:

$$C_p = C_x C_y / (C_x + C_y) \quad (66)$$

The final measured capacitance between the corners 1-2 is:

$$C_{12} = C_{ps1} + C_{ps1}' + C_p \quad (67)$$

In general, the capacitance C_{ps1} can be expressed as a function of the measured capacitance C_{12} and all the capacitances from inside the capacitance network as:

$$C_{ps1} = f(C_{12}, C_{ps2}, C_{pb}, C_{s1s2}, C_{s1b}, C_{s2b}) \quad (68)$$

Or, if Eq. (67) is rewritten using Eqs. (63)-(66), we get:

$$C_{ps1} = C_{12} - \frac{C_{pb} C_{s1b}}{C_{pb} + C_{s1b} + C_{s2b}} - \frac{(C_{ps2} + \frac{C_{pb} C_{s2b}}{C_{pb} + C_{s1b} + C_{s2b}})(C_{s1s2} + \frac{C_{s2b} C_{s1b}}{C_{pb} + C_{s1b} + C_{s2b}})}{(C_{ps2} + C_{s1s2} + \frac{C_{s2b} C_{s1b} + C_{pb} C_{s2b}}{C_{pb} + C_{s1b} + C_{s2b}})} \quad (69)$$

Eq. (69) is the final equation for the PT model capacitance estimation based on measurements. The symbol explanations are the same as appear below Eq. (38).

B.5 Measurement of the cable capacitance

The capacitance of the cable connected to the secondary of the voltage transformer was measured in Fingrid’s 110 kV substation at Ruotsinkylä, Tuusula, Finland. In the substation, two cables are connected to the voltage transformer, one for measurement and one for protection purposes. The shields of both cables are grounded. The cable consists of 4 conductors, 3 for the phases and one return conductor, which is normally grounded. During the measurement the ground was disconnected from the return wire to reduce the possible influence of the ground on the measurement. The cables were open-ended during the test.

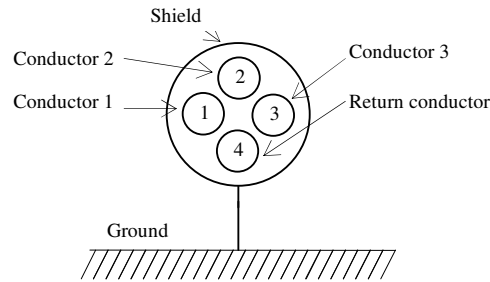


Fig. 116 Cable configuration.

Tab. 45 The capacitance of both the measurement and protection cables

Protection and measurement cable connected. Cable types: MLJM 4*10 and MLJM 4*4, App.length=75 m. Return wires are connected. Shield grounded.			
Between conductors:	Measured, [nF]	Error of meter on 200nF scale, [nF]	Capacitance, [nF]
1-2	20.1	1.1	19
1-3	22.9	1.1	21.8
2-3	23	1.1	21.9
1-return	22.9	1.1	21.8
2-return	22.8	1.1	21.7
3-return	20	1.1	18.9
Average:	21.95	1.1	20.85

Tab. 46 The capacitance of the measurement cable

Measurement cable. Cable type: MLJM 4*10, Shield grounded. App.length=75 m			
Between conductors:	Measurements, [nF]	Error of meter on 20nF scale, [nF]	Capacitance, [nF]
1-2	9.35	0.12	9.23
1-3	10.97	0.12	10.85
2-3	10.91	0.12	10.79
1-return	10.91	0.12	10.79
2-return	10.75	0.12	10.63
3-return	9.35	0.12	9.23
Average:	10.37	0.12	10.25

B Modelling of instrument transformers

Tab. 47 The capacitance of the protection cable

Protection cable. Cable type: MLJM 4*4, App.length=75 m, Shield grounded.			
Between conductors:	Measurements [nF]	Error of meter on 20nF scale, [nF]	Capacitance, [nF]
1-2	9.84	0.12	9.72
1-3	11.13	0.12	11.01
2-3	11.29	0.12	11.17
1-return	11.16	0.12	11.04
2-return	11.25	0.12	11.13
3-return	9.84	0.12	9.72
Average:	10.75	0.12	10.63

C Transient propagation in HV OH lines

C.1 Description of the overhead line

The high voltage overhead lines at the 110 kV level usually consist of three phase wires and two return overhead ground wires. A typical example of a Finnish pole is shown in Fig. 117.

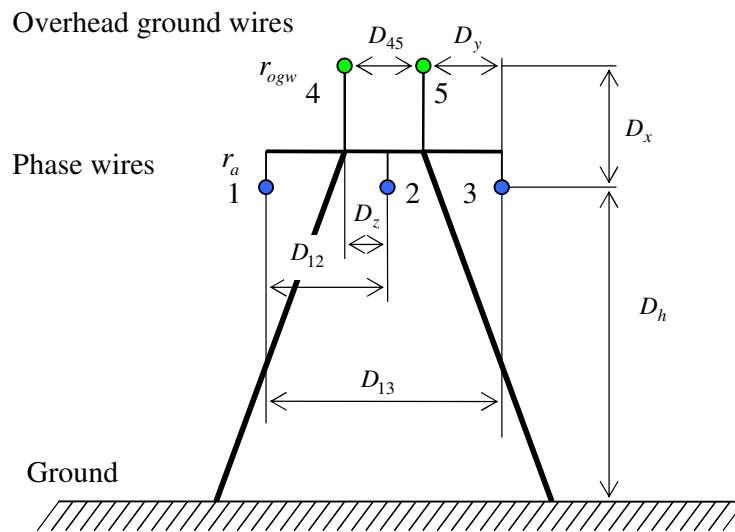


Fig. 117 Typical construction of 110 kV poles in Finland.

Tab. 48 Dimensions of 110 kV poles.

	Dimensions						
	D_x	D_y	D_z	D_{12}	D_{13}	D_{45}	D_h
Distances [m]	3.6	1.85	2	3.85	2*3.85	4	16.1

Note: All overhead ground conductors are connected in parallel and are grounded at regular intervals (each pole) along the line. The phase conductors are insulated from each other and from the ground.

$r_a = 1$ cm, Aluminium ($\rho_{Al} = 2.655 \times 10^{-8} \Omega\text{m}$, $\mu_r = 1$),

$r_{ogw} = 1$ cm, Aluminium ($\rho_{Al} = 2.655 \times 10^{-8} \Omega\text{m}$, $\mu_r = 1$), Steel ($\rho_{Fe} = 7.2 \times 10^{-7} \Omega\text{m}$, $\mu_r = 50$)

C.2 Detailed calculations of reduction factor

In order to simplify the derivation of the reduction factor, the three phase system of wires can be reduced to a single “composite phase wire -a” and the two overhead ground wires to a single “composite overhead ground wire -g”. The ground is represented by the “fictional ground conductor”, Fig. 118.

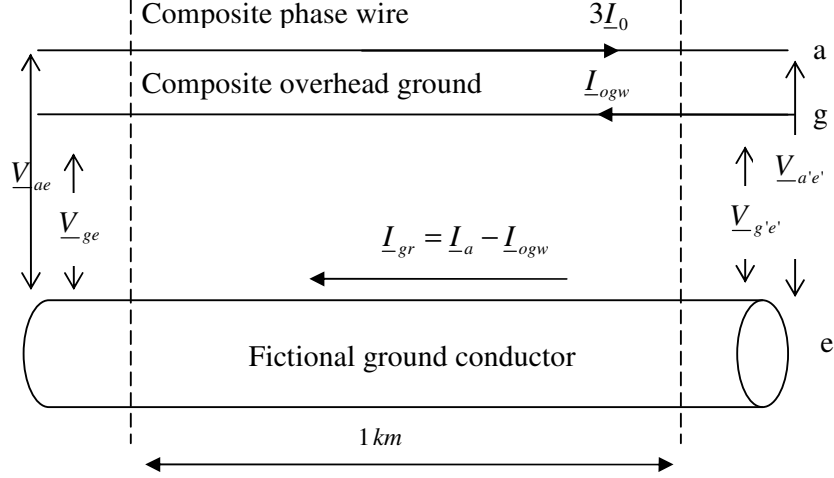


Fig. 118 Overhead conductor “a” with return circuit through the ground wire “g” in parallel with the ground represented by conductor “e”.

The voltage drop per kilometer of circuit ae, including the conductor a and the ground return in Eq. (70), and the voltage drop per kilometer of circuit ge, including the conductor g and the ground return in Eq. (71) and which is equal to zero, are:

$$\underline{V}_{ae} - \underline{V}_{a'e'} = 3\underline{I}_0 \underline{Z}_{aa} - \underline{I}_{ogw} \underline{Z}_{ag} \quad (70)$$

$$0 = \underline{V}_{ge} - \underline{V}_{g'e'} = 3\underline{I}_0 \underline{Z}_{ag} - \underline{I}_{ogw} \underline{Z}_{gg} \quad (71)$$

where:

\underline{Z}_{aa} is the self-impedance of the phase conductor-ground loop

\underline{Z}_{gg} is the self-impedance of the overhead ground conductor-ground loop

\underline{Z}_{ag} is the mutual impedance between the “phase conductor-ground loop” and the “overhead ground conductor-ground loop”

Solving Eqs. (70) and (71) we obtain the impedance of the single-phase circuit model.

$$\left(\underline{Z}_{aa} - \frac{\underline{Z}_{ag}^2}{\underline{Z}_{gg}}\right) = \underline{Z}_0 / 3 \quad (72)$$

The zero-sequence impedance \underline{Z}_0 of the original 3-phase system is therefore three-times greater than this impedance. i.e.,

$$\underline{Z}_0 = 3\left(\underline{Z}_{aa} - \frac{\underline{Z}_{ag}^2}{\underline{Z}_{gg}}\right) \quad (73)$$

Developing Eqs. (70), (71) and (73) in relation to Fig. 118, we can write the following equations for the return current in the overhead ground wire, Eq. (74), or the ground, Eq. (75), respectively. If $3\underline{I}_0$ is the sum of the zero-sequence currents in the phases, then:

$$\frac{\underline{I}_{ogw}}{3\underline{I}_0} = \frac{1 + \frac{\underline{Z}_{ag}}{\underline{Z}_{gg}}}{1 + \frac{\underline{Z}_{gg}}{\underline{Z}_{ag}}} \quad (74)$$

$$\frac{\underline{I}_{gr}}{3\underline{I}_0} = \frac{\frac{\underline{Z}_{ag}}{\underline{Z}_{gg}} - \frac{\underline{Z}_{gg}}{\underline{Z}_{ag}}}{1 + \frac{\underline{Z}_{gg}}{\underline{Z}_{ag}}} \quad (75)$$

Equation (75) can be further simplified (this is known as the reduction factor):

$$k_u = \frac{\underline{I}_{gr}}{3\underline{I}_0} = \frac{\frac{\underline{Z}_{ag}}{\underline{Z}_{gg}} - \frac{\underline{Z}_{gg}}{\underline{Z}_{ag}}}{1 + \frac{\underline{Z}_{gg}}{\underline{Z}_{ag}}} = \frac{\frac{\underline{Z}_{ag}^2 - \underline{Z}_{gg}^2}{\underline{Z}_{gg}\underline{Z}_{ag}}}{\frac{\underline{Z}_{ag} + \underline{Z}_{gg}}{\underline{Z}_{ag}}} = \frac{(\underline{Z}_{ag} - \underline{Z}_{gg})(\underline{Z}_{ag} + \underline{Z}_{gg})\underline{Z}_{ag}}{\underline{Z}_{gg}\underline{Z}_{ag}(\underline{Z}_{ag} + \underline{Z}_{gg})} = \frac{\underline{Z}_{ag} - \underline{Z}_{gg}}{\underline{Z}_{gg}} \quad (76)$$

where $3\underline{I}_0$ is the zero sequence current which consists of the current in each phase. The other indices are introduced in the next page.

When Eq. (76) is fitted with the variables \underline{Z}_{ag} and \underline{Z}_{gg} presented on the next page, we obtain the reduction coefficient:

$$k_u = \frac{\underline{I}_{gr}}{3\underline{I}_0} = \frac{R_{gr} + j\omega M_{ag} - (R_{ogw}/2 + R_{gr} + j\omega L_{gg})}{R_{ogw}/2 + R_{gr} + j\omega L_{gg}} = -\frac{(R_{ogw}/2 + j\omega(M_{ag} - L_{gg}))}{R_{ogw}/2 + R_{gr} + j\omega L_{gg}} \quad (77)$$

Symbol explanations

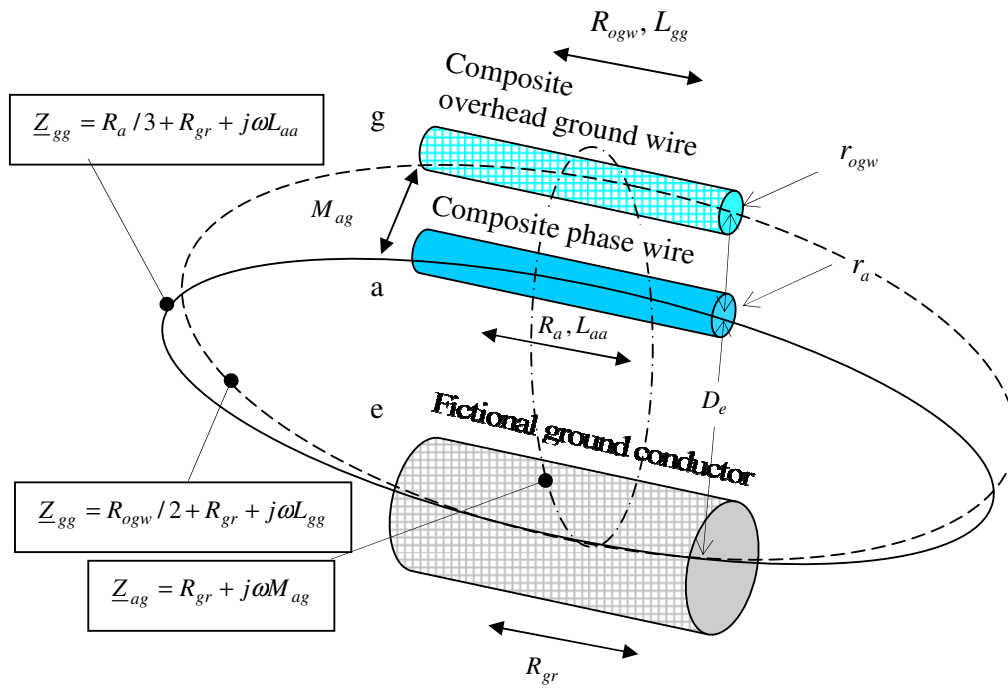


Fig. 119 Impedances and geometric distances in the model.

Impedances

- $\underline{Z}_{aa} = R_a / 3 + R_{gr} + j\omega L_{aa}$ Self-impedance of the phase conductor-ground loop
- $\underline{Z}_{gg} = R_{ogw} / 2 + R_{gr} + j\omega L_{gg}$ Self-impedance of overhead ground conductor-ground loop
- $\underline{Z}_{ag} = R_{gr} + j\omega M_{ag}$ Mutual impedance between the “phase conductor-ground loop” and the “overhead ground conductor-ground loop”

Inductances

- $L_{aa} = \frac{\mu_0 l}{2\pi} \ln \frac{D_e}{D_{aa}}$ Inductance of the phase conductor-ground loop
- $L_{gg} = \frac{\mu_0 l}{2\pi} \ln \frac{D_e}{D_{gg}}$ Inductance of overhead ground conductor-ground loop
- $M_{ag} = \frac{\mu_0 l}{2\pi} \ln \frac{D_e}{D_{ag}}$ Mutual inductance between the “phase conductor-ground loop” and the “overhead-ground conductor-ground loop”

GMD-Geometric mean distances

$D_{aa} = \sqrt[3]{r_a' D_{123}^2}$	Self GMD of the composite line conductor
$D_{gg} = \sqrt[3]{r_{ogw}' D_{45}}$	Self GMD of the composite ground wire
$D_{ag} = \sqrt[6]{D_{14}^4 D_{15}^2}$	GMD between line conductors and ground wires
$D_{123} = \sqrt[3]{D_{12} D_{13} D_{23}}$	Equivalent distance between the phase conductors

Geometric distances according to Fig. 117.

Radii

$r_a' = r_a e^{-1/4}$	Equivalent radius of phase conductor
$r_{ogw}' = r_{ogw} e^{-1/4}$	Equivalent radius of overhead ground wire

Ground calculations

$D_e = 658,5 \sqrt{\frac{\rho}{f}}$	Depth of the equivalent ground conductor
$R_{gr} = \omega \mu_0 l / 8$	Resistance of the ground return circuit
R_a	Resistance per km of the phase conductors

C.3 Detailed calculations for the matrix method

The impedance matrix components

$$\underline{Z}_{km} \begin{cases} R_{kk} + j\omega \frac{\mu_0}{2\pi} \ln\left(\frac{1}{D_{kk}}\right) & \text{for } k = m \\ -j\omega \frac{\mu_0}{2\pi} \ln\left(\frac{1}{D_{km}}\right) & \text{for } k \neq m, \text{ for } (k < 4 \text{ and } m > 3) \text{ or } (k > 3 \text{ and } m < 4) \\ +j\omega \frac{\mu_0}{2\pi} \ln\left(\frac{1}{D_{km}}\right) & \text{for } k \neq m, \text{ elsewhere} \end{cases}$$

The distance matrix calculations

Diagonal elements - GMR

$$\begin{aligned} D_{11} = D_{22} = D_{33} = D_a = r_a e^{-1/4} & \quad \text{GMR of phase wires} \\ D_{66} = D_{77} = D_{88} = D_a = r_a e^{-1/4} & \quad \text{GMR of phase wires in the ground} \\ D_{44} = D_{55} = D_g = r_{ogw} e^{-1/4} & \quad \text{GMR of ground wires} \\ D_{99} = D_{1010} = D_g = r_{ogw} e^{-1/4} & \quad \text{GMR of ground wires in the ground} \end{aligned}$$

Geometric distances between wires, 1/2 of the matrix

$$\begin{aligned} D_{12} = D_{23} = D_{67} = D_{78}, D_{13} = D_{68}, D_{45} = D_{910}, D_x, D_y, D_z, D_{kk'} = f(f, \rho), \\ D_{14} = D_{35} = D_{69} = D_{810} = \sqrt{D_y^2 + D_x^2}; D_{18} = D_{36} = \sqrt{(D_{kk'})^2 + (2D_y + 2D_z)^2}, \\ D_{15} = D_{34} = D_{610} = D_{89} = \sqrt{(D_y + 2D_z)^2 + D_x^2}; \\ D_{110} = D_{39} = \sqrt{(D_{kk'} - D_x)^2 + (D_y + 2D_z)^2}, \\ D_{17} = D_{28} = D_{37} = D_{26} = \sqrt{(D_{kk'})^2 + (D_y + D_z)^2}, \quad D_{19} = D_{310} = \sqrt{(D_{kk'} - D_x)^2 + (D_y)^2}, \\ D_{16} = D_{27} = D_{38} = D_{49} = D_{510} = D_{kk'} \\ D_{24} = D_{25} = D_{79} = D_{710} = \sqrt{(D_z)^2 + (D_x)^2}, D_{29} = D_{210} = \sqrt{(D_{kk'} - D_x)^2 + (D_z)^2}, \\ D_{46} = D_{58} = \sqrt{(D_{kk'} + D_x)^2 + (D_y)^2}, D_{47} = D_{57} = \sqrt{(D_{kk'} + D_x)^2 + (D_z)^2}, \\ D_{48} = D_{56} = \sqrt{(D_{kk'} + D_x)^2 + (2D_z + D_y)^2}, D_{410} = D_{59} = \sqrt{(D_{kk'})^2 + (2D_z)^2}, \end{aligned}$$

The second half of the matrix is symmetrical

$$D_{mk} = D_{km}, \text{ for } k, m = <1 \text{ to } 10>$$

Case parameters, (according to Fig. 59 and Fig. 117)

C.4 Carson's formula

C.4.1 Definition

Carson's formula is based on the following assumptions (more details can be found in [19],[20], [34]):

- a. The conductors are perfectly horizontal above ground, and long enough so that three-dimensional end effects can be neglected (this makes the field problem two-dimensional). The sag is taken into account indirectly by using the average height above ground.
- b. The aerial space is homogeneous without loss, with permeability μ_0 and permittivity ϵ_0 .
- c. The earth is homogeneous with uniform resistivity ρ , permeability μ_0 and permittivity ϵ_0 , and it is bounded by a flat plane with infinite extent, to which the conductors are parallel. The earth behaves as a conductor.
- d. The spacing between conductors is at least an order of magnitude larger than the radius of the conductors.

The elements of the series impedance matrix can be calculated from the geometry of the tower configuration, Fig. 117, and from the characteristics of the conductors.

For self impedances:

$$\underline{Z}_{ii} = \underline{Z}_{int} + \underline{Z}_{ext} + \Delta\underline{Z}_g \quad (78)$$

And for mutual impedances

$$\underline{Z}_{ij} = \underline{Z}_{ij}' + \Delta\underline{Z}_{gm} \quad (79)$$

where:

- | | |
|----------------------------|--|
| \underline{Z}_{int} | is the internal impedance of the wire, [Ω/m], |
| \underline{Z}_{ext} | is the external impedance of the wire, [Ω/m], |
| $\Delta\underline{Z}_g$ | is Carson's correction term for earth self impedance, [Ω/km], |
| \underline{Z}_{ij}' | is the mutual impedance of the two conductors i and j, [Ω/km], |
| $\Delta\underline{Z}_{gm}$ | is Carson's correction term for earth mutual impedance, [Ω/km], |

The symbols used in Eqs. (78) and (79) are explained in the following, Appendix C.4.2.

C.4.2 Terms and definitions

C.4.2.1 Terms in Eqs. (78) and (79)

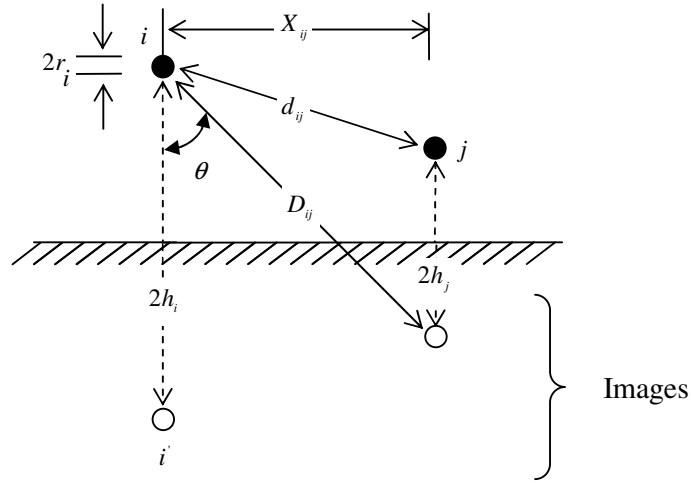


Fig. 120 Allocation of conductors i and j and their images.

The mutual impedance of conductors i and j , Fig. 120

$$\underline{Z}_{ij}' = j\omega \frac{\mu_0}{2\pi} \ln \frac{D_{ij}}{d_{ij}} \quad (80)$$

Internal and external impedance of a conductor

Internal impedance of conductor i

$$\underline{Z}_{int} = R_{int} + j\omega L_{int} = R_{int} + j\omega \frac{\mu_0}{2\pi} \left(\frac{1}{4}\right) \quad (81)$$

External impedance of conductor i , Fig. 120

$$\underline{Z}_{ext} = j\omega L_{ii} = j\omega \frac{\mu_0}{2\pi} \left(\ln \frac{2h_i}{r_i}\right) \quad (82)$$

Carson's correction terms for earth return effects

The ground self impedance

$$\Delta \underline{Z}_g = R_g + jX_g \quad (83)$$

The ground mutual impedance

$$\Delta Z_{gm} = R_{gm} + jX_{gm} \quad (84)$$

The symbols used in Eqs. (80) to (84) are explained in the following:

C.4.2.2 Terms in Eqs. (80) to (84)

Carson's correction terms for earth return effects

For self resistance

$$R_g = 4\omega \times 10^{-7} \left\{ \frac{\pi}{8} - b_1 k^1 + b_2 [(C_2 - \ln k)k^2] + b_3 k^3 - d_4 k^4 - \dots \right\} \quad (85)$$

For self reactance

$$X_g = 4\omega \times 10^{-7} \left\{ \frac{1}{2} (0.6159315 - \ln k) + b_1 k^1 - d_2 k^2 + b_3 k^3 - b_4 [(C_4 - \ln k)k^4] + \dots \right\} \quad (86)$$

For mutual resistance

$$R_{gm} = 4\omega \times 10^{-7} \left\{ \frac{\pi}{8} - b_1 k_m^1 \cos \theta + b_2 [(C_2 - \ln k_m)k_m^2 \cos 2\theta + \theta k_m^2 \sin 2\theta] \right. \\ \left. + b_3 k_m^3 \cos 3\theta - d_4 k_m^4 \cos 4\theta - \dots \right\} \quad (87)$$

For mutual reactance

$$X_{gm} = 4\omega \times 10^{-7} \left\{ \frac{1}{2} (0.6159315 - \ln k_m) + b_1 k_m^1 \cos \theta - d_2 k_m^2 \cos 2\theta + b_3 k_m^3 \cos 3\theta \right. \\ \left. - b_4 [(C_4 - \ln k_m)k_m^4 \cos 4\theta + \theta k_m^4 \cos 4\theta] + \dots \right\} \quad (88)$$

The symbols used in Eqs. (85) to(88) are explained in the following:

C.4.2.3 Terms of Eq. (85) to(88)

The coefficients b_i , C_i and d_i are constants which can be calculated as follows:

Coefficients b

$$b_1 = \frac{\sqrt{2}}{6} \quad (89)$$

$$b_2 = \frac{1}{16} \quad (90)$$

$$b_i = b_{i-2} \frac{\text{sign}}{i(i+2)}, \quad i = 3, 4, 5, \dots \quad (91)$$

Note sign= ± 1 and changes after each successive term (sign=1 for i=1,2,3,4 and sign=-1 for i=5,6,7,8 etc.)

Coefficients C

$$C_2 = 1.3659315 \quad (92)$$

and

$$C_i = C_{i-2} + \frac{1}{i} + \frac{1}{i+2}, \quad i = 4, 6, 8, \dots \quad (93)$$

Coefficients d

$$d_i = \frac{\pi}{4} b_i, \quad i = 3, 4, 5, \dots \quad (94)$$

Variables k and k_m are frequency related and are given by:

$$k = 4\pi\sqrt{5} \times 10^{-4} (2h_i) \sqrt{f / \rho} \quad (95)$$

and

$$k_m = 4\pi\sqrt{5} \times 10^{-4} (D_{ij}) \sqrt{f / \rho} \quad (96)$$

The angle is indicated in Fig. 120

$$\theta = a \sin(x_{ij} / D_{ij}) \quad (97)$$

Other symbols

h_i	is the average height above ground of conductor i , [m],
D_{ij}	is the distance between conductor i and the image of conductor j , [m],
d_{ij}	is the distance between conductors i and j , [m],
r_i	is the radius of conductor i , [m],
ω	is the angular frequency, [rad],
R_{int}	is the ac resistance of the conductor, [Ω /km],
L_{int}	is the internal inductance of the conductor, [H/km],
R_g	Carson's correction term for self resistance due to the earth, [Ω /km],
R_{gm}	Carson's correction term for mutual resistance due to the earth, [Ω /km],
X_g	Carson's correction term for self reactance due to the earth, [Ω /km],
X_{gm}	Carson's correction term for mutual reactance due to the earth, [Ω /km].

C.5 Line impedance transformation

The series impedance of the line is in a general matrix of $n \times n$ elements. After reducing the voltage drop over the ground and ground wires it can be written as follows:

$$\begin{bmatrix} \underline{[V_p]} \\ [0] \end{bmatrix} = \begin{bmatrix} \underline{[Z_A]} & \underline{[Z_B]} \\ \underline{[Z_C]} & \underline{[Z_D]} \end{bmatrix} \begin{bmatrix} \underline{[I_p]} \\ \underline{[I_n]} \end{bmatrix} \quad (98)$$

where $\underline{[V_p]}$ is the matrix of the voltage drops over the phase conductors, $[0]$ is the matrix of the voltages over the ground and overhead ground wires, equal to zero, $\underline{[I_p]}$ is the matrix of phase currents and $\underline{[I_n]}$ is the matrix of the currents in the ground or overhead ground wires. $\underline{[Z_A]}$ is the series impedance of the phase wires, always with dimensions 3×3 . $\underline{[Z_B]}$, $\underline{[Z_C]}$ and $\underline{[Z_D]}$ form the rest of the impedance matrix.

The transformation of the $n \times n$ series impedance matrix of the line into a 3×3 **series-phase impedance** is as follows:

$$\underline{[Z_p]} = \underline{[Z_A]} - \underline{[Z_B]} \underline{[Z_D]}^{-1} \underline{[Z_C]} \quad (99)$$

Transposition of the line

Normally the line is not transposed, therefore the transposition can be performed numerically by:

$$\underline{[Z_s]} = \frac{1}{3} \left(\begin{bmatrix} \underline{Z}_{p1,1} & \underline{Z}_{p1,2} & \underline{Z}_{p1,3} \\ \underline{Z}_{p2,1} & \underline{Z}_{p2,2} & \underline{Z}_{p2,3} \\ \underline{Z}_{p3,1} & \underline{Z}_{p3,2} & \underline{Z}_{p3,3} \end{bmatrix} + \begin{bmatrix} \underline{Z}_{p2,2} & \underline{Z}_{p2,3} & \underline{Z}_{p2,1} \\ \underline{Z}_{p3,2} & \underline{Z}_{p3,3} & \underline{Z}_{p3,1} \\ \underline{Z}_{p1,2} & \underline{Z}_{p1,3} & \underline{Z}_{p1,1} \end{bmatrix} + \begin{bmatrix} \underline{Z}_{p3,3} & \underline{Z}_{p3,1} & \underline{Z}_{p3,2} \\ \underline{Z}_{p1,3} & \underline{Z}_{p1,1} & \underline{Z}_{p1,2} \\ \underline{Z}_{p2,3} & \underline{Z}_{p2,1} & \underline{Z}_{p2,2} \end{bmatrix} \right) \quad (100)$$

The sequence impedances are then the diagonal elements of the matrix:

$$\underline{[Z_{sym}]} = \underline{[A]}^{-1} \underline{[Z_s]} \underline{[A]} \quad (101)$$

where:

The zero-sequence impedance $\underline{Z}_0 = \underline{Z}_{sym1,1}$


The positive-sequence impedance $\underline{Z}_1 = \underline{Z}_{sym2,2}$

The negative-sequence impedance $\underline{Z}_2 = \underline{Z}_{sym3,3}$

and

$$\underline{[A]} = \begin{bmatrix} 1 & 1 & 1 \\ 1 & a^2 & a \\ 1 & a & a^2 \end{bmatrix} \quad (102)$$

where $a = e^{2\pi j/3}$



ISBN 951-22-8370-0
ISBN 951-22-8371-9 (PDF)
ISSN 1795-2239
ISSN 1795-4584 (PDF)